ADVANCED CHARACTERIZATIONS FOR THE IDENTIFICATION OF CATALYST STRUCTURES AND REACTION INTERMEDIATES

by

Nicole LiBretto

A Dissertation

Submitted to the Faculty of Purdue University

In Partial Fulfillment of the Requirements for the degree of

Doctor of Philosophy

Davidson School of Chemical Engineering

West Lafayette, Indiana

August 2020

THE PURDUE UNIVERSITY GRADUATE SCHOOL
STATEMENT OF COMMITTEE APPROVAL

Dr. Jeffrey T. Miller, Chair

Davison School of Chemical Engineering

Dr. Rajamani Gounder

Davidson School of Chemical Engineering

Dr. Jeffrey Greeley

Davidson School of Chemical Engineering

Dr. Christina Li

Department of Chemistry

Approved by:

Dr. John Morgan

For my family

ACKNOWLEDGMENTS

The past four years have been an amazing journey, which would have not been possible without the support from others, acknowledged here.

I am incredibly thankful to have Jeff Miller as my advisor. His commitment to scientific discovery and my professional development has motivated me to exceed expectations and always take on new challenges. Through this, I have been involved with at least a dozen projects and was afforded the opportunity to work with leading scientists across the country. Jeff taught me how to design experiments, analyze data, and tailor presentations and reports. He encourages me to challenge conventional wisdom to creatively approach problems with innovative solutions. Most importantly, Jeff taught me to celebrate all successes, no matter how small.

I am grateful for my other committee members and other professors that I have interacted with during my PhD. Specifically, Dr. Rajamani Gounder, Dr. Jeffrey Greeley, and Dr. Christina Li have provided me with insightful technical discussions.

Several of my colleagues were irreplaceable during this experience. Dr. Evan Wegener and Dr. Stephen Purdy were my mentors when I first joined Jeff's group in 2016. They answered every silly question I had and taught me how to do everything from synthesizing catalysts, building reactors, and analyzing data. Dr. Guanghui Zhang has been a mentor to me. He always finds time to discuss new results, no matter how busy he is. His thorough understanding of chemistry and passion for teaching has helped me understand many of the catalytic systems I study.

I would like to acknowledge other members of the Miller group, who have each day at work more enjoyable. Dr. Zhenwei Wu and Dr. Laryssa Cesar were welcoming and friendly when I first joined the group and have since participated in many technical discussions with me. I also would like to acknowledge other current Miller group members for fun-filled companionship: Matt Conrad, Che-wei Chang, Kurt Russell, Junxian Gao, and Jiajing Kou.

I have also been fortunate enough to work with several collaborators who share contagious enthusiasm and motivation for progress: Yinan Xu, Arunima Saxena, Dr. Ravi Joshi. In addition, Johnny Zhuchen and Nicole Escorcia have been irreplaceable during this time, not only academically but also personally. I am grateful to have worked beside them for these last four years, whether it was practicing talks, building or running equipment, or just relaxing after a long day of meetings.

I would not have been successful without the help of three undergraduate students who have worked with me: Aubrey Quigley, Rhea Nargund, and Ethan Edwards. I will continue to be impressed by their ability to learn quickly with high levels of understanding. Working with them has been incredibly rewarding as it taught me how to communicate my ideas and teach other researchers. I was also able to watch them grow into independent researchers and mentors of their own. They readily accept responsibility and challenges to learn new things. While being excellent coworkers, they have also become great friends and I am excited to see how they proceed with their own academic and professional careers.

Finally, I would like to acknowledge my friends and family who have supported me throughout this journey. To all my friends here, the time we spent together has made my Purdue experience memorable. Thank you to my parents for their unwavering support and constant encouragement.

TABLE OF CONTENTS

8

LIST OF TABLES

LIST OF FIGURES

LIST OF ABBREVIATIONS

Elements

Au   Gold

C   Carbon

Co   Cobalt

Cr   Chromium

Cu   Copper

Fe   Iron

Ga   Gallium

H   Hydrogen

He   Helium

In   Indium

Ir   Iridium

Ni   Nickel

O   Oxygen

Pd   Palladium

Pt   Platinum

Re   Rhenium

Rh   Rhodium

Ru   Ruthenium

Sn   Tin

Ti   Titanium

V   Vanadium

Zn   Zinc

Zr   Zirconium

Chemical Compounds

CH_4 Methane

C_2H_4 Ethylene

C_2H_6 Ethane

C_3H_6 Propylene

C_3H_8 Propane

C_4H_8, $C_4=$ Butenes

C_4H_{10} Butane

C_6H_{12}, $C_{6=}$ Hexenes

CO   Carbon monoxide

D_2 Deuterium

H_2 Hydrogen

NH_3 Ammonia

OH   Hydroxide

SiO_2 Silica

Characterizations

DFT   Density functional theory

EPR   Electron paramagnetic spectroscopy

FT   Fourier transform

FWHM   Full width half maximum

IR   Infrared spectroscopy

RIXS   Resonant inelastic x-ray scattering

TEM   Transmission electron microscopy

TOR   Turnover rate

XAS   X-ray absorption spectroscopy

XRD   X-ray diffraction

XPS   X-ray photoelectron spectroscopy

Reactions

GHSV   Gas hourly space velocity

LAD   Light alkane dehydrogenation

PDH   Propane dehydrogenation

WHSV weight hourly space velocity

Units

Å   Angstrom

atm   atmospheres

a.u.   atomic units

ccm   cubic centimeters

eV   electron volts

g   grams

keV   kiloelectron volts

mL   milliliters

nm   nanometer

psig   pounds per square inch gauge

DEFINITIONS

1. **Absorption:** the process or action by which one thing absorbs or is absorbed by another

2. **Adsorption:** the process by which a solid holds molecule of a gas or liquid

3. **Alloy:** a metal made by combining two or more metallic elements

4. **Bimetallic Catalyst:** a metal made by combining two or more metallic elements

5. **Bronsted Acid:** a site that donates protons to form carbocations from hydrocarbons

6. **Chemisorption:** adsorption where the adsorbate is bound by chemical bonds

7. **Cossee-Arlman Mechanism:** (coordination-insertion mechanism) a form of oligomerization catalyzed by transition metal catalysts

8. **Dehydrogenation:** chemical reaction that involves the removal of hydrogen from an organic molecule

9. **Density Functional Theory (DFT):** a computational quantum mechanical modelling method used to investigate the electronic structure of many-body systems

10. **Dispersion:** a measurement of the number of exposed atoms on the catalyst surface

11. **Fourier Transform Infrared Spectrscopy (FTIR):** used to determine the functional group in any given organic sample given dipole moment exists as dipole moments that changes as function of time are capable of absorbing IR

12. **Hydrogenation:** a chemical reaction between molecular hydrogen (H_2) and another compound or element to saturate organic compounds

13. **Intermetallic Compound:** a type of alloy with an ordered structure

14. **Isotope:** two or more forms of the same element that contain equal numbers of protons but different numbers of neutrons in their nuclei, and hence differ in relative atomic mass but not in chemical properties (*i.e.* H_2 and D_2)

15. **Lewis Acid:** a site that accepts electrons to form carbocations from hydrocarbons

16. **Metallacycle:** oxidative coupling of two ethylene molecules at an electrophilic metal center affords a metallacyclopentane intermediate, which undergoes ethylene insertion to give a metallacycloheptane that eliminates 1-hexene

17. **Metathesis:** redistribution of fragments of alkenes by the scission and regeneration of C=C double bonds

18. **Olefin:** alkene; a hydrocarbon that contains one or more C=C double bonds

19. **Oligomerization:** The process of converting a monomer or a mixture of monomers into an oligomer

20. **Paraffin:** a hydrocarbon containing only C-C single bonds

21. **Physisorption:** an interaction between an adsorbate and catalyst surface that leaves the surface unchanged

22. **Schultz Flory Distribution:** the chain growth probability during oligomerization reaction

23. **Shale Gas:** natural gas trapped within shale formations

24. **Single Site:** a catalyst which contains an isolated ion with bonds only to the catalyst support

25. **Solid Solution:** a type of alloy with a disordered structure

26. **Transmission Electron Microscopy (TEM):** a powerful tool to measure the particle size, structure, and defects in nano materials which works by shining high energy electron beam through the sample to observe the interaction between electrons and atoms

27. **Turnover Rate (TOR):** the number of moles of reactant consumed/ mole of catalyst/ reaction time

28. **X-ray Absorption Spectroscopy (XAS):** widely used technique for determining the local geometric and/or electronic structure of materials; usually performed at synchrotron radiation facilities

29. **X-ray Diffraction (XRD):** rapid analytical technique primarily used for phase identification of a crystalline material and can provide information on unit cell dimensions

ABSTRACT

In recent decades, alternatives to traditional coal and fossil fuels were utilized to reduce carbon emissions. Among these alternatives, natural gas is a cleaner fuel and is abundant globally. Shale gas, a form of natural gas that also contains light alkanes (C2-C4), is presently being employed to produce olefins, which can be upgraded to higher molecular weight hydrocarbons. This thesis describes efforts to develop new catalytic materials and characterizations for the conversion of shale gas to fuels.

In the first half, silica supported Pt-Cr alloys containing varying compositions of Pt and Pt_3Cr were used for propane dehydrogenation at 550°C. Although a change in selective performance was observed on catalysts with varying promoter compositions, the average nano-particle structures determined by *in situ*, synchrotron x-ray absorption spectroscopy (XAS) and x-ray diffraction (XRD) were identical. Further, this work presents a method for the characterization of the catalytic surface by these methods to understand its relationship with olefin selectivity. From this, we can gain an atomically precise control of new alloys compositions with tunable surface structures.

Once formed by dehydrogenation, the intermediate olefins are converted to fuel-range hydrocarbons. In the second half, previously unknown single site, main group Zn^{2+} and Ga^{3+} catalysts are shown to be effective for oligomerization and the resulting products follow a Schutlz Flory distribution. Mechanistic studies suggest these catalysts form metal hydride and metal alkyl reaction intermediates and are active for olefin insertion and β-H elimination elementary steps, typical for the homogeneous, Cossee-Arlman oligomerization mechanism. Evidence of metal hydride and metal alkyl species were observed by XAS, Fourier transform infrared spectroscopy (FTIR), and H_2/D_2 isotope exchange. Understanding the reaction intermediates and elementary steps is critical for identifying novel oligomerization catalysts with tunable product selectivity for targeted applications.

Through controlled synthesis and atomic level *in situ* characterizations, new catalysts compositions can be developed with high control over the resulting performance. An atomically precise control of the catalyst structure and understanding how it evolves under reaction conditions can help shed light on the fundamental principles required for rational catalyst design.

1. INTRODUCTION

Energy is vital to sustain the quality of life held in modern society and meet household, industrial, and transportation demands. The growing population and desire to improve the standard of living will continue to drive increased energy consumption. While these needs have been traditionally met by burning fossil fuels (petroleum, coal, and natural gas), environmental concerns necessitate emission controls and strict regulations on energy production. Although capital costs for renewable energy sources are becoming more economically feasible, the infrastructure is not yet in place to substitute conventional energy sources. Instead, better utilization of fossil fuels can lead to the extended lifetime of these energy reserves with a lower environmental impact.

Natural gas is among the cleanest fossil fuels and is domestically available in the United States. The increased substitution of coal with natural gas will lead to reduced air pollution, including the emission abatement of CO_2, NO_x, and SO_x, while maintaining a similar energy output. Because natural gas leads to lower air pollution emissions, there has been an increased natural gas use for electric power and transportation within in the United States. For instance, in 2019, the average natural gas consumption was approximately 85 billion cubic feet of natural gas per day and is expected to increase by about 1.7% in 2020.

In the United States, shale gas – a form of natural gas found in shale reserves in as many as 30 states– is readily available with the largest amounts produced in Texas, Pennsylvania, Oklahoma, Louisiana, and Ohio. While shale gas contains mostly methane (up to 80%), it also contains other light hydrocarbons including ethane, propane, and butane, which can be converted to higher molecular weight products.

1.1 Catalytic Shale Gas Conversion

1.1.1 Shale Gas Boom

In the past decade, a shale gas revolution occurred in the United States leading to increased domestic production. Shale gas is an unconventional type of natural gas extracted from shale gas deposits by horizontal drilling, hydraulic fracturing, and micro seismic monitoring. Shale gas provides an abundant supply of methane (up to 80%), but also a considerable amount of other light

hydrocarbons (ethane, propane, and butane, up to 20%).[1–4] The latter has had a large impact on the chemical industry, as these light alkanes can be upgraded to olefins, which can be further converted to petrochemicals and fuel products by oligomerization.[4,5] The recent shale gas boom led to lower natural gas prices and promoted increased total olefin production by the implementation of light alkane dehydrogenation (LAD), an on-purpose production method. This has also helped replace traditional steam cracking feeds of oil-based naphtha with shale-based ethane.

Advancing technologies have facilitated increased shale gas production in the United States. As of 2018, shale gas production in the United States increased to from approximately 79 billion cubic feet per day (bcfd) in 2014 to 95 bcfd. This is in excess compared to the need of feed steam cracking plants, allowing for surplus shale gas to be exported.

The rapidly increasing availability of shale gas has sparked industrial and academic research for better utilization of shale resources. Due to insufficient processing and distribution infrastructures, the gas reserves in isolated shale basins currently offers little usable potential. The ability for on-site gas-to-liquid conversion would allow for the transportation of usable products from shale gas without modifying the current infrastructure. Within the last four years, the National Science Foundation (NSF) funded the Center for Innovative and Strategic Transformation of Alkane Resources (CISTAR), an engineering research center led by Purdue University, to develop chemical processes for the economical production of valuable products from shale gas. CISTAR currently envisions a modular, local, and highly networked processing plant for the conversion of light alkanes to higher molecular weight olefins by dehydrogenation, followed by oligomerization, in two separate reaction steps under different process conditions. The aim of this thesis is to explore the active catalytic structures and reaction intermediates of materials used to both produce and convert olefins.

1.2   Alkane Dehydrogenation to Produce Olefins

The conversion of light alkanes is facilitated by the activation of a carbon-hydrogen (C-H) bond, which can be performed by steam reforming, halogenation, and oxidative and non-oxidative dehydrogenation. Non-oxidative dehydrogenation is the most efficient pathway to convert alkanes to olefins. Dehydrogenation converts one mole of light alkane (*i.e.* ethane, propane, butane) to the corresponding olefin and hydrogen (Equation 1.1). This on-purpose production of light olefins is an important step in the production of value-added chemicals.

$$C_3H_8 \leftrightarrow C_3H_6 + H_2 \qquad (\Delta H_{298}= 124.3 \text{ kJ/mol}) \qquad\qquad \text{Equation 1.1}$$

$$C_3H_8 + H_2 \rightarrow CH_4 + C_2H_6 \qquad (\Delta H_{298}= -53.7 \text{ kJ/mol}) \qquad\qquad \text{Equation 1.2}$$
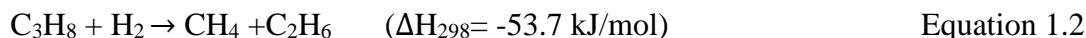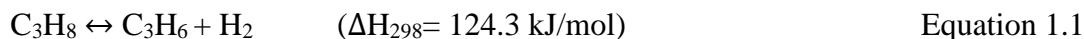
Propane dehydrogenation is a highly endothermic and the equilibrium-limited reaction ($\Delta H_{298}= 124.3$ kJ/mol) requires high reaction temperatures (>500 ºC) to achieve high equilibrium conversion (50-65%). Higher partial pressures of propane lead to lower equilibrium conversions. Once H_2 is produced, propane can form CH_4 and C_2H_6 (hydrogenolysis), which is more thermodynamically favored (Equation 1.2). These side products, which occur from carbon-carbon (C-C) bonds breaking, degrade the chemical value of the resulting products. Higher concentrations of H_2 typically lead to higher rates of side reactions and lower olefin selectivity.

Most monometallic catalysts favor hydrogenolysis. Therefore, catalyst selection for LAD reactions requires the C-H bond activation to be much more favorable than the C-C bond activation.[2,5] This is achieved on both noble metal based bimetallic Pt catalysts and metal oxides.[6–8] The former is known to typically have higher rates, longer lifetime, and higher olefin selectivity (Table 1.1).

Table 1.1. Comparison of noble metal based bimetallic Pt catalysts and metal oxides[1]

Active Component	Promoter Pt	Metal Oxides
Selectivity (%)	90-100	80-100
TOR (s^{-1})	10^{-1}	10^{-5}
Deactivation rate (h^{-1})	0.01	0.1
Life (h)	100	0.5
Space velocity (h^{-1})	10	1

Two alkane dehydrogenation technologies that dominate propylene production are UOP's Oleflex process and Lummus Catofin process, utilizing Pt-Sn and Cr_2O_3/SiO_2 respectively.[5,9] The lower rate of Cr_2O_3/SiO_2, and its susceptibility to rapid poisoning, ultimately increased interest in bimetallic catalysts, like Pt-Sn, containing a promoted noble metal.[1] Because the desired olefins are more reactive than alkanes, undesired side reactions including hydrogenolysis, and coking typically occur, which leads to lower olefin selectivity.

1.2.1 Bimetallic Catalysts for Light Alkane Dehydrogenation

Monometallic noble metal catalysts, such as Pt nanoparticles, have high rates for LAD, but poor olefin selectivity and unsatisfactory stability. When a second metal, or promoter, is added to modify the Pt crystal structure, higher olefin selectivity is typically observed. Sn is the most widely studied promoter, and commercial processes utilize supported Pt-Sn catalysts. This post-transition metal is known to modify the Pt active sites, and consequently suppress hydrogenolysis and isomerization reactions while minimizing sintering.[1,10] The Sn promoter also neutralizes the support and prevents coke from deactivating the dehydrogenation reaction. It is believed that Sn electronically modifies Pt by transferring electrons to the valence band, which enhances olefin desorption and suppresses dissociative adsorption of alkanes.[1,11] In addition, proposed geometric effects suggest that the addition of Sn causes a reduction in the ensemble size by alloying with Pt and covering low coordination sites on the Pt.[11] Likewise, particles utilized on the nanoscale (<50 nm) exhibit size effects. The properties of nanoparticles, which are generally different than those of bulk materials, cannot be predicted based on periodic trends. Consequently, definitive conclusions explaining the improved performance of Pt-Sn catalysts compared to Pt alone have not been determined because the interactions between the metal nanoparticles are not widely studied.[3] The literature surrounding the use of bimetallic catalysts fails to address their specific structures resulting in a limited understanding of the impact the dual-metal system has on catalytic performance.

Both geometric and electronic arguments have been proposed to explain the properties of highly selective catalysts. Geometric effects involve the size of the Pt-ensemble, or the number of adjacent Pt atoms. C-C bond breaking requires Pt ensembles containing five or six Pt atoms.[12,13] When a bimetallic catalyst is formed, the size of the Pt ensemble is reduced and C-H bond breaking becomes more favorable, resulting in improved selectivity towards olefins. This is because dehydrogenation is a structure insensitive reaction, requiring only a single Pt atom to occur. As the promoter reduces the size of Pt ensembles, the structure sensitive reaction, hydrogenolysis, is inhibited, while the structure insensitive reaction, dehydrogenation, remains unchanged.

Electronic effects are associated with changes in the energy of the Pt 5d orbitals and changes in adsorption energies of Pt.[14] Bimetallic catalysts often lead to lower adsorption energies, resulting in less coking and the attenuation of hydrogenolysis both of which favor higher olefin selectivity.

Other post-transition metals have been studied as promoters when paired with Pt in the alkane dehydrogenation. Most notably, Zn has similar effects as a promoter on Pt to those of Sn in that it prevents undesired side reactions and limits coke formation.[1,11] Additional post-transition metal promoters include Ga and In, which are expected to function analogously to Sn, but are thought to have weaker electronic effects.[1]

1.2.2   Bimetallic Catalysts: History and Opportunity

Because structure-property relationships have not yet been determined for bimetallic catalysts, the chemical and electronic behavior of these materials relative to their parent materials cannot be determined without catalyst development and, consequently, they have gained considerable interest. Previous work indicates that improved catalytic performance of bimetallic catalysts is attributed to the isolated noble metal.[3] When two metals are combined there is a change in metal-metal (M-M) bond length and the structural changes may occur such that metal atoms receive different neighbors. Ultimately the functionality of each catalyst is dependent on the interactions between the metals and the support, in addition to particle size. This class of catalysts is expected to promote structure insensitive reactions (dehydrogenation), while inhibiting structure sensitive reactions (hydrogenolysis), thus yielding high olefin selectivity during dehydrogenation and inhibiting the formation of undesired products.[1]

As early as the 1960s, bimetallic catalysts of various compositions were investigated to understand how different combinations of metal pairs improve the catalytic performance compared to their monometallic counterparts. At the time, few characterizations were able to precisely identify the catalyst structure, especially that on the active catalytic surface, leading to an incomplete understanding of the resulting nanoparticle structures.

Early bimetallic catalysts include Pt-Re and Pt-Ir, which were extensively studied for naphtha reforming. Typically, H_2 and CO chemisorption was performed on these catalysts to identify changes in the adsorption character on modified surfaces. Early understanding of bimetallic catalysts is explained by the rigid band theory, which emphasizes the concept of d character leading to changes in adsorption properties. This incorrectly ascribed that there was significant electron transfer between the active metal and its promoter, which was later proved wrong with XPS studies.

The ensemble effect was later investigated by John Sinfelt. His early work on bimetallic catalysts found that the addition of small concentrations of Cu to Ni nanoparticles led to improved

alkane hydrogenolysis activity.[15] This was explained by Cu reducing the number of neighboring Ni atoms. However, the earliest studies on bimetallic catalysts including groups 8 -10 elements such as Ni and Cu often formed solid solutions, where a lack of precise control over the resulting nanoparticle morphologies inhibit the understanding of bimetallic formation.

Here, a few definitions become important for understanding the different morphologies of such catalysts. A bimetallic catalyst describes a nanoparticle containing two metals. A bimetallic catalyst can either have an ordered structure, where an intermetallic compound is formed, or a disordered structure, where a solid solution is formed. Solid solutions (Pt-Cu, Ni-Cu) often form due to mutual solubility and usually occur between metals with the same crystal structure (*e.g.* FCC). Other combinations of metals such as Ru-Cu, Pt-Re, Pt-Ir, and Pt-Sn do not have mutual solubility and it was initially believed that there were two individual layers each containing a different metal.[16–18]

As the characterization capabilities advanced, it was found that, at least under reforming conditions (*i.e.* in H_2), ordered alloy phases were achieved. A combination of bulk characterizations including transmission electron microscopy (TEM) and x-ray absorption spectroscopy (XAS) have been used to identify the local arrangement of atoms in bimetallic catalysts to understand the specific geometric structure under reaction conditions. Similarly, both techniques can be used to identify the energy of the unoccupied states in nanoparticles. Atomic resolution TEM can be used to map the electron density in nanoparticles but is challenging to perform on < 5 nm nanoparticles. XAS also does not provide information about the occupied electron states. These techniques can be coupled with x-ray diffraction (XRD) to determine the long-range order leading to appropriate phase identification. *In situ* and operando capabilities for all these techniques have also led to an understanding of the average nanoparticle structures under reaction conditions.

Early research on bimetallic catalysts can be used for important insight in understanding these corresponding geometric and electronic structures with modern characterization capabilities. In recent years, our group has made significant effort to deconvolute the geometric and electronic effects of bimetallic nanoparticles to determine what controls high olefin selectivity in dehydrogenation.[3,19–25] Through this, an atomic level understanding of the resulting materials is being developed, which will aid further catalyst development. For this, identifying the precise catalyst structure is important.

1.2.3 Identification of Precise Catalytic Structures

Identifying the bulk and surface structures of nanoparticles is key to understanding their selective performance and could ultimately lead to further atomic control in the synthesis of bimetallic catalysts. Approaches for characterization of the nanoparticle surface are needed to better understand bimetallic catalysts and their performance. In many cases, the combination of metals improves the catalytic behavior compared to their monometallic substituents, but few characterizations are performed to precisely identify the resulting structure, and especially that of the catalytic surface. In recent years, improvements in nanoparticle synthesis to control the particle size and metal incorporation, have led to a better understanding of the atomic order of nanoparticles.[8,26] For instance, core-shell structures, solid solutions, and intermetallic alloys, of which several structures may be possible, can be formed depending on the metal pairs and synthesis conditions. The determination between these structures is often subtle, especially in nanoparticles.[3,11,21]

Determining the atomic distribution and alloy structures of supported bimetallic nanoparticles is challenging and requires a combination of techniques to identify the specific phases present. For instance, XAS has been used to determine if a bimetallic phase is achieved, and the specific phases can be confirmed by *in situ* synchrotron XRD.[2,3,21–23,27,28] The use of synchrotron radiation leads to a high signal-to-noise ratio in small nanoparticles of less than 2 nm and thus, it is possible to resolve the atomic order.[2] These characterizations, however, are not sufficient to determine the nanoparticles surface structure, especially when it differs from the average composition. For example, surface segregation, or when the two metals de-alloy causing one to preferentially move to the surface, is possible. This could lead to changes in the surface compared to the average composition and structure, which has been reported for Pt-Au, where the alloy exhibited a Pt-rich alloy core with Au-rich shell.[18] Alternatively, when the alloy structure is maintained the nanoparticle may exist as a core-shell structure, which could behave differently from a full alloy of the same structure.[18] While the commercial Pt-Sn catalyst has high initial selectivity (>90%), frequent regeneration leads to the deactivation of surface sites, resulting in low yield due to poor thermal stability and decreased selectivity.[9] This further suggests a subsequent change in the surface structure, contributing to different catalytic performance. Similar results have been observed on bimetallic catalysts containing other post transition metal promoters (*i.e.* In, Ga, Zn).

In the first part of this thesis, a method for identifying the catalytic surface using synchrotron XAS and XRD of Pt-based nanoparticles has been developed to explain changes in catalytic reactivity. Bulk characterization methods revealed that the catalysts had similar morphologies, despite having different catalytic selective performance behaviors. To distinguish the active catalytic surface, a new approach by difference analysis was developed. It was revealed that although the average nanoparticle structures were similar, their specific morphologies varied slightly. Through this partial core shell structures were distinguished from core shells and full alloys. Beyond that, this technique allows us to estimate the fractional composition of alloy in a nanoparticle and shell thickness in core shell nanoparticles. From this understanding, we can gain an atomic precise control of the alloys we synthesize, which will ultimately allow for more tunable surface structures and enhanced selectivity towards the desired product.

1.3   Olefin Transformation by Oligomerization

The oligomerization of olefins is of high academic and industrial interest because it produces the building blocks of industrial and consumer products including plastics, detergents, lubricants, petrochemicals, and a variety of industrial chemicals.[29] Oligomerization is the process by which short chain olefins (like ethylene (C_2H_4) and propylene (C_3H_6)) are converted to intermediate chain-length olefins. This chain growth depends on the number of reacting molecules. For example, in C_2H_4 oligomerization, at low conversions, two C_2H_4 molecules combine to form butenes (C_4H_8), but low molar concentrations of C_4H_8 inhibits further chain growth. At higher conversions, when enough C_4H_8 is produced, it can either combine with C_2H_4 or another C_4H_8 to form hexenes (C_6H_{12}) or octenes (C_8H_{16}) and so on. If only oligomerization occurs with an even number carbon reactant, then only products containing even numbers of carbons are possible. Similarly, C_3H_6 oligomerization would yield a normal distribution of hexenes (C_6H_{12}), nonenes (C_9H_{18}) and so on.

The conversion of short chain olefins (formed from steam cracking, fluid catalytic cracking, dehydrogenation, Fischer Tropsch processes, *etc.*) to long chain hydrocarbons, has been of considerable interest in the past. Fuel products have been produced by oligomerization since the early 1930s.[30] Linear alpha olefins, which can be produced by ethylene oligomerization, are also of interest in the petrochemical industry, where millions of tons are produced annually.[31,32] Oligomerization is a necessary step to produce the precursors for many consumer products.

Current commercial oligomerization catalysts are mainly based on homogeneous catalysts including nickel (Ni), titanium (Ti), zirconium (Zr), and chromium (Cr). These catalysts show high activity and selectivity towards linear alpha olefins, although it is difficult to control the resulting chain length.[33]

For example, the Shell Higher Olefin Process (SHOP) utilizes Ni-based organometallic complexes, bearing a chelating ligand with a neutral phosphine and an anionic oxygen donor.[34] The critical discovery by Karl Ziegler and Heinz Martin that titanium chloride, in combination with aluminum ethyl chloride $Al(C_2H_5)_2Cl$ catalyzes the conversion of ethylene to 1-butene with high selectivity, paved the way for the Ziegler type of catalysts.[35] Various combinations of these have been used for the development of commercial processes. For example, the Alphabutol process is used to convert ethylene to 1-butenes with Ti catalysts. This is also performed using Zr-alkoxides, which have lower activity, but comparable selectivity.[31] The Gulfene and Ethyl processes by Chevron Phillips and Ineos respectively also utilize these catalysts. The relatively newer processes by IFP Energies nouvelles (IFPEN) and SABIC-Linde developed processes based on a Ziegler catalytic system composed of a Zirconium precursor, a ligand, and an Aluminum co-catalyst.[35] Cr-based catalysts can also be used for ethylene trimerization to produce 1-hexene.[36] For example, the Phillip's catalyst, Cr/SiO_2, is the only catalyst that can perform this commercially and is responsible for producing 47000 tons per annum of 1-hexene.[31]

After the commercial successes of Ni and Cr, other transition metal catalysts involving cobalt (Co) and iron (Fe) are also being explored as potential oligomerization catalysts, but the catalysts require activation with additional ligands. Current homogeneous oligomerization catalysts require the use of catalyst activators, as well as additional separation steps to recover and regenerate the catalysts, both of which are economically and practically infeasible.

To address this, the heterogeneous counterparts have been extensively studied on a variety of metals and supports. Among many transition metals utilized for ethylene oligomerization, nickel catalysts supported on silica, silica-alumina, and various zeolites have shown high activity.[37] Typically this is performed at low temperatures (150°C -250°C) and high pressures (0.5 atm – 15 atm) in batch and flow reactors, no reports have high temperature (> 450°C) oligomerization have been made.[38]

1.3.1   Heterogeneous Oligomerization Catalysts

Significant effort has been devoted to the development of heterogeneous oligomerization catalysts. These catalysts can be described in three general categories: 1) solid acids 2) Ni complexes immobilized on a support and 3) Ni supported inorganic porous materials. Bifunctional catalysts containing metallic and acid sites are also utilized to evoke different product distributions and catalysts lifetimes.[33]

Acid catalysts include supported phosphoric acid and zeolites have a high potential to oligomerize propylene. However, at mild reaction conditions, the oligomerization rate of ethylene is much lower than on other olefins because the initial activation involves highly unstable primary carbocation intermediate. This requires higher reaction temperatures, which are also known to catalyze various side reactions including isomerization, disproportionation, cracking, and aromatization. Such catalysts also rapidly deactivate by coke formation.

Supported Ni complexes suffer from lower rates and poorer olefin selectivity than their homogeneous analogs. Typically, supported Ni catalysts are highly selective towards butenes, whereas, higher molecular weight products are necessary to produce fuel products. This has led to extensive studies on Ni-based oligomerization catalysts to determine the active phase of Ni. Early studies claim that supported NiO is active for oligomerization. Later, effort to isolate Ni^{2+} or Ni^{+} ions was made to assess their catalytic performance and determine the active Ni site. Ni^{+} is not a common oxidation state but is thought to be produced by the reduction of Ni^{2+} to Ni^{+} in various support materials. Distinguishing Ni^{+}, Ni^{2+}, and NiO requires a way of counting specific sites using electron paramagnetic/spin resonance (EPR/ESR) and IR spectroscopy with specific probe molecules (CO, NH_3).

Bifunctional catalysts containing Ni^{2+} and solid acids are currently thought to be the most promising for the synthesis of C_6+ higher olefins by ethylene oligomerizations. The Bronsted acid function comes from the acidic supports, like zeolites (*e.g.* BEA, MCM-41, ZSM-5). The production of higher molecular weight products requires large pores, which can accommodate products such as hexene. The Bronsted acid function typically allows for further oligomerization of the butenes produced by Ni^{2+}, in addition to side reactions including cracking, isomerization, and hydrogen transfer. Therefore, the resulting product mixture would contain both linear and branched hydrocarbons with both even and odd carbon numbers.

However, the development of new oligomerization catalysts is necessary improve reaction rates and understand the driving forces of selectivity. Tuning the length of the resulting carbon chain can lead to better process design for targeted products.

1.3.2   Known Oligomerization Mechanisms on Transition Metal Catalysts

Two oligomerization mechanisms have been proposed. The metallacycle is a ring expansion mechanism where oxidative coupling of two ethylene molecules occurs at an electrophilic metal center. The metallacyclopentene intermediate undergoes ethylene insertion to form a metallacycloheptane and eliminate hexene.[39] Here, a β-hydrogen shift is prevented by the geometry of the reaction intermediates leading to high selectivity towards hexenes and octenes, but low amounts of butenes are produced.[40,41] Alternatively, the Cossee-Arlman mechanism is where an alkyl chain grows by coordination of the olefin to a vacant site on the metal center, and then subsequent formation of the metal alkyl bond by alkylation of a metal hydride. Desorption of the olefin product can take place by β-hydride elimination or transfer, restoring the metal hydride site and leaving a surface OH group.

On transition metal catalysts, the coordination insertion mechanism is generally accepted. This is marked by the products following a Schultz Flory distribution, or the relative ratio of alkenes of different lengths that occur in an ideal step growth oligomerization process. For catalysts following a Schultz Flory distribution in ethylene oligomerization, the molar composition of products will follow butene > hexene > octene.[42] This distribution implies that shorter chain products are favored over longer ones.

In heterogeneous catalysis, single site catalyst refers to an isolated metal ion with metal-oxygen bonds only to the support. Single site catalysts are increasingly being used to facilitate oligomerization and polymerization. Like Ni^{2+}, other single sites such as Cr^{3+}, Fe^{3+}, Ti^{2+}, and Zr^{2+} can be used to convert ethylene to higher molecular weight products. Under standard reaction conditions, there is little control of the resulting products on each catalyst center.

Control of the product distribution can allow for catalyst selection to target the formation of specific products whether for fuels or polymers. This would require an understanding of the specific reaction intermediates and elementary steps. Though, few other catalysts are as active as Ni^{2+} for oligomerization and are therefore few mechanistic studies are available.

In the second half of this thesis, heterogeneous, non-acidic oligomerization catalysts are investigated. Silica supported Ga^{3+}, Zn^{2+}, and Co^{2+} single site catalysts were developed to perform oligomerization under flexible reaction conditions. While Ni^{2+} reduces to Ni^0 under reaction temperatures higher than 300°C, the catalysts introduced in this thesis are resistant to reduction. In addition, mechanistic studies revealed the formation of metal hydride and metal alkyl intermediates and suggest that the latter follow the same Cossee-Arlman mechanism as Ni^{2+} to produce longer chain oligomers.

1.4   Thesis Overview

Olefins, most notably ethylene and propylene, are important chemical intermediates that are used in the production of petrochemicals and can be further converted to fuel products via oligomerization. The recent shale gas boom led to lower natural gas prices and promoted increased total olefin production by the implementation of light alkane dehydrogenation (LAD), an on-purpose production method. The olefins produced by dehydrogenation can then be upgraded to higher molecular weight hydrocarbons by oligomerization. This thesis highlights the characterization of novel catalytic structures to both produce and transform olefins. Using emerging techniques like *in situ* x-ray absorption spectroscopy and x-ray diffraction, the long-range order of catalyst bulk and surface structures can be determined. Other *in situ* characterizations such as infrared spectroscopy and isotopic exchange experiments can be used to identify the structures of relevant reaction intermediates. The insights gained through these advanced characterizations under reaction conditions can lead to the design of targeted catalyst structures to control fundamental catalyst proprieties like reaction rates and product distributions.

In the first half of this thesis, the structural evolution of Pt-Cr bimetallic nanoparticles was explored as a function of Cr content and reduction temperature. Through this, it was determined that Pt nanoparticles first form at low temperatures. The reduced Pt nanoparticle can facilitate H_2, dissociation and promote the reduction and incorporation of Cr_2O_3 to form a bimetallic phase. Through this, it was found that the addition of Cr to Pt nanoparticles leads to improved propylene selectivity in propane dehydrogenation. For instance, catalysts containing 1 wt% Cr had a propylene selectivity of 88% while those containing 3 wt% Cr had 97%. Despite these differences in the selective behavior, the bulk characterizations of these catalysts were nearly identical. To understand these changes in catalytic performance, a new method of surface analysis by difference

to identify the structures of the active catalytic surface was developed. Through this, it was determined that the surface was Cr-rich relative to the bulk, consistent with the formation of the of a surface alloy and further inward incorporation. While high Cr concentrations (> 3 wt%) led to the formation of a full core shell morphology with a Pt core and Pt_3Cr shell (and eventually a full alloy at a high enough reduction temperature), low Cr concentrations had exposed Pt on the nanoparticle surface. The catalyst synthesis, pretreatment, and reaction conditions can all change the catalyst structure and therefore change the catalytic performance.

This method of difference analysis to study catalytic surfaces was applied to a variety of catalyst systems (*i.e.* Pt-Cr, Pt-Co, Pt-V). These case studies emphasized that knowing the precise structure of the catalytic surface is critical for drawing conclusions about not only the catalytic performance, but also the electronic structures of nanoparticles.

The second half of this thesis explores the catalytic performance of silica supported, non-acidic single site catalysts for oligomerization. Like the commercially known Ni^{2+} single sites, Ga^{3+}, Zn^{2+}, and Co^{2+} all perform oligomerization, though with varying activities and product distributions. On the latter, higher reaction temperatures are needed to promote higher rates. While Zn^{2+} favors the formation of dimers, like Ni^{2+}, Ga^{3+} and Co^{2+} form higher molecular weight hydrocarbons. A mechanistic study on these catalysts was performed to identify reaction intermediates, which have been proposed to be metal hydrides (M-H) and metal alkyls (M-R).

Initiation on these heterogeneous single site catalysts could be achieved by the activation of C-H bonds in high concentrations of ethylene. Spectroscopic evidence suggests the formation of metal hydrids. Subsequent alkylation on a metal hydride produces a metal alkyl and facilitates oligomerization following the traditional Cossee-Arlman mechanism. For these heterogenous analogs to traditional oligomerization catalysts, the heterolytic activation of C-H and H_2 bonds is critical. Consequently, higher reaction temperatures lead to higher reaction rates.

Catalysts to facilitate the conversion of light alkanes from shale gas to higher molecular weight hydrocarbons are being developed. Using controlled synthesis and advanced characterizations approaches can help provide a fundamental understanding of the structures and reaction intermediates needed to control catalyst performance.

1.5   References

1. Sattler, J.J.H.B.; Ruiz-Martinez, J.; Santillan-Jimenez, E.; Weckhuysen, B.M. Catalytic Dehydrogenation of Light Alkanes on Metals and Metal Oxides. *Chem. Rev.* **2014**, 114, 16013–16063.

2. Gallagher, J.R.; Childers, D.J.; Zhao, H.; Winans, R.E.; Meyer, R.J.; Miller, J.T. Structural evolution of an intermetallic Pd–Zn catalyst selective for propane dehydrogenation. *J. Phys. Chem.* **2015**, 17, 28144–28153.

3. Wu, Z.; Wegener, E.C.; Tseng, H-T.; Gallagher, J.R.; Harris, J.W.; Diaz, R.E.; Ren, Y.; Ribeiro, F.H.; Miller, J.T. Pd–In intermetallic alloy nanoparticles: highly selective ethane dehydrogenation catalysts. *Catal. Sci. Technol.* **2016**, 6, 18, 6965–6976.

4. Siirola, J. J. The impact of shale gas in the chemical industry. *AIChE J.* **2014**, 60, 810–819.

5. Vora, B. V. Development of Dehydrogenation Catalysts and Processes. *Top. Catal.* **2012**,55, 1297–1308.

6. Nawaz, Z. Light alkane dehydrogenation to light olefin technologies: a comprehensive review. *Rev. Chem. Eng.* **2015**, 31.

7. James, O.O.; Mandal, S.; Alele, N.; Chowdhury, B.; Maity, S. Lower alkanes dehydrogenation: Strategies and reaction routes to corresponding alkenes. *Fuel Process. Technol.* **2016**, 149, 239–255.

8. Furukawa, S.; Komatsu, T. Intermetallic Compounds: Promising Inorganic Materials for Well-Structured and Electronically Modified Reaction Environments for Efficient Catalysis. *ACS Catal.* **2017**, 7, 735–765.

9. Bricker, J.C. Advanced Catalytic Dehydrogenation Technologies for Production of Olefins. *Top. Catal.* **2012**, 55, 1309–1314.

10. Hartley, F.R. Chemistry of the Platinum Group Metals. in *Studies in Inorganic Chemistry.* **1991**, 11.

11. Alexeev, O.S.; Gates, B.C. Supported Bimetallic Cluster Catalysts. *Ind. Eng. Chem.* **2003**, 42, 1571–1587.

12. Windham, R.G.; Koel, B.E.; Paffett, M.T. Studies of the ensemble size requirements for ethylene adsorption and decomposition on platinum(111): ethylene and bismuth coadsorption. *Langmuir.* **1988**, 4, 1113–1118.

13. Cortright, R.D.; Dumesic, J.A. Microcalorimetric, Spectroscopic, and Kinetic Studies of Silica Supported Pt and Pt/Sn Catalysts for Isobutane Dehydrogenation. *J. Catal.* **1994**, 148, 771–778.

14. Nykänen, L.; Honkala, K. Selectivity in Propene Dehydrogenation on Pt and Pt3Sn Surfaces from First Principles. *ACS Catal.* **2013**, 3, 3026–3030.

15. Sinfelt, J.H. Catalysis by Alloys and Bimetallic Clusters. *Bimetallic Clust. Catal.* **1977**, 10, 15–20.

16. Bugaev, A.L.; Guda, A.A.; Lomachenko, K.A.; Shapovalov, V.V.; Lazzarini, A.; Vitillo, J.G.; Bugaev, L.A.; Groppo, E.; Pellegrini, R.; Soldatov, A.V.; van Bokhoven, J.A.; Lamerti, C. Core–Shell Structure of Palladium Hydride Nanoparticles Revealed by Combined X-ray Absorption Spectroscopy and X-ray Diffraction. *J. Phys. Chem. C*. **2017**, 121, 18202–18213.

17. Tao, F.; Grass, M.E.l Zhang, Y.; Butcher, D.R.; Renzas, J.R.; Liu, Z.; Chung, J.Y.; Mun, B.S.; Salmeron, M.; Somorjai, G.A. Reaction-Driven Restructuring of Rh-Pd and Pt-Pd Core-Shell Nanoparticles. *Science*. **2008**, 322, 5903, 932-934.

18. Wanjala, B.N.; Luo, J.; Loukrakpam, R.; Fang, B.; Mott, D.; Njoki, P.N.; Engelhard, M.; Naslund, H.R.; Wu, J.K.; Wang, L.; Malis, O.; Zhong, C-J. Nanoscale Alloying, Phase-Segregation, and Core−Shell Evolution of Gold−Platinum Nanoparticles and Their Electrocatalytic Effect on Oxygen Reduction Reaction. *Chem. Mater.* **2010**, 22, 14, 4282–4294.

19. Cesar, L.G.; Yang, C.; Lu, Z.; Ren, Y.; Zhang, G.; Miller, J.T. Identification of a Pt 3 Co Surface Intermetallic Alloy in Pt–Co Propane Dehydrogenation Catalysts. *ACS Catalysis*. **2019**, 9, 6, 5231–5244.

20. Purdy, S.C.; Ghanekar, P.; Mitchell, G.; Kropf, A.J.; Zemlyanov, D.Y.; Ren, Y.; Ribeiro, F.; Delgas, W.N.; Greeley, J.; Miller, J.T. Origin of Electronic Modification of Platinum in a Pt3V Alloy and Its Consequences for Propane Dehydrogenation Catalysis. *ACS Appl. Energy Mater.* **2020**, 3, 2, 1410-1422.

21. Ma, Z.; Wu, Z.; Miller, J.T. Effect of Cu content on the bimetallic Pt–Cu catalysts for propane dehydrogenation. *Catal. Struct. React.* **2017**, 3, 43–53.

22. Wegener, E.C.; Wu, Z.; Tseng, H-T.; Gallagher, J.R.; Ren, Y.; Diaz, R.E.; Ribeiro, F.H.; Miller, J.T. Structure and reactivity of Pt–In intermetallic alloy nanoparticles: Highly selective catalysts for ethane dehydrogenation. *Catal. Today*. **2017**, 299, 1, 146-153.

23. Ye, C.; Wu, Z.; Liu, W.; Ren, Y.; Zhang, G.; Miller, J.T. Structure Determination of a Surface Tetragonal Pt1Sb1 Phase on Pt Nanoparticles. *Chem. Mater.* **2018**, 30, 14, 4503-4507.

24. Chen, J.Z.; Wu, Z.; Zhang, X.; Choi, S.; Xiao, Y.; Varma, A.; Liu, W.; Zhang, G.; Miller, J.T. Identification of the structure of the Bi promoted Pt non-oxidative coupling of methane catalyst: a nanoscale Pt3Bi intermetallic alloy. *Catal. Sci. Technol.* **2019**, 9, 1349–1356.

25. LiBretto, N.J., Yang, C., Ren, Y., Zhang, G.; Miller, J.T. Identification of Surface Structures in Pt3Cr Intermetallic Nanocatalysts. *Chemistry of Materials*. **2019**, 31, 5, 1597–1609.

26. Wong, A.; Liu, Q.; Griffin, S.; Nicholls, A.; Regalbuto, J.R. Synthesis of ultrasmall, homogeneously alloyed, bimetallic nanoparticles on silica supports. *Science*. **2017**, 358, 1427–1430.

27. Yang, C.; Wu, Z.; Zhang, G.; Sheng, H.; Tian, J.; Duan, Z.; Sohn, H.; Kropf, A.J.; Wu, T.; Krause, T.R.; Miller, J.T. Promotion of Pd nanoparticles by Fe and formation of a Pd3Fe intermetallic alloy for propane dehydrogenation. *Catal. Today.* **2018**, 323, 15, 123-128.

28. Childers, D.J.; Schweitzer, N.M.; Shahari, S.M.K.; Rioux, R.M.; Miller, J.T.; Meyer, R.J. Modifying structure-sensitive reactions by addition of Zn to Pd. *J. Catal.* **2014**, 318, 75–84.

29. Keim, W. Nickel: An Element with Wide Application in Industrial Homogeneous Catalysis. **1990**, 29, 235-244.

30. Nicholas, C.P. Applications of light olefin oligomerization to the production of fuels and chemicals. *Appl. Catal. Gen.* **2017**, 543, 82–97.

31. McGuiness, D.S. Olefin Oligomerization via Metallacycles: Dimerization, Trimerization, Tetramerization, and Beyond. *Chemical Reviews*, **2011**, 111, 2321–2341.

32. Toch, K.; Thybaut, J.W.; Arribas, M.A.; Martínez, A.; Marin, G.B. Steering linear 1-alkene, propene or gasoline yields in ethene oligomerization via the interplay between nickel and acid sites. *Chem. Eng. Sci.* **2017**, 173, 49–59.

33. Finiels, A.; Fajula, F.; Hulea, V. Nickel-based solid catalysts for ethylene oligomerization – a review. *Catal. Sci. Technol.* **2014**, 4, 2412–2426.

34. Keim, W. Nickel hydrides: catalysis in oligomerization and polymerization reactions of olefins. *Ann. N. Y. Acad. Sci.* **1983**, 415, 191–200.

35. Breuil, P.A.R.; Magna, L.; Olivier-Bourbigou, H. Role of homogeneous catalysis in oligomerization of Olefins: focus on selected examples based on Group 4 to Group 10 transition metal complexes. *Catal. Lett.* **2015**, 145, 173–192.

36. Alferov, K.A.; Belov, G.P.; Meng, Y. Chromium catalysts for selective ethylene oligomerization to 1-hexene and 1-octene: Recent results. *Appl. Catal. Gen.* **2017**, 542, 71–124.

37. Henry, R.; Komurcu, M.; Ganjkhanlou, Y.; Brogaard, R.Y.; Lu, L.; Jens, K.J.; Berlier, G.; Olsbye, U. Ethene oligomerization on nickel microporous and mesoporous-supported catalysts: Investigation of the active sites. *Catalysis Today,* **2018**, 9, 154–163.

38. Forget, S.; Olivier-Bourbigou, H.; Delcroix, D. Homogeneous and Heterogeneous Nickel-Catalyzed Olefin Oligomerization: Experimental Investigation for a Common Mechanistic Proposition and Catalyst Optimization. *ChemCatChem*, **2017**, 9, 2408–2417.

39. Do, L.H.; Labinger, J.A.; Bercaw, J.E. Mechanistic Studies of Ethylene and α-Olefin Co-oligomerization Catalyzed by Chromium-PNP Complexes. *Organometallics.* **2012**, 31, 5143–5149.

40. McGuinness, D.S.; Suttil, J.A.; Gardiner, M.G.; Davies, N.W. Ethylene Oligomerization with Cr−NHC Catalysts: Further Insights into the Extended Metallacycle Mechanism of Chain Growth. *Organometallics.* **2008**, 27, 4238–4247.

41. Emrich, R.; Heinemann, O.; Jolly, P.W.; Krüger, C.; Verhovnik, G.P.J. The Role of Metallacycles in the Chromium-Catalyzed Trimerization of Ethylene. *Organometallics.* **1997**, 16, 1511–1513.

42. Britovsek, G.J.P.; Malinowski, R.; McGuinness, D.S.; Nobbs, J.D.; Tomov, A.K.; Wadsley, A.W.; Young, C.T. Ethylene Oligomerization beyond Schulz−Flory Distributions. *ACS Catal.* **2015**, 4, 6922-6925.

2. IDENTIFICATION OF SURFACE STRUCTURES IN PT$_3$CR INTERMETALLIC NANOCATALYSTS

2.1   Introduction

Supported bimetallic nanoparticles are used in a large number of applications including heterogeneous catalysis, electro-catalysis, chemical sensing, and biomedicine.[1–4] As early as the 1970s, high surface area, highly dispersed bimetallic catalysts containing transition metals were investigated to understand how the combination of different metal pairs impacts catalytic performance.[5] While it was clear in most cases that the combination of metals improves the catalytic behavior compared to the monometallic substituents, few characterizations were able to precisely identify the resulting structure, and especially that of the catalytic surface. In recent years, improvements in nanoparticle synthesis to control the particle size and metal incorporation, have led to a better understanding of the atomic order of nanoparticles.[6,7] For instance, core-shell structures, solid solutions, and intermetallic alloys, of which several structures may be possible, can be formed depending on the metal pairs and synthesis conditions. The determination between these structures is often subtle, especially in supported nanoparticles smaller than 5 nm in size.[8–10]

Determining the atomic distribution and alloy structures of supported bimetallic nanoparticles is challenging and requires a combination of techniques to identify the specific phases present.[11,12] For instance, X-ray absorption spectroscopy (XAS) has been used to determine if a bimetallic phase is achieved, and the specific phases can be confirmed by *in situ* synchrotron X-ray diffraction (XRD).[8,9,13–17] The use of synchrotron radiation leads to a high signal-to-noise ratio in small nanoparticles of less than 2 nm and thus, it is possible to resolve the atomic order.[13] These characterizations, however, are not sufficient to determine the nanoparticles surface structure, especially when it differs from the average composition. For example, surface segregation, or when the two metals de-alloy causing one to preferentially move to the surface, is possible. This could lead to changes in the surface compared to the average composition and structure, which has been reported for Pt-Au, where the alloy exhibited a Pt-rich alloy core with Au-rich shell.[18]

Alternatively, the core-shell nanoparticles may behave differently from full alloys of the same structure.[19,20] Identifying the surface composition and structure in bimetallic nanoparticles will lead to a better understanding of the catalytic performance; however, better methods for characterization of the surface are needed.

Here we have prepared bimetallic Pt-Cr nanoparticle catalysts with a Pt$_3$Cr surface – Pt core structure, which are selective for propane dehydrogenation. The average structures were determined using *in situ* XRD and XAS analysis. In addition, a method is described to determine the surface structure composition, where the surface XAS and XRD were isolated using the difference spectrum of the reduced and oxidized spectra. This approach led to high resolution even in nanoparticles smaller than 2 nm. Through this difference analysis, surface structures can be identified with resolution down to a single atomic layer.

2.2   Materials and Methods

2.2.1   Catalyst Preparation

Three Pt-Cr catalysts containing target weight loadings of 2 wt% Pt with 0, 1, and 3 wt% Cr were synthesized using sequential incipient wetness impregnation (IWI), so that the resulting catalysts contained Cr:Pt molar ratios of 0, 1.9, and 5.6 respectively. The samples are named by their target weight loadings. Chromium nitrate nonahydrate ($Cr(NO_3)_3 \cdot 9H_2O$, Sigma Aldrich), and citric acid (Sigma Aldrich) were dissolved in 3 mL of Millipore water in a 1:1 molar ratio and the resulting solution was added dropwise to 5 g of silica with grade 636 (pore size = 60 Å, surface area = 480 m^2/g). The obtained Cr/SiO$_2$ catalyst precursors were dried for 16 hours at 125°C and then calcined at 350°C for 3 hours. A second solution was made using 0.2 g of tetraamine platinum nitrate ($Pt(NH_3)_4(NO_3)_2$, Sigma Aldrich) dissolved in 2 mL of Millipore water and 1.75 mL of 30% ammonium hydroxide solution was added to adjust the pH to 11. The resulting solution was added dropwise to the Cr/SiO$_2$ following the charge enhanced dry impregnation (CEDI) method.[6] The Pt-Cr/SiO$_2$ catalysts were dried for 16 hours at 125°C and then calcined at 250°C for 3 hours. The catalysts were reduced in flowing H$_2$ at various temperatures from 250°C to 800°C to alter the degree of Cr incorporation.

2.2.2 Scanning Transmission Electron Microscopy (STEM)

Catalysts were analyzed by STEM at Electron Microscopy Center at Argonne National Laboratory using FEI Talos Scanning Transmission Electron Microscope (80-300 kV). The as-synthesized catalysts were pre-reduced at the desired reduction temperatures (250, 400, 550, 700, and 800°C) using a ramp rate of 10°C/min in H_2. Samples were dispersed in hexane and deposited on a Au-coated holey carbon grid (TedPella). Images were taken using the high angle annular dark field (HAADF) detector at 300 kV. The measurements were performed on the samples after they were exposed to air, which is not expected to change the particle size distribution. The average particle size was determined by performing a statistical distribution analysis on a sample size of 250-300 particles imaged using ImageJ particle size counting software.[21]

2.2.3 *In Situ* X-Ray Absorption Spectroscopy (XAS)

In situ XAS experiments were performed at the 10-BM-B beamline at the Advanced Photon Source (APS), Argonne National Laboratory at the Pt L_{III} (11.564 keV) edge in transmission mode, with energy resolution of 0.3 eV and edge energy precision greater than 0.1 eV. $2Pt/SiO_2$, $2Pt1Cr/SiO_2$, and $2Pt3Cr/SiO_2$ were ground into a powder, pressed into a sample holder, and sealed in a sample cell with leak-tight Kapton end caps. The sample cell was treated with 3.5% H_2/He for 30 minutes at 250, 400, 550, 700, and 800°C sequentially. The cell was cooled to room temperature in flowing He between each temperature exposure, sealed, and moved to the beamline to acquire data. The He tank was connected to a gas purifier to reduce the possibility of O_2 exposure. A 1 nm Pt/SiO_2 sample was used for reference to verify that the cell was not accidently exposed to O_2 in between the H_2 pretreatment and scanning. After H_2 treatment at each temperature, the sample cell was purged with 20% O_2 at room temperature for 15 minutes to allow for surface oxidation of the nanoparticles, and a second spectrum was acquired.[22] Each measurement was accompanied by simultaneous measurement of a Pt foil scan obtained through a third ion chamber for internal energy calibration.

All data were analyzed using WinXAS 3.1 software[23] using standard fitting procedures to find the coordination number and bond distances between Pt and its neighbors. EXAFS was obtained using a least squared fit in r- space performed on isolated k^2- weighted Fourier transform data. The data were fit using experimental Pt-Pt phase and amplitude files obtained from a Pt foil. Theoretical

Pt-Cr phase and amplitude files were obtained from FEFF6[24] calculations. Each sample was fit using two scattering paths (Pt-Pt and Pt-Cr).

Difference XAS analysis was used to determine the surface composition of the nanoparticles. First, spectra were obtained after reducing the samples at varying temperatures in H_2. Then, the samples were subsequently oxidized by exposure to air at room temperature and scanned again. The difference in k^0-weighted chi's (reduced-oxidized) was used to show changes in the surface. The resulting difference chi spectrum, representing the surface of the nanoparticles, was then k^2-weighted and a Fourier transform was fit. The data was fit using three scattering paths (Pt-Pt, Pt-Cr, and Pt-O). An experimental phase and amplitude were obtained for Pt-O using PtO as a reference compound. The phase of the Pt-O scattering pair was π radians out of phase from the normal EXAFS. The Pt-O amplitude is unchanged.

2.2.4 *In Situ* X-Ray Diffraction (XRD)

In situ XRD measurements were performed at the 11-ID-C beamline at the APS, using X-rays of λ=0.1173 Å (105.715 keV) and data was acquired using a PerklinElmer large area detector. The high-energy and high-flux X-rays are necessary for collecting diffraction patterns on nanoparticles < 10 nm in size to increase the signal to noise ratio and reduce the background from the SiO_2 support. Samples were pressed into a self-supported pellet (< 2 mm thickness) and then loaded into a thermal stage. The cell was purged with He before a flow of 3.5% H_2/He at 100 ccm was introduced and the temperature was increased to the target temperature (250, 400, 550, 700, and 800 °C). After diffraction measurements were completed at the reduction temperature, the cell was cooled to 35°C and a second diffraction measurement was obtained. A third set of diffraction measurements were obtained at room temperature for each sample after being exposed to room temperature air, post-reduction.

The background scattering of the empty cell and silica were obtained under the same conditions and subtracted from the XRD pattern. The diffraction patterns were collected as 2-D Scherrer rings and were integrated using Fit2D software[25] to obtain 1-D diffraction patterns as scattering intensity vs. 2θ plots. Theoretical diffraction patterns for possible Pt and Pt-Cr structures were simulated at room temperature using crystal information files imported to Materials Analysis Using Diffraction (MAUD)[26] and were used to identify the catalyst phase. All diffraction patterns were used to obtain the unit cell size and Pt-Pt and Pt-Cr bond distances. The nanoparticle size (d) was calculated using

the Scherrer equation ($d = \frac{\lambda}{\beta \cos\theta}$), where λ is the X-ray wavelength, β is the full width at half maximum (FWHM), a peak broadening parameter, and θ is the Bragg angle. Bragg's law ($d_{111} = \frac{\lambda}{\sin\theta}$) was used to find the lattice spacing (d_{111}) of the nanoparticle and then the lattice constant (a) was calculated using the geometry of the (111) plane ($d_{111}^2 = \frac{a^2}{\sqrt{3}}$). The Pt-Pt and Pt-Cr bond distances were calculated from the obtained lattice parameter.

2.2.5 Catalyst Performance Evaluation

Propane dehydrogenation was used to indicate structural changes to monometallic Pt with the addition of Cr to form bimetallic catalysts of different morphologies. Catalyst performance tests were performed at 550°C in a fixed bed reactor with a quartz reactor tube of 3/8-inch outer diameter. The weight of the catalyst (particle size 250-500 µm) loaded into the reactor ranged from 25 mg to 500 mg to vary the initial propane conversion and was diluted with silica to reach a total of 1 g. A thermocouple was used to measure the temperature in the center of the bed. Before each test, the catalyst was reduced for 30 minutes at a minimum temperature of 550°C under 100 ccm 5% H_2/N_2 and then cooled down to target reaction temperature (550°C). Pretreatment reduction temperatures lower than 550°C could lead to a change in catalyst structure when heated to reaction temperature, thus were not evaluated for the catalytic performance. The reaction was performed in 2.5% C_3H_8, 2.5% H_2, balanced with N_2. The products were analyzed with a Hewlett Packard 6890 Series gas chromatograph using a flame ionization detector (FID) with a Restek Rt-Alumina Bond/Na_2SO_4 GC column (30 m in length, 0.32 mm inner diameter, and 0.5 µm film thickness).

2.3   Results

2.3.1   STEM
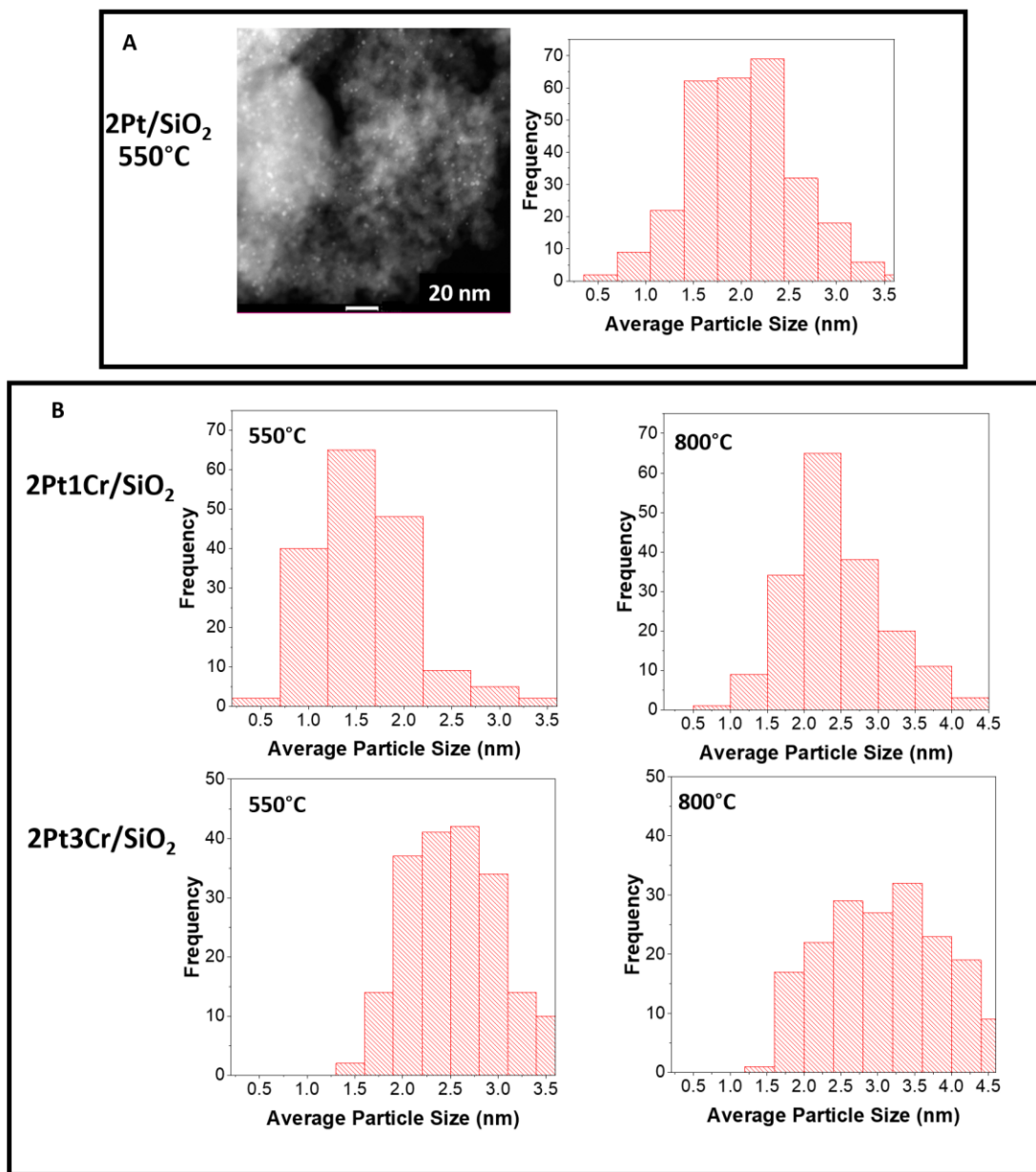
Figure 2.1. A) STEM image and particle size distribution for 2Pt/SiO$_2$ after reduction at 550°C B) Particle size as a function of reduction temperature for Pt-Cr catalysts, where higher reduction temperatures lead to larger particle size

Catalysts containing loadings of 2 wt% Pt (2Pt/SiO$_2$) with 1 wt% Cr (2Pt1Cr/SiO$_2$) and 3 wt% Cr (2Pt3Cr/SiO$_2$) were prepared by the pH modified impregnation method.[6] The catalysts were reduced at various temperatures starting as low as 250°C up to 800°C. A representative STEM image and particle size distribution is shown for 2Pt/SiO$_2$ after reduction at 550°C (Figure 2.1a). STEM particle size distributions are shown for the Cr-containing catalysts reduced at 550°C and 800°C and show slightly larger particle sizes after reduction at higher temperatures (Figure 2.1b). In each instance there is a narrow particle size distribution of uniform, small sized nanoparticles, similar to previous catalysts prepared by this synthesis method.[6] Upon increasing the reduction temperature, the averaged particle size of 2Pt3Cr/SiO$_2$ increased from 2.5 nm to 3.3 nm, while for 2Pt1Cr/SiO$_2$, the particle size increased from 1.9 nm to 2.4 nm. STEM indicates the presence of few particles larger than 5 nm in both 2Pt1Cr/SiO$_2$ and 2Pt3Cr/SiO$_2$ after reduction at 800°C. The particle sizes are summarized in Table 2.1.

Table 2.1. Average particle size of Pt-Cr catalysts compared to monometallic Pt

	Reduction Temperature (°C)	**Average Particle Size (nm)**
2Pt/SiO$_2$	550	1.9
2Pt1Cr/SiO$_2$	550	1.9
	800	2.4
2Pt3Cr/SiO$_2$	550	2.5
	800	3.3

2.3.2   In Situ XAS

The local geometry of the reduced Pt at various stages of particle growth was determined by performing *in situ* XAS at the Pt L$_{III}$ edge. The change in energy and shape of the XANES is characteristic of a change in the Pt coordination environment. Shifts to higher energies are observed in 2Pt3Cr/SiO$_2$ with increasing reduction temperature and are consistent with increasing amounts of metallic Cr in the nanoparticles (Figure 2.2), as also evidenced in the EXAFS described below.
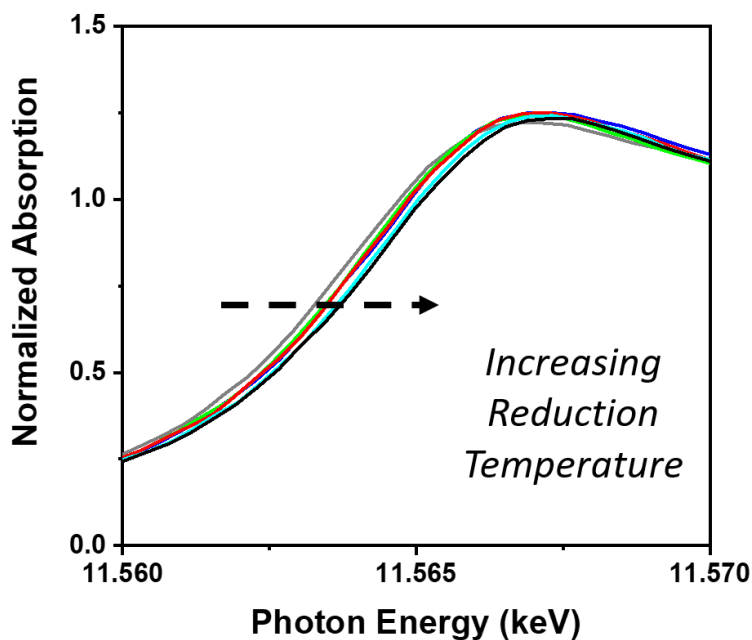
Figure 2.2. Pt L_{III} edge normalized XANES of $2Pt3Cr/SiO_2$ after reduction at 250°C (blue), 400°C (green), 550°C (red), 700°C (light blue), 800°C (black) in flowing H_2 compared to $2Pt/SiO_2$ reduced at 550°C (gray)

A XANES energy shift of 0.1 eV was observed after reduction at 250°C, presumably due to the incorporation of some reduced Cr. The XANES energy of $2Pt3Cr/SiO_2$ increased by 0.3 eV and 0.6 eV as the catalyst is reduced at 550°C and 800°C respectively. Larger XANES energy shifts are observed in $2Pt3Cr/SiO_2$ than in $2Pt1Cr/SiO_2$ at the same reduction temperatures (Figure 2.3), which suggests that the amount of CrO_x available to form bimetallic nanoparticles plays a role in the resulting nanoparticle composition. For instance, after reduction at 800°C, the XANES energy shifts from 11.5640 keV in monometallic Pt to 11.5644 keV in $2Pt1Cr/SiO_2$ and 11.5646 keV in $2Pt3Cr/SiO_2$.
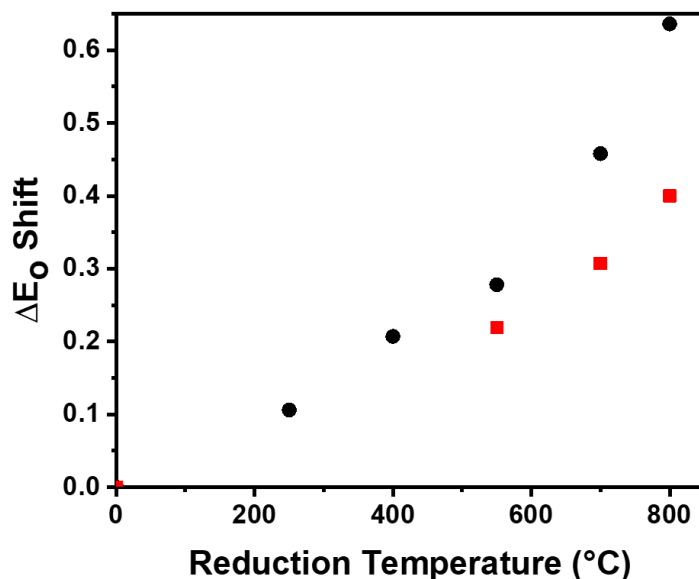
Figure 2.3. The change in XANES energy shift compared to Pt (11.5640 keV) as a function of reduction temperature for 2Pt1Cr/SiO$_2$ (red) and 2Pt3Cr/SiO$_2$ (black)

Evidence for the formation of bimetallic nanoparticles was obtained by EXAFS (Figure 4), which confirmed the presence of Pt-Cr scatters. The shape of the Fourier transforms, representing scattering from Pt neighbors, demonstrates a changing peak ratio in Pt-Cr catalysts after reduction at increasing temperatures. The magnitude of the Fourier transform (Figure 2.4a) shows an increased intensity of the first peak at ~1.8 Å and decreased intensity of the third peak at ~2.8 Å compared to monometallic Pt with increasing reduction temperature to 800°C, where the intensities of both peaks are about the same. The addition of Cr also changes the imaginary part of the Fourier transform of 2Pt3Cr/SiO$_2$, consistent with the addition of different ratios of metallic Cr (Figure 2.4b).
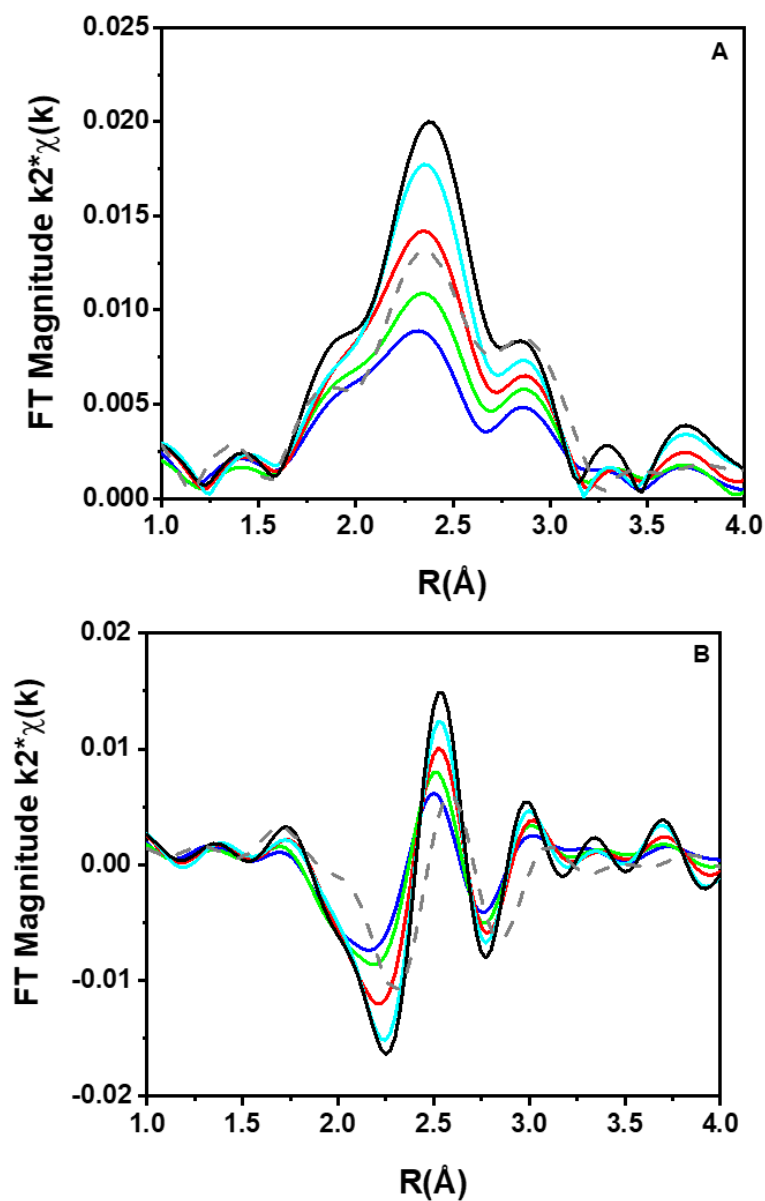
Figure 2.4. Pt L_{III} edge EXAFS A) magnitude and B) imaginary part for $2Pt3Cr/SiO_2$ after reduction at 250°C (blue), 400°C (green), 550°C (red), 700°C (light blue), 800°C (black) in flowing H_2 compared to $2Pt/SiO_2$ reduced at 550°C (gray dashed)

The EXAFS were fit to determine the Pt-Pt (CN_{Pt-Pt}) and Pt-Cr (CN_{Pt-Cr}) coordination number and bond distances (Table 2.2). After reduction at 550°C, $2Pt1Cr/SiO_2$ has a CN_{Pt-Pt} of 8.0 and a CN_{Pt-Cr} of 2.2 or a ratio of Pt-Cr to Pt-Pt neighbors of 0.28. Thus, the nanoparticle is Pt-rich. As the reduction temperature increases to 700°C and 800°C, the ratio increases to 0.38 and although the nanoparticle is still Pt-rich, at higher reduction temperature the Cr content of the bimetallic

nanoparticles increases. The average Pt-Pt (R_{Pt-Pt} = 2.73 Å) and Pt-Cr (R_{Pt-Cr} = 2.70 Å) bond distances in 2Pt1Cr/SiO$_2$ are nearly constant at all reduction temperatures (Table 2.2).

Similar results were observed for 2Pt3Cr/SiO$_2$. After reduction at 250°C, the CN_{Pt-Cr}/CN_{Pt-Pt} is 0.16 and the nanoparticle is Pt-rich. The CN_{Pt-Cr}/CN_{Pt-Pt} ratio increases to 0.25 and 0.50 after reduction at 550°C and 800°C, respectively, which is the maximum ratio observed in these catalysts. The average bond distances in 2Pt3Cr/SiO$_2$ are very similar to those in 2Pt1Cr/SiO$_2$ (Table 2.2).

Table 2.2. Pt L_{III} edge XAS fitting parameters for 2Pt1Cr/SiO$_2$ and 2Pt3Cr/SiO$_2$ after reduction in H$_2$ at successively increasing temperatures.

Sample	Reduction Temperature (°C)	XANES energy (keV)	Scattering Path	CN	R (Å)	$\Delta\sigma^2$ (Å^2)	ΔE_o (eV)
2Pt/SiO$_2$	550	11.5640	Pt-Pt	10.2	2.76	0.003	-0.4
2Pt1Cr/SiO$_2$	550	11.5643	Pt-Pt	8.0	2.73	0.004	-1.3
			Pt-Cr	2.2	2.70	0.003	0.9
	700	11.5643	Pt-Pt	8.3	2.73	0.004	-1.3
			Pt-Cr	2.9	2.70	0.003	0.0
	800	11.5644	Pt-Pt	8.4	2.73	0.004	-1.6
			Pt-Cr	3.2	2.71	0.003	-1.6
2Pt3Cr/SiO$_2$	250	11.5641	Pt-Pt	7.5	2.75	0.006	-0.2
			Pt-Cr	1.2	2.69	0.003	0.7
	400	11.5642	Pt-Pt	8.0	2.74	0.005	-0.2
			Pt-Cr	1.9	2.69	0.003	-1.5
	550	11.5643	Pt-Pt	8.1	2.73	0.004	-1.6
			Pt-Cr	2.4	2.70	0.003	1.1
	700	11.5645	Pt-Pt	7.8	2.73	0.003	-0.8
			Pt-Cr	3.6	2.70	0.003	1.1
	800	11.5646	Pt-Pt	7.9	2.73	0.003	0.5
			Pt-Cr	4.1	2.73	0.003	2.1

In both catalysts, a simultaneous increase in CN_{Pt-Cr} and decrease in CN_{Pt-Pt} is observed with increasing reduction temperature. Reduction at 550°C leads to very similar coordination geometries in 2Pt1Cr/SiO$_2$ and 2Pt3Cr/SiO$_2$. Both catalysts are Pt-rich, where the average CN_{Pt-Cr}/CN_{Pt-Pt} is about 0.30. As the reduction temperature is increased to 800°C, 2Pt3Cr/SiO$_2$ (CN_{Pt-Cr}/CN_{Pt-Pt} = 0.52) is slightly more Cr rich than 2Pt1Cr/SiO$_2$ (CN_{Pt-Cr}/CN_{Pt-Pt} = 0.38), consistent with a slightly larger XANES energy shift in the former. The larger amount of Cr incorporation in the 2Pt3Cr/SiO$_2$ is likely due to higher Cr loading.

2.3.3   In Situ XRD

While XAS indicates the formation of bimetallic nanoparticles, *in situ* synchrotron XRD was performed to identify the resulting bimetallic phase. The X-ray energy was 105.715 keV resulting in diffraction patterns at low 2θ angle, *e.g.*, less than about 8 degrees, compared to laboratory XRD. The high flux of the synchrotron XRD gives better signal to noise and the high energy X-rays allow for increased sensitivity for heavy scatters, for example, Pt nanoparticles compared to SiO_2. Finally, the large area detector can be moved to a long distance from the sample to allow for better spatial resolution of closely spaced reflections from different phases.[27] After reduction at temperatures below 550°C, the small nanoparticles (< 3 nm) have broad diffraction peaks, and the features are difficult to resolve. In the diffraction pattern of monometallic Pt nanoparticles (FCC crystal structure), there are four main reflections representing the (111), (200), (220), and (311) planes. With increasing particle size, monometallic Pt results in a slight shift in reflection to slightly lower 2θ values due to longer bond distances.[28,29] Simulations for known bulk phase Pt-Cr phases (Pt_3Cr, PtCr, and $PtCr_3$) at room temperature are compared to the diffraction patterns of the bimetallic catalysts (Figure 2.5).[30] Each catalyst's diffraction pattern at elevated temperature of reduction and after cooling to room temperature were nearly identical indicating the identical structures. Data is reported at room temperature, where there is less thermal strain. The bimetallic catalysts' diffraction patterns do not match those for the PtCr or $PtCr_3$ phases. However, the near proximity of monometallic Pt and Pt_3Cr reflection positions make it difficult to distinguish between the two phases in small nanoparticles. The shifts in the diffraction could also possibly be due to formation of a Pt-Cr randomly ordered solid solution (containing Pt and Cr atoms). Solid solutions typically occur in metals that have the same crystal structure; however, Cr has a BCC structure and Pt is FCC. The Pt-Cr phase diagram indicates that Cr is insoluble in Pt.[30] Finally, increasing weight percent compositions of Cr, which is observed by EXAFS, would lead to increasing shifts to higher 2θ in the diffraction patterns, which is not observed. If these were a solid solution between Pt and Cr with compositions from 10-33%, for example, larger shifts in the diffraction patterns would have occurred and been easily resolved from Pt. The constant position of diffraction peaks with increasing Cr composition are characteristic of two phases and not a solid solution phase.
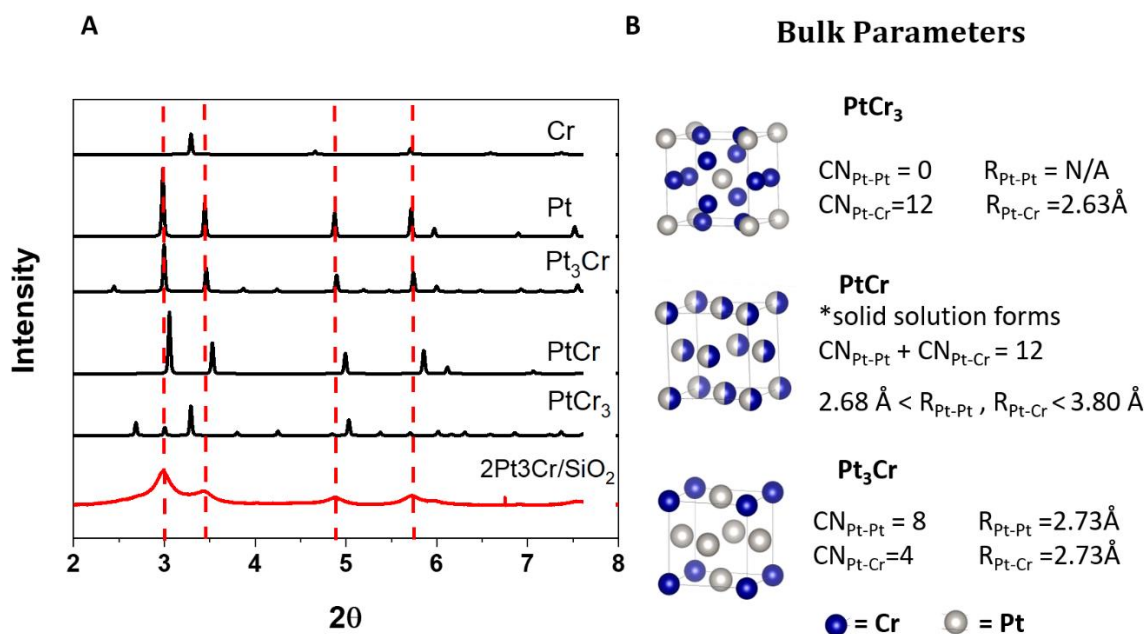
Figure 2.5. A) XRD of 2Pt3Cr/SiO$_2$ reduced at 550ºC compared to simulations of Pt-Cr alloy structures (X-ray energy = 105.715 keV) B) Unit cells and bulk parameters of possible Pt-Cr phases

After reduction at 250°C, 400°C, and 550°C the diffraction patterns are broad, spanning over both Pt and Pt$_3$Cr simulation positions (Figure 2.6a). The nanoparticles formed after reduction at low temperatures (<550°C) are similar to Pt, but the EXAFS indicates that some Cr is present. As the Cr content increases, the Pt reflections decrease slightly while the reflections for Pt$_3$Cr increase slightly. The reflections from the two very similar diffraction patterns change in shape with increasing Cr content, but not in position, suggesting increasing amounts of the ordered Pt$_3$Cr phase.
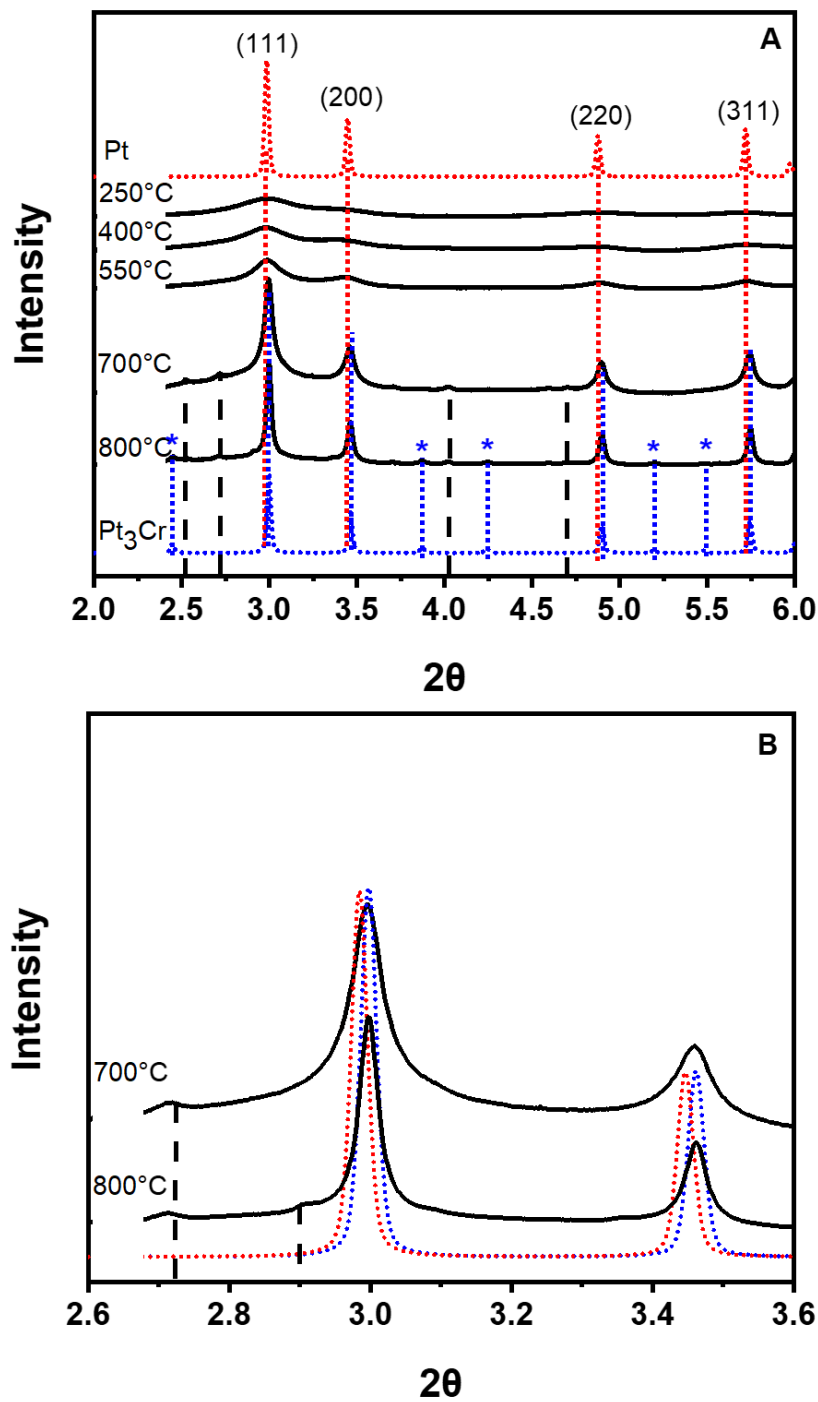
Figure 2.6. A) XRD patterns for 2Pt3Cr/SiO$_2$ as the reduction temperature increases compared to simulations for Pt (red dotted) and Pt$_3$Cr (blue dotted) with blue * representing super lattice diffraction peaks and guidelines for Cr$_2$O$_3$ (black dashed) B) XRD pattern corresponding to (111) and (200) planes for 2Pt3Cr/SiO$_2$ after reduction at 700°C and 800°C

To confirm the Pt_3Cr nanoparticle structure, $2Pt3Cr/SiO_2$ was reduced at higher temperatures (700°C and 800°C) in order to produce a full alloy. At the higher reduction temperature, the particles also were slightly larger (increasing from 2.5 nm to 3.3 nm) with increased intensities and narrower peaks. These slightly larger particles also result in superlattice diffraction peaks or features corresponding to lower symmetry crystal planes. The diffraction patterns obtained after reduction at higher temperatures are shown in Figure 2.6b. Although reflections are larger after reduction at 700°C, Pt and Pt_3Cr still cannot be resolved due to the close peak proximity. The increasing reduction temperature also led to additional reflections that match the diffraction pattern for Cr_2O_3 (black dashed guidelines). After reduction at 800°C, the larger diffraction peaks (Table 2.3) and the smaller superlattice diffraction peaks were observed at 2.45°, 3.87°, 4.24°, 5.20° and 5.48° (indicated by *) confirms the formation of the Pt_3Cr structure.[31]

Table 2.3. Particle size and lattice parameter calculated from (111) plane of experimental XRD patterns.

Sample	Reduction Temperature (°C)	d_{XRD} (nm)	a (Å)	R_{Pt-Pt} (Å)	Reflections (2θ, °)
2Pt/SiO₂	550	1.8	3.91	2.77	2.957, 3.396, 4.852, 5.702
	700	2.1	3.92	2.77	2.969, 3.146, 4.844, 5.702
2Pt1Cr/SiO₂	550	4.3	3.89	2.73	2.999, 3.460, 4.897, 5.749
	700	10.3	3.88	2.73	2.997, 3.460, 4.897, 5.749
2Pt3Cr/SiO₂	250	1.5	3.89	2.75	2.978, 3.452, 4.871, 5.717
	400	1.8	3.90	2.74	2.978, 3.441, 4.882, 5.740
	550	3.2	3.90	2.74	2.978, 3.447, 4.882, 5.740
	700	12.3	3.88	2.73	2.997, 3.460, 4.895, 5.742
	800	18.1	3.87	2.73	2.997, 3.462, 4.897, 5.745

With increasing reduction temperature, the lattice parameter changes with slight changes in particle size and composition (Table 2.3). Particles smaller than 3 nm typically have shorter bond distances, which lead to slight lattice parameter contraction.[32] In addition, because Cr is a smaller element than Pt, a structure formed between these two atoms also decreases the size of the unit cell compared to Pt. Pt nanoparticles have a lattice parameter, a, of 3.91 Å. An increase in size of Pt nanoparticles results in lattice parameter expansion to slightly larger values ($a_{bulk\ Pt}$ = 3.92 Å), while the addition of Cr reduces the lattice parameter of monometallic Pt ($a_{bulk\ Pt3Cr}$ = 3.87 Å). The lattice parameter of $2Pt3Cr/SiO_2$ increased from 3.89 Å after reduction at 250°C to 3.90 Å at 400°C

and 550°C. The EXAFS indicates that the nanoparticles have increasing amounts of metallic Cr, which should lead to a decreased lattice parameter, however, the lattice parameter increases slightly, likely due to increase in particle size and the low Cr levels in the nanoparticles. When the nanoparticles are reduced at 700°C and 800°C, although the particles continue to increase slightly in size, the lattice parameter decreases to 3.88 Å and 3.87 Å, respectively, consistent with the formation of Pt_3Cr.

In summary, at lower reduction temperatures, the diffraction patterns are shifted slightly to higher 2θ, *i.e.*, smaller lattice parameter, due to incorporation of Cr into the bimetallic nanoparticle. Although the reflections are broad and asymmetric and the peaks from Pt and Pt_3Cr cannot be resolved, but the reflection positions and peak shapes are consistent with these two phases. At reduction of 800°C, Pt_3Cr intermetallic alloy formation is confirmed by XRD. The XRD of $2Pt1Cr/SiO_2$ are also very similar to those of $2Pt3Cr/SiO_2$, although the full Pt_3Cr alloy does not form on the former even after reduction at 800°C. Thus, $2Pr1Cr/SiO_2$ forms two phases at all reduction temperatures, consistent with the higher Pt-Pt coordination in the EXAFS compared to $2Pt3Cr/SiO_2$.

2.3.4   Catalyst Evaluation: Propane Dehydrogenation

The catalytic performance of $2Pt1Cr/SiO_2$ and $2Pt3Cr/SiO_2$ for propane dehydrogenation was compared to monometallic Pt. Because catalysis is a surface phenomenon, any change in the surface composition and structure will result in different performance. The conversion and selectivity were determined for propane dehydrogenation with 2.5% C_3H_8, 2.5% H_2 with balance N_2 at 550°C after the catalysts were pre-reduced at 550°C and 800°C. The catalysts were evaluated in the presence of H_2 since increased hydrogen to hydrocarbon ratio increases the probability for hydrogenolysis and is, therefore, a more rigorous test for the dehydrogenation selectivity. Under these conditions, propane is converted to predominately propylene, but methane, ethane, and ethylene are also formed. The carbon balance for these tests were approximately 100%.

The initial propylene selectivity of the catalysts was compared over a range of conversions up to about 40% (Figure 2.7). For $2Pt/SiO_2$ reduced at 550°C (1.9 nm), at about 10% propane conversion, the propylene selectivity was near 80%. The selectivity decreases rapidly with increasing conversion, for example, the propylene selectivity was about 50% at 40% propane conversion. Reduction of $2Pt/SiO_2$ at 800°C, leads to lower selectivity, especially for propane

conversions over about 20%. For 2Pt1Cr/SiO$_2$ reduced at 500ºC (1.9 nm) and at 800ºC (2.4 nm), the selectivity at any conversion is significantly improved compared to monometallic Pt. However, like 2Pt/SiO$_2$, the resulting olefin selectivity decreases with increasing conversion.
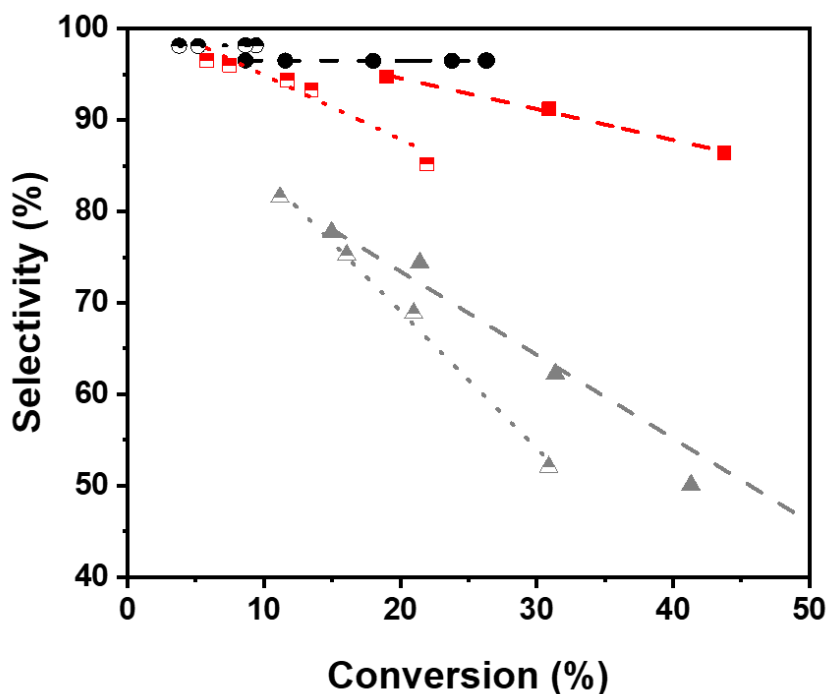
Figure 2.7. Initial selectivity for Pt-Cr catalysts containing 1wt% Cr (red) and 3 wt% Cr (black) in C$_3$H$_8$ dehydrogenation reactions after reduction at 550°C (full) and 800°C (half-full) compared to monometallic Pt (gray) with linear fit lines (dashed) in 2.5% C$_3$H$_8$, 2.5% H$_2$ with balance N$_2$

On the other hand, very high olefin selectivity (98%) is obtained at all conversions for 2Pt3Cr/SiO$_2$ reduced at 500ºC (2.7 nm) and 800ºC (3.3 nm) (Table 2.4). The difference in catalyst selectivities implies that 2Pt1Cr/SiO$_2$ and 2Pt3Cr/SiO$_2$ have different surface compositions, despite their similar EXAFS and XRD characterizations.

Table 2.4. C_3H_8 dehydrogenation was performed at 550°C in 2.5% C_3H_8, 2.5% H_2 balanced in N_2.

	Reduction Temperature (°C)	S_{C3H6} (%) at 20% Conversion	Rate (molC_3H_6 /g_{cat}/s)	Pt dispersion**	TOR (1/s)	Phases Present
2Pt/SiO₂	550	74	1.5×10^{-5}	0.20	0.3	Pt
	800	70	2.1×10^{-6}	0.15	0.1	
2Pt1Cr/SiO₂	550	95	3.3×10^{-5}	0.20	0.4	Pt, Pt₃Cr
	800	88	1.8×10^{-6}	0.15	0.1	
2Pt3Cr/SiO₂	550	98	8.4×10^{-5}	0.18	0.3	Pt, Pt₃Cr
	800	98	1.8×10^{-6}	0.10	0.2	Pt₃Cr
1Cr/SiO₂ *	550	97	8.0×10^{-7}	-	-	CrOₓ
3Cr/SiO₂ *	550	98	2.6×10^{-7}	-	-	

*Selectivity reported at 5% conversion

** Pt dispersion was determined using the Pt-O coordination number of the oxidized XAS spectra

Industrially, both Pt and CrO_x are known dehydrogenation catalysts.[33–35] The rates per gram of Pt (or per g Cr for Cr/SiO₂ catalysts) is reported in Table 2.4. The rates of Pt are significantly higher than those of Cr oxide implying that Pt is the active site. H_2-O_2 titration is a standard way to determine the fraction of surface Pt. Since these catalysts also contain Cr_2O_3, which can also be oxidized, this method is unreliable for these catalysts. However, the fraction of oxidized Pt can be determined by XAS and the Pt-O coordination number can be used to estimate the dispersion and calculate a turnover rate (TOR).

The Pt-O coordination numbers obtained from the oxidized catalysts are given in Table 2.5. Fully oxidized Pt nanoparticles has a $CN_{Pt-O} = 4$; thus, the dispersion is obtained by dividing the oxidized catalyst's Pt-O coordination number by 4. This method works well for small nanoparticles with a high fraction of surface atoms but become less reliable at sizes above about 6-8 nm where the Pt-O coordination number is small. The Pt dispersions are also given in Table 2.5. Comparison of the TOR's of the bimetallic Pt-Cr catalysts with those of monometallic Pt (Table 2.5) are very similar suggesting that Pt is the active site in the Pt₃Cr alloy and that the TOR of monometallic Pt is not much different from that in the Pt₃Cr alloy. The TOR of Pt₃Cr is also very similar to those reported for other intermetallic Pt alloys.[9,14–16,19]

Table 2.5. XAS fitting parameters for oxidized 2Pt1Cr/SiO$_2$ and 2Pt3Cr/SiO$_2$ post reduction in H$_2$

Sample	Reduction Temperature (°C)	Scattering Path	CN	R (Å)	$\Delta\sigma^2$ (Å^2)	ΔE_o (eV)	Pt dispersion
2Pt1Cr/SiO$_2$	550	Pt-Pt	6.5	2.73	0.004	-0.9	0.20
		Pt-Cr	1.6	2.70	0.003	0.9	
		Pt-O	0.8	2.05	0.001	0.7	
	700	Pt-Pt	7.5	2.73	0.004	1.4	0.15
		Pt-Cr	2.3	2.70	0.003	-2.0	
		Pt-O	0.6	2.05	0.001	1.6	
	800	Pt-Pt	7.9	2.73	0.004	1.3	0.15
		Pt-Cr	3.3	2.71	0.003	-1.5	
		Pt-O	0.6	2.05	0.001	1.8	
2Pt3Cr/SiO$_2$	250	Pt-Pt	5.8	2.73	0.006	1.4	0.23
		Pt-Cr	0.6	2.69	0.003	2.0	
		Pt-O	0.9	2.05	0.001	-0.7	
	400	Pt-Pt	6.5	2.74	0.005	0.1	0.20
		Pt-Cr	0.9	2.69	0.003	-2.8	
		Pt-O	0.8	2.05	0.001	0.7	
	550	Pt-Pt	7.9	2.75	0.004	1.3	0.18
		Pt-Cr	1.8	2.69	0.003	-6.2	
		Pt-O	0.7	2.05	0.001	3.0	
	700	Pt-Pt	7.4	2.73	0.003	-1.8	0.15
		Pt-Cr	3.2	2.73	0.003	1.0	
		Pt-O	0.6	2.05	0.001	6.3	
	800	Pt-Pt	7.9	2.73	0.003	-2.0	0.10
		Pt-Cr	3.9	2.73	0.003	-2.0	
		Pt-O	0.4	2.05	0.001	0.8	

2.4   Discussion

Formation of Pt–Cr bimetallic nanoparticles on carbon electrocatalysts has previously been reported by Antolini *et. al.* (2005)[31]. While improved ORR performance was observed with the addition of Cr, this was not correlated to alloy formation. Rather, the activity was suggested to be due to the presence of Cr oxides. Similarly, Cui *et. al.* (2015)[36] studied Pt-Cr/C for ORR reactions as a function of annealing temperature. It was also suggested that the Pt$_3$Cr phase was formed, but only after treatment at 600°C.

In this study, the combination of XAS and XRD indicated that at reduction temperatures below about 700°C, the nanoparticles contain two phases (Pt and Pt$_3$Cr). While both 2Pt1Cr/SiO$_2$ and 2Pt3Cr/SiO$_2$ form bimetallic catalysts with similar average compositions and structures, the difference in catalytic selectivity indicate that that the surface compositions are not equivalent. To

quantify these differences a surface sensitive characterization is needed. Surface oxidation of the nanoparticles was used to determine the Pt dispersion. However, Cr was also oxidized as evidenced by the loss of Pt-Cr coordination.[37] Since the metallic bonds of the oxidize nanoparticles are identical to the particle interior of the reduced sample, the difference spectrum represents those bonds only from the surface. For EXAFS, in this difference spectrum (reduced minus oxidized), there are surface Pt-Pt, Pt-Cr and Pt-O scatters. This is shown schematically in Figure 2.8. In the difference fit, since the oxidized catalysts is subtracted from the reduced spectrum, the Pt-O scattering path is π-radians out of phase from a normal scattering pair, *i.e*, a direct EXAFS fit.
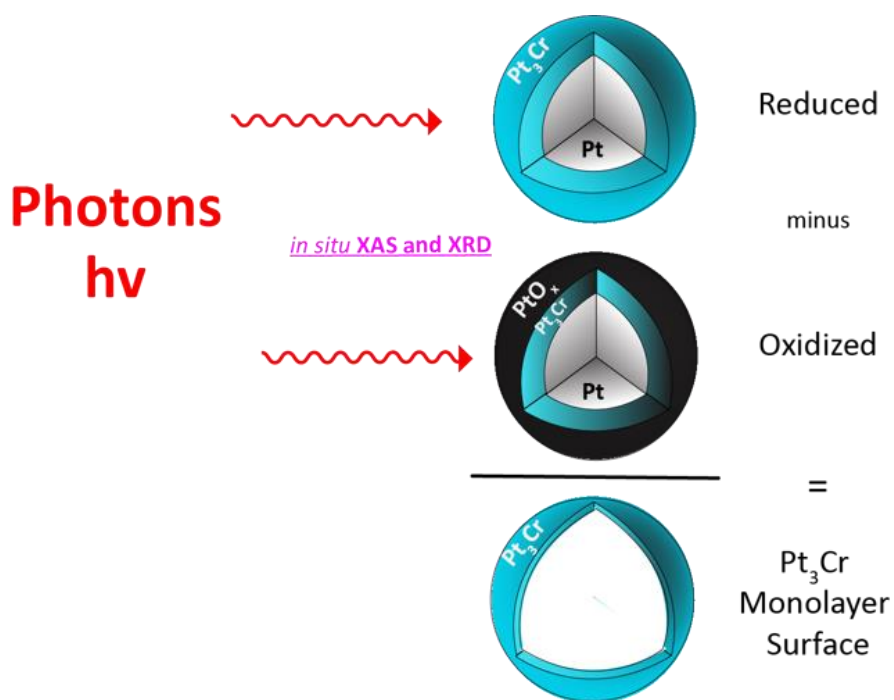
Figure 2.8. Approach for difference analysis, where reduced Pt-Cr nanoparticles are subsequently oxidized, and the raw data is subtracted to isolate the non-oxidized surface

The reduced and oxidized magnitude and imaginary parts for the 2Pt3Cr/SiO$_2$ catalysts are shown in Figure 2.9a. The small difference represents the loss of metallic peaks upon oxidation and formation of Pt-O bonds. The difference EXAFS is shown if Figure 2.9b. Since the metallic peaks that are common to both the reduced and oxidized nanoparticles are removed in the difference spectrum, the surface Pt-O and surface Pt-Pt and Pt-Cr are more easily resolved and analyzed. The fits of the difference EXAFS are given in Table 2.6. The Pt-O coordination number

in the difference fit are consistent with those in the oxidized catalyst. For 2Pt3Cr/SiO$_2$, reduction at 250°C gives a surface CN_{Pt-Cr}/CN_{Pt-Pt} ratio of 0.31, which is higher than that of the reduced catalyst, 0.16, indicating that the surface is more Cr-rich than the average composition. Also, in a Pt$_3$Cr alloy the $CN_{Pt-Cr}/CN_{Pt-Pt} = 0.5$; thus, reduction at 250°C does not lead to a full Pt$_3$Cr surface alloy. For reduction at temperatures above about 400°C, however, the CN_{Pt-Cr}/CN_{Pt-Pt} ratio of about 0.5 is consistent with full monolayer coverage of Pt$_3$Cr.
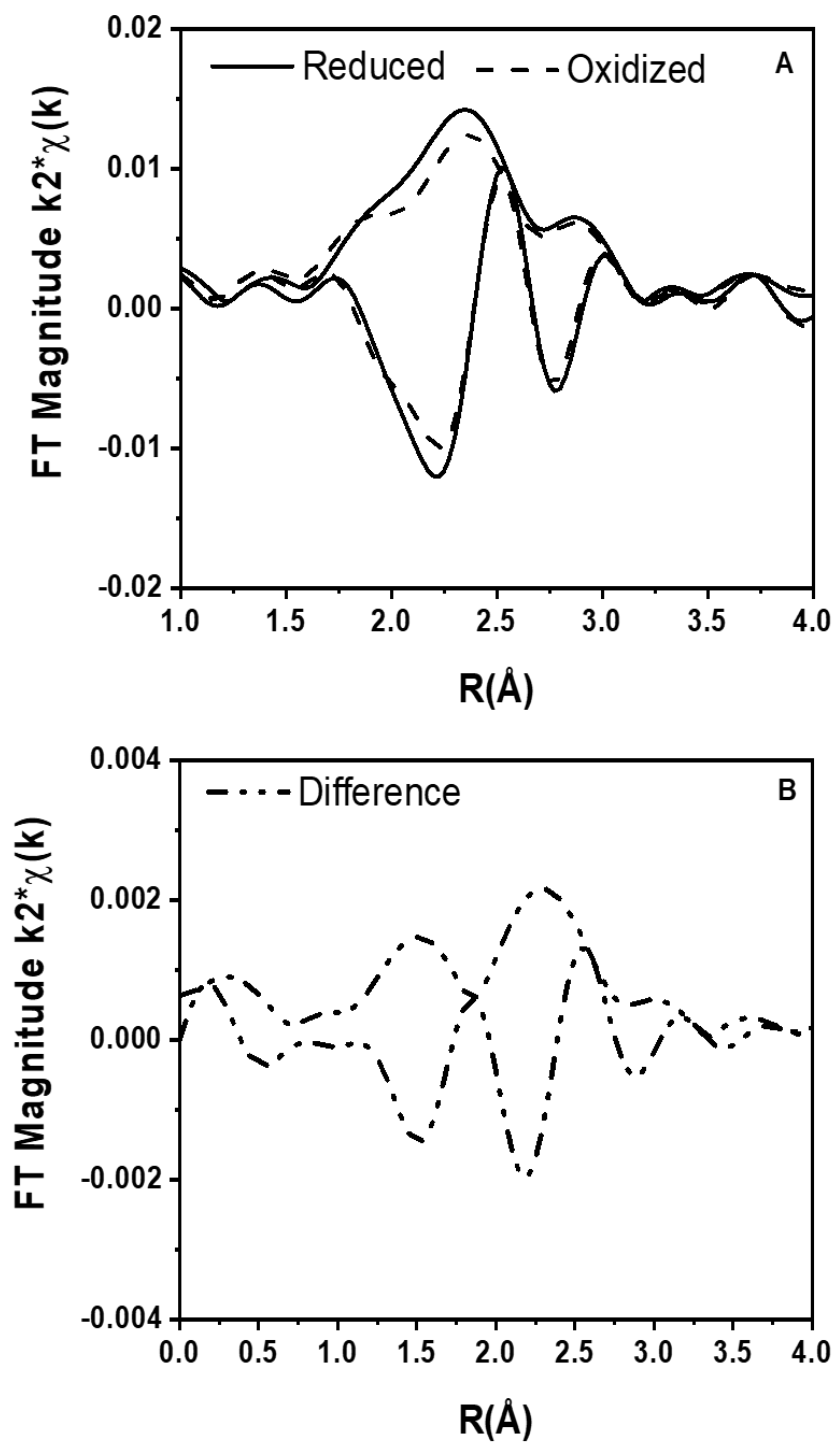
Figure 2.9. 2Pt3Cr/SiO₂ after reduction at 550°C: A) Fourier transform magnitude and imaginary components of the reduced and oxidized catalyst B) Difference EXAFS

Table 2.6. Difference XAS fitting parameters for the surface compositions of 2Pt1Cr/SiO$_2$ and 2Pt3Cr/SiO$_2$ after reduction in H$_2$ at subsequently increasing temperatures

Sample	Reduction Temperature (°C)	Scattering Path	CN	R (Å)	$\Delta\sigma^2$ (Å^2)	ΔE_o (eV)	Pt dispersion
2Pt1Cr/SiO$_2$	550	Pt-Pt	1.5	2.75	0.003	-1.0	0.16
		Pt-Cr	0.6	2.71	0.003	3.8	
		Pt-O	0.4	2.05	0.001	-3.5	
	700	Pt-Pt	1.5	2.75	0.003	-2.9	0.13
		Pt-Cr	0.6	2.68	0.003	-2.8	
		Pt-O	0.3	2.05	0.001	-4.3	
2Pt3Cr/SiO$_2$	250	Pt-Pt	1.6	2.74	0.003	2.1	0.22
		Pt-Cr	0.5	2.73	0.003	6.3	
		Pt-O	0.6	2.05	0.001	-2.5	
	400	Pt-Pt	1.1	2.73	0.003	0.9	0.20
		Pt-Cr	0.5	2.73	0.003	5.6	
		Pt-O	0.4	2.05	0.001	-1.7	
	550	Pt-Pt	0.9	2.73	0.003	-4.0	0.18
		Pt-Cr	0.5	2.73	0.003	5.1	
		Pt-O	0.3	2.05	0.001	-2.7	
	700	Pt-Pt	0.7	2.73	0.003	-0.3	0.14
		Pt-Cr	0.5	2.73	0.003	2.0	
		Pt-O	0.2	2.05	0.001	-2.8	

The surface fits (Table 2.6) also show that the surface of 2Pt1Cr/SiO$_2$ is more Pt-rich than that of 2Pt3Cr/SiO$_2$. For example, reduction at 550°C, the CN$_{Pt-Cr}$/CN$_{Pt-Pt}$ surface composition is 0.40 and 0.55 in 2Pt1Cr/SiO$_2$ and 2Pt3Cr/SiO$_2$, respectively. For the former, even at 800°C, the difference EXAFS indicates a surface with both monometallic Pt and Pt$_3$Cr in 2Pt1Cr/SiO$_2$. The excess surface Pt explains why this catalyst has lower selectivity than that of 2Pt3Cr/SiO$_2$. The CN$_{Pt-Cr}$/CN$_{Pt-Pt}$ ratios for the reduced, oxidized and surface are given in Table 2.7.

In 2Pt3Cr/SiO$_{2,}$ after reduction at 250°C, the reduced particle has a CN$_{Pt-Cr}$/CN$_{Pt-Pt}$ of 0.16, while the surface is 0.31. The particle interior has less Cr than the average composition. Thus, the initial Cr is formed at the particle surface. At 250°C, the surface composition is not consistent with full monolayer of Pt$_3$Cr (CN$_{Pt-Cr}$/CN$_{Pt-Pt}$ = 0.5). Increasing the reduction temperature, leads to an increase in the CN$_{Pt-Cr}$/CN$_{Pt-Pt}$ ratio of the reduced nanoparticle (0.24) and surface (0.45). The particle interior is a mixture of Pt and Pt$_3$Cr, while the surface is nearly a complete Pt$_3$Cr monolayer. At higher reduction temperatures, the surface is little changed, while the Cr composition of the particle interior increases. Above about 700°C, the nanoparticles are nearly a full Pt$_3$Cr alloy with little remaining monometallic Pt. At 700°C, the surface EXAFS appears to be Cr-rich compared

to the Pt_3Cr alloy, however, as the particle size increase, the errors in the difference spectrum become less reliable.

In principle, the difference analysis can be applied to the XRD patterns. Direct oxidation of the surface leads to the formation of Pt-O and Cr-O, which are amorphous. Although the difference XRD pattern of catalysts reduced at low temperatures were narrower, more symmetric and shifted slightly to higher angle compared to the reduced pattern, it was not possible to resolve the surface structure due to the very similar peak positions of Pt and Pt_3Cr. For $2Pt3Cr/SiO_2$ reduced at 700°C and 800°C where the peaks were larger and sharper, the difference XRD was possible. The small shifts in the difference XRD were consistent with only the Pt_3Cr phase at the surface (Figure 2.10). At these high reduction temperatures, the surface and average composition indicate the same Pt_3Cr structure.

Table 2.7. EXAFS coordination ratios for the reduced (average), oxidized (particle interior), and surface of bimetallic Pt-Cr nanoparticles

		CN_{Pt-Cr}/CN_{Pt-Pt}		
Sample	**Reduction Temperature (°C)**	**Average**	**Interior**	**Surface**
2Pt1Cr/SiO₂	550	0.28	0.25	0.40
	700	0.35	0.31	0.40
	800	0.38	-	-
2Pt3Cr/SiO₂	250	0.16	0.11	0.31
	400	0.24	0.14	0.45
	550	0.30	0.22	0.56
	700	0.46	0.43	0.71
	800	0.52	-	-
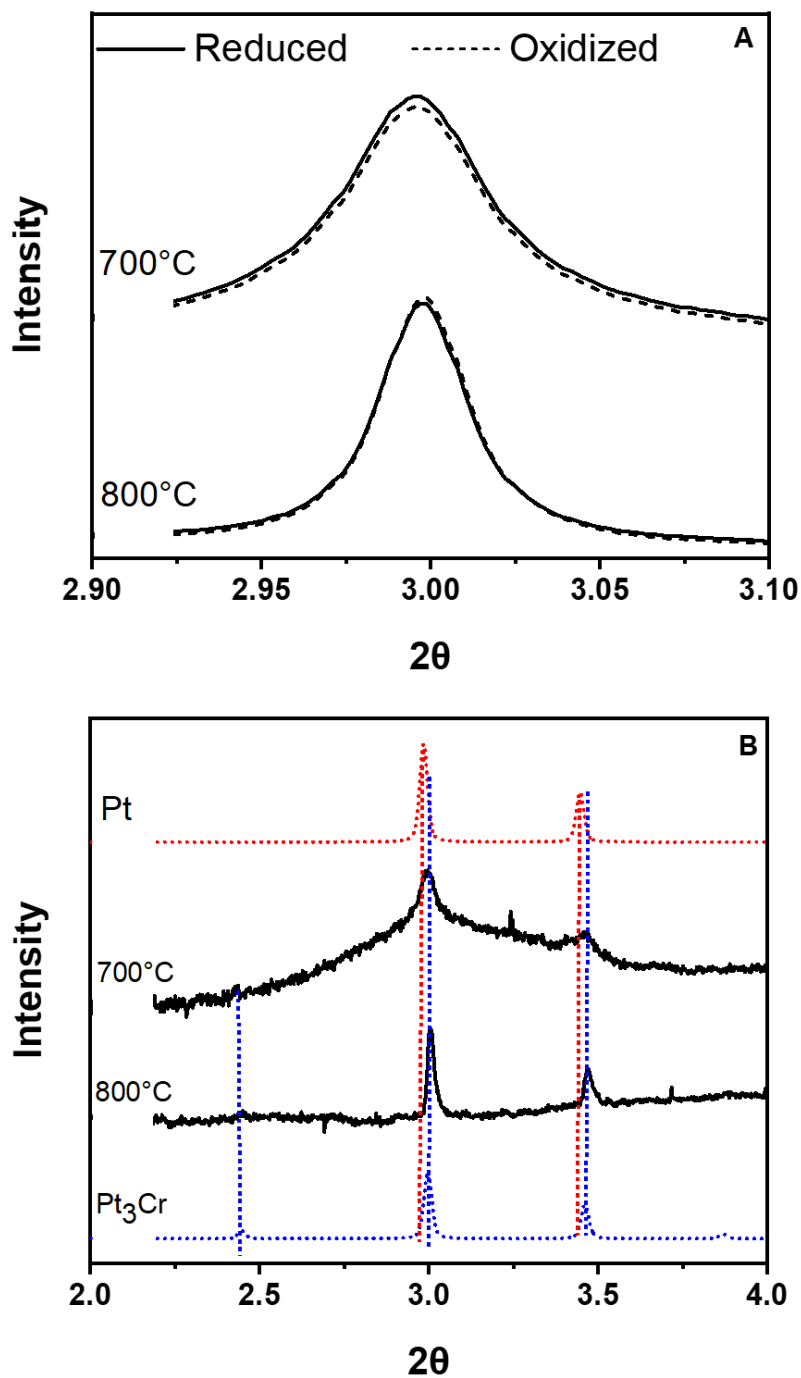
Figure 2.10. A) Diffraction patterns for (111) and (200) peaks after catalyst was reduced (solid) and oxidized (dashed). Pt and Pt$_3$Cr simulations at the appropriate lattice parameter of the reduced sample are provided for reference B) Difference XRD where the diffraction pattern of the oxidized sample is subtracted from that of the reduced

The catalyst characterizations, *e.g.*, fully reduced, oxidized, and surface, lead to a better understanding of the resulting structure of nanoparticles. Both the composition and reduction temperature affect the resulting structure and morphology (Figure 2.11). Although the metal oxides of Pt and Cr are deposited on the SiO_2 surface, the reduction of PtO_x is more kinetically favorable than Cr_2O_3, thus, Pt is initially reduced.[38–40] Pt activates H_2, reducing Cr_2O_3 at lower temperatures than in the absence of Pt.[41–44] Small amounts of metallic Cr is incorporated in the initially formed Pt nanoparticles as low as 250°C. At this temperature, in 2Pt3Cr/SiO$_2$ the average nanoparticle composition has 8 times more Pt than Cr. The surface analysis, however, indicates that the surface has more metallic Cr than the reduced nanoparticle, but that a full monolayer has not yet formed. In addition, the EXAFS of the particle interior shows little Cr. These analysis are consistent with a mechanism of alloy formation where catalytic reduction of nearby Cr_2O_3 leads to a surface alloy.[43,45–47] This mechanism is consistent with that reported for β_1-PdZn alloy.
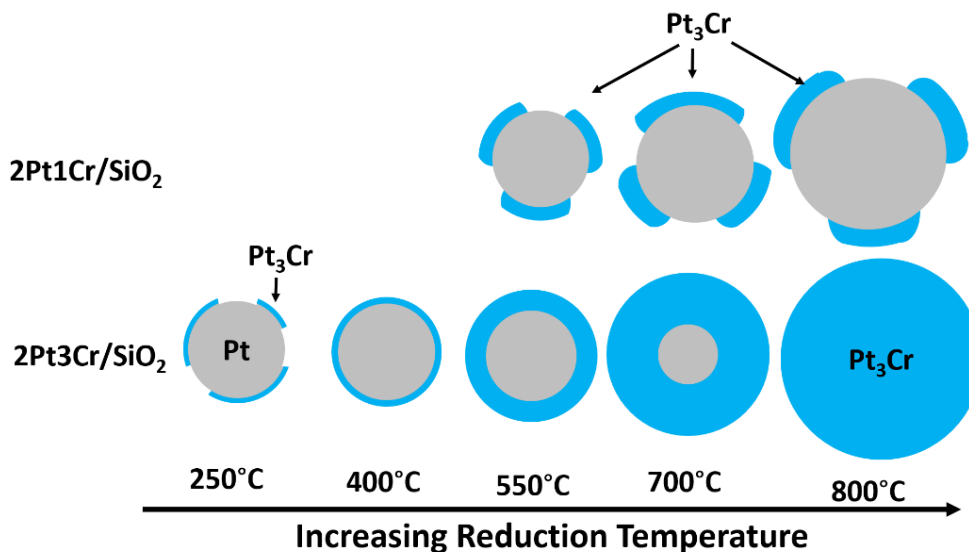
Figure 2.11. Cr incorporation into Pt nanoparticles in 2Pt1Cr/SiO$_2$ and 2Pt3Cr/SiO$_2$ with increasing reduction temperature

The amount of metallic Cr in the nanoparticle increases with increasing reduction temperature, but the surface composition remains nearly constant with a structure consistent with Pt$_3$Cr. The additional Cr incorporation occurs in the subsurface of the nanoparticles. Cr diffusion continues at higher temperature, until a full Pt$_3$Cr intermetallic alloy is formed. To form a Pt$_3$Cr nanoparticle,

only about 6% of Cr_2O_3 in 2Pt3Cr/SiO_2 is reduced. Most of the Cr (> 94%) remains oxidized in these samples, presumably the Cr oxide that is distant from the Pt nanoparticles. XAS analysis at the Cr K edge was not be able to detect the small fraction of metallic Cr. Although there is sufficient Cr in the catalyst to form bimetallic nanoparticles with higher content, due to the difficulty to reduce Cr oxide on SiO_2, Cr-rich phases (PtCr and $PtCr_3$) are not formed even after reduction at 800°C.

At 1 wt% Cr loading, there is still a larger molar excess of Cr than is needed to form a surface alloy and even a full Pt_3Cr nanoparticles, but a full surface layer of Pt_3Cr does not form under any reduction condition. This suggests that there is an insufficient amount of CrO_x near the Pt nanoparticles.

As the amount of Cr increases, the shift in the XANES energy also increases proportional to the amount of Pt_3Cr in the nanoparticles, *e.g.*, plotted as the CN_{Pt-Cr} /CN_{Pt-Pt} (Figure 2.12). For Pt_3Cr the ratio of 0.5 is a fully alloyed nanoparticle. By fitting the XANES spectra for any catalyst with the Pt and Pt_3Cr (2Pt3Cr/SiO_2 reduced at 800°C) XANES, one can determine the fraction of each phase. This fraction can also be obtained by using ratios of EXAFS coordination numbers.
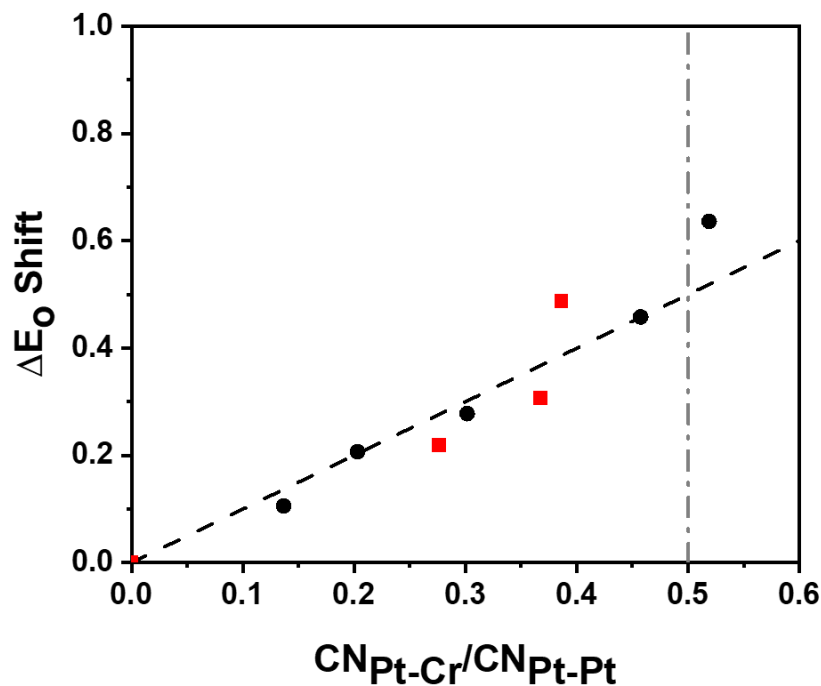
Figure 2.12. XANES energy shift for 2Pt1Cr/SiO$_2$ (red) and 2Pt3Cr/SiO$_2$ (black) as a function of coordination number ratio, where the expected E$_o$ shift (gray dot dash) occurs when CN$_{Pt-Cr}$/CN$_{Pt-Pt}$=0.5

With the fraction of each phase and the TEM particle size, the shell thickness can be approximated. For example, in 2Pt3Cr/SiO$_2$, after reduction at 550°C, CN$_{Pt-Pt}$ is 8.1 and CN$_{Pt-Cr}$ is 2.4. Since all Pt-Cr scattering is due to formation of Pt$_3$Cr and the ratio of CN$_{Pt-Pt}$ in the alloy is twice that for Pt-Cr, the CN$_{Pt-Pt}$ in the alloy fraction is 4.8, leaving CN$_{Pt-Pt}$ =3.3 in the core. These ratios indicate that about 60% (4.8/8.1) of the Pt is present at Pt$_3$Cr and 40% is monometallic Pt. This can be visualized in the left portion of Figure 2.13 for 2Pt3Cr/SiO$_2$ after reduction at 550°C, where the total particle size was 2.5 nm. Approximating nanoparticles as a sphere ($V = \frac{4}{3}\pi\,r^3$), the ratio of the volume of the nanoparticle to the volume of a Pt$_3$Cr unit cell can be used to determine the number of atoms in the nanoparticle.
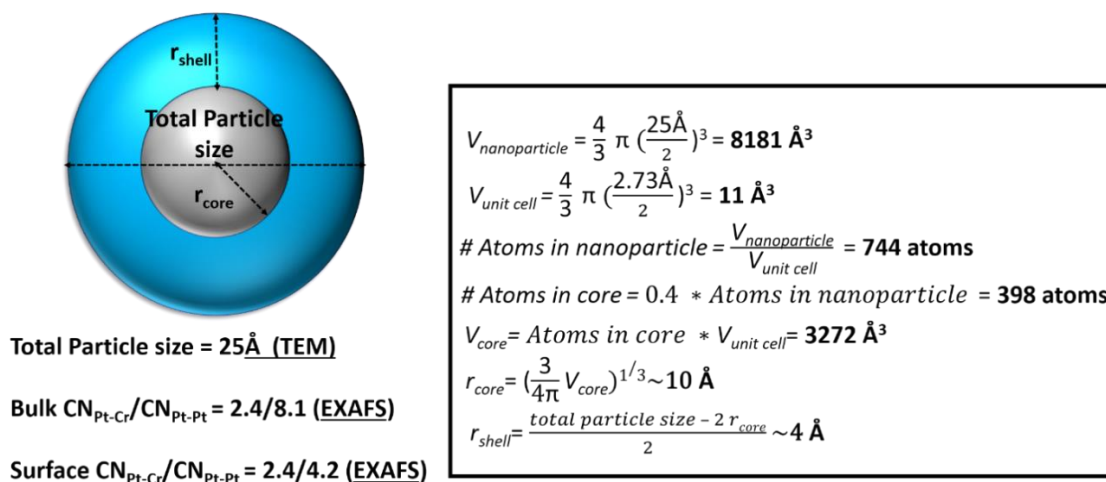
Figure 2.13. Sample calculation for shell thickness in Pt$_3$Cr@Pt core-shell nanoparticle after reduction at 550°C

The total shell contributes about 0.8 nm, so that the shell thickness is approximately 0.4 nm, or about 1.3 atomic layers. The shell thickness estimates for the 2Pt3Cr/SiO$_2$ catalyst at different reduction temperatures (Table 2.8). Similar calculations for 2Pt1Cr/SiO$_2$ reduced at 550°C give a surface fraction of about 0.3 Pt and 0.7 Pt$_3$Cr. This model is based on the average (reduced) and surface compositions of the nanoparticles.

Table 2.8. Fraction of Pt$_3$Cr in 2Pt3Cr/SiO$_2$ and 2Pt1Cr/SiO$_2$ as a function of reduction temperature

Sample	Reduction Temperature (°C)	Fraction of Pt$_3$Cr (%)	r$_{shell}$ (nm)	# atomic layers in Pt$_3$Cr shell
2Pt1Cr/SiO$_2$	550	37	0.2	0.8
	700	47	0.4	1.3
	800	51	0.5	1.7
2Pt3Cr/SiO$_2$	250	30	0.1	0.3
	400	42	0.2	0.6
	550	60	0.4	1.3
	700	91	1.0	3.7
	800	100	1.7	6.2

The two Pt-Cr bimetallic catalysts were very similar from their bulk characterization after reduction at 550°C. Both were bimetallic nanoparticles by XANES and EXAFS with similar change in the XANES energy. The XRD patterns were also very similar. However, the EXAFS of the difference spectrum of the 2Pt1Cr/SiO$_2$ indicates that a full surface alloy is not formed and

about 30% of the surface remains monometallic Pt. This correlates with the lower olefin selectivity (88%) compared to 2Pt3Cr/SiO$_2$ (> 97%) which forms a complete monolayer of Pt$_3$Cr intermetallic alloy.

In summary, Pt$_3$Cr bimetallic nanoparticles were synthesized with different Cr loadings, and evaluated for their catalytic performance for propane dehydrogenation. While characterization methods of the average structure suggested similar morphologies, higher Cr loading displayed higher olefin selectivity. Small changes in surface composition were only observed using difference XAS and XRD, which showed that the morphology of the catalyst changes with Cr content and reduction temperature. The best catalytic performance was observed in nanoparticles containing at least a full Pt$_3$Cr surface alloy.

2.5   Conclusion

Confirmation of the Pt$_3$Cr structure in these bimetallic catalysts is not enough to understand their catalytic performance since several structures and morphologies are possible. In this study, Pt-Cr alloys were prepared at increasing reduction temperatures and containing varying amounts of Cr. While reduction at high temperatures and higher Cr loading led to the formation of a full Pt$_3$Cr alloy, Pt core with Pt$_3$Cr shell nanoparticles were formed at lower temperatures. At lower Cr loading, there was insufficient Cr$_2$O$_3$ near Pt nanoparticles to form a complete surface alloy. However, the addition of even small amounts of Cr led to improvements in olefin selectivity for propane dehydrogenation compared to monometallic Pt.

XAS and XRD confirms the presence of bimetallic nanoparticles with a two-phase composition (Pt and Pt$_3$Cr) but is insufficient to determine the structure of the catalytic surface. By analysis of the oxidized catalysts, the structure of the particle interior could be determined. The difference spectrum of reduced and oxidized catalysts also allowed for determination of the surface composition and structure. The nanoparticles were shown to contain more Cr at the surface than at the interior. In addition, from the surface XAS and XRD, the identification of the specific intermetallic Pt$_3$Cr phase was more easily determined than in the fully reduced, two-phase (Pt + Pt$_3$Cr) nanoparticles. Utilizing these analyses along with the TEM particle size also allows for determination of the shell thickness in core-shell bimetallic nanoparticles.

2.6   Acknowledgement

2.7   References

1. Singh, A. K.; Xu, Q. Synergistic Catalysis over Bimetallic Alloy Nanoparticles. *ChemCatChem*. **2013**, *5*, 652–676.

2. Chen, T.; Rodionov, V. O. Controllable Catalysis with Nanoparticles: Bimetallic Alloy Systems and Surface Adsorbates. *ACS Catal.* **2016**, *6*, 4025–4033.

3. Louis, C. Chemical Preparation of Supported Bimetallic Catalysts. Gold-Based Bimetallic, a Case Study. *Catalysts*. **2016**, *6*, 110.

4. Sattler, J. J..; Ruiz-Martinez, J.; Santillan-Jimenez, E.; Weckhuysen, B. M. Catalytic Dehydrogenation of Light Alkanes on Metals and Metal Oxides. *Chem. Rev.* **2014**, *114*, 16013–16063.

5. Sinfelt, J. H. Catalysis by Alloys and Bimetallic Clusters. *Bimetallic Clust. Catal.* **1977**, *10*, 15–20.

6. Wong, A.; Liu, Q.; Griffin, S.; Nicholls, A.; Regalbuto, J. R. Synthesis of ultrasmall, homogeneously alloyed, bimetallic nanoparticles on silica supports. *Science*. **2017**, *358*, 1427–1430.

7. Furukawa, S.; Komatsu, T. Intermetallic Compounds: Promising Inorganic Materials for Well-Structured and Electronically Modified Reaction Environments for Efficient Catalysis. *ACS Catal.* **2017**, *7*, 735–765.

8. Wu, Z.; Wegener, E.C.; Tseng, H.; Gallagher, J.R.; Harris, J.W.; Diaz, R.E.; Ren, Y.; Riberiro, F.H.; Miller, J.T. Pd–In intermetallic alloy nanoparticles: highly selective ethane dehydrogenation catalysts. *Catal. Sci. Technol.* **2016**, *6*, 6965–6976.

9. Ma, Z.; Wu, Z.; Miller, J. T. Effect of Cu content on the bimetallic Pt–Cu catalysts for propane dehydrogenation. *Catal. Struct. React.* **2017**, *3*, 43–53.

10. Alexeev, O. S.; Gates, B. C. Supported Bimetallic Cluster Catalysts. *Ind. Eng. Chem.* **2003**, *42*, 1571–1587.

11. Bugaev, A. L.; Guda, A.A.; Lomachenko, K.A.; Shapovalov, V.V.; Lazzarini, A.; Vitillo, J.G.; Bugaev, L.A.; Groppo, E.; Pellegrini, R.; Soldatov, A.V.; van Bokhoven, J.A.; Lamberti, C. Core–Shell Structure of Palladium Hydride Nanoparticles Revealed by Combined X-ray Absorption Spectroscopy and X-ray Diffraction. *J. Phys. Chem. C.* **2017**, *121,* 18202-18213.

12. Bugaev, A. L.; Guda, A.A.; Lomachenko, K.A.; Srabionyan, V.V.; Bugaev, L.A.; Soldatov, A.V.; Lamberti, C.; Dmitriev, V.P.; van Bokhoven, J.A. Temperature- and Pressure-Dependent Hydrogen Concentration in Supported PdHx Nanoparticles by Pd K-Edge X-ray Absorption Spectroscopy. *J. Phys. Chem. C* **2014**, *118,* 10416–10423.

13. Gallagher, J. R.; Childers, D.J.; Zhao, H.; Winans, R.E.; Meyer, R.J.; Miller, J.T. Structural evolution of an intermetallic Pd–Zn catalyst selective for propane dehydrogenation. *J. Phys. Chem.* **2015**, *17*, 28144–28153.

14. Yang, C.; Wu, Z.; Zhang, G.; Sheng, H.; Tian, J.; Duan, Z.; Sohn, H.; Kropf, J.A.; Wu, T.; Krause, T.R.; Miller, J.T. Promotion of Pd nanoparticles by Fe and formation of a Pd3Fe intermetallic alloy for propane dehydrogenation. *Catal. Today.* **2019,** *323*, 123-128.

15. Ye, C.; Wu, Z.; Liu, W.; Ren, Y.; Zhang, G.; Miller, J.T. Structure Determination of a Surface Tetragonal Pt1Sb1 Phase on Pt Nanoparticles. *Chem. Mater.* **2018**, *30*, 4503-4507.

16. Wegener, E. C.; Wu, Z.; Tseng, H.; Gallagher, J.R.; Ren, Y.; Diaz, R.E.; Ribeiro, F.H.; Miller, J.T. Structure and reactivity of Pt–In intermetallic alloy nanoparticles: Highly selective catalysts for ethane dehydrogenation. *Catal. Today*. **2017**, *299*, 146-153.

17. Childers, D. J.; Schweitzer, N.M.; Shahari, S.M.K; Rioux, R.M.; Miller, J.T.; Meyer, R.J. Modifying structure-sensitive reactions by addition of Zn to Pd. *J. Catal.* **2014**, *318*, 75-84.

18. Wanjala, B. N.; Luo, J.; Loukrakpam, R.; Fang, B.; Mott, D.; Njoki, P.N.; Engelbard, M.; Naslund, R.H.; Wu, J.K.; Wang, L.; Malis, O.; Zhong, C.J. Nanoscale Alloying, Phase-Segregation, and Core−Shell Evolution of Gold−Platinum Nanoparticles and Their Electrocatalytic Effect on Oxygen Reduction Reaction. *Chem. Mater.* **2010**, *22*, 4282–4294.

19. Wu, Z.; Bukowski, B.C.; Li, Z.; Milligan, C.; Zhou, L.; Ma, T.; Wu, Y.; Ren, Y.; Ribeiro, F.H.; Delgass, N.W.; Greeley, J.P.; Zhang, G.; Miller, J.T. Changes in Catalytic and Adsorptive Properties of 2 nm Pt3Mn Nanoparticles by Subsurface Atoms. *J. Am. Chem. Soc.* **2018**, *140*, 14870-14877.

20. Tao, F.; Grass, M.E.; Zhang, Y.; Butcher, D.R.; Renzas, J.R.; Liu, Z.; Chung, J.Y.; Mun, B.S.; Salmerson, M.; Somojai, G.A. Reaction-Driven Restructuring of Rh-Pd and Pt-Pd Core-Shell Nanoparticles. *Science*. **2008**, *322,* 932-934.

21. Cai, Z.; Chattopadhyay, N.; Liu, W.J.; Chan, C.; Pignol, J.P.; Reilly, R.M. Optimized digital counting colonies of clonogenic assays using ImageJ software and customized macros: Comparison with manual counting. *Radiat. Biol.* **2011**, *87,* 1135–1146.

22. Yoshida, H.; Omote, H.; Takeda, S. Oxidation and reduction processes of platinum nanoparticles observed at the atomic scale by environmental transmission electron microscopy. *Nanoscale*. **2014**, *6*, 13113–13118.

23. Ressler, T. WinXAS: a Program for X-ray Absorption Spectroscopy Data Analysis under MS-Windows. *J Synchrotron Rad* . **1998,** *5,* 118–122.

24. Rehr, J. J.; Booth, C. H.; Bridges, F; Zabinsky S. I. X-ray-absorption fine structure in embedded atoms. *Phys. Rev. B.* **1994**, *49*, 12347-12350.

25. Hammersley, A.P.; Svensson, S.O.; Hanfland, M.; Fitch, A.N.; Hausermann, D. Two-dimensional detector software: From real detector to idealised image or two-theta scan: High Pressure Research. *High Press. Res.* **1996,** *14,* 235-248.

26. Chateigner, D.; Modreanu, M.; Murtagh, M. E.; Ricote, J.; Schreiber, J. Thin Solid Films | Proceedings of Symposium M on Optical and X-Ray Metrology for Advanced Device Materials Characterization, *Thin Solid Films,* **2004**, *450*, 34–41.

27. Hejral, U.; Muller, P.; Shiplin, M.; Gustafson, J.; Franz, D.; Shayduk, R.; Rutt, U.; Zhang, C.; Merte, L.R.; Lundgren, E.; Vonk, V.; Stierle, A. High-energy x-ray diffraction from surfaces and nanoparticles. *Phys. Rev. B* **2017.** *96*, 195433.

28. Leontyev, I. N.; Kuriganova, A.B.; Leontyev, N.G.; Hennet, L.; Rakhmatullin, A.; Smirnova, N.V.; Dmitriev, V. Size dependence of the lattice parameters of carbon supported platinum nanoparticles: X-ray diffraction analysis and theoretical considerations. *RSC Adv.* **2014**, *4*, 35959–35965.

29. Yang, W.; Zou, L.; Huang, Q.; Zou, Z.; Hu, Y.; Yang, H. Lattice Contracted Ordered Intermetallic Core-Shell PtCo@Pt Nanoparticles: Synthesis, Structure and Origin for Enhanced Oxygen Reduction Reaction. *J. Electrochem. Soc.* **2017**, *164*, H331–H337.

30. Okamoto, H. *Phase Diagrams for Binary Alloys*; ASM International: Materials Park, OH, 2010.

31. Antolini, E.; Salgado, J. R. C.; Santos, L. G. R. A. Carbon supported Pt-Cr alloys as oxygen-reduction catalysts for direct methanol fuel cells. *J. Appl. Electrochem.* **2006**, *36,* 355–362.

32. Lei, Y.; Jelic, J.; Nitsche, L.C.; Meyer, R; Miller, J.T. Effect of Particle Size and Adsorbates on the L3, L2 and L1 X-ray Absorption Near Edge Structure of Supported Pt Nanoparticles. *Top. Catal.* **2011.** *54,* 334–348.

33. Chakrabarti, A.; Wachs, I. E. The Nature of Surface CrOx Sites on SiO2 in Different Environments. *Catal. Lett.* **2015**, *145*, 985–994.

34. Delley, M. F.; Conley, M. P.; Copéret, C. Polymerization on CO-Reduced Phillips Catalyst initiates through the C–H bond Activation of Ethylene on Cr–O Sites. *Catal. Lett.* **2014**, *144*, 805–808.

35. Conley, M.P.; Delley, M.F.; Núñez-Zarur, F.; Comas-Vives, A.; Copéret, C. Heterolytic Activation of C-H Bonds on Cr(III)-O Surface Sites Is a Key Step in Catalytic Polymerization of Ethylene and Dehydrogenation of Propane. *Inorg. Chem.* **2015**, *54*, 5065–5078.

36. Cui, Z.; Chen, H.; Zhou, W.; Zhao, M.; DiSalvo, F. J. Structurally Ordered Pt3Cr as Oxygen Reduction Electrocatalyst: Ordering Control and Origin of Enhanced Stability. *Chem. Mater.* **2015**, *27*, 7538–7545.

37. Gallagher, J. R.; Li, T.; Zhao, H.; Liu, J.; Lei, Y.; Zhang, X.; Ren, Y.; Elam, J.W.; Meyer, R.J.; Winans, R.E.; Miller, J.T. In situ diffraction of highly dispersed supported platinum nanoparticles. *Catal. Sci. Technol.* **2014**, *4,* 3053–3063.

38. Anderson, J. R. *Structure of Metallic Catalysts*; Academic Press: New York, NY, 1975.

39. Klissurski, D.; Dimitrova, R. Reducibility of Metal Oxides in Hydrogen and Strength of Oxygen Bond in Their Surface Layer. *Bull. Chem. Soc. Jpn.* **1990**, *63*, 590–591.

40. Fang, Z.; Vasiliu, M.; Peterson, K. A.; Dixon, D. A. Prediction of Bond Dissociation Energies/Heats of Formation for Diatomic Transition Metal Compounds: CCSD(T) Works. *J. Chem. Theory Comput.* **2017**, *13*, 1057–1066.

41. Bond, G.; Tripathi, J. B. Studies of hydrogen spillover. Part 3.—Catalysis of the reduction of metal oxides by palladium on silica. *J. Chem. Soc. Faraday Trans. 1 Phys. Chem. Condens. Phases.* **1976**, *72*, 933–941.

42. Karim, W.; Spreafico, C.; Kleibert, A.; Gobrecht, J.; VandeVondele, J.; Ekinci, Y.; van Bokhoven, J.A. Catalyst support effects on hydrogen spillover. *Nature*. **2017**, *541*, 68.

43. Tew, M. W.; Emerich, H.; van Bokhoven, J. A. Formation and Characterization of PdZn Alloy: A Very Selective Catalyst for Alkyne Semihydrogenation. *J. Phys. Chem. C.* **2011**, *115*, 8457–8465.

44. Choi, M.; Yook, S.; Kim, H. Hydrogen Spillover in Encapsulated Metal Catalysts: New Opportunities for Designing Advanced Hydroprocessing Catalysts. *ChemCatChem*. **2015**, *7*, 1048–1057.

45. Föttinger, K.; van Bokhoven, J. A.; Nachtegaal, M.; Rupprechter, G. Dynamic Structure of a Working Methanol Steam Reforming Catalyst: In Situ Quick-EXAFS on Pd/ZnO Nanoparticles. *J. Phys. Chem. Lett.* **2011**, *2*, 428–433.

46. Pham, H. N.; Sattler, J. J.; Weckhuysen, B. M.; Datye, A. K. Role of Sn in the Regeneration of Pt/γ-Al2O3 Light Alkane Dehydrogenation Catalysts. *ACS Catal.* **2016**, *6*, 2257–2264.

47. Cortright, R. D.; Hill, J. M.; Dumesic, J. A. Selective dehydrogenation of isobutane over supported Pt/Sn catalysts. *Catal. Today*. **2000**, *55*, 213–223.

3. SURFACE STRUCTURE DETERMINATION BY X-RAY ABSORPTION SPECTRSCOPY

3.1   Introduction

The identification of the geometric and electronic structures of catalysts and their evolution under realistic reaction conditions is essential for developing structure-function relations that drive catalyst development. This has been enabled with the availability of synchrotron radiation, allowing scientists to characterize catalytic nanomaterials under working conditions with control of specific reaction conditions (*e.g.* temperature, pressure, reactor configuration, chemical feedstock). X-ray absorption spectroscopy (XAS) has been extensively used in the catalysis community to identify the oxidation state and geometric arrangement of atoms. The development of a new generation of radiation facilities and sophisticated experimental setups have allowed for the precise identification of the structures of working catalysts. This has further been enabled through the development of fast scan modes, allowing for the capture of information about key reaction intermediates and mechanistic steps in the catalytic cycle.[1–4] Many elements of interest in catalytic materials have absorption edges in the hard x-ray regime. This allows for a variety of *in-situ* sample environments since hard x-rays can penetrate cell windows, gas or liquid reactants, support materials, *etc*. Hence, one can make measurements under realistic reaction conditions and detect all atoms in the sample. While XAS measures every atom, which is important for understanding the nanoparticle structure, chemical reactions occur at the surfaces of the heterogeneous catalysts, which may differ from the average structure.[5–12] A precise understanding of the surface structures in nanoparticle, therefore, is critical for relating the active site structure to catalytic performance.

There are many excellent books and reviews on the theory and practice of XAS.[13–22] Here, a method for determination of the surface composition and structure of alloy nanoparticle is described with three examples using synchrotron x-ray techniques. In the first, the average nanoparticle composition of two catalysts is similar, but their catalytic performance is not. The second demonstrates an example where the surface structure is constant, but the structure of the subsurface changes with varying the metal loadings. The third example describes the formation of bimetallic catalysts with differing composition and average structure, while the catalytic surface structure and reaction performance is identical. To assess the changes in the energy of the valence

orbitals responsible for catalysis, for example, by resonant inelastic x-ray scattering (RIXS), requires that the surface and bulk nanostructures are identical.

3.2 Surface XAS of Metal Nanoparticle Catalysts: Basic Approach

In monometallic nanoparticle catalysts, for example Pt, chemisorption of CO or H_2 is often used to determine the number of surface atoms, *i.e.*, the dispersion. Alternatively, the catalytic surface can be selectively oxidized by O_2 at room temperature and the dispersion determined by re-reduction of the oxidized surface by H_2 titration. For many (reduced) nanoparticle catalysts, ambient oxidation leads to selective oxidation of the (monolayer) catalytic surface. In the oxidized nanoparticle, the interior atoms remain unchanged. For surface EXAFS analysis using hard x-rays, the spectrum of the reduced nanoparticle is determined along with the spectrum of the oxidized catalyst. Subtraction of the oxidized from the reduced spectra gives a difference EXAFS spectrum that allows for determination of the surface structure. Since the interior atoms in both the reduced and oxidized nanoparticle are unchanged, these subtract and are not present in the difference spectrum leaving only EXAFS from surface atoms. Specifically, there are fewer metallic atoms in the oxidized sample, while oxidation also leads to new metal-oxygen bonds. The difference spectrum (reduced – oxidized) has metal-metal scattering with phases identical to those in the reduced catalyst, while the metal-oxygen bonds are π-radians out of phase (due to the subtraction process) from a normal scattering pair. As will be demonstrated in the examples, this method works well when the fraction of surface atoms is large enough to get a reliable EXAFS in the difference spectrum, for example, nanoparticle less than about 5 nm in size where there are greater than about 20% surface atoms. For nanoparticle larger than about 8 nm, the error in the difference EXAFS fit becomes unreliable. The surface EXAFS technique will be demonstrated in the following three examples.

3.3 Case Study 1: Formation of Pt₃Cr Surface Alloys

Pt-Cr bimetallic catalysts show promising performance for propane dehydrogenation with propylene selectivity higher than 95% compared to monometallic Pt nanoparticles.[23] 2%Pt/SiO₂ (denoted 2Pt), 2%Pt-1%Cr/SiO₂ (denoted 2Pt-1Cr), and 2%Pt-3%Cr/SiO₂ (denoted 2Pt-3Cr) were prepared by incipient wetness impregnation, and all catalysts had a similar particle size of about 2

nm measured by scanning transmission electron microscope (STEM). Detailed structural characaterization and catalytic performance have been previously reported.[23] Therefore, only a brief summary will be given here to demonstrate why it is necessary to determine the surface structure and how it can be done using the surface EXAFS analysis. The propane dehydrogenation selectivity of 2Pt shows lower propylene selectivity (75%) than 2Pt-1Cr (95%) and 2Pt-3Cr (98%) at ~15% conversion. Additionally, the selectivity of 2Pt and 2Pt1Cr decrease with increasing propane conversion; while that of 2Pt3Cr remains little changed at all conversions, Figure 3.1.
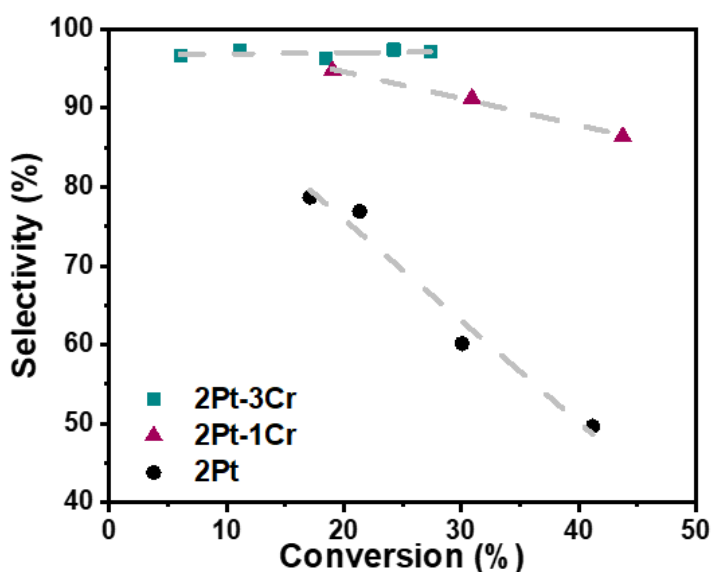
Figure 3.1. Proplyene selectivity as a function of propane dehydrogenation conversion at 550°C, 2.5% C_3H_8 and 2.5% H_2 (balanced with N_2)

The crystalline phases (long-range order) and coordination environment (local structure) of 2Pt and 2Pt-3Cr was determined using *in situ* x-ray diffraction (XRD) and XAS, respectively. The XRD pattern of 2Pt-3Cr after reduction at 800°C showed that the bimetallic phase was a Pt_3Cr intermetallic alloy. Under these conditions, the XAS indicated that a Pt has about 8 Pt neighbors and 4 Cr neighbors, with a Pt-Cr to Pt-Pt coordination number ratio ($CN_{Pt-Cr:Pt-Pt}$) of 0.5, consistent with the Pt_3Cr phase (Cu_3Au structure type). However, when 2Pt-3Cr was reduced at 550°C under the conditions of the catalytic reaction, XRD indicates that both Pt and Pt_3Cr phases were present. The XAS was also consistent with a Pt-rich morphology with the $CN_{Pt-Cr:Pt-Pt}$ ratio of about 0.25.

For 2Pt-1Cr reduced at 550°C, the XRD pattern and EXAFS $CN_{Pt-Cr:Pt-Pt}$ ratio and bond distances were nearly identical to that of 2Pt-3Cr indicating that both catalysts have very similar average structures (Figure 3.2). The catalytic performances, however, suggest some difference in the surface compositions.
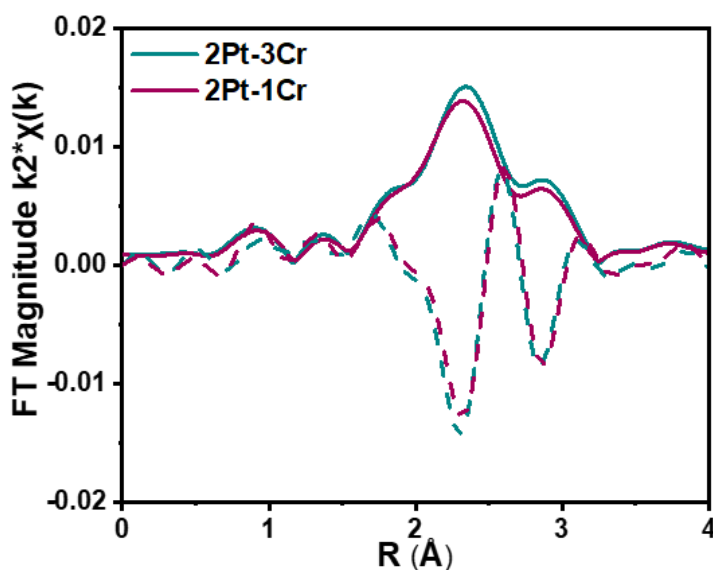
Figure 3.2. EXAFS of Pt-Cr bimetallic nanoparticles containing 1wt% and 3wt% Cr after reduction at 550°C in 3.5% H_2

As discussed above, the difference XAS difference spectrum of the reduced minus oxidized catalyst, depicted in Figure 3.3, provides surface sensitive structural information about the two Pt-Cr catalysts.
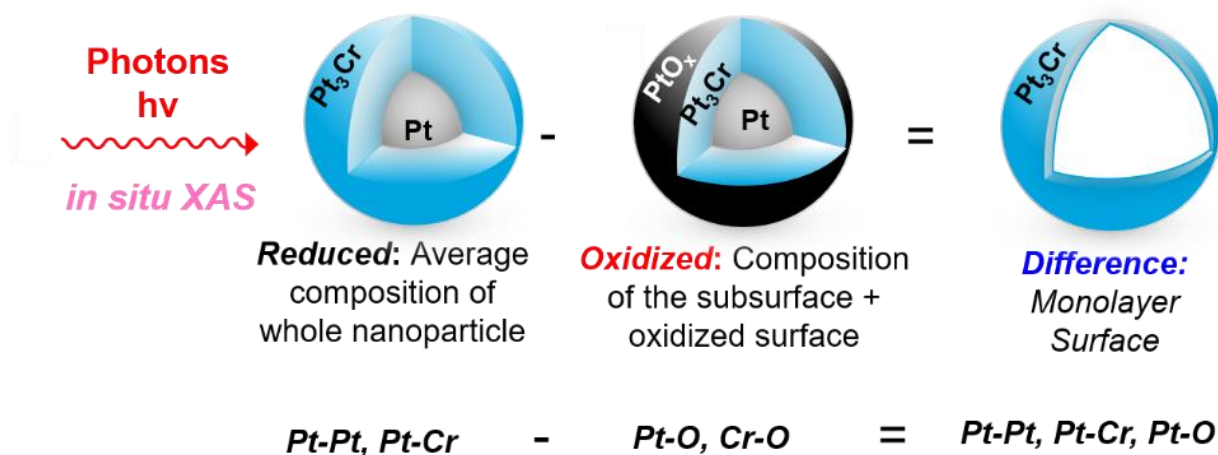
Figure 3.3. Approach for difference analysis, where reduced Pt-Cr nanoparticles are subsequently oxidized, and the EXAFS (chi) data is subtracted to isolate the surface atoms.

Figure 3.4a shows the two Fourier transform of the k^2-weighted EXAFS spectra (reduced and oxidized) for 2Pt-3Cr after reduction at 550°C. Upon room temperature oxidation there is a small loss of surface Pt-Pt and Pt-Cr bonds and the formation of Pt-O bonds. Cr-O bonds formed from the oxidation of surface chromium in the alloy are not observed at the Pt edge due to the element specificity of XAS. While the oxidized spectrum could be fit directly, the small changes and overlapping features makes determination of the change in coordination numbers and bond distances inaccurate. By subtracting the oxidized from reduced EXAFS spectrum, Figure 3.4b; however, the changes in the two catalysts are more readily resolved and can be more accurately fit, Table 3.1.
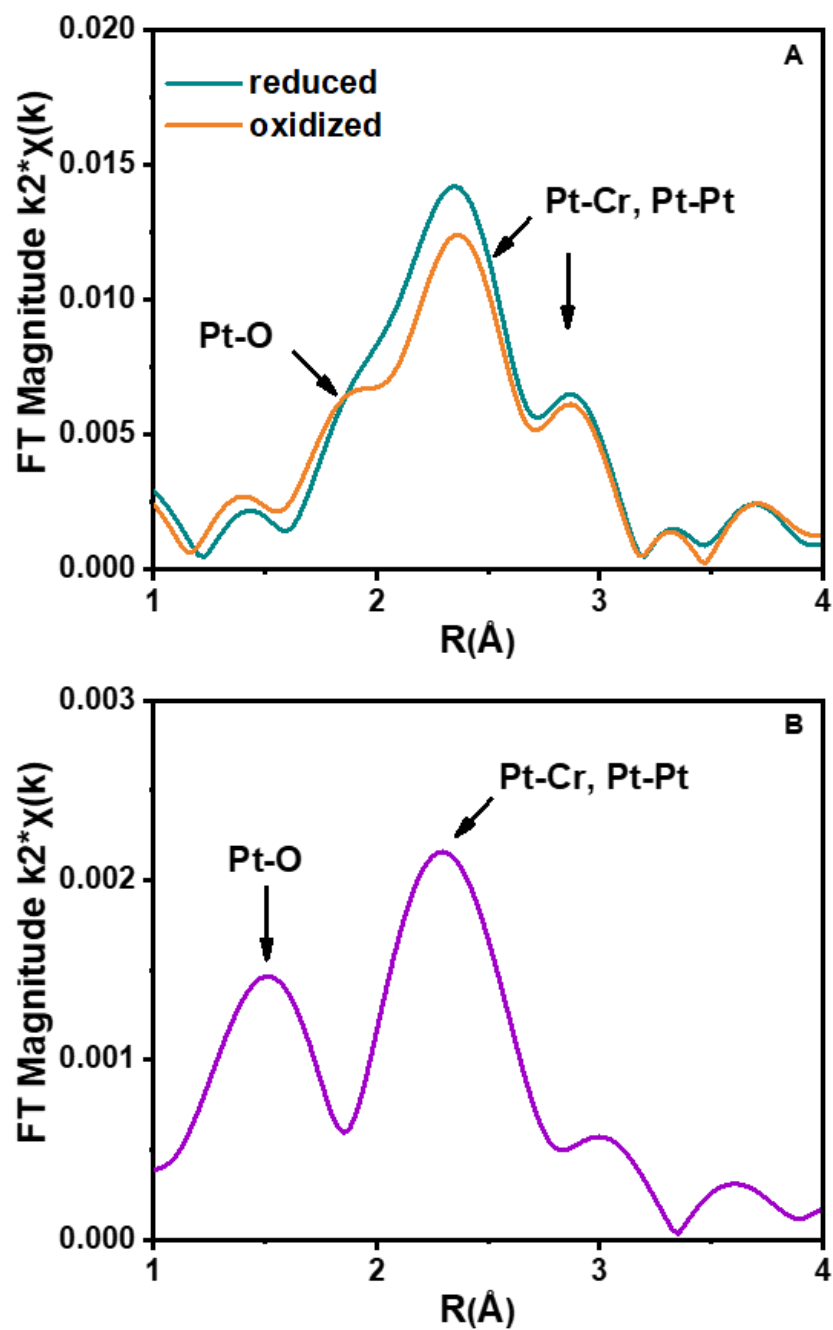
Figure 3.4. The k^2-weighted Fourier transform of Chi of 2Pt-3Cr after reduction at 550°C; A) the reduced, oxidized, and B) difference EXAFS

Table 3.1. Difference EXAFS fits for 2Pt-1Cr and 2Pt-3Cr after reduction at 550°C and room temperature oxidation

Catalyst	Scattering Path	CN	R (Å)
2Pt-1Cr	Pt-Pt	1.5	2.75
	Pt-Cr	0.6	2.71
	Pt-O	0.4	2.05
2Pt-3Cr	Pt-Pt	0.9	2.73
	Pt-Cr	0.5	2.73
	Pt-O	0.3	2.05

The Pt-Cr to Pt-Pt coordination ratio, $CN_{Pt-Cr:Pt-Pt}$, can be used to determine the Cr incorporation into these nanoparticles, Table 3.2. In the average EXAFS fit of 2Pt-3Cr, *i.e.*, the reduced catalyst, the $CN_{Pt-Cr:Pt-Pt}$ was 0.30, while from the surface EXAFS the ratio is near 0.5, consistent with a stoichiometric Pt_3Cr intermetallic alloy surface. The oxidized EXAS fit also represents the structure of the non-surface atoms in the nanoparticle. Although the surface is a Pt_3Cr phase, the interior is much more Pt-rich than the surface. The analysis of the surface and particle interior also suggest that Cr alloy formation starts at the surface of a reduced Pt nanoparticle.

A similar difference surface EXAFS analysis of the reduced and oxidized 2Pt-1Cr shows that the surface $CN_{Pt-Cr:Pt-Pt}$ is 0.40 compared to 0.56 for the 2Pt-3Cr catalyst. In other words, the surface of 2Pt-1Cr is Pt-rich suggesting incomplete formation of a surface Pt_3Cr monolayer (Table 3.2), which leads to lower catalytic selectivity. By identifying the surface structures and compositions, small changes in the catalytic performance can be explained. For these two catalysts, the 2Pt-3Cr had a full monolayer Pt_3Cr intermetallic alloy composition; while the surface of the 2Pt-1Cr was an incomplete monolayer, see schematic in Table 3.2.

Table 3.2. The average, interior and surface CN_{Pt-Cr}/CN_{Pt-Pt} ratios of the reduced, room temperature oxidized and difference EXAFS of 2Pt-1Cr and 2Pt-3Cr catalysts.

	Average	Interior	Surface	Catalyst Structure
2Pt-1Cr	0.28	0.25	0.40	Pt
2Pt-3Cr	0.30	0.22	0.56	Pt

3.4 Case 2: Identification of Different Alloy Structures in Pt-Co Bimetallic Catalysts

Bimetallic Pt-Co nanoparticles containing 2 wt% Pt with 0.6 (2Pt-0.6Co), 1 (2Pt-1Co), 2 (2Pt-2Co), and 4 wt% Co (2Pt-4Co) are compared to a monometallic Pt nanoparticle (3Pt). The difference analysis approach to EXAFS was utilized to determine the specific nanoparticle morphology (including the surface compositions) for each composition of metals. While all four catalyst compositions contained at least a surface layer of Pt_3Co, the composition of the core was found to change with increasing nominal Co content. At low Co loading, the bimetallic nanoparticles form a Pt_3Co intermetallic surface alloy with Pt-rich core. With increasing Co loading, a full alloy forms where both the surface and nanoparticle compositions are Pt_3Co. A further increase in Co loading leads to a Co-rich nanoparticle core, likely PtCo, with a surface of Pt_3Co. Although Pt-Co intermetallic alloys form two different phases and several morphologies, the surface structure is similar in all catalysts.[10]

The k^2-weighted magnitude of the Fourier Transform (FT) of the EXAFS spectra at the Pt L_3 edge show different shapes between the four bimetallic particles and Pt (Figure 3.5 and Table 3.3). The shape of the EXAFS spectrum of 2Pt-0.6Co particles is distorted compared to monometallic Pt, Figure 3.5. The EXAFS fitting results suggest a 7.3 Pt-Pt bonds at 2.73 Å and 2.5 Pt-Co bonds at 2.56 Å. Higher Pt-Pt coordination numbers are consistent with Pt-rich phases.

As the nominal Co content increases, the number of Pt-Co bonds also increases, though Pt-rich phases are maintained. For instance, 2Pt-1Co has 4.5 Pt-Pt bonds at 2.73 Å and 2.2 Pt-Co bonds at 2.56 Å (Table 3.3). The Pt-Co to Pt-Pt coordination number ratio ($CN_{Pt-Co:Pt-Pt}$) is about 0.5, which matches the Pt_3Co phase. In 2Pt-2Co, (Figure 3.5c and Table 3.3), the number of Pt-Pt bonds decreases to 3.0 and the number of Pt-Co bonds increase to 2.9 so that the $CN_{Pt-Co:Pt-Pt}$ was

about 1.0. This means that 2Pt-2Co contains about equal amounts of Pt-Pt and Pt-Co bonds. With increased Co, in 2Pt-4Co the $CN_{Pt-Co:Pt-Pt}$ was approximately doubled to 2.0.
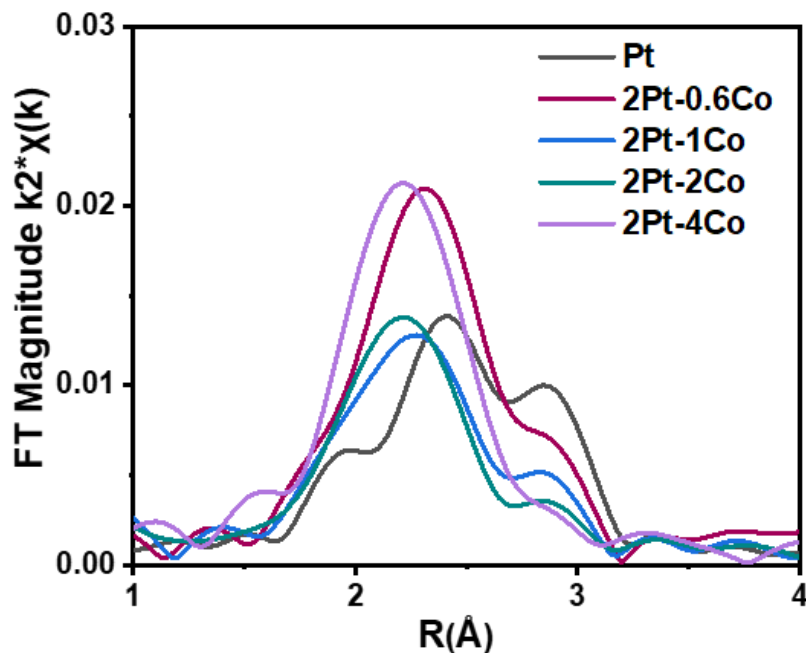
Figure 3.5. Comparison of EXAFS magnitudes of Pt and Pt-Co catalysts

Table 3.3. Summary of EXAFS Analysis for the reduced bimetallic samples and monometallic Pt and Co samples.

Sample	Bond	Bond Length (Å)	CN	$CN_{Pt-Co:Pt-Pt}$	Phase identified by XRD
3Pt	Pt-Pt	2.75	9.3	0	Pt
2Pt0.6Co	Pt-Pt	2.73	7.8	0.32	Pt + Pt_3Co
	Pt-Co	2.56	2.5		
2Pt1Co	Pt-Pt	2.73	4.5	0.49	Pt_3Co
	Pt-Co	2.56	2.2		
2Pt2Co	Pt-Pt	2.73	3.0	0.97	Pt_3Co + PtCo
	Pt-Co	2.56	2.9		
2Pt4Co	Pt-Pt	2.73	2.5	2.08	Pt_3Co + PtCo

The average composition of Pt-Pt and Pt-Co bonds changed with increasing Co content. Because these nanoparticles are small (1-2 nm), there is a sufficiently large fraction of surface atom and difference XAS can be performed to identify the surface composition. Upon oxidation,

there are loss of surface Pt-Pt and Pt-Co metallic bonds. The remaining metallic bonds in the spectra (Pt-Co and Pt-Pt), therefore, are due to metallic atoms from the nanoparticle interior, *i.e.* the nanoparticle core. Through this, it is possible to evaluate whether the composition is homogeneous throughout the particle. In addition, the ratio of Pt-Co to Pt-Pt neighbors can be useful to identify the ordered surface structure.

The reduced, oxidized, and difference spectra of 2Pt-1Co are shown in Figure 3.6. In Figure 3.6a, the large peaks (solid line between about 2 to 3 Å) of the reduced catalysts represent both Pt-Pt and Pt-Co bonds. The dotted spectrum in Figure 3.6a shows the oxidized spectrum with loss of metallic neighbors and addition of a Pt-O peak at about 1.5 Å (phase uncorrected distance). In these bimetallic Pt-Co catalysts, since the fraction of surface atoms is high, there is a significant Pt-O peak, which can be fit. In the difference spectrum, any atoms that are unchanged are not present in the difference spectrum. Thus, the Pt-Pt, Pt-Co and Pt-O are more easily resolved and fit in the difference EXAFS spectra (Figure 3.6b). The fits for the difference EXAFS are shown in Table 3.4.
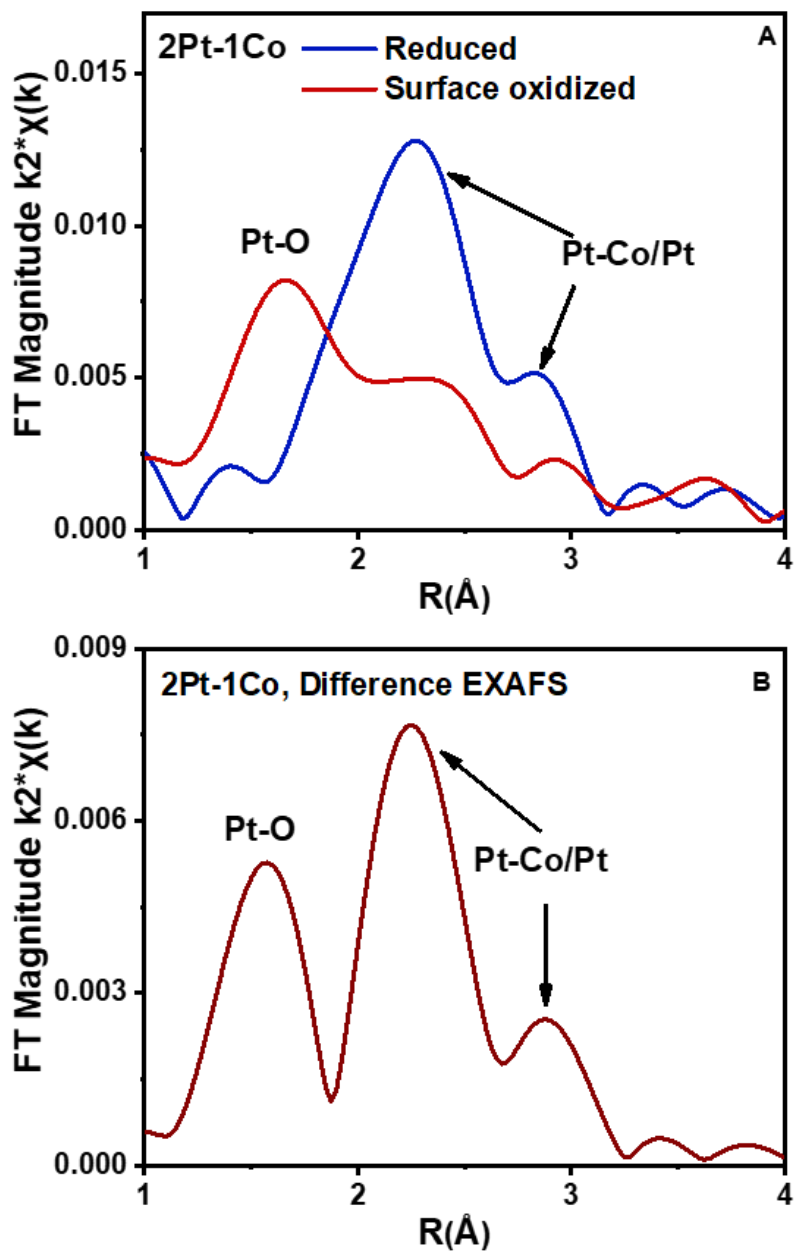
Figure 3.6. FT magnitude of the EXAFS for 2Pt-1Co at the Pt L_3 edge for A) the reduced and oxidized spectra and B) the difference spectra

Table 3.4. Fitting results for the Fourier transform magnitude for the difference Spectra at the Pt L_3 edge

Sample	Scattering Path	Bond Distance (Å)	CN	CN_{Pt-Co}/CN_{Pt-Pt}
3Pt	Pt-O	2.05	0.9	
	Pt-Pt	2.77	2.5	
2Pt0.6Co	Pt-O	2.05	0.2	
	Pt-Pt	2.73	0.6	0.5
	Pt-Co	2.56	0.3	
2Pt1Co	Pt-O	2.05	0.9	
	Pt-Pt	2.73	2.1	0.5
	Pt-Co	2.56	1.0	
2Pt2Co	Pt-O	2.05	0.9	
	Pt-Pt	2.73	2.4	0.5
	Pt-Co	2.56	1.2	
2Pt4Co	Pt-O	2.05	0.7	
	Pt-Pt	2.73	1.9	0.5
	Pt-Co	2.56	0.9	

An unexpected result in Table 3.4 is that the $CN_{Pt-Co:Pt-Pt}$ is near 0.5 for all catalysts, despite the clear difference in their average and core compositions. This suggests that all catalysts likely have the same surface structure, *i.e.*, Pt_3Co (structure type $AuCu_3$) with different core compositions from Pt-rich to Pt_3Co to PtCo.

3.5 Case 3: Identification of Bimetallic Alloy Compositions Suitable for Determination of Electron Changes

The surface EXAFS analysis is generally applicable to many bimetallic catalysts. While the surface alloy composition and structure are important, there are also important electronic changes in the energy of the catalytic valence orbitals, which control the metal-reactant bond energies, surface coverage and performance. For the row 5 catalytic elements, *e.g.*, Pt, the L_2 and L_3 edge XANES measure the energy of the unfilled 5d orbitals, while resonant inelastic X-ray scattering (RIXS), allows for determination of the energy of the filled 5d orbitals, Figure 3.7.[24–28] It is the energy of the filled 5d orbitals, which is responsible for the catalytic performance. As shown in the case studies above, the composition of bimetallic catalysts is often not uniform, and the surface can have a different composition from that of the average nanoparticle. Since hard X-rays sample all atoms in the catalyst, in order to accurately determine the energy shifts due to catalytic surface, one must measure the XANES, or RIXS, on catalysts where the nanoparticle and surface

compositions are identical, *i.e.*, a fully alloyed nanoparticle with the same surface and interior structure. The following example shows two Pt-V bimetallic alkane dehydrogenation catalysts with similar catalytic selectivity and rates but differ in their structure. Determination of the nanoparticle and surface structures allows for identification of the catalyst in which all atoms have identical geometry and electronic properties allowing for accurate determination of the changes in energy of the Pt valence orbitals due to alloy formation with V.[28]
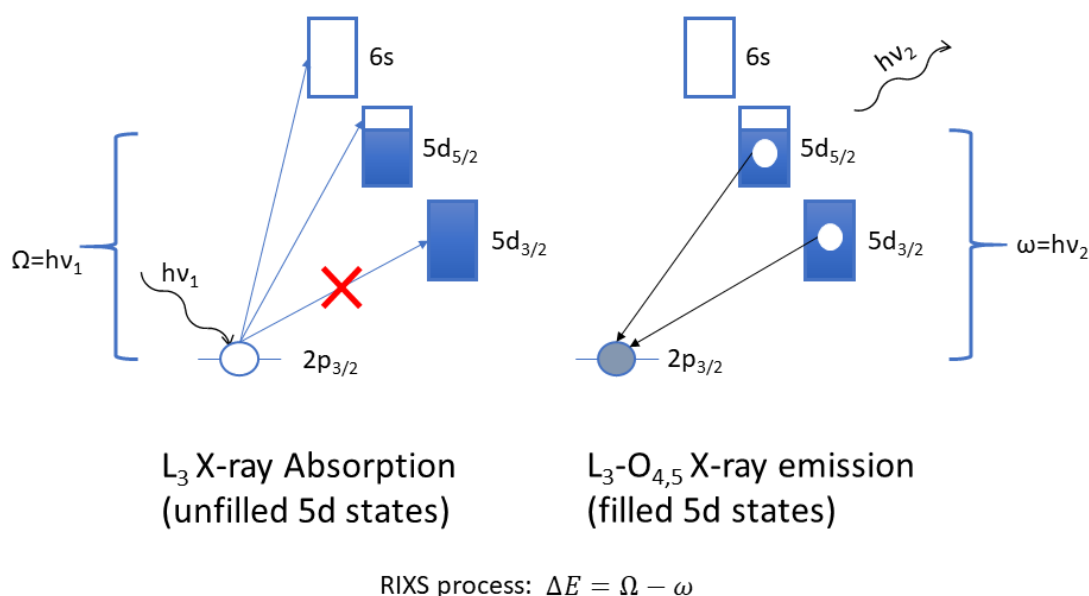
Figure 3.7. RIXS spectroscopy: excitation of the 2p electron to the empty 5d orbitals (XANES absorption spectra) and decay to the core hole from the filled 5d state (emission spectrum). The difference in energy of the absorbed (Ω) and emitted (ω) photon gives the energy difference between filled and unfilled 5d valence orbitals

A 3%Pt/SiO$_2$ catalyst (denoted 3Pt) and two Pt-V/SiO$_2$ catalysts with different Pt loadings, 2%Pt-5%V/SiO$_2$ (2Pt-5V) and 5%Pt-5%V/SiO$_2$ (5Pt-5V), were synthesized and full characterization of the structures and catalytic performance have been recently reported.[28] Thus, a brief summary is given. All three catalysts had metal particle sizes of approximately 2.5 nm. Both Pt-V catalysts had propylene selectivity above 95% at 20% propane conversion, and comparable propylene turnover rates of 0.3±0.1 s^{-1}. The bimetallic structure of the catalyst was verified using *in-situ* EXAS, Figure 3.8. The 3Pt catalyst showed scattering from Pt neighbors, with three characteristic peaks between 2-3 Å. The ratio of the three peaks in the 2Pt-5V catalyst

is modified due to Pt-V scattering. First shell fits of the two spectra are given in Table 3.5. The coordination number ratio of Pt-V to Pt-Pt ($CN_{Pt-V:Pt-Pt}$)for 5Pt-5V was 0.31, while the ratio for 2Pt-5V was 0.47, demonstrating that 5Pt-5V was Pt-rich compared to 2Pt-5V. The coordination number ratio of Pt_3V intermetallic alloy is 0.5, suggesting that 2Pt-5V is a full alloy; while 5Pt-5V is a phase mixture, *i.e.*, Pt + Pt_3V.
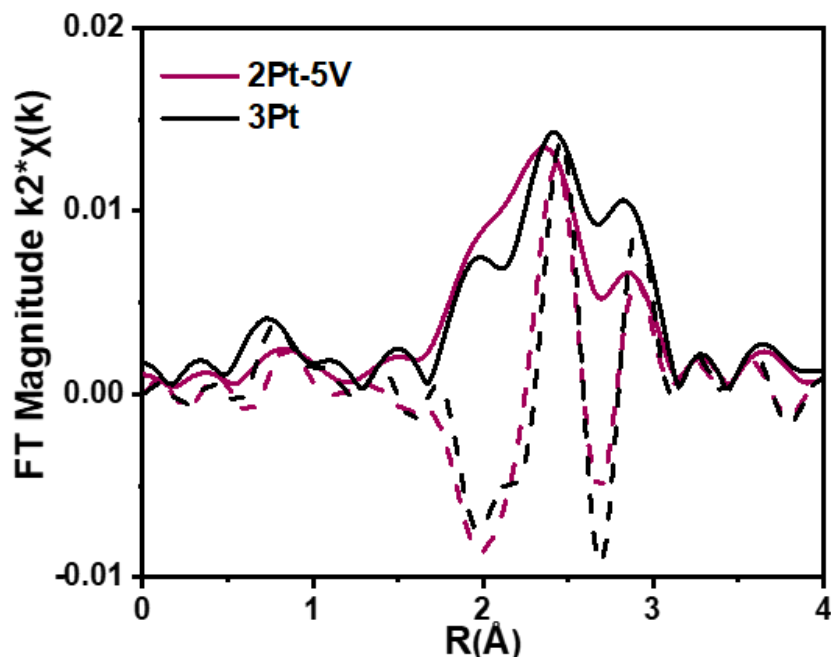
Figure 3.8. R space EXAFS magnitude (solid lines) and imaginary components (dashed lines) for 2Pt-5V/SiO_2 (blue) and 3Pt (black) collected after reduction in hydrogen at 550°C.

Table 3.5. XANES energies and EXAFS first shell fitting results (coordination number and bond distance) for 3Pt and two Pt-V catalysts reduced at 550°C.

Sample	XANES edge energy (keV)	Scattering Pair	CN	R (Å)
3Pt	11.5640	Pt-Pt	8.8	2.74
5Pt-5V	11.5642	Pt-Pt	6.5	2.73
		Pt-V	2.0	2.71
2Pt-5V	11.5644	Pt-Pt	6.2	2.72
		Pt-V	2.9	2.72

The nanoparticle surface compositions of 2Pt-5V and 5Pt-5V were determined using the difference EXAFS spectra (reduced-oxidized) and are shown in Figure 3.9, and fits are given in Table 3.6. Both spectra show Pt-O scattering between 1-2 Å from the surface oxidation process and Pt-Pt and Pt-V scattering between 2-3 Å. Fitting the difference spectra and taking the ratio of CN_{Pt-V} to CN_{Pt-Pt} gave a ratio close to 0.5 for both catalysts, which is consistent with their similar catalytic performance, and suggests a Pt_3V surface structure. While the surface and bulk ratio for 2Pt-5V were similar, suggesting a pure phase Pt_3V nanoparticle, the bulk coordination ratio of 5Pt-5V was lower than that of the surface suggesting a structure with a Pt-rich core and a Pt_3V shell consistent with the XRD.
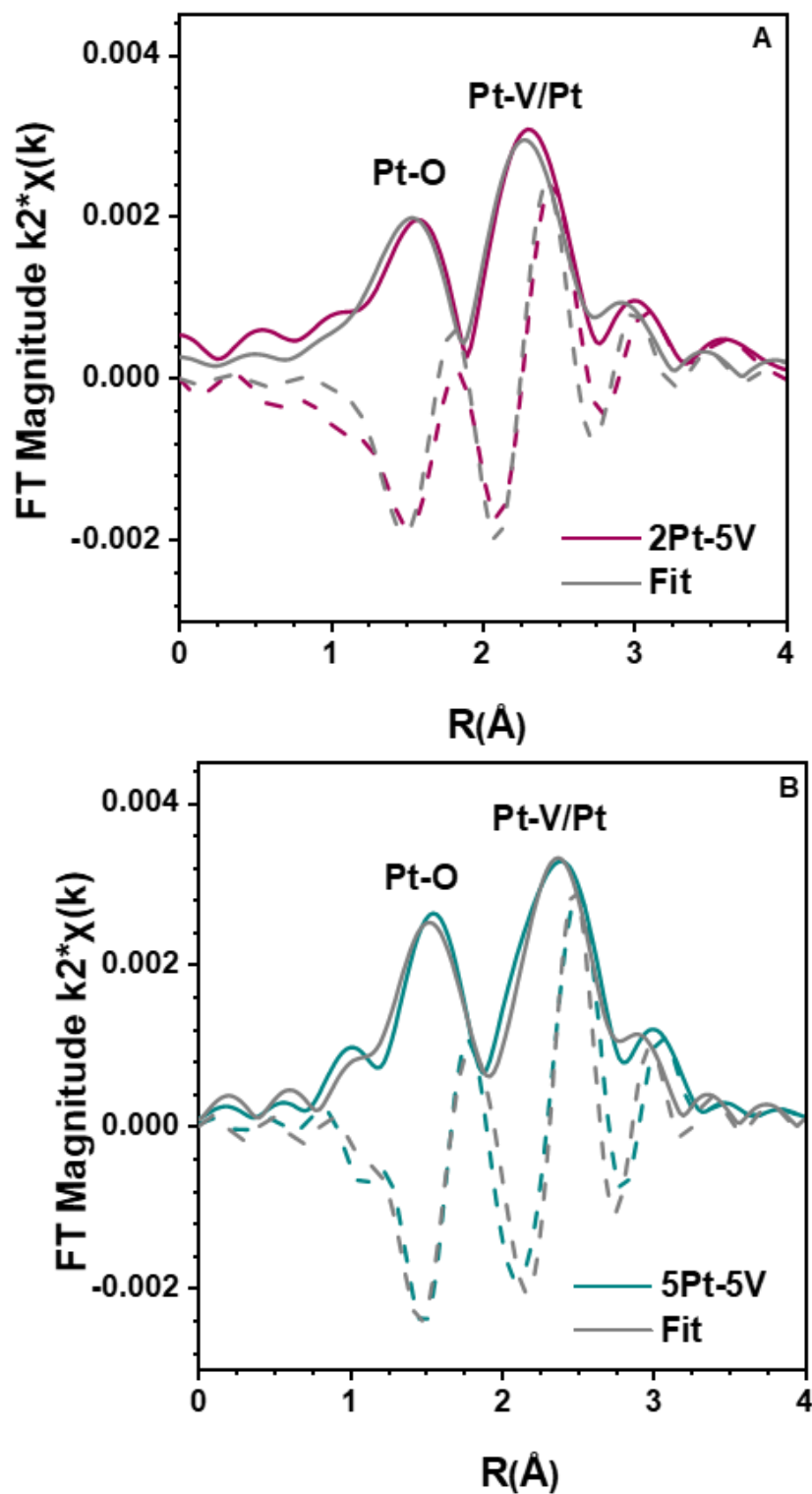
Figure 3.9. Pt EXAFS difference spectra for A) 2Pt-5V B) and 5Pt-5V (magnitude: solid, imaginary part: dashed) and difference spectra fit (magnitude fit: solid, imaginary part fit: dashed)

Table 3.6. EXAFS fit for Pt-V difference spectra

Sample	Path	CN	R (Å)	CN_{Pt-V}/CN_{Pt-Pt}
5Pt-5V	Pt-O	0.6	2.03	0.58
	Pt-Pt	1.2	2.74	
	Pt-V	0.7	2.74	
2Pt-5V	Pt-O	0.5	2.05	0.66
	Pt-Pt	0.9	2.70	
	Pt-V	0.6	2.72	

Consistent with changes in average coordination geometry in the bimetallic Pt-V catalyst, the XANES spectra and edge energies shift slightly to higher energy with increasing V content in the nanoparticles suggesting changes in the energy of the unfilled Pt 5d orbitals, see Figure 3.10 and Table 3.5. For the 5Pt-5V and 2Pt-5V bimetallic catalysts, there is a shift to higher energy, 11.5642 and 11.5644 keV, respectively, compared to Pt (11.5640 keV); however, edge energy 5Pt-5V is the average of atoms in the nanoparticle, Pt_3V + Pt, rather than the catalytic surface, *i.e.*, Pt_3V. Only in the 2Pt-5V is the surface composition and structure the same as the nanoparticle. Thus, the true shift in the energy of the empty Pt 5d orbitals between Pt and Pt_3V phases is an increase of 0.4 eV. Thus, to obtain accurate determination of the electronic properties of the catalytic surface, *i.e.*, the Pt_3V phase, one not only has to determine the nanoparticle composition, but also confirm that the surface and bulk are the same.
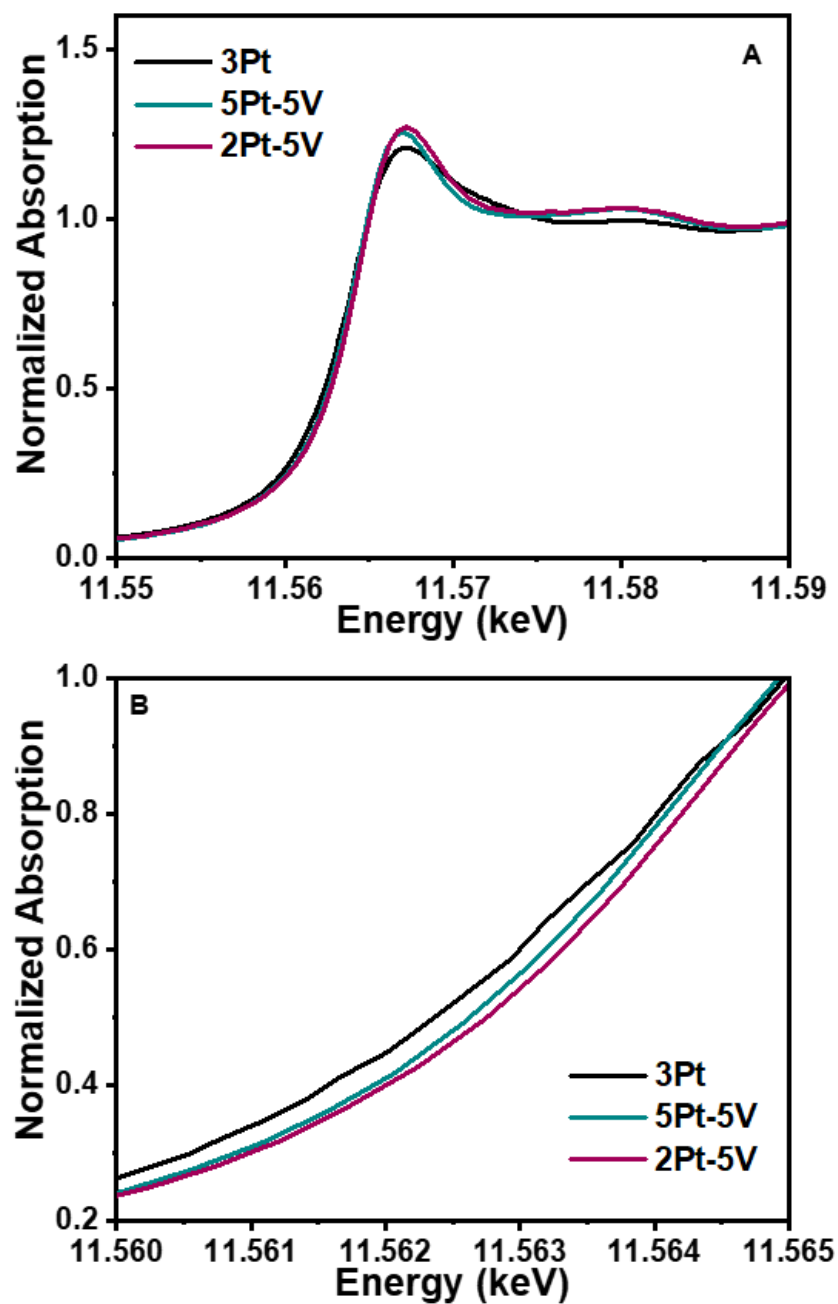
Figure 3.10. A) In-situ Pt L_3 edge XANES from 11.54 to 11.58 keV of 3Pt (Black), 2Pt-5V (red) and 5Pt-5V; spectra were collected at room temperature in He after reduction at 550°C in 3.5% H_2 B) inset showing shorter energy range to illustrate shift in XANES energy with Pt/V ratio

Since the average and surface EXAFS of 2Pt-5V indicate a full Pt_3V intermetallic alloy, the RIXS spectrum was obtained and compared to that of Pt, Figure 3.11. The energy transfer is the difference in energy between the absorbed (XANES) and emitted photon. When the energy transfer is combined with the XANES energy, the energy of the filled 5d orbitals, which are responsible for adsorbate bonding and surface chemistry, can be determined. For Pt, the energy transfer value is 2.7 eV. For Pt_3V, the energy transfer value is larger, 3.5 eV. The energy separation between the filled and unfilled states in Pt_3V is 0.8 eV larger than Pt, which can be separated into a 0.4 eV increase in the energy of the unfilled states and a 0.4 eV decrease in the energy of the filled 5d states relative to Pt. These values in Pt 5d orbital energies reflect the true nature of the electronic changes due to alloy and, thus, are comparable with density functional theory (DFT) calculations and essential for understanding of the catalytic properties.
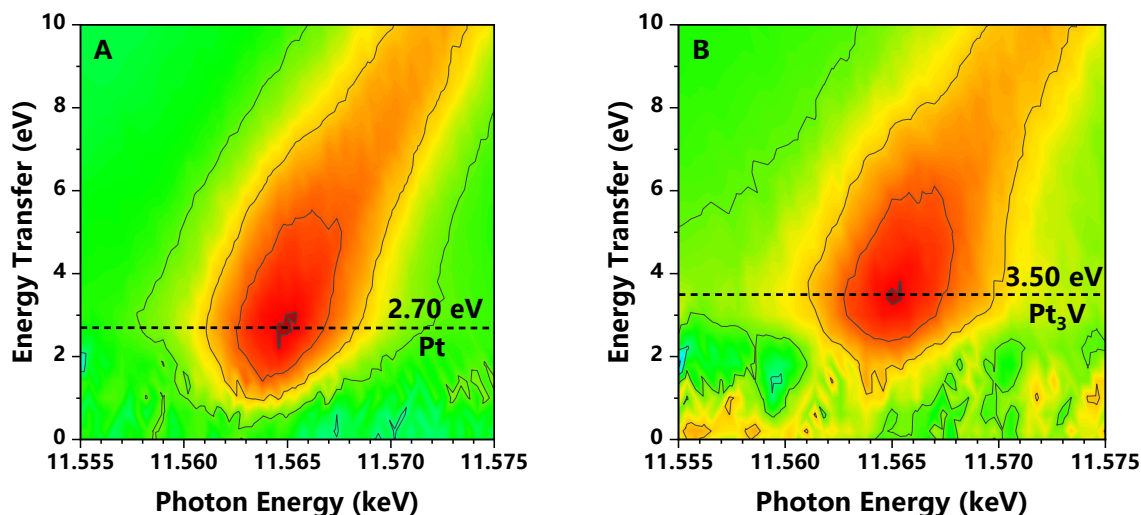
Figure 3.11. A) Pt L_3-$L\beta_5$ RIXS maps of 3Pt and B) 2Pt-5V (Pt_3V). Spectra were collected after a reduction treatment at 550°C in 3.5% H_2. Horizontal dashed lines denote the maximum of energy transfer (difference in the absorbed and emitted photons) for each catalyst.

3.6   Summary

Bimetallic nanoparticles often have complex morphologies where the average and surface structures differ significantly. In the examples highlighted in this paper, a method is presented with allows for determination of the surface even though hard X-rays sample all atoms in the

nanoparticle. The difference XAS approach relies on the selective oxidation of surface atoms. For particle sizes of less than about 5 nm, there is a sufficient fraction of surface atoms to provide accurate surface analysis. As demonstrated for the bimetallic Pt-V catalysts, for example, the small difference in diffraction patterns makes identification of the alloy structure, or solid solutions difficult, especially for small nanoparticles where the peaks are small, broad, and can overlap. The surface EXAFS coordination ratio can be useful for assignment of possible surface structures or, at least, can eliminate some structures, which are not consistent with the fits. While these examples focused on differences in structure resulting from different compositions, this method is equally applicable to the surface composition under reaction conditions including changes due to the reacting gases, deactivation, or poisoning. This method is also useful for determination of surface and interior compositions under synthesis and pre-treatment conditions, which allow for determination of the mechanisms of formation and optimization of better performing catalysts.

3.7   Acknowledgement

This chapter was prepared in collaboration with Dr. Laryssa Cesar, Dr. Stephen Purdy, Dr. Guanghui Zhang, and Dr. Jeff Miller for submission to the of Advanced Catalyst Characterization.

3.8   References

1. Zhang, G.; Yi, H.; Zhang, G.; Deng, Y.; Bai, R.; Zhang, H.; Miller, J.T.; Kropf, A.J.; Benel, E.E.; Lei, A. Direct observation of reduction of Cu(II) to Cu(I) by terminal alkynes. *J. Am. Chem. Soc.* **2014**, 136, 3, 924–926.

2. MacMillan, S.N.; Lancaster, K.M. X-ray Spectroscopic Interrogation of Transition-Metal-Mediated Homogeneous Catalysis: Primer and Case Studies. *ACS Catal.* **2017**, 7, 1776–1791.

3. Paolucci, C.; Khurana, I.; Parekh, A.A.; Li, S.; Shih, A.J.; Li, H.; Di Iorio, J.R.; Albarracin-Caballerro, J.D.; Yezerets, A.; Miller, J.T.; Delgass, W.N.; Ribeiro, F.H.; Schneider, W.F.; Gounder, R. Dynamic multinuclear sites formed by mobilized copper ions in NOx selective catalytic reduction. *Science* **357**, 898–903 (2017).

4. Zhang, G.; Yi, H.; Xin, J.; Deng, Y.; Bai, R.; Huang, Z.; Miller, J.T.; Kropf, A.J.; Benel, E.E.; Qi, X.; Lan, Y.; Lei, A. Aromatic C–H bond cleavage by using a Cu(I) ate-complex. *Org. Chem. Front.* **2016**, 3, 975–978.

5. Wu, Z.; Wegener, E.C.; Tseng, H.; Gallagher, J.R.; Harris, J.W.; Diaz, R.E.; Ren, Y.; Riberiro, F.H.; Miller, J.T. Pd–In intermetallic alloy nanoparticles: highly selective ethane dehydrogenation catalysts. *Catal. Sci. Technol.* **2016**, *6*, 6965–6976.

6. Ye, C.; Wu, Z.; Liu, W.; Ren, Y.; Zhang, G.; Miller, J.T. Structure Determination of a Surface Tetragonal Pt1Sb1 Phase on Pt Nanoparticles. *Chem. Mater.* **2018**, *30*, 4503-4507.

7. Wegener, E. C.; Wu, Z.; Tseng, H.; Gallagher, J.R.; Ren, Y.; Diaz, R.E.; Ribeiro, F.H.; Miller, J.T. Structure and reactivity of Pt–In intermetallic alloy nanoparticles: Highly selective catalysts for ethane dehydrogenation. *Catal. Today*. **2017**, *299*, 146-153.

8. Wu, Z.; Bukowski, B.C.; Li, Z.; Milligan, C.; Zhou, L.; Ma, T.; Wu, Y.; Ren, Y.; Ribeiro, F.H.; Delgass, N.W.; Greeley, J.P.; Zhang, G.; Miller, J.T. Changes in Catalytic and Adsorptive Properties of 2 nm Pt3Mn Nanoparticles by Subsurface Atoms. *J. Am. Chem. Soc.* **2018**, *140*, 14870-14877.

9. Zhang, G.; Ye, C.; Liu, W.; Zhang, X.; Su, D.; Yang, X.; Zhu Chen, J.; Wu, Z.; Miller, J.T. Diffusion-Limited Formation of Nonequilibrium Intermetallic Nanophase for Selective Dehydrogenation. *Nano Lett.* **2019**, 19, 4380–4383.

10. Cesar, L.G.; Yang, C.; Lu, Z.; Ren, Y.; Zhang, G.; Miller, J.T. Identification of a Pt 3 Co Surface Intermetallic Alloy in Pt–Co Propane Dehydrogenation Catalysts. *ACS Catalysis*. **2019**, 9, 6, 5231–5244.

11. Chen, J.Z.; Wu, Z.; Zhang, X.; Choi, S.; Xiao, Y.; Varma, A.; Liu, W.; Zhang, G.; Miller, J.T. Identification of the structure of the Bi promoted Pt non-oxidative coupling of methane catalyst: a nanoscale Pt3Bi intermetallic alloy. *Catal. Sci. Technol.* **2019**, 9, 1349–1356.

12. Shen, X.; Zhang, C.; Zhang, S.; Dai, S.; Zhang, G.; Ge, M.; Pan, Y.; Sharkey, S.M.; Graham, G.W.; Hunt, A.; Waluyo, I.; Miller, J.T.; Pan, X.; Peng, Z. Deconvolution of octahedral Pt 3 Ni nanoparticle growth pathway from in situ characterizations. *Nat. Commun.* **2018**, 9, 1–7 .

13. Rehr, J. J.; Booth, C. H.; Bridges, F; Zabinsky S. I. X-ray-absorption fine structure in embedded atoms. *Phys. Rev. B.* **1994**, *49*, 12347-12350.

14. Frenkel, A.I. Applications of extended X-ray absorption fine-structure spectroscopy to studies of bimetallic nanoparticle catalysts. *Chem. Soc. Rev.* **2012**, 41, 8163–8178.

15. Newville, M. Fundamentals of XAFS. *Rev. Mineral. Geochem.* **2014**, 78, 33–74.

16. Bordiga, S.; Groppo, E.; Agostini, G.; Bokhoven, J.A. van; Lamerti, C. Reactivity of Surface Species in Heterogeneous Catalysts Probed by In Situ X-ray Absorption Techniques. *Chem. Rev.* **2013**, 113, 1736–1850.

17. Koningsberger, D.C.; Prins, R. *X-Ray Absorption: Principles, Applications, Techniques of EXAFS, SEXAFS and XANES.* (Wiley).

18. Bunker, G. *Introduction to XAFS: A Practical Guide to X-ray Absorption Fine Structure Spectroscopy.* (2010).

19. Calvin, S. *XAFS for Everyone.* (CRC Press, 2013).

20. van Bokhoven, J.; Lamberti, C. *X-Ray Absorption and X-Ray Emission Spectroscopy: Theory and Applications.* (Wiley, 2016).

21. Nelson, R.C.; Miller, J.T. An introduction to X-ray absorption spectroscopy and its in situ application to organometallic compounds and homogeneous catalysts. *Catal. Sci. Technol.* **2012**, 2, 461–470.

22. Frenkel, A.I.; Rodriguez, J.A.; Chen, J.G. Synchrotron Techniques for In Situ Catalytic Studies: Capabilities, Challenges, and Opportunities. *ACS Catal.* **2012**, 2, 2269–2280.

23. LiBretto, N.J., Yang, C., Ren, Y., Zhang, G.; Miller, J.T. Identification of Surface Structures in Pt3Cr Intermetallic Nanocatalysts. *Chemistry of Materials.* **2019**, 31, 5, 1597–1609.

24. Ravel, B.; Kropf, A.J.; Yang, D.; Wang, M.; Topsokal, M.; Lu, D.; Stennett, M.C.; Hyatt, N.C. Nonresonant valence-to-core x-ray emission spectroscopy of niobium. *Phys. Rev. B.* **2018**, 97, 125139.

25. Cybulskis, V.J.; Bukowski, B.C.; Tseng, H-T.; Gallagher, J.R.; Wu, Z.; Wegener, E.; Kropf, A.J.; Ravel, B.; Ribeiro, F.H.; Greeley, J.; Miller, J.T. Zinc Promotion of Platinum for Catalytic Light Alkane Dehydrogenation: Insights into Geometric and Electronic Effects. *ACS Catal.* **2017**, 7, 4173–4181.

26. Glatzel, P.; Sikora, M.; Smolentsev, G.; Fernández-García, M. Hard X-ray photon-in photon-out spectroscopy. *Catal. Today.* **2009**, 145, 294–299.

27. Glatzel, P.; Singh, J.; Kvashnina, K.O.; van Bokhoven, J.A. In Situ Characterization of the 5d Density of States of Pt Nanoparticles upon Adsorption of CO. *J. Am. Chem. Soc.* **2010**, 132, 2555–2557.

28. Purdy, S.C.; Ghanekar, P.; Mitchell, G.; Kropf, A.J.; Zemlyanov, D.Y.; Ren, Y.; Ribeiro, F.; Delgas, W.N.; Greeley, J.; Miller, J.T. Origin of Electronic Modification of Platinum in a Pt3V Alloy and Its Consequences for Propane Dehydrogenation Catalysis. *ACS Appl. Energy Mater.* **2020**, 3, 2, 1410-1422.

4. OLIGOMERIZATION ON MAIN GROUP GA^{3+} AND ZN^{2+} SINGLE SITE CATALYSTS

4.1   Introduction

Olefin oligomerization to produce higher molecular weight olefins was commercialized in the 1960's and often utilizes homogeneous, transition metal catalysts containing Cr^{3+} and Ni^{2+}.[1–3] Such homogeneous catalysts require chemical activators, which often inhibit regenerability and lead to thermal instability. Consequently, in order to obtain a high selectivity for linear alpha-olefins (1-butene and 1-hexene), mild reaction temperatures ranging from 30°C-170°C are generally utilized.[4–6] High pressures of at least 27 atm (400 psig) are required to obtain high olefin conversion. Homogenous Ni^{2+} catalysts offer high oligomerization rates, and the selectivity is often tailored to favor low molecular weight products, such as linear alpha olefins, useful for polymer applications.[7–9] Commercial processes utilizing Ni-based homogeneous catalysts include the Shell Higher Olefins and Paraffins (SHOP) and UOP Linear-1 processes.[1,7,10] BASF, Commonweath Scientific, Phillips, and the Tokyo Institute also utilize similar catalysts and reaction conditions.[11]

For homogenous Ni catalysts, the Cossee-Arlman reaction mechanism (Figure 4.1) is generally accepted, which indicates that in the catalytic cycle Ni-alkyl and hydrides are key reaction intermediates, and olefin insertion and β-hydride elimination are the key elementary reaction steps. [12,13]   Activation and initiation of the catalytic cycle often occurs by alkyl transfer from an Al-alkyl co-catalyst to the Ni complex. Molecular weight growth occurs by olefin insertion. β-hydride elimination of the longer metal-alkyl leads to the olefin products plus formation of a metal-hydride intermediate. Ethylene insertion to the metal hydride regenerates the metal alkyl intermediate completing the catalytic cycle.
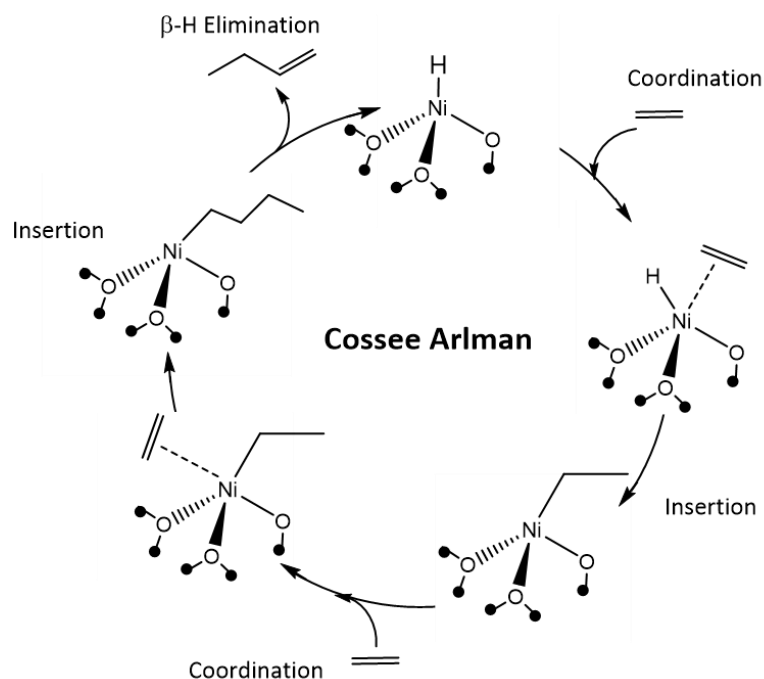
Figure 4.1. Cossee-Arlman homogeneous Ni-based oligomerization mechanism[14]

Separation and regeneration of homogenous catalysts is generally not possible, thus there is interest in development of heterogeneous transition metal catalysts. The latter include Ni^{2+} sites on zeolite (BEA, MFI), or mesoporous (MCM-41) or amorphous silica (SiO_2) and other high surface area oxide supports.[9,15–20] Generally, heterogeneous catalysts suffer from lower rates than homogenous catalysts requiring higher reaction temperatures, which also leads to poor selectivity for alpha-olefins. Like homogenous catalysts, supported Ni oligomerization catalysts have a high selectivity to low molecular weight products. The butene products, however, are often mixture of linear olefins with an equilibrium distribution of 1-butene, cis-2-butene and trans-2-butene. The Cossee-Arlman reaction mechanism is also thought to occur on heterogeneous catalsyts,[15] and while supported by DFT calculations, spectroscopic evidence for the reaction intermediates (metal hydrides and metal alkyls) is limited.[16]

While the linear alpha-olefins, mainly 1-butene and 1-hexane, formed during ethylene oligomerization on Ni-based catalysts are utilized as comonomers in the production of polyethylene, the production of fuel range (C_{10}-C_{16}) hydrocarbons, which have a high cetane index and would be sustainable for blending into distillate fuels, requires higher molecular weight hydrocarbons.[18,21] Conversion of the light alkanes in abundant US shale gas liquids, for example,

to olefins followed by oligomerization (and saturation) to diesel range products could lead to new processes for premium diesel fuels. This, however, requires the development of new oligomerization catalysts capable of higher selectivity towards higher molecular weight products that are atypical of Ni^{2+} catalysts.

While main group elements have not been reported for oligomerization, silica-supported, single site Ga^{3+} and Zn^{2+} were reported for alkane dehydrogenation and olefin hydrogenation.[22–26] For these reactions (dehydrogenation, hydrogenation, and oligomerization), metal hydride and alkyl intermediates, olefin insertion, and β-hydride elimination elementary steps were proposed in these reaction pathways. Here, we report that silica-supported, single site Ga^{3+} and Zn^{2+} catalysts are also active for olefin oligomerization. While low rates are obtained at 250°C and 1 atm, higher rates can be achieved at higher olefin pressures. In addition, for heterogeneous catalysts, initiation of the catalytic cycle also requires heterolytic C-H bond dissociation.

4.2   Materials and Methods

4.2.1   Catalyst Preparation

Single site Ga/SiO_2 and Zn/SiO_2 were prepared following the procedures previously reported in literature, using standard catalyst synthesis techniques, and compared to a Ni/SiO_2 control.[23,24,27]

Ga/SiO_2 was synthesized with a chelating agent to prevent the formation of Ga_2O_3 using pH-controlled incipient wetness impregnation (IWI). 10 g of Davisil silica with grade 636 (pore size = 60 Å, surface area = 480 m^2/g) was impregnated with an aqueous solution containing 1.5 g of gallium nitrate solution ($Ga(NO_3)_3$ xH_2O, Fluka chemical) and 1.5 g of citric acid (Sigma Aldrich) dissolved in Millipore water. The catalyst was dried for 16 hours at 125°C and then calcined at 500°C for 3 hours. Atomic absorption spectroscopy (AAS) was used to determine that the final catalyst contained approximately 2.6 wt% Ga.

Zn/SiO_2 was synthesized using pH-controlled strong electrostatic adsorption (SEA). A solution containing 2.5 g of zinc nitrate hexahydrate ($Zn(NO_3)_2$ $6H_2O$, Sigma Aldrich) was made and the pH was adjusted to 11 using 30% ammonium hydroxide (NH_4OH) solution, until a clear solution was obtained. 10 g of Davisil silica was suspended 100 mL of Millipore water in a separate beaker and the pH was adjusted to 11 using NH_4OH. The Zn solution was added rapidly to the SiO_2 solution and stirred for 20 minutes. After the solid was settled, the solution was decanted,

and the resulting slurry was washed with Millipore water and collected by vacuum filtration. The catalyst was dried for 16 hours at 125°C and then calcined at 300°C for 3 hours. AAS was used to determine that the final catalyst contained approximately 4.0 wt% Zn.

Ni/SiO$_2$ was prepared by pH-controlled SEA. A solution containing 3.0 g of nickel nitrate hexahydrate (Ni(NO$_3$)$_2$ 6H$_2$O) was prepared and the pH was adjusted to 11 using 30% NH$_4$OH solution until a clear blue solution was obtained. 10 g of Davisil silica was added to the solution and the suspension was stirred for 20 minutes. At the end of the reaction, additional NH$_4$OH was added to the solution to maintain a pH of 11. The suspension was stirred for another 10 minutes before being filtered and the catalyst was recovered. The catalyst was dried for 16 hours at 125°C and then calcined at 300°C for 3 hours. AAS was used to determine that the final catalyst contained approximately 3.1 wt% Ni.

4.2.2 *In Situ* X-Ray Absorption Spectroscopy (XAS)

In-situ XAS was performed at the Ga K (10.3670 keV), Zn K (9.659 keV), and Ni K (8.333 keV) edges at the 10-BM sector at the Advanced Photon Source at Argonne National Laboratory using transmission mode with scan ranges from 250 keV below the edge to 800 keV above the edge. At the Ga K edge, the samples were calibrated to Ga$_2$O$_3$ (10.3751 keV). Samples were pressed into a stainless-steel sample holder and placed in a quartz-tube sample cell with gas flow capabilities. The structure of each catalyst was studied after dehydration at 550°C in He. The sample cell was cooled to room temperature and scanned. The resulting structure of each was compared to known references including Ga acetylacetonate (Ga(AcAc)$_3$), Ga oxide (Ga$_2$O$_3$), Zn oxide (ZnO), and Ni oxide (NiO) to confirm the oxidation state and coordination environment (*i.e.* coordination number and bond distance). The data was processed using the WinXAS v.3.1 software[48] to find the coordination number and bond distance using standard procedures. Feff6 calculations were performed using Ga$_2$O$_3$ (50% at CN=4, R=1.83 Å and 50% CN=6 at 2.00 Å), ZnO (CN=4, R=1.98 Å), and NiO (CN=6, R=2.09 Å) respectively for reference. A least squared fit for the first shell of r-space and isolated q-space were performed on the k^2 weighted Fourier transform data over the range of 2.7 to 10 Å^{-1} in each spectrum to fit the magnitude and imaginary components.

An understanding of reactive intermediates was obtained on Ga/SiO$_2$ and Zn/SiO$_2$ using *in situ* XAS. A furnace was placed on the beamline around the sample cell to allow for structural

measurements at high temperature. Data was continuously collected as the temperature ramped in pure H_2 to 550°C. Once the structure was stabilized (*i.e.* the resulting XAS spectra remained unchanged), the cell was cooled to 250°C in pure H_2 while scanning continuously. When the structure was stabilized, the temperature was held constant at 250°C and the gas flow was switched from pure H_2 to pure C_2H_4. Measurements in He were also obtained at 250°C and 550°C. The XANES were used to determine the oxidation state and geometry while select EXAFS spectra were used to determine the coordination number and bond distances of the M-O bonds (M = Ga, Zn).

4.2.3 H_2/D_2 Isotope Exchange

To confirm the formation of the metal hydride intermediates and count the number of active metal hydride sites that form, a H_2/D_2 isotopic exchange experiment was performed using a Micromeritics Autochem II 2920 chemisorption analyzer, equipped with a residual gas analyzer (RGA). Calibrations for the H_2, D_2, and HD signal were performed in a bypass line while the sample was being dehydrated at 500°C in inert gas. For the HD calibration, two separate gas mixtures containing 5% H_2/95% Ar and 5% D_2/95% Ar were combined in different relative amounts in a bypass line to measure initial feed H_2/D_2 in balance Ar compositions. Samples were loaded into a quartz U-tube reactor and treated in flowing air for dehydration at 500°C before being cooled to 250°C. The sample was exposed to 5% H_2/Ar for 1 hour and then switched to 5% D_2/Ar while the signals for H_2, D_2 and HD were recorded on the RGA. During this time, the H_2 signal returned to its baseline, the D_2 signal increased to its feed value, and the HD signal increased immediately and decreased with time as D_2 reacted with H atoms in metal hydrides to form HD and metal deuterides. Once the HD signal reached baseline values, the gas flow was switched from 5% D_2/Ar to 5% H_2/Ar to quantify the HD formed in the reverse isotopic exchange experiment, and this was repeated for a total of four switches and averaged to estimate the number of metal-hydride sites present.

H_2/D_2 isotopic exchange in a temperature programmed surface reaction (TPSR) was performed to identify the number of different metal specific in a catalyst. First, the catalyst was dehydrated at 500°C treated in air for 2 h. Then, the sample was cooled to 450°C in air. The catalyst was treated in 5% H_2/95% Ar at 450°C for 2 h. The temperature was cooled to ambient in 5%

H_2/95% Ar. Then, 5% H_2/95% Ar was switched to 5% D_2/95% Ar and the temperature was increased from 35 to 900°C.

4.2.4 Transmission Infrared Spectroscopy (FTIR)

Infrared (IR) spectra were collected using a Nicolet 4700 spectrometer with a Hg-Cd-Te detector (MCT, maintained at -196 °C by liquid N_2). Each spectrum represents the average of 64 scans at 2 cm^{-1} resolution from 4000 to 400 cm^{-1} and were taken using an empty cell background reference (30 °C) collected under dynamic vacuum (rotary vane rough pump, Alcatel 2008A, <0.01 kPa). In a typical experiment, 0.02-0.04 g cm^{-2} of sample were pressed into self-supporting wafers of Ga/SiO$_2$ and held in a custom-built quartz IR cell with CaF$_2$ windows. IR cells were inserted into a mineral-insulated heating coil (ARi Industries) contained within an alumina silicate ceramic chamber (Purdue Research Machining Services). The quartz IR cell was connected to a glass vacuum manifold that was used for sample pretreatment and exposure to gas-phase, pure ethylene. When the Ga/SiO$_2$ sample was loaded, it was dehydrated in He at 550°C for 2 h and a spectrum of the dehydrated sample was obtained. Then, the catalyst was cooled to ambient temperature and exposed to pure H_2. The temperature was ramped to 550°C in pure H_2 at a rate of 10°C/min while spectra were collected every 5 minutes. The temperature was held at 550°C in pure H_2 for 1 h and then cooled to ambient temperature. The gas was switched to pure C_2H_4 and the temperature was ramped at 10°C/min to 250°C, while collecting spectra every 5 minutes. The temperature was held at 250°C for 2 h. A second Ga/SiO$_2$ wafer was prepared and dehydrated using the same method as detailed above. The catalyst was cooled to ambient temperature and exposed directly to pure C_2H_4. The temperature was ramped at 10°C/min to 250°C while collecting spectra every 5 minutes, and the C_2H_4 treated sample spectra were compared the sample with and without H_2 pretreatment. IR spectra reported here were baseline corrected, and the spectra shown are difference spectra with that of the dehydrated catalyst subtracted from those of the treated catalysts.

4.2.5 Density Functional Theory (DFT)

Ga/SiO$_2$ systems are based on a recently developed amorphous silica model using molecular dynamics and continuous dehydration processes.[49] A periodic amorphous silica model (21.6 Å ×

21.6 Å × 34.5 Å; 372 atoms) was used to analyze the energetics of ethylene oligomerization. Ga sites were generated by substituting -Si atoms with a consideration of charge balance. All DFT calculations are performed with self-consistent and periodic density function theory using Vienna Ab-initio Simulation Package (VASP). The BEEF-vdw exchange-correlation function using projector augmented wave (PAW) pseudopotentials was used. A dipole correction was applied parallel to the plane of the slab to reduce image–image interaction errors. A cutoff energy of 400 eV was considered with a force-convergence criterion of 20 meV Å^{-1}. The activation barriers were calculated using nudged elastic band method, and the transition states are located using dimer method.

4.2.6   Catalyst Evaluation: Propane Dehydrogenation and Propylene Hydrogenation

Catalyst performance tests for hydrogenation and dehydrogenation were performed in a fixed bed reactor with a quartz reactor tube of 3/8-inch outer diameter. Dehydrogenation was performed in 3% C_3H_8 and 2% H_2 balanced in N_2 at 550°C on 1 g of catalyst using varying total flow rates of the same gas composition ranging from 41 ccm to 165 ccm to vary conversion (GHSV = 0.32 s^{-1} – 1.28 s^{-1}). Before each dehydrogenation test, the catalyst was pretreated in flowing N_2 while the temperature ramped to 550°C. The temperature was stabilized for 1 hour prior to starting the reaction.

Hydrogenation was performed in 1% C_3H_6, 3% H_2, balanced with N_2 at 200°C on 250 mg of catalyst diluted to 1 g with silica using a total flow rate of 104 ccm (GHSV = 0.81 s^{-1}). Before each hydrogenation test, the catalysts were pretreated using one of the following pretreatments: 1) ramped to 200°C in flowing N_2, 2) ramped to 200°C in flowing H_2, or 3) ramped to 550°C in flowing H_2 and then cooled to 200°C for the reaction. In each case, the temperature was stabilized for 1 hour prior to starting the reaction.

Dehydrogenation and hydrogenation products were analyzed with a Hewlett Packard (HP) 6890 Series gas chromatograph (GC) using a flame ionization detector (FID) with a Restek Rt-Alumina Bond/Na$_2$SO$_4$ GC column (30 m in length, 0.32 mm inner diameter, and 0.5 µm film thickness).

4.2.7   Catalyst Evaluation: Olefin Oligomerization

Oligomerization tests were performed at atmospheric pressure in pure ethylene or pure propylene using a fixed bed reactor of 3/8-inch outer diameter. The weight of catalyst loaded into the reactor ranged from 0.5 g to 1 g and was diluted with silica to reach a total of 1 g. The catalyst was treated in 50 ccm of N_2 while it ramped to 250°C for the reaction. The reaction was performed in 100% C_2H_4 using GHSVs ranging from 0.08 s^{-1} to 0.38 s^{-1}. Products from the atmospheric pressure reactor were analyzed with a Hewlett Packard (HP) 6890 Series gas chromatograph (GC) using a flame ionization detector (FID) with an Agilent HP-Al/S column (25 m in length, 0.32 mm inner diameter, and 8 µm film thickness).

To increase the conversion, oligomerization was performed in a high-pressure-capable, fixed bed reactor of 1/2-inch outer diameter. 2 g of catalyst was loading into the reactor. The reactor was pressurized to 450 psig (30.6 atm) and the catalyst was treated in 50 ccm of N_2 while it ramped to 250°C for the reaction. The reaction was performed in a mixture of 10 ccm 5% CH_4/N_2 for an internal standard and 50 ccm 100% C_2H_4 at a total pressure of 450 psig. Products were analyzed with a Hewlett Packard (HP) 7890 Series gas chromatograph (GC) using a flame ionization detector (FID) with an Agilent HP-1 column (60 m in length, 0.32 mm inner diameter, and 25 µm film thickness).

4.3   Results

4.3.1   Catalyst Preparation

Silica supported Ga and Zn single site catalysts were prepared using previously published synthesis methods.[23,24] Ga/SiO$_2$ was prepared by impregnation using a citric acid chelating agent. Zn/SiO$_2$ was prepared using strong electrostatic absorption (SEA). All solutions were pH adjusted to 11. Due to the slightly acidic nature hydroxyl groups on groups on SiO$_2$, at high pH deprotonation of the SiOH groups leads to a negative surface charge. This allows a strong interaction between the cationic ligands and the negative surface, resulting in homogeneously dispersed metal ions on the SiO$_2$ surface. Ni/SiO$_2$ was prepared using a similar procedure to that of Zn/SiO$_2$. Atomic absorption spectroscopy revealed that the metal content was 2.6 wt%, 4.1 wt%, and 3.1 wt% metal for Ga/SiO$_2$, Zn/SiO$_2$, and Ni/SiO$_2$ respectively.

To confirm that the catalysts were consistent with those previously reported, their initial structures were determined by XAS, and the turnover rates (TOR) for olefin hydrogenation and alkane dehydrogenation were determined.

4.3.2 Catalytic Structure Characterization

The pre-reaction catalyst structure was determined by *in situ* x-ray absorption spectroscopy (XAS), including both XANES and EXAFS on Ga/SiO_2 and Zn/SiO_2 and compared to that of Ni/SiO_2. The catalysts were dehydrated at $550°C$ in He and compared to known reference compounds at each metal edge (Figure 4.2). The EXAFS fits of each catalyst are given in Table 4.1.
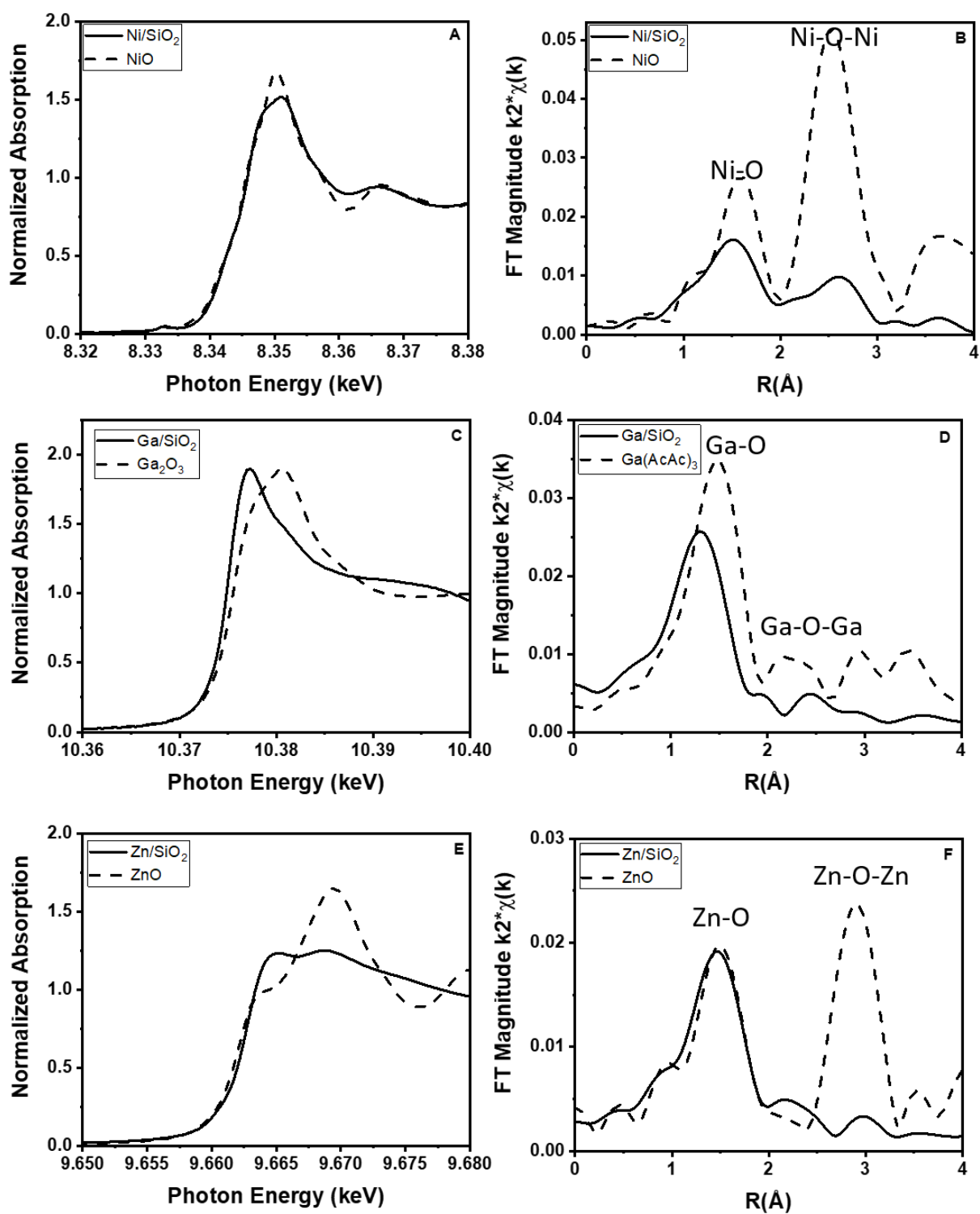
Figure 4.2. XAS of dehydrated catalyst structures for Ni/SiO₂ (A-B), Ga/SiO₂ (C-D), and Zn/SiO₂ (E-F)

Table 4.1. EXAFS fits of the as-prepared structures of Ni/SiO_2, Ga/SiO_2, and Zn/SiO_2 after dehydration at 550°C in He compared to bulk references at each edge

Sample	Pre-edge Energy (keV)	XANES Energy (keV)	Scattering Path	CN	R (Å)	$\Delta\sigma^2$ (Å^2)	ΔE_o (eV)	
NiO	8.3335	8.3410	Ni-O	6.0	2.09	-	-	Ni^{2+} (Oh)
Ni/SiO_2	8.3331	8.3421	Ni-O	4.0	2.03	0.006	-1.3	Ni^{2+} (Td)
Ga_2O_3	-	10.3751	Ga-O	3.0	2.00	-	-	Ga^{3+}
				2.0	1.83	-	-	(Td+Oh)
$Ga(AcAc)_3$	-	10.3793	Ga-O	6.0	1.93	-	-	Ga^{3+} (Oh)
Ga/SiO_2	-	10.3751	Ga-O	4.0	1.81	0.006	-2.2	Ga^{3+} (Td)
ZnO	-	9.6625	Zn-O	4.0	1.98	-	-	Zn^{2+} (Td)
Zn/SiO_2	-	9.6628	Zn-O	4.0	1.95	0.006	-0.6	Zn^{2+} (Td)

[*] NiO, Ga_2O_3, $Ga(AcAc)_3$, and ZnO are references of known structures

The XANES was used to determine the oxidation state of each catalyst, while the EXAFS was used to identify the coordination environments prior to any catalytic treatment. On Ni/SiO_2, the Ni K-edge XANES pre-edge energy (8.3331 keV) is slightly lower than that of NiO (8.3335 keV) (Figure 4.2a). The NiO XANES is consistent with Ni^{2+} in an octahedral coordination, while the pre-edge energy of the former is consistent with Ni^{2+} in s tetrahedral geometry.[27] The first shell EXAFS fit of Ni/SiO_2 has 4 Ni-O bonds at 2.03 Å, while NiO has Ni-O bonds at 2.09 Å (Figure 4.2b). The EXAFS Ni/SiO_2 and is consistent with the single site Ni^{2+} catalyst previously reported.[15,16,27]

Since Ga/SiO_2 and Zn/SiO_2 have d^{10}-electron configuration, there is no pre-edge feature in the XANES region. The XANES energy relative to known references was used to identify the oxidation state of each catalyst. The XANES energy of Ga^{3+} is also dependent on the coordination geometry[22,29]. Tetrahedral (Td) Ga^{3+} (10.3745 keV) has a XANES energy, lower than that in octahedral (Oh) coordination (10.3793 keV). Ga_2O_3 has 50% Td and 50% Oh Ga^{3+}.[30] Since the edge energy of Td is lower than Oh Ga^{3+}, the XANES of Ga_2O_3 is 10.3751 keV, (Figure 4.2c). The XANES energy of $Ga(AcAc)_3$, Oh Ga^{3+} is 10.3765 keV. The XANES energy (10.3751 keV) of Ga/SiO_2 is consistent with Td Ga^{3+}.

The Ga coordination geometry also affects the Ga-O bond distance. The bond distance of Ga-O in a Td Ga compound is about 1.83 Å; while in Oh compounds Ga-O bonds are longer, about 1.90-2.00 Å.[30] The k^2-weighted magnitude of the EXAFS of Ga/SiO$_2$ is lower than that of Ga(AcAc)$_3$ (6 Ga-O at 1.93 Å) (Figure 4.2d). The fit of Ga/SiO$_2$ EXAFS, Table 4.1, indicates about 4 Ga-O bonds at 1.81 Å, both consistent with Td Ga^{3+}. The absence of Ga-O-Ga bonds also suggests isolated Ga^{3+} bound to the support.

Similarly, the XANES energy for Zn/SiO$_2$ (9.6628 keV) is similar to that of ZnO (9.6625 keV) (Figure 4.2e) consistent with Zn^{2+} oxidation state. The magnitude of the k^2-weighted EXAFS of Zn/SiO$_2$ has 4 Zn-O bonds at 1.96 Å and is also similar to ZnO (4 Zn-O at 1.98 Å). The absence of Zn-O-Zn higher shell coordination in the catalyst, however, suggests a single site Zn^{2+} structure.

In summary, Ga/SiO$_2$ and Zn/SiO$_2$ have a similar structure to Ni/SiO$_2$, *i.e.*, each has 4 M-O bonds with no evidence of M-O-M higher shell bonds (M = Ni, Ga, Zn). These results are consistent with previous single site structures reported for Ga^{3+}, Zn^{2+} and Ni^{2+} hydrogenation and dehydrogenation catalysts.[23,24,31,32]

4.3.3   Propane Dehydrogenation and Propylene Hydrogenation

Catalytic performance for dehydrogenation and hydrogenation on single site Ga/SiO$_2$ and Zn/SiO$_2$ have been previously reported.[24,29] Since the proposed elementary steps and reaction intermediates for these reactions are similar to those required for oligomerization, catalytic performance of these catalysts and reactions was determined and compared to previous literature.[24,29] The turnover rate and selectivity for C$_3$H$_8$ dehydrogenation was determined with and without H$_2$ cofeed. Dehydrogenation in the presence of H$_2$ is a more rigorous way to test for selective performance towards the production of C$_3$H$_6$. Both Ga/SiO$_2$ and Zn/SiO$_2$ were highly selective towards olefins (> 95%) up to 20% conversion, even in the presence of H$_2$. High C$_3$H$_6$ selectivity was maintained as a function of conversion. In addition, the catalysts were stable under reaction conditions at 550°C for over 6 hours. The turnover rates (TOR) for each catalyst were calculated by normalizing the amount of C$_3$H$_6$ production by the moles of metal on the surface of the catalyst (2.6% for Ga/SiO$_2$ and 4.0% for Zn/SiO$_2$). The TOR is shown for 10% conversion (Table 4.2).

Table 4.2. Initial selectivity and TOR for Ga/SiO$_2$ and Zn/SiO$_2$ at 10% conversion during propane dehydrogenation performed at 550°C in 3% C$_3$H$_8$ and 2% H$_2$

	Without H$_2$		*With H$_2$*	
	Initial Selectivity (%)	**TOR (1/s)**	**Initial Selectivity (%)**	**TOR (1/h)**
Ga/SiO$_2$	97	2.1	98	1.6
Zn/SiO$_2$	99	1.9	99	2.1

The TOR on Ga/SiO$_2$ and Zn/SiO$_2$ are of the same order of magnitude, and co-feeding H$_2$ does not significantly change the TOR during dehydrogenation. These results are consistent with what has previously been reported.[24,29]

Both catalysts also perform the microscopic reverse reaction of propane dehydrogenation (propylene hydrogenation) at lower reaction temperatures. Propane was the only product indicating few side reactions occurred at 200°C. The influence of H$_2$ pretreatment on C$_3$H$_6$ hydrogenation activity at 200°C was explored to demonstrate how the catalysts behave in the presence of H$_2$ (Table 4.3).

Table 4.3. Initial TORs for Ga/SiO$_2$ and Zn/SiO$_2$ at 15% conversion during propylene hydrogenation performed at 200°C in 1% C$_3$H$_6$ and 3% H$_2$ after treatment various pretreatments

Pretreatment	Ga/SiO$_2$: Initial TOR (1/s)	Zn/SiO$_2$: Initial TOR (1/h)
200°C N$_2$	0.3	0.8
200°C H$_2$	2.5	1.7
550°C H$_2$	2.1	2.4

The initial TOR of the catalysts treated in H$_2$ at 200°C and 550°C was compared to that of the dehydrated catalyst (200°C N$_2$). Pretreatment in H$_2$ leads to higher initial TOR than what was achieved on the dehydrated catalyst. However, after approximately 30 minutes, the TOR for all pretreatment conditions stabilized to approximately the same value.

4.3.4   Olefin Oligomerization

Like the structural characterizations, the catalytic rates and selectivities for propane dehydrogenation and propylene hydrogenation of these Ga/SiO$_2$ and Zn/SiO$_2$ catalysts are very similar to reported performance, reaction intermediates and elementary reaction steps suggesting that these may also be catalytic for olefin oligomerization.

At 1 atm and varying space velocities of C_2H_4, up to 5% conversion to oligomerization products were obtained at 250°C with stable performance for at least 40 hours for both Ga/SiO$_2$ and Zn/SiO$_2$. From the conversion and catalyst compositions, the relative oligomerization TOR, given in Table 4, indicate $Ni^{2+} > Ga^{3+} > Zn^{2+}$.

Table 4.4. Product selectivity at varying conversions for each catalyst during ethylene oligomerization at 250°C and 1 atm

Catalyst	Conversion (%)*	Selectivity (%)				
		Ethane (C_2H_6)	Butenes ($C_4^=$)	Hexenes ($C_6^=$)	Octenes ($C_8^=$)	TOR s^{-1} (x 10^{-4})
Ni/SiO$_2$	1	1.0	89.2	9.7	0.5	8
	2	2.6	86.5	9.6	1.0	13
	5	1.4	86.1	11.8	0.4	15
	10	1.1	85.1	13.5	0.5	10
Ga/SiO$_2$	1	4.5	87.0	2.6	5.8	2
	2	3.3	85.2	3.6	7.9	2
	5	1.8	75.9	16.8	16.4	7
Zn/SiO$_2$	1	5.7	91.5	2.8	0.0	1
	2	11.6	87.3	1.1	0.0	1
	5	12.5	85.5	2.0	0.0	1

* Conversion was varied using different space velocities over 1g of catalyst in a 3/8 in diameter quartz reactor tube

The product selectivity as a function of conversion by varying the space velocity is shown for Ga/SiO$_2$ and Zn/SiO$_2$ relative to Ni/SiO$_2$ in Table 4.4. Ni/SiO$_2$ is a known for high selectivity to dimers, *i.e.*, butenes. On Ni/SiO$_2$, there is a high selectivity towards butenes ($C_4^=$) (85-90%) and moderate selectivity towards hexenes ($C_6^=$) (10-15%). Little to no octenes ($C_8^=$) and higher molecular weight products are formed. Interestingly, a small amount of ethane (C_2H_6) (< 1%) is observed in the product stream.

For Ga/SiO$_2$ at the same conversion, for example 5%, the $C_4^=$ selectivity is lower and the $C_8^=$ selectivity is higher than that observed for Ni/SiO$_2$. Ga/SiO$_2$ also has a comparable TOR to Ni/SiO$_2$. Alternatively, Zn/SiO$_2$ almost exclusively makes $C_4^=$. For example, at 5% ethylene conversion, the butene selectivity of Zn/SiO$_2$ is slightly higher than Ni/SiO$_2$, which is a well-known

dimerization catalyst. The TOR of the former, however, is three times lower than that of Ni/SiO$_2$ and Ga/SiO$_2$. The C$_2$H$_6$ selectivity of Zn/SiO$_2$ is also higher than the latter catalysts.

At low conversion oligomerization leads to formation of C$_4^=$ with an equilibrium distribution of 1-butene, cis-2-butene, and trans-2-butene. No isobutene (iC$_4^=$) was observed on any of these SiO$_2$-supported catalysts, indicating that there is no skeletal isomerization and only olefin isomerization occurs. Further interaction of C$_2$H$_4$ with produced olefins forms C$_6^=$ or C$_8^=$ and so on. Five C$_6^=$ isomers were observed in the GC chromatogram, consistent with the formation of only linear olefins.

The product distributions on each catalyst can be predicted by determining a Schulz Flory coefficient, which inherently compares the rate of olefin insertion, or propagation (α), and β-hydride elimination, or termination (1-α), can be calculated using equations 4.1-4.5. R is the rate that the olefin insertion and T$_n$ is the rate β-hydride elimination, and C is a constant coefficient.[33] If the β-H elimination elementary step is fast relative to olefin insertion, the selectivity favors lower molecular weight products, *e.g.* C$_4^=$. The chain growth selectivity for these catalysts with an ethylene reactant is shown in Figure 4.3.

$$T_{n+1} = \alpha T_n \qquad\qquad 4.1$$

$$T_n = Cr^n \qquad\qquad 4.2$$

$$r = \frac{(1-\alpha)R}{\alpha} \qquad\qquad 4.3$$

$$mol(n) = (1-\alpha)\alpha^{n-1}R \qquad\qquad 4.4$$

$$mol\%(n) = \frac{Cr^n}{R} = (1-\alpha)\alpha^{n-1} \qquad\qquad 4.5$$
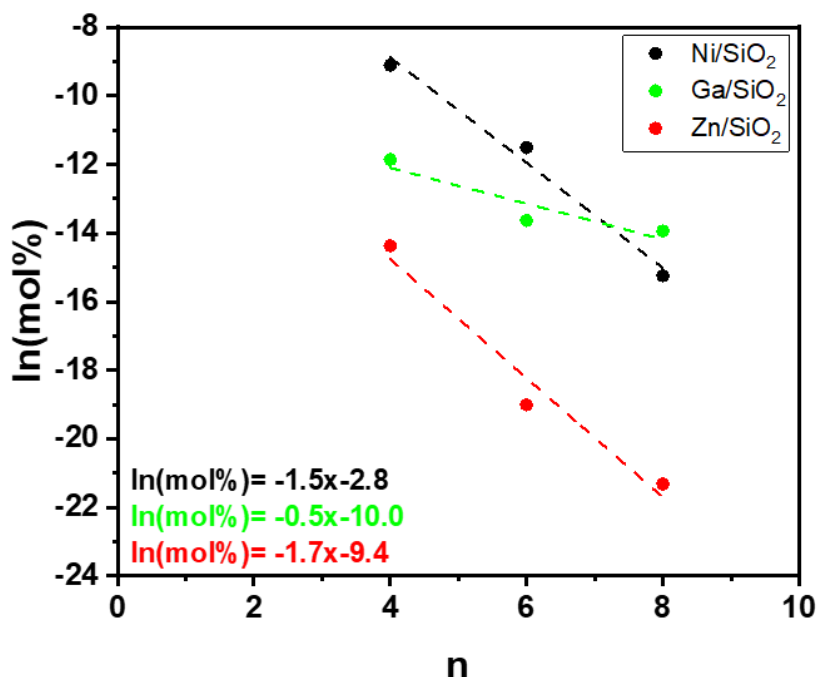
Figure 4.3. Schultz Flory distribution of linear hydrocarbons produced during ethylene oligomerization on Ni/SiO$_2$ (black), Ga/SiO$_2$ (green), and Zn/SiO$_2$ (red)

For ethylene oligomerization, the coefficient of propagation for Ga/SiO$_2$ (α_{Ga}) is 0.59; while that of Zn/SiO$_2$ (α_{Zn}) is 0.18, and Ni/SiO$_2$ (α_{Ni}) is 0.22. Ni^{2+} is known to selectively perform olefin dimerization and has shown α values between 0.2-0.3. Zn^{2+}, like Ni^{2+}, favors low molecular weight products like butenes, while Ga^{3+} produces some higher molecular weight oligomers. This suggests that the rate β-H elimination is lower on Ga/SiO$_2$ than on Ni/SiO$_2$ and Zn/SiO$_2$, which are similar.[8]

At atmospheric pressure, olefin conversion was generally low ($< 10\%$). Higher conversion is achieved at higher pressures. For example, at 250°C and 30.6 atm C$_2$H$_4$, conversions up to 20%, and rates two orders of magnitude higher than at atmospheric pressures were obtained (Table 4.5). These results include only the quantification of gas-phase products using online GC sampling. Liquid products were collected continuously during the reaction and were used for a qualitative analysis of the higher molecular weight products.

Table 4.5. Product selectivity and conversion for ethylene oligomerization at 250°C and 30.6 atm

Catalyst	Conversion (%)	Selectivity (%)					TOR s^{-1}
		Ethane (C$_2$H$_6$)	Butenes (C$_4^=$)	Hexenes (C$_6^=$)	Octenes (C$_8^=$)	C$_{10}$+	
Ni/SiO$_2$	20.7	0.6	86.2	11.1	2.9	0.0	7 x 10^{-2}
Ga/SiO$_2$	20.6	0.6	74.2	16.1	4.9	4.2	8 x 10^{-2}
Zn/SiO$_2$	15.2	0.5	96.0	0.8	0.0	0.0	5 x 10^{-2}

Higher conversion resulted in higher selectivity to higher molecular weight products. On Ga/SiO$_2$, liquid products were condensed and analyzed offline at the end of reaction using mass spectrometry (GC-MS). GC-MS was used to identify the composition of the liquid phase products, which showed signs of products up to C18 hydrocarbons (higher molecular weight products likely did not elude from the GC column), including paraffins, olefins, and saturated rings, however, there was little evidence of branched hydrocarbons. This is consistent with the nonacidic nature of the SiO$_2$ support.

Likewise, propylene oligomerization was performed at 250°C and atmospheric pressure with product selectivities listed in Table 4.6.

Table 4.6. Product selectivity at varying conversions for each catalyst during propylene oligomerization at 250°C and 1 atm

Catalyst	Conversion (%)*	Selectivity (%)				
		Propane (C$_3$H$_8$)	Hexenes (C$_6^=$)	Nonenes (C$_9^=$)	Dodecenes (C$_{12}^=$)	TOR s^{-1}
Ga/SiO$_2$	2	1.4	88.5	6.6	0.3	9 x 10^{-4}
	3	1.9	84.3	4.4	5.0	12 x 10^{-4}
	5	1.9	77.5	10.9	4.5	9 x 10^{-4}
	8	3.8	64.5	15.3	7.0	14 x 10^{-4}
	15	3.4	56.6	20.4	8.6	16 x 10^{-4}
Zn/SiO$_2$	2	0.8	83.8	14.4	0.0	8 x 10^{-4}
	3	0.3	83.8	21.1	0.0	7 x 10^{-4}
	5	4.9	65.4	24.8	0.0	4 x 10^{-4}
	8	3.9	66.8	24.1	0.0	4 x 10^{-4}
	15	1.5	66.5	34.9	0.0	3 x 10^{-4}

* Conversion was varied using different space velocities over 1g of catalyst in a 3/8 in diameter quartz reactor tube

Higher conversion of propylene was observed than ethylene on both Ga/SiO_2 and Zn/SiO_2. In addition, small amounts of products from side reactions were also observed. On Ga/SiO_2, there is a high selectivity towards $C_6^=$ (60-80%) and moderate selectivity towards $C_9^=$ (5-15%) and higher carbon numbers (1-5%). Zn/SiO_2 had a rate approximately 3 times lower than Ga/SiO_2, but maintained a similar product distribution, however, no products with carbon numbers greater than 9 were observed. From this, a Schultz Flory distribution was obtained (Figure 4.4).
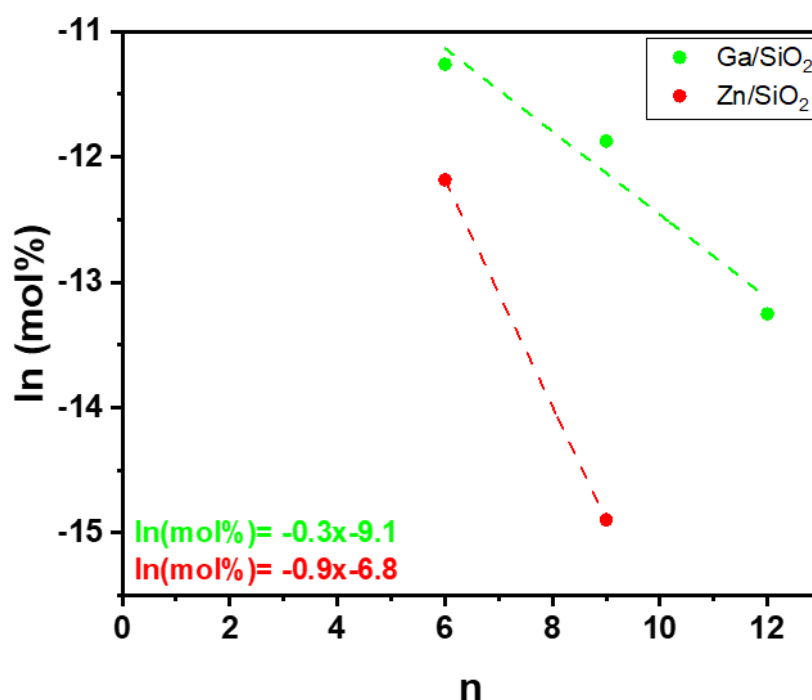
Figure 4.4. Schultz Flory distribution of linear hydrocarbons produced during propylene oligomerization on Ga/SiO_2 (green) and Zn/SiO_2 (red)

Here, the coefficient of propagation on Ga/SiO_2 ($\alpha_{Ga} = 0.70$) and Zn/SiO_2 ($\alpha_{Zn} = 0.40$) were both higher in a propylene feed than in ethylene, which is consistent to the Schultz Flory trends observed on Mo oligomerization catalysts.[34] This implies that there is a greater likelihood of making higher molecular weight products with propylene than ethylene and could be due to the

lower C-H bond activation energy.[35] This would increase the rate of initiation, while either decreasing or holding constant the rate of termination.

4.3.5   Evidence for Oligomerization Intermediates on Ga/SiO$_2$ and Zn/SiO$_2$

Ga^{3+} and Zn^{2+} catalysts heterolytically dissociate H$_2$ and C-H bonds, for example, during olefin hydrogenation and alkane dehydrogenation, respectively. When H$_2$ dissociates on Ga^{3+} and Zn^{2+} or other single site catalysts, it forms a M-H bond and a proton that coordinates to the M-O-Si bond in the support. Protonation of the latter leads to breaking of the M-O bond and formation of a new Si-OH group. This has been observed through *in situ* spectroscopic studies to identify the reaction intermediates. While Ga/SiO$_2$ and Zn/SiO$_2$ activate H$_2$ and ethylene, the former forms a higher concentration of reaction intermediates.

XAS and IR spectroscopies demonstrate that Ga^{3+} and Zn^{2+} activate H$_2$ bonds. In H$_2$ with increasing temperatures from room temperature to 550°C, there are continual changes in the shape of the Ga and Zn K-edge XANES. For Ga/SiO$_2$ (Figure 4.5a), the white line intensity decreases and there is a formation of a feature before the edge. Similar, though less obvious, changes were observed on Zn/SiO$_2$ (Figure 4.5c). Here, the while line intensity decreases and the ratio of the two XANES peaks change subtly. These changes were isolated by subtraction of the dehydrated sample from the sample treated in H$_2$ (Figure 4.5b, 4.5d) and are due to changes in electron on the active metal center.[26] This has also previously been assigned to formation of Ga^{3+} hydride intermediates and the hydride was confirmed by x-ray photoelectron spectroscopy (XPS).[23] Zn^{2+} hydrides have also been proposed based on DFT modeling but have not previously been reported.[24] For both catalysts, at 250°C, the changes are small but increase with increasing temperature indicating both react with H$_2$.
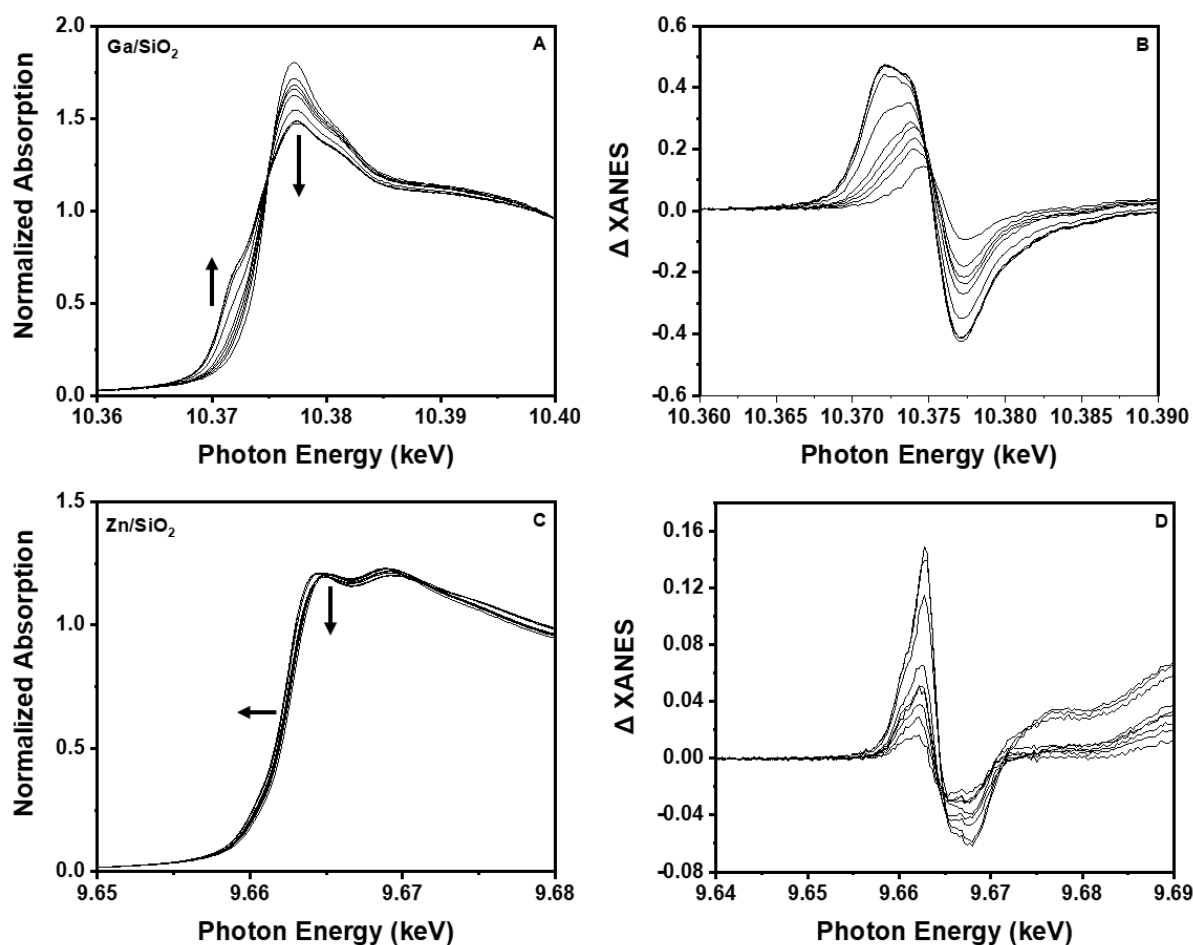
Figure 4.5. Operando XAS for Ga/SiO$_2$ and Zn/SiO$_2$ while the temperature was ramped continuously to 550°C in pure H$_2$ where A) is the normalized Ga K edge XANES with B) the difference between the high temperature scan and dehydrated structure for Ga/SiO$_2$ C) is the normalized Zn K edge XANES with D) the difference between the high temperature scan and dehydrated structure for Zn/SiO$_2$

The magnitude of the k^2-weighted EXAFS of the catalysts treated in H$_2$ at elevated temperatures is shown in Figure 4.5. The peak at about 1.5 Å (phase uncorrected distance) is due to Ga-O and Zn-O bonds. With increasing temperature there is a decrease in the M-O coordination number for both catalysts. Metal-hydrogen bonds are not detected by EXAFS, and the loss of M-O bonds has been suggested to be due for formation of M-H bonds.[24,29,31] Fits of the EXAFS are given in Table 4.7. There is a loss from 4 M-O to about 3 M-O bonds in the dehydrated and H$_2$ treated catalysts, respectively. In addition, the absence of second shell metal-oxygen-metal

scattering in the EXAFS indicates that the single site structure is maintained at high temperature in H_2.
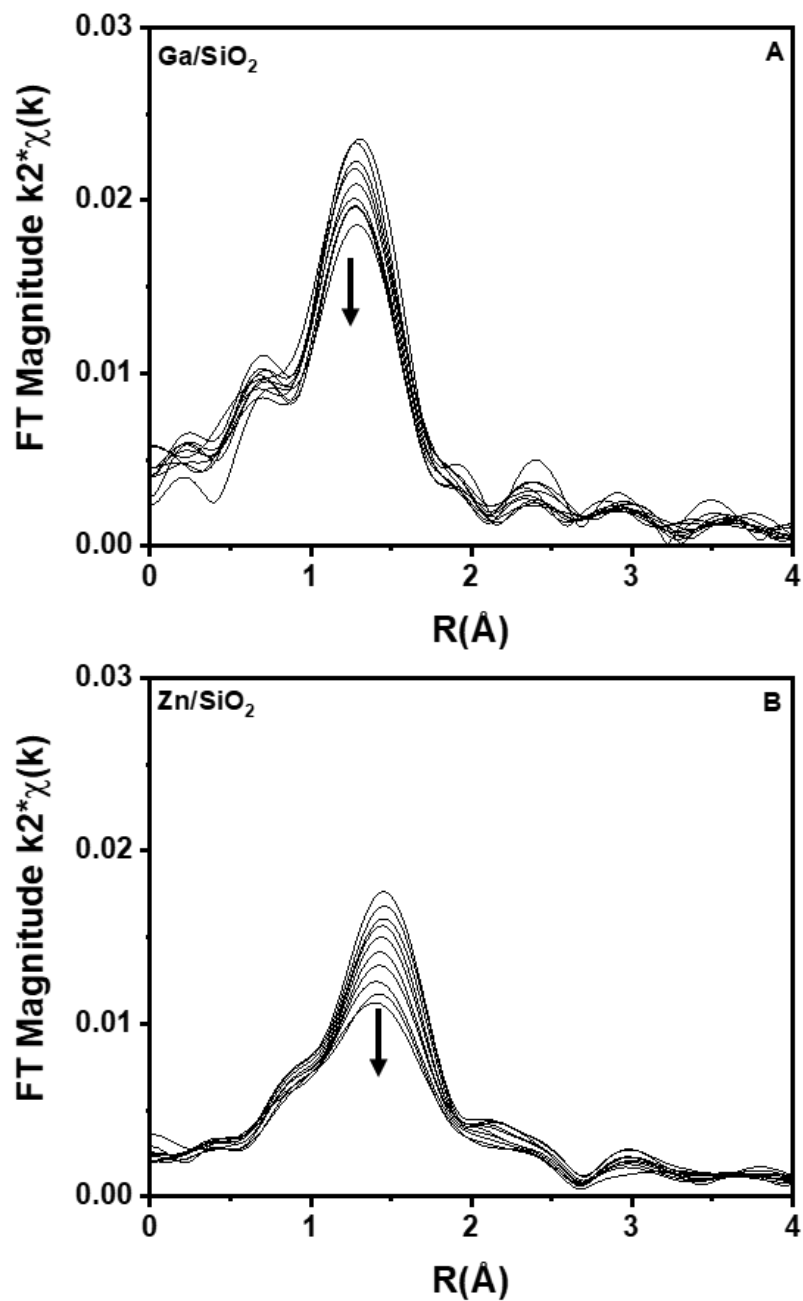
Figure 4.6. k^2-weighted magnitude of the Fourier transform ($\Delta k = 2.7 - 10.5 \text{ Å}^{-1}$) for A) Ga/SiO$_2$ and B) Zn/SiO$_2$ as the temperature ramps to 550°C in pure H_2

When the temperature was decreased to 250°C from 550°C in pure H_2, the changes to the XANES were reversed. This was previously interpreted as a temperature dependent equilibrium between the initial single site structure containing 4 M-O bonds and a metal hydride intermediate containing 3 M-O and 1 M-H bonds.[29] The XANES spectra incrementally shifted back to the initial position while the intensity of the Fourier transform magnitude (EXAFS) continued to increase with decreasing temperature, suggesting an increasing metal oxygen coordination number. When the temperature was stabilized at 250°C in H_2, and the structure stopped changing, the treatment gas composition was switched from pure H_2 to pure C_2H_4, which led to restoration of the XANES spectra back to its original position (Figures 4.7A and 4.7C). This suggests that the metal hydride can facilitate olefin insertion thus forming at least small concentrations of metal alkyls. The EXAFS also shows a slight increase in the first coordination shell, consistent with formation of new M-C bonds (Figures 4.7B and 4.7D). However, the XANES and EXAFS spectra are not completely restored to their original position because under the catalytic cycle, there is likely a combination of metal hydride and metal alkyl intermediates which have competing effects on the resulting spectra.
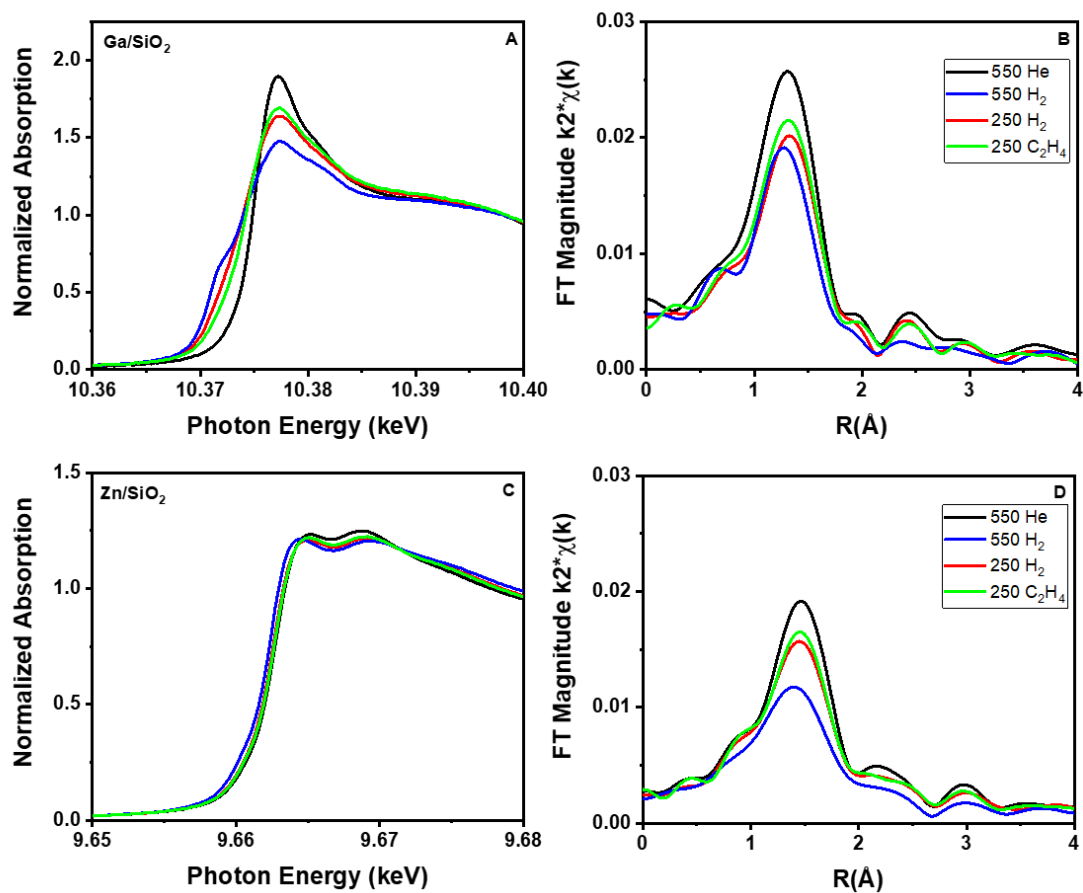
Figure 4.7. Demonstrates the ability for alkylation on the metal hydride for Ga/SiO$_2$ (A, B) and Zn/SiO$_2$ (C,D)

Table 4.7. Ga K and Zn K edge XAS fitting parameters the metal-oxygen bonds in Ga/SiO$_2$ and Zn/SiO$_2$ after treatment in pure H$_2$ at successively increasing temperatures

Sample	Pretreatment Conditions	XANES Energy (keV)	Scattering Path	CN	R (Å)	$\Delta\sigma^2$ (Å^2)	ΔE_o (eV)
Ga/SiO₂	[a] He 550°Ca	10.3751	Ga-O	4.0	1.81	0.006	-2.2
	H$_2$ 250°C	10.3750	Ga-O	3.1	1.81	0.006	-1.0
	H$_2$ 550°C	10.3747	Ga-O	2.8	1.80	0.006	-1.8
	C$_2$H$_4$ 250°C	10.3750	Ga-O	3.5	1.81	0.006	-2.2
Zn/SiO₂	[a] He 550°C	9.6628	Zn-O	4.0	1.95	0.006	-0.6
	H$_2$ 250°C	9.6627	Zn-O	3.3	1.93	0.006	-0.9
	H$_2$ 550°C	9.6625	Zn-O	2.9	1.93	0.006	-2.3
	C$_2$H$_4$ 250°C	9.6627	Zn-O	3.4	1.93	0.006	-1.0

[a] Fits for the dehydrated samples were copied from Table 4.1 and are used for comparison

To identify the number of metal carbon bonds, a difference between the C_2H_4 and H_2 treated catalysts at 250°C was performed. Although the resulting feature is small (Figure 4.8), it can be fit (Table 4.8) to reveal 0.4 and 0.2 metal-carbon bonds in Ga/SiO_2 and Zn/SiO_2 respectively.
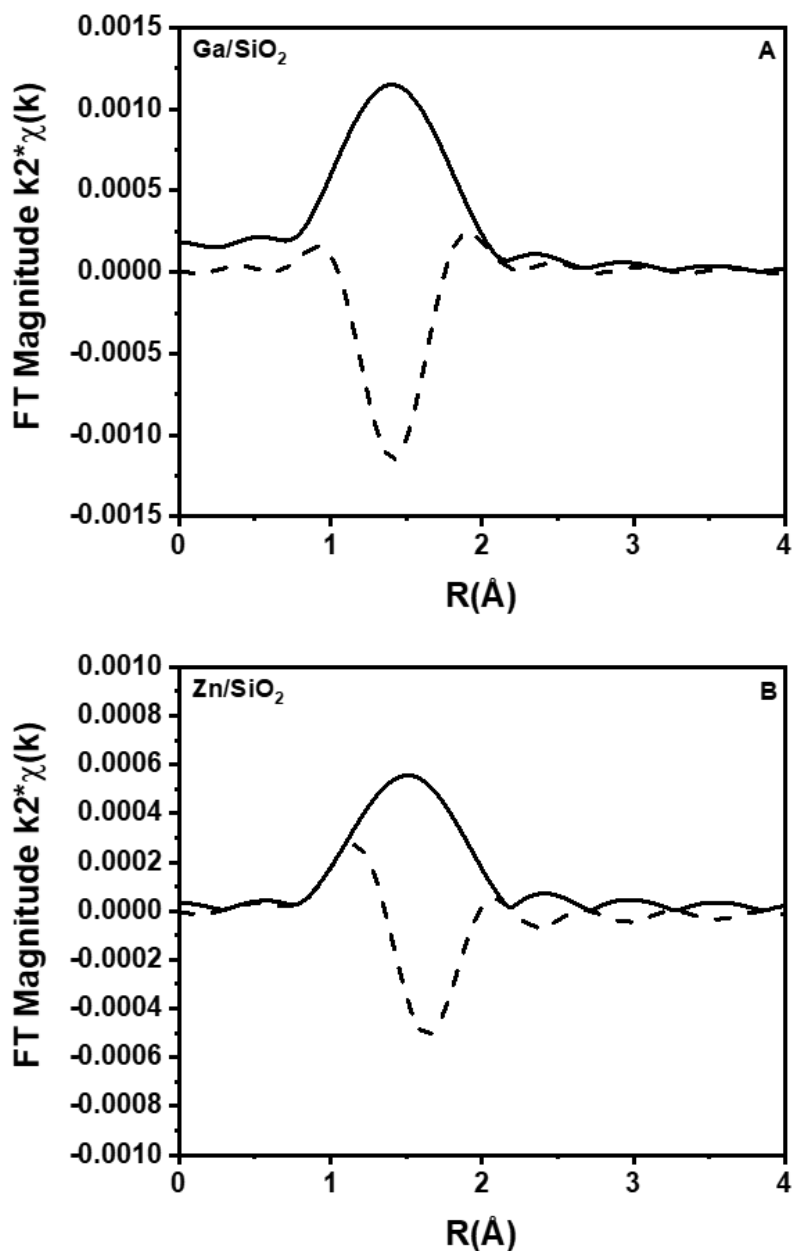
Figure 4.8. Difference EXAFS for A) Ga/SiO_2 and B) Zn/SiO_2 after treatments 250°C in C_2H_4-250°C in H_2

Table 4.8. Difference EXAFS (C_2H_4 - H_2) fitting parameters at the Ga K and Zn K edges to identify the number of metal-carbon bonds at 250°C

Sample	Scattering Path	CN	R (Å)	$\Delta\sigma^2$ (Å^2)	ΔE_o (eV)
Ga/SiO$_2$	Ga-C	0.4	1.94	0.005	6.1
Zn/SiO$_2$	Zn-C	0.2	2.01	0.005	3.2

Further reaction of M-H with D_2 in a temperature programmed surface reaction (TPSR) results in H/D isotopic exchange to form HD, in which the amount of HD formed corresponds to the number of metal hydride sites present on the surface. On Ga/SiO$_2$, after H_2 treatment at 250°C, about 0.70 mol HD/mol Ga was formed, which is very similar to the decrease in Ga-O coordination in H_2 observed by EXAFS (Figure 4.7, Table 4.7). The shape of the TPSR profile is consistent with only one type of Ga species present. Similarly, Zn/SiO$_2$ forms 0.19 mol HD/mol Zn at 250°C, consistent with the changes in coordination number observed in Table 4.7. Higher reaction temperatures lead to an increased number of sites that contribute to metal hydride formation.

In situ IR for Ga/SiO$_2$ also provides evidence for the heterolytic dissociation of H_2. The feature at 3745 cm^{-1} corresponds to Si-OH vibrations (Figure 4.9A). The spectra presented in Figure 4.9 correspond to the difference between the treated and dehydrated catalysts (Ga/SiO$_{2;\ H2}$-Ga/SiO$_{2;\ dehydrated}$). As the temperature increases from 35 to 550°C (in H_2), the intensity of this feature also increases, suggesting that higher temperatures facilitate increased H_2 dissociation. Under these same conditions, there are two broad peaks at 2034 cm^{-1} and 1875 cm^{-1}, which have been previously attributed to Ga-H stretching (Figure 4.9B).[36–38] As the temperature increases, the intensity of both peaks also increase, consistent with the increase in number of Ga-H sites formed. IR features observed for Si-OH and Ga-H indicate that H_2 dissociation is possible at temperatures as low as 200°C, where olefin hydrogenation occurs. Higher temperatures likely favor the presence of more Ga-H sites, leading to larger intensity of IR bands.
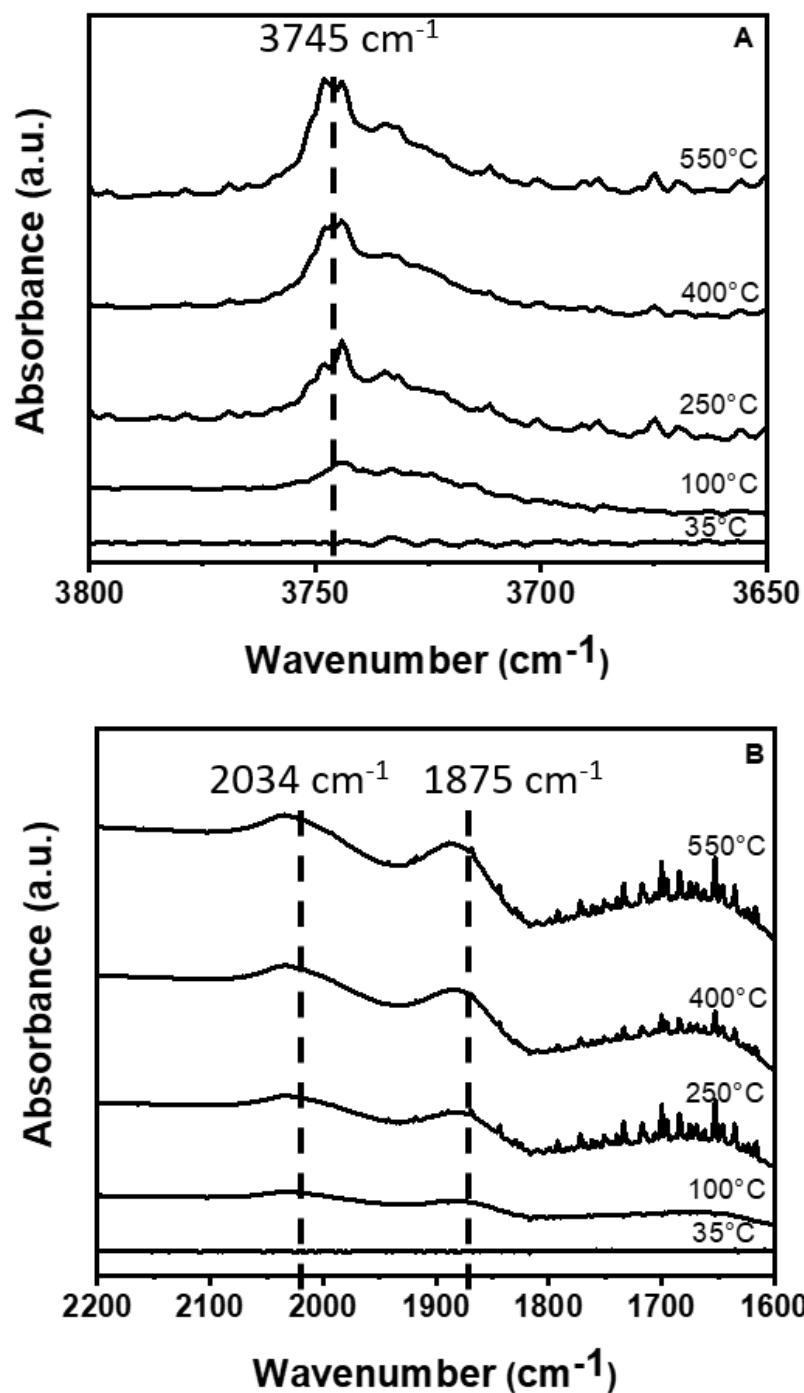
Figure 4.9. IR O-H stretching region for Ga/SiO$_2$ after treatment in pure H$_2$ at increasing temperature from 35°C to 550°C where the treated pattern from the treated catalyst- the dehydrated catalyst is provided (Ga/SiO$_{2;\ H2}$-Ga/SiO$_{2;\ dehydrated}$) for A) 3800-3650 cm^{-1} corresponding to Si-OH stretching and B) 2200-1600 cm^{-1} corresponding to Ga-H stretching

Exposure of Ga/SiO$_2$ to C$_2$H$_4$ at temperatures from 35 to 250°C revealed C-H stretching vibrations between 2975-2940 cm^{-1} (Figure 4.10). The spectra shown in Figure 4.10 correspond to the difference between the treated and dehydrated catalysts (Ga/SiO$_{2; C2H4}$-Ga/SiO$_{2; dehydrated}$) and suggests that these C-H vibrations are due to ethylene coordinated to the metal center to form a metal alkyl, as opposed to gas phase ethylene in the cell. In addition, there is a feature at 2970 cm^{-1}, which has been previously attributed to the formation of a vinylic C-H stretching.[39] The broad feature within this region also increases with temperature from 35°C to 250°C, where the oligomerization reaction is performed. This suggests that the heterolytic C-H bond activation is also possible, and the pre-formation of a metal hydride is not required to activate olefins.
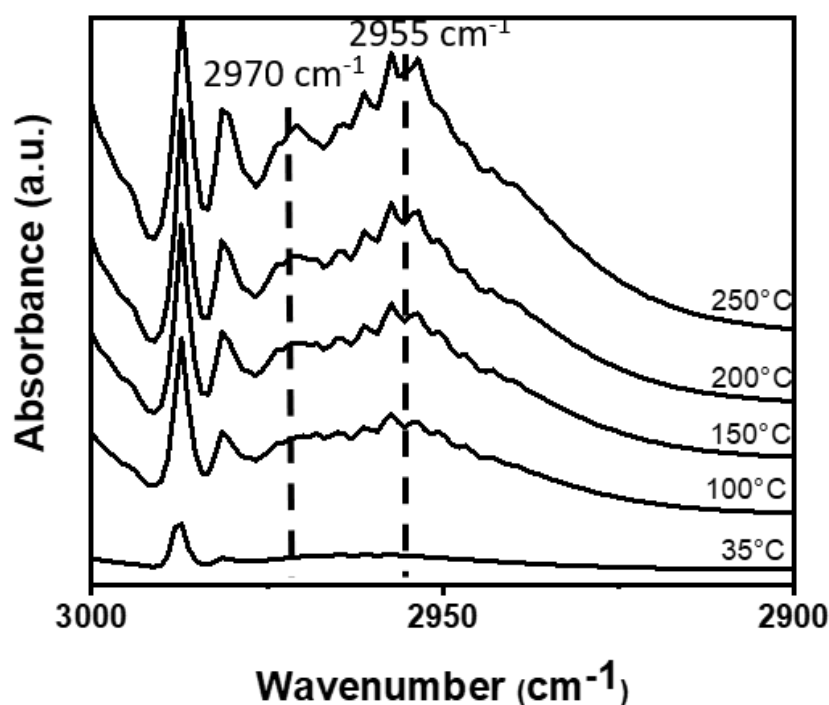
Figure 4.10. IR C-H stretching region for Ga/SiO$_2$ after treatment in pure C$_2$H$_4$ at increasing temperature from 35°C to 250°C where the treated pattern from the treated catalyst- the dehydrated catalyst is provided (Ga/SiO$_{2; C2H4}$-Ga/SiO$_{2; dehydrated}$)

When the H$_2$-treated Ga/SiO$_2$ was exposed to C$_2$H$_4$, the spectra looked nearly identical to that in Figure 4.10, except the feature at 2970 cm^{-1} was absent. This implies that the pre-formation of Ga-H can also facilitate alkylation, as has been shown by XAS. This suggests that the heterolytic

122

C-H bond activation is also possible, and the pre-formation of a metal hydride is not required to activate olefins.

4.3.6 Theoretical Calculations for the Mechanism of Oligomerization on Ga/SiO$_2$

Ga/SiO$_2$ was modeled by replacing Si atoms with Ga atoms in an amorphous SiO$_2$ model. To account for the local charge balance, a proton was added onto the oxygen atom adjacent to the Ga, resulting in a silanol group. Multiple DFT optimizations were performed to develop the basis structure for modeling ethylene oligomerization on Ga/SiO$_2$. Five Ga sites were tested (Figure 4.11), each corresponding to four oxygen atoms that were originally bonded to Si.
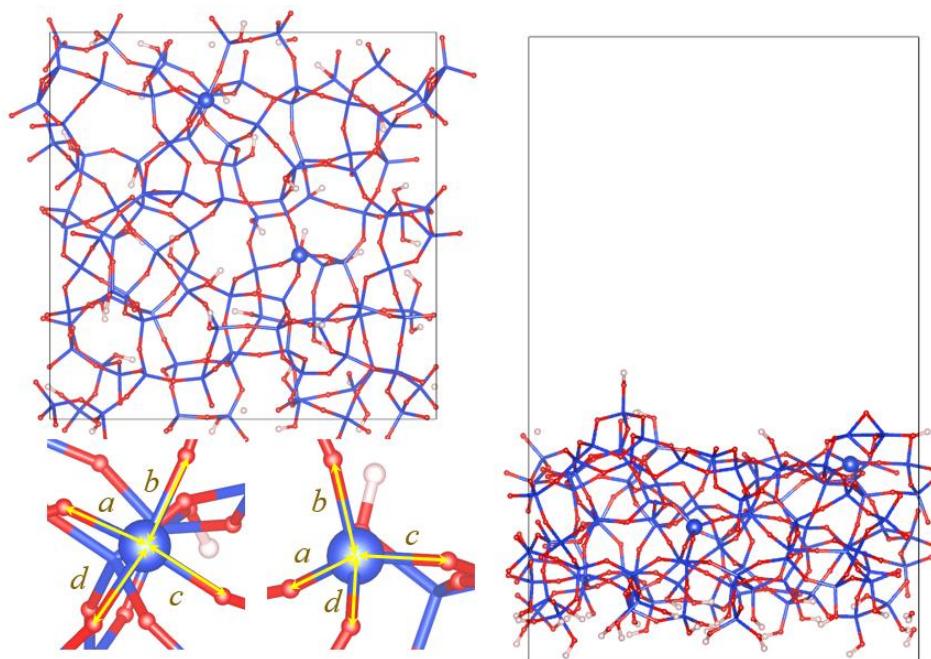
Figure 4.11. Amorphous silica model with highlighted Si atoms to be substituted with Ga (Si = blue, O = red; H= white)

During the optimizations, a nearby Si-OH group was generated. Two representative Ga sites, including a three-coordinated (3CN) and four-coordinated (4CN), were evaluated (Figure 4.12). The different coordination environments are attributed to the original local binding condition of the Si atoms substituted. For the 3CN site, the Si atom is in a less constrained framework, where the Si-O bonds were elongated (a=1.80 Å, b=1.66 Å, c=1.76 Å, and d=1.69 Å). The cleavage of the Si-O bond (a) to generate the 3CN Ga site led to Ga-O bond distances: 4.51 Å, 1.86 Å, 1.82 Å, and 1.86 Å. A bond distance of 4.51 Å is sufficiently far away that it does not interact with the

123

3CN Ga site. Whereas the Si atom used for creating the 4CN site is located in a more constrained environment containing shorter Si-O bonds (a=1.62 Å, b=1.67 Å, c=1.64 Å, and d=1.66 Å). Consequently, the Si-OH formed on the 4CN Ga site is nearer to the metal center and there are 4 Ga-O bonds at 2.02 Å, 1.85 Å, 1.82 Å, and 1.88 Å. The average Ga-O bond distance of the 4CN Ga site is 1.93 Å, which agrees with the experimental characterization (XAS).
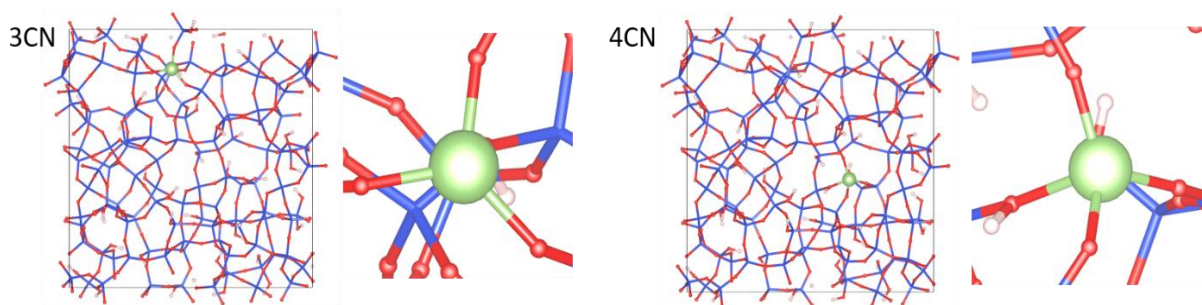
Figure 4.12. Amorphous silica model with substituted Ga (Si = blue, O = red, H= white, Ga = green)

While the 4CN Ga site is thermodynamically less stable than the analogous 3CN Ga sites, experimental evidence suggests that the initial Ga structure contains four Ga-O bonds. This suggests that the 4CN Ga site may exist in a metastable state and was used in further analysis for ethylene oligomerization.

Initiation of the catalytic cycle begins with heterolytic dissociation of a vinyl C-H bond of ethylene across one Ga-O bond. The vinyl alkyl C atom has a negative charge and neighboring Si-OH group is formed. Migratory insertion of ethylene is the rate limiting step with an effective activation barrier of 3.28 eV. Ethylene insertion into the Ga-vinyl intermediate forms a Ga-butenyl intermediate and subsequent β-H elimination leads to stoichiometric amounts of butadiene and a Ga-H intermediate (Figure C.1, Table C.1). Because of the stoichiometric amounts of the initiation product, butadiene is not detected experimentally, but has been proposed based on DFT calculations for Ni^{2+} heterogeneous oligomerization catalysts.[16,17]

The pre-catalyst structure has a bridging Si-OH and a second non-bridging Si-OH is formed during the initial activation of C_2H_4. Due to the low chemical potential of water, there is a high thermodynamic favorability for dehydration of these two adjacent Si-OH. The intrinsic enthalpy of dehydration is +1.62 eV, which is consistent with that obtained using a similar silica model.[41] Dehydration of adjacent Si-OH lowers the energy landscape of Ga-H formation (Figures 4.13A,

C.2, Table C.2). With this, the free energy of C_2H_4 insertion decreases to 3.10 eV and that of β-H elimination decreases to 2.84 eV.
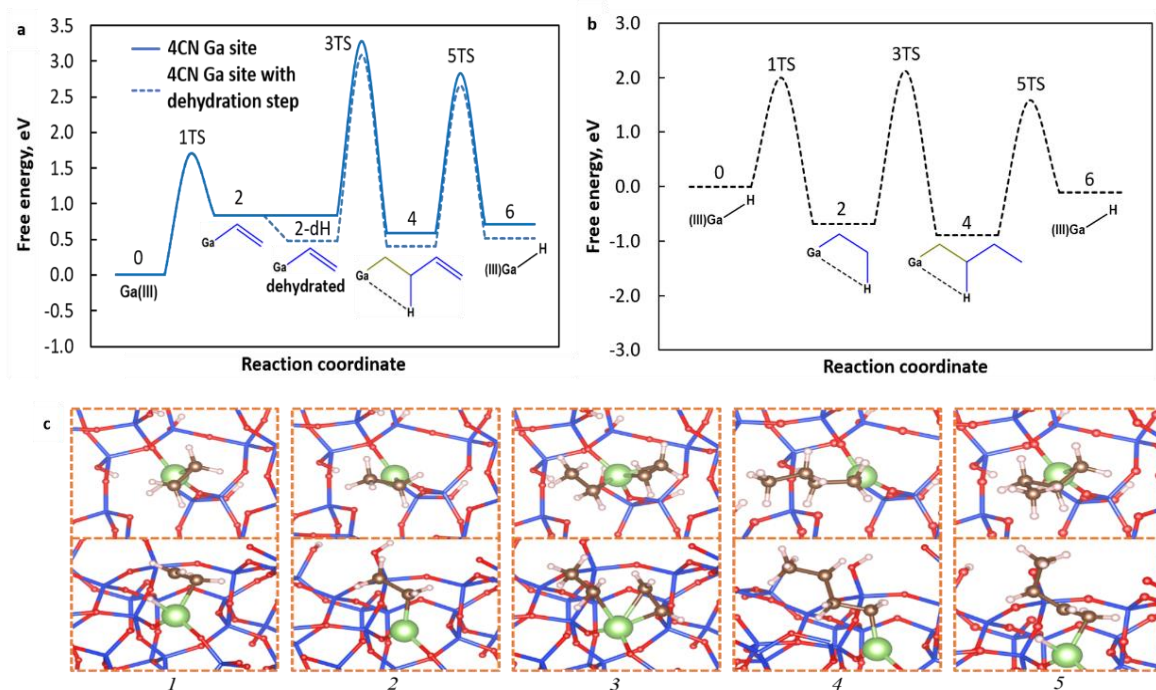
Figure 4.13. Theoretical mechanistic insight on Ga/SiO$_2$ A) Free energy diagram of Ga-H formation on 4CN Ga site with and without dehydration B) Free energy diagram of oligomerization on Ga-H C) Schematic of ethylene oligomerization on Ga-H and relative reaction intermediates

DFT modeling of the oligomerization pathway was performed starting from the Ga-H intermediate and yielded an energy landscape with transition states illustrated in Figure 4.13C (Figures 4.13B, C.3-C.4, Tables C.3-C.4). The C-H(sp2) activation of C_2H_4 by Ga-H forms a Ga-alkyl intermediate and has a free energy of approximately 1.99 eV. Subsequent insertion of a second C_2H_4 to the Ga-alkyl intermediate yields a Ga-butyl transition state and is the rate limiting step with a free energy of 2.25 eV. This is consistent with higher partial pressures of C_2H_4 leading to higher TORs. Finally, β-H elimination (1.67 eV) results in desorption of the final olefin product, re-forming Ga-H and completing the catalytic cycle. This energy is consistent with previous DFT calculations for the β-H elimination of a propyl group on Zn/SiO$_2$ (1.99 eV) for C_3H_8 dehydrogenation.[23] Oligomerization on Ga-H generated from a less constrained model, for example starting from a 3CN Ga site, was also calculated (Figure C.5, Table C.5). Because the Ga

site may be in a variety of strain conditions, the resulting DFT calculations provide the lower (3CN) and upper (4CN) limits of the energetics of olefin oligomerization (Figure C.6). Using the less constrained model, the free energy for migratory insertion and β-H elimination decreased to 1.14 eV and 1.10 eV, respectively. This proposed mechanism (Figure 4.15) is in line with the Cossee-Arlman mechanism previously proposed for Ni^{2+} ions on zeolite supports.

Both Ga/SiO_2 and Zn/SiO_2 are main group metal elements with no available d orbitals to participate in the catalytic cycle. For transition metal oligomerization catalysts like Ni^{2+}, one would expect that d orbitals would participate in the reaction steps involving dissociation of C-H bonds, *e.g.*, initiation and β-H elimination. On a transition metal, the transition state corresponding to step 6 in Figure 4.13C involves the HOMO of the ethylene donating electrons to the hybridized M orbital while the filled d orbital from M donates electrons to the LUMO of ethylene, thus forming a π-bond. On Ga^{3+} and Zn^{2+}, this is different because neither can accommodate more than four bonds. Therefore, it is possible that a filled 3d orbital can facilitate the M donating electrons to the ethylene, thus forming a π-bond. Alternatively, using an unfilled 4d orbital, the ethylene will donate electrons to the M hybridized orbital, thus forming a σ−bond. In both cases, the metal alkyl intermediate will contain a weaker bond than in the same intermediates using transition metals, and therefore likely have a lower stability and a higher energy barrier for β-H elimination.

4.4 Discussion

Ga/SiO_2 and Zn/SiO_2 have the same 4-coordinate (Td) structure as Ni/SiO_2. These structures are stable at high temperatures and Ga^{3+} and Zn^{2+} do not reduce to a lower oxidation state, even in the presence of H_2. Whereas, when Ni^{2+} single sites are exposed to temperatures higher than 350°C in reducing conditions, Ni^{2+} reduces to Ni^0 and loses oligomerization activity.[27] While neither Ga/SiO_2 nor Zn/SiO_2 has been reported to perform oligomerization, this work shows that they perform oligomerization with varying product distributions. This performance was investigated through a mechanistic understanding of the elementary steps and reaction intermediates required for oligomerization to occur. For this, the ability to heterolytically activate C-H bonds is important for catalyst activation. This capability is known through the previously reported dehydrogenation activity.[23,24] Dehydrogenation has the same elementary steps (insertion, and β-hydride elimination) and reaction intermediates (metal alkyl and metal hydride) as oligomerization (Figure 4.14).
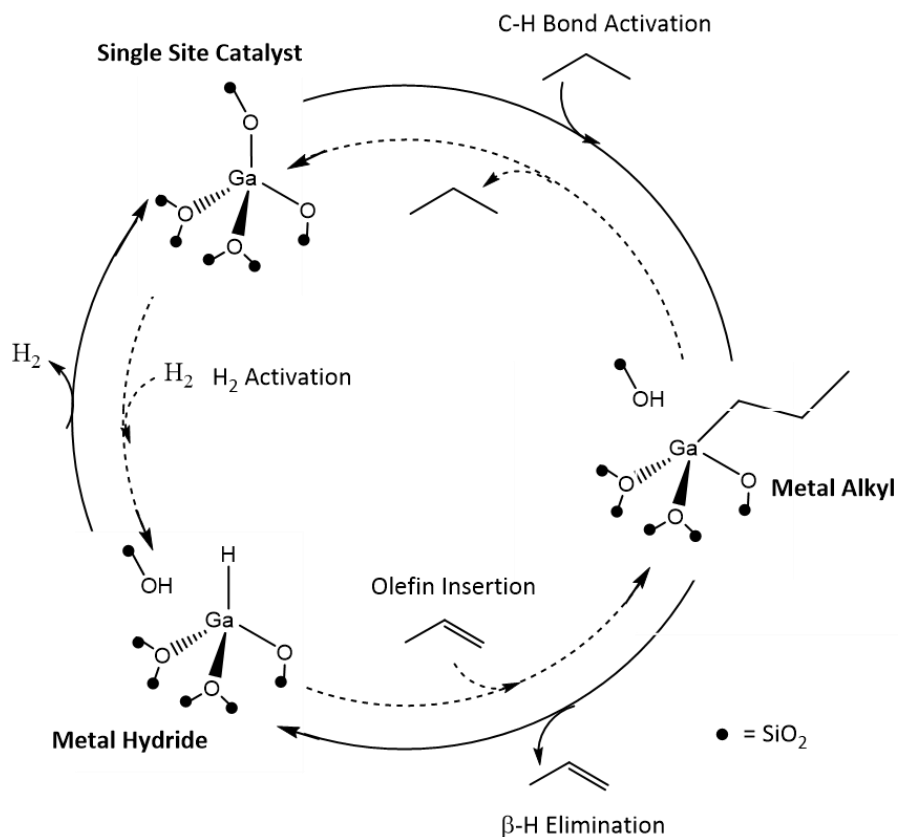
Figure 4.14. Dehydrogenation (solid line) and hydrogenation (dashed line) reaction pathways

In dehydrogenation (550°C, 1 atm), an alkane is inserted to the 4-coordinate single site catalyst metal center, forming a metal alkyl. Subsequent β-hydride elimination produces the olefin and forms a metal hydride intermediate. C-H bond activation restores the initial 4-coordinate catalyst. In hydrogenation (200°C, 1 atm), the microscopic reverse of dehydrogenation that occurs at lower reaction temperatures, the single site catalyst can activate H_2 to form a metal hydride. Olefin insertion to the metal hydride forms a metal alkyl which produces a paraffin when it is desorbed from the metal surface, reforming the initial catalysts, thus restarting the catalytic cycle.

Oligomerization occurs at temperatures where C-H bond activation occurs, which is required for the initiation of the catalyst. IR demonstrates that increasing temperatures in C_2H_4 leads to an increase in the broad peak ranging from 2975-2940 cm^{-1}, corresponding to increased formation of metal alkyls. At 250°C, the intensity of this feature is notable, consistent with the oligomerization

reactivity observed at that temperature on both Ga/SiO$_2$ and Zn/SiO$_2$. However, the effect of pure C$_2$H$_4$ on the catalysts could not be studied using XAS because metal oxygen and metal carbon bonds cannot be distinguished.

The ability to heterolytically dissociate H$_2$ is also critical for carrying out oligomerization. Both IR and XAS demonstrate that increasing temperature in pure H$_2$ leads to increased interaction with the catalyst. IR shows that as the temperature increases from room temperature to 550°C, there is an increase in the 3745 cm^{-1} peak, corresponding to increasing Si-OH vibrations. This is consistent with increased H$_2$ dissociation at higher temperatures and is in line with the H$_2$/D$_2$ results. When a metal hydride forms, a metal oxygen bond is lost to the formation of a metal hydrogen bond and the remaining hydrogen forms a surface silanol on the support. This is consistent with the loss of approximately one metal-oxygen bond observed by XAS under the same conditions.

From this, it is interpreted that hydrogenation/dehydrogenation and oligomerization are related through the formation of the same reaction intermediates and the ability to perform the same elementary reaction steps (Figure 4.15). However, different reaction conditions are required. While dehydrogenation and hydrogenation can be performed at atmospheric pressure with high rates, oligomerization requires higher pressure to obtain high conversion and reasonable rates. Here, low ethylene conversions up to 5% were obtained at 250°C and 1 atm and the conversion increased to about 20% at 250°C and 30.6 atm.
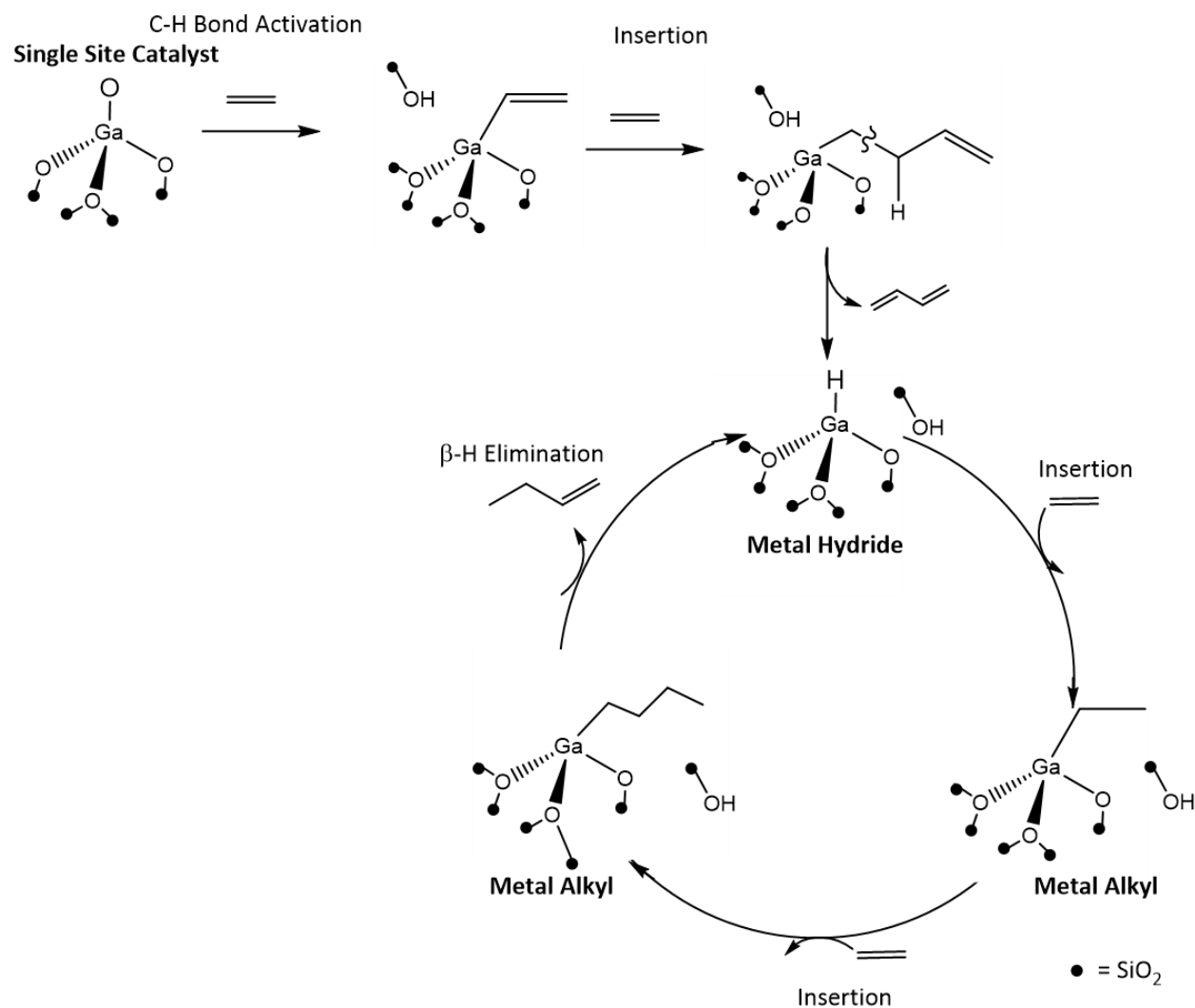
Figure 4.15. Heterogeneous oligomerization reaction pathway

The heterogeneous oligomerization mechanism on Ga/SiO_2 and Zn/SiO_2 is likely the same as has been previously proposed for Ni/BEA, except that it requires the initial activation of a C-H bond to form a vinylic intermediate.[16] This C-H bond activation frequently occurs at higher temperatures than required for traditional Ni-based oligomerization catalysts (250°C on Ga^{3+} and Zn^{2+} vs. 150-200°C on Ni^{2+}). A subsequent olefin can insert in the vinylic intermediate and β-H elimination can simultaneously form butadiene and a metal hydride, thus activating the traditional oligomerization cycle. Butadiene, although is not detected experimentally, has been proposed to form in a stoichiometric amount during the initiation of oligomerization catalysts.[16,17]

Once a metal hydride is formed, ethylene can insert to form a metal alkyl intermediate. Chain growth is carried out by the tendency of a catalyst to perform sequential olefin insertion (propagation) over β-H elimination (termination). Catalysts that favor β-H elimination over olefin insertion will likely favor the formation of dimers (Zn/SiO_2), whereas the reverse can produce higher molecular weight hydrocarbon products (Ga/SiO_2). DFT shows that ethylene insertion is the rate determining step. The experimental results demonstrate that Ga/SiO_2 has a higher activity than Zn/SiO_2. This could be due to the higher stability of Ga-H relative to Zn-H, which suggests that the energy barrier for ethylene insertion to the M-H is lower on Ga^{3+} and therefore allows for more ethylene insertions prior to β-H elimination, thus forming higher molecular weight products. Desorption of the long chain olefin product and restore the metal hydride site, allowing it to go through the catalytic cycle again.

For this, understanding the reaction intermediates and elementary steps is critical for identifying novel oligomerization catalysts with tunable product selectivity for targeted applications. Ga/SiO_2 and Zn/SiO_2 are not traditionally used for olefin oligomerization. While Ni-based catalysts are usually used to perform oligomerization, the products are limited to primarily butenes and some hexenes, which is not desirable to make fuel-range products. Some studies have been performed on bifunctional Ni/MCM-41, which have metal (Ni^{2+}) and acid (H^+) function leading to the formation of both linear and branched products containing C_3+ carbon numbers.[9,18] The introduction of acid character leads to cracking and isomerization, as evidenced by the formation of branched hydrocarbons (*e.g.* isobutene). Whereas C_2H_4 oligomerization on a metal site should only form linear products of even carbon numbers.

Oligomerization on Ga^{3+} and Zn^{2+} single site catalysts were compared to that on Ni^{2+} all supported on SiO_2 (non-acidic). Silica supported catalysts are not expected to result in products containing odd carbon numbers because cracking ($C_8^=$ $\rightarrow$ $iC_4^=$ or $C_3^=$ + $iC_5^=$) is not expected in the absence of H^+ sites. Consistent with the lack of acidity of the silica support, no isobutene is produced during ethylene oligomerization and higher molecular weight products were not formed during propane dehydrogenation. Each of these catalysts formed varying product distributions of linear olefins including an equilibrium distribution of $C_4^=$ (1-butene, cis-2-butene, and trans-2-butene), $C_6^=$ and $C_8^=$ isomers, in addition to trace amounts of interesting products like methane and ethane. The formation of paraffins could be explained by the formation of butadiene during initiation.

Understanding the reaction intermediates and elementary steps is critical for identifying novel oligomerization catalysts with tunable product selectivity for targeted applications. Ga/SiO_2 and Zn/SiO_2 are not traditionally used for olefin oligomerization. Though reports on Ga/ZSM-5 suggest the possibility of oligomerization on Ga ions, the acidic character of the support complicates the understanding of the metal activity.[25] ZSM-5 will protonate ethylene at room temperature and perform oligomerization at higher temperature. The lack of linear olefins and observation of high Bronsted activity suggest that the acid character dominates performance on Ga/ZSM-5. Whereas the SiO_2 support in our study is nonreactive and the activity comes only from Ga^{3+} and Zn^{2+} sites respectively, thus forming linear olefins.

4.5   Conclusion

Ga^{3+} and Zn^{2+} single site catalysts can perform oligomerization at temperatures as low as 250^oC. While both Ga/SiO_2 and Zn/SiO_2 are atypical oligomerization catalysts, they can form the necessary intermediates required to facilitate the reaction (*i.e.* metal hydride and metal alkyl) through the Cossee-Arlman mechanism. By changing the identity of the active metal, we can increase control over the resulting product distribution and operate under various process conditions because unlike Ni^{2+}, neither Ga^{3+} nor Zn^{2+} will reduce to a lower oxidation state, even at high temperatures in H_2. Finally, dehydrogenation and oligomerization are related through the formation of the same reaction intermediates. This work presents opportunity for the development of oligomerization catalysts, as well as new insights into main group metal chemistry.

4.6   Acknowledgements

4.7 References

1. Sydora, O.L. Selective Ethylene Oligomerization. *Organometallics*. **2019**, 38, 997–1010.

2. Lavrenov, A.V.; Karpova, T.R.; Buluchevskii, E.A.; Bogdanets, E.N. Heterogeneous oligomerization of light alkenes: 80 years in oil refining. *Catal. Ind.* **2016**, 8, 316–327.

3. Keim, W. Nickel: An Element with Wide Application in Industrial Homogeneous Catalysis. **1990**, 29, 235-244.

4. Mathys, G. M. K.; Martens, L. R. M.; Baes, M. A., Verduijn, J. P.; Huybrechts, D. R. C. 1997. Alkene oligomerization. US Patent 20040006250, filed April 14, 2003, and issued January 8, 2004.

5. Brown, S. H.; Godsmark, J. S.; Mathys, G. M. K. 2010. Olefin oligomerization process. US Patent 20070173676A1, filed June 1, 2004, and issued August 31, 2010.

6. Verrelst, W. H.; Martens, L. R. M. 1995. Oligomerization and catalysts therefor. French Patent WO1995022516A1, filed February 22, 1994, and issued August 24, 1995.

7. Forestière, A.; Olivier-Bourbigou, H.; Saussine, L. Oligomerization of Monoolefins by Homogeneous Catalysts. *Oil & Gas Science and Technology - Rev. IFP* **2009**, 64, 649–667.

8. Killian, C. M.; Johnson, L. K.; Brookhart, M. Preparation of Linear α-Olefins Using Cationic Nickel(II) α-Diimine Catalysts. *Organometallics*. **1997**, 16, 2005–2007.

9. Finiels, A.; Fajula, F.; Hulea, V. Nickel-based solid catalysts for ethylene oligomerization – a review. *Catal. Sci. Technol.* **2014**, 4, 2412–2426.

10. Keim, W. Oligomerization of Ethylene to α-Olefins: Discovery and Development of the Shell Higher Olefin Process (SHOP). *Angewandte Chemie*. **2013**, 52,12492–6.

11. Al-Jarallah, A. M.; Anabtawi, J. A.; Siddiqui, M. A. B.; Aitani, A. M.; Al-Sa'doun, A. W. Ethylene dimerization and oligomerization to butene-1 and linear α-olefins: A review of catalytic systems and processes. *Catalysis Today*. **1992**, 14, 1-121.

12. McGuiness, D.S. Olefin Oligomerization via Metallacycles: Dimerization, Trimerization, Tetramerization, and Beyond. *Chemical Reviews*, **2011**, 111, 2321–2341.

13. Biscardi, J.A.; Meitzner, G.D.; Inglesia, E. Structure and Density of Active Zn Species in Zn/H-ZSM5 Propane Aromatization Catalysts. *Journal of Catalysis*, **1998**, 179, 192–202.

14. Forget, S.; Olivier-Bourbigou, H.; Delcroix, D. Homogeneous and Heterogeneous Nickel-Catalyzed Olefin Oligomerization: Experimental Investigation for a Common Mechanistic Proposition and Catalyst Optimization. *ChemCatChem*, **2017**, 9, 2408–2417.

15. Joshi, R., Zhang, G., Miller, J. T. & Gounder, R. Evidence for the Coordination–Insertion Mechanism of Ethene Dimerization at Nickel Cations Exchanged onto Beta Molecular Sieves. *ACS Catal.* **2018**, 8, 11407–11422.

16. Brogaard, R. Y.; Olsbye, U. Ethene Oligomerization in Ni-Containing Zeolites: Theoretical Discrimination of Reaction Mechanisms. *ACS Catal.* **2016**, 6, 1205–1214.

17. Henry, R.; Komurcu, M.; Ganjkhanlou, Y.; Brogaard, R.Y.; Lu, L.; Jens, K.J.; Berlier, G.; Olsbye, U. Ethene oligomerization on nickel microporous and mesoporous-supported catalysts: Investigation of the active sites. *Catalysis Today,* **2018**, 9, 154–163.

18. Nicholas, C. P. Applications of light olefin oligomerization to the production of fuels and chemicals. *Applied Catalysis A: General*, **2017**, 543, 82–97.

19. Moussa, S.; Concepción, P.; Arribas, M. A.; Martínez, A. Nature of Active Nickel Sites and Initiation Mechanism for Ethylene Oligomerization on Heterogeneous Ni-beta Catalysts. *ACS Catal.* **2018**, 8, 3903–3912.

20. Martínez, A.; Arribas, M. A.; Concepción, P.; Moussa, S. New bifunctional Ni–H-Beta catalysts for the heterogeneous oligomerization of ethylene. *Applied Catalysis A: General*, **2013**, 467, 509–518.

21. Camara Greiner, E.O.; Inoguchi, Y. *Chemical Economics Handbooks (CEH)*. **2010**.

22. Phadke, N. M.; Van der Mynsbrugge, J.; Mansoor, E.; Getsoian, A.B.; Head-Cordon, M.; Bell, A.T. Characterization of Isolated Ga3+ Cations in Ga/H-MFI Prepared by Vapor-Phase Exchange of H-MFI Zeolite with GaCl3. *ACS Catal.* **2018**, 8, 6106–6126.

23. Cybulskis, V. J.; Pradhan, S.U.; Lovon-Quintana, J.J.; Hock, A.S.; Hu, B.; Zhang, G.; Delgass, W.N.; Ribeiro, F.H.; Miller, J.T. The Nature of the Isolated Gallium Active Center for Propane Dehydrogenation on Ga/SiO2. *Catal Lett.***2017**, 147, 1252–1262.

24. Schweitzer, N. M.; Hu, B.; Das, U.; Kim, H.; Greeley, J.; Curtiss, L.A.; Stair, P.C.; Miller, J.T.; Hock, A.S. Propylene Hydrogenation and Propane Dehydrogenation by a Single-Site Zn2+ on Silica Catalyst. *ACS Catal.* **2014**, 4, 1091–1098.

25. Pidko, E. A.; Hensen, E. J. M.; van Santen, R. A. Dehydrogenation of Light Alkanes over Isolated Gallyl Ions in Ga/ZSM-5 Zeolites. *J. Phys. Chem. C.* **2007**, 111, 13068–13075.

26. Schreiber, M. W.; Plaisance, C.P.; Baumgartl, M.; Reuter, K.; Jentys, A.; Bermejo-Deval, R.; Lercher, J.A. Lewis–Brønsted Acid Pairs in Ga/H-ZSM-5 To Catalyze Dehydrogenation of Light Alkanes. *J. Am. Chem. Soc.* **2018**, 140, 4849–4859.

27. Zhang, G.; Yang, C.; Miller, J. T. Tetrahedral Nickel(II) Phosphosilicate Single-Site Selective Propane Dehydrogenation Catalyst. *ChemCatChem*. **2017**, 10, 961–964.

28. Ressler, T. WinXAS: a Program for X-ray Absorption Spectroscopy Data Analysis under MS-Windows. *J Synchrotron Rad* . **1998,** *5,* 118–122.

29. Getsoian, A.B.; Das, U.; Camacho-Bunquin, J.; Zhang, G.; Gallagher, J.R.; Hu, B.; Cheah, S.; Schaidle, J.A.; Ruddy, D.A.; Hensley, J.E.; Krause, T.R.; Curtiss, L.A.; Miller, J.T.; Hock, A.S. Organometallic model complexes elucidate the active gallium species in alkane dehydrogenation catalysts based on ligand effects in Ga K-edge XANES. *Catalysis Science & Technology*. **2016**, 6, 6339–6353.

30. Geller, S. Crystal Structure of β-Ga2O3. *J. Chem. Phys.* **1960**, 33, 676–684.

31. Hu, B.; Getsoian, A.B.; Schweitzer, N.M.; Das, U.; Kim, H.; Niklas, J.; Poluektov, O.; Curtiss, L.A.; Stair, P.; Miller, J.T.; Hock, A.S. Selective propane dehydrogenation with single-site CoII on SiO2 by a non-redox mechanism. *Journal of Catalysis*. **2015**, 322, 24–37.

32. Hu, B.; Getsoian, A.B.; Schweitzer, N.M.; Das, U.; Zhang, G.; Kraft, S.J.; Childers, D.J.; Lanci, M.P.; Miller, J.T.; Hock, A.S.. Isolated FeII on Silica As a Selective Propane Dehydrogenation Catalyst. *ACS Catalysis.* **2015**, 5, 3494–3503.

33. Britovsek, G. J. P.; Malinowski, R.; McGuinness, D.S.; Nobbs, J.D.; Tomov, A.K.; Wadsley, A.W.; Young, C.T. Ethylene Oligomerization beyond Schulz−Flory Distributions. *ACS Catal.* **2015**, 4, 6922-6925.

34. Bartlett, B.; Hossain, M. M.; Tysoe, W. T. Reaction Pathway and Stereoselectivity of Olefin Metathesis at High Temperature. *Journal of Catalysis*. **1998**, 176, 439–447.

35. Martínez, A.; Arribas, M. A.; Concepción, P.; Moussa, S. New bifunctional Ni–H-Beta catalysts for the heterogeneous oligomerization of ethylene. *Applied Catalysis A: General*. **2013**, 467, 509–518.

36. Collins, S. E.; Baltanás, M. A.; Bonivardi, A. L. Hydrogen Chemisorption on Gallium Oxide Polymorphs. *Langmuir*. **2005**, 21, 962–970.

37. Rodrigues, V. de O.; Faro Júnior, A. C. On catalyst activation and reaction mechanisms in propane aromatization on Ga/HZSM5 catalysts. *Applied Catalysis A: General*. **2012**, 5, 68–77.

38. Serykh, A. I. On the formation of surface gallium hydride species in supported gallium catalysts. *Applied Surface Science*. **2012**, 259, 252–255.

39. Kazansky, V. B.; Pidko, E. A. Intensities of IR Stretching Bands as a Criterion of Polarization and Initial Chemical Activation of Adsorbed Molecules in Acid Catalysis. Ethane Adsorption and Dehydrogenation by Zinc Ions in ZnZSM-5 Zeolite. *J. Phys. Chem. B.* **2005**, 109, 2103–2108.

40. Comas-Vives, A. Amorphous SiO2 surface models: energetics of the dehydroxylation process, strain, ab initio atomistic thermodynamics and IR spectroscopic signatures. *Phys. Chem. Chem. Phys.* **2016**, 18, 7475–7482.

5. METATHESIS ON SILICA-SUPPORTED GA^{3+} AND ZN^{2+} SINGLE SITE CATALYSTS

5.1 Introduction

Olefin metathesis provides an alternative, more selective, route to thermal cracking for converting ethylene to propylene, which is necessary for meeting the high demand for polypropylene and propylene oxide to produce chemicals and consumer products.[1–3] There are three types of olefin metathesis including 1) cross metathesis, or the exchange of double bonds in linear olefins, 2) ring opening metathesis, or opening a closed olefin followed by polymerization, and 3) ring closing metathesis, which is the opposite of ring opening metathesis.[4] In each instance, C=C bonds are interconverted, and the original feed olefin is disproportionated to a longer and shorter chain olefin. This versatility leads to several industrial applications important for petrochemicals, polymers, and specialty chemicals.[4–7]

One of the first catalyzed metathesis reactions was observed in the 1950's by researchers at Du Pont, when ethylene and butene were formed from propylene over $Mo(CO)_6/Al_2O_3$.[8] Independently, Natta discovered ring opening metathesis when cyclopentene polymerization was performed with a $MoCl_5$ catalyst. Eventually, supported WO_x was utilized by Phillip's Petroleum in the first large-scale industrial metathesis process called Phillips Triolefin Process, which converted propylene to ethylene and butene. Later, BP used Re_2O_7/Al_2O_3 and Shell used MoO_x/Al_2O_3 for the disproportionation of short and long chain olefins.[9]

Early metathesis catalysts were poorly defined multicomponent heterogeneous and homogeneous systems. To address this, subsequent catalyst development of carefully prepared, single component homogeneous, organometallic complexes, provided the fundamental insight that metal carbene complexes were required to facilitate metathesis. Analogous, well-defined heterogeneous catalysts including W, Mo, and Re organometallic centers were developed to yield high catalytic activity.

While the nature of active site for these heterogeneous catalysts has not yet been defined, it is best understood that metathesis initiation occurs on a metal alkylidene species coordinated to a metal center. This is followed by a shift of the coordinated olefin to form a metallocyclobutane intermediate, and a subsequent shift of the newly coordinated olefin in the perpendicular direction to the initial olefin shift. The new olefin contains a carbene from the catalyst and another carbene

from the starting olefin, which can reenter the catalytic cycle.[8,10] Due to the high stability of the metal alkylidene intermediate, homogeneous catalysts are used with co-catalysts to pre-form the intermediate prior to reaction. The alkylidene is not typically known to readily form under reaction conditions, leading to low reaction rates.[11]

This work investigates the unique formation of propylene during ethylene oligomerization at high temperature on four coordinate Ga/SiO_2 (Ga^{3+}) and Zn/SiO_2 (Zn^{2+}) single site catalysts. This reactivity was attributed to olefin metathesis, and can be performed in the reverse, *i.e.* when propylene is fed it produces ethylene and butylene. However, metathesis chemistry is unprecedented on metal centers that do not contain unpaired d electrons, such as Zn^{2+} and Ga^{3+}. This reactivity is best understood as sigma bond metathesis using the p-orbitals of these main group metal ions.

5.2 Materials and Methods

5.2.1 Catalyst Preparation

Single site Ga^{3+}/SiO_2 and Zn^{2+}/SiO_2 catalysts were prepared following the procedures previously reported in literature, using standard catalyst synthesis techniques resulting in a 2.6 wt% and 4.0 w% catalyst respectively.[12,13]

Ga/SiO_2 was synthesized with a chelating agent to prevent the formation of Ga_2O_3 using pH-controlled incipient wetness impregnation (IWI). 10 g of Davisil silica with grade 636 (pore size = 60 Å, surface area = 480 m^2/g) was impregnated with an aqueous solution containing 1.5 g of gallium nitrate solution ($Ga(NO_3)_3$ xH_2O, Fluka chemical) and 1.5 g of citric acid (Sigma Aldrich) dissolved in Millipore water. The catalyst was dried for 16 hours at 125°C and then calcined at 500°C for 3 hours. Atomic absorption spectroscopy (AAS) was used to determine that the final catalyst contained approximately 2.6 wt% Ga.

Zn/SiO_2 was synthesized using pH-controlled strong electrostatic adsorption (SEA). A solution containing 2.5 g of zinc nitrate hexahydrate ($Zn(NO_3)_2$ $6H_2O$, Sigma Aldrich) was made and the pH was adjusted to 11 using 30% ammonium hydroxide (NH_4OH) solution, until a clear solution was obtained. 10 g of Davisil silica was suspended 100 mL of Millipore water in a separate beaker and the pH was adjusted to 11 using NH_4OH. The Zn solution was added rapidly to the SiO_2 solution and stirred for 20 minutes. After the solid was settled, the solution was decanted,

and the resulting slurry was washed with Millipore water and collected by vacuum filtration. The catalyst was dried for 16 hours at 125°C and then calcined at 300°C for 3 hours. AAS was used to determine that the final catalyst contained approximately 4.0 wt% Zn.

5.2.2   *In Situ* X-Ray Absorption Spectroscopy (XAS)

In-situ XAS was performed at the 10-BM sector at the Advanced Photon Source at Argonne National Laboratory. All measurements were performed at the Zn K (9.659 keV) or Ga K (10.3670 keV) edge in transmission mode in fast scan from 250 eV below the edge to 800 eV above the edge. Samples were pressed into a stainless-steel sample holder and placed in a sample cell. To identify the initial catalyst structure, Ga/SiO_2 and Zn/SiO_2 were dehydrated at 550°C in He, cooled to room temperature and scanned. The data was processed using the WinXAS v.3.2 software[14] to find the coordination number and bond distance using standard procedures. Feff6 calculations were performed using Ga_2O_3 (50% at CN=4, R=1.83 Å and 50% CN=6 at 2.00 Å), ZnO (CN=4, R=1.98 Å), and NiO (CN=6, R=2.09 Å) respectively for reference. A least squared fit for the first shell of r-space and isolated q-space were performed on the k^2 weighted Fourier transform data over the range of 2.7 to 10 Å^{-1} in each spectrum to fit the magnitude and imaginary components.

5.2.3   Catalyst Evaluation

Catalyst performance tests were performed in a fixed bed reactor with a quartz reactor tube of 1/8-inch outer diameter. The catalyst was treated in 50 ccm N_2 while ramping to reaction temperature until the temperature was stabilized. Olefin reactions were performed in 100% C_2H_4 at 450°C and atmospheric pressure on 1 g of catalyst using GHSVs ranging from 0.08 s^{-1} to 0.38 s^{-1}. Additional olefin reactions were performed in 100% C_3H_6 at 250, 350, and 450°C and atmospheric pressure on 1 g of catalyst using GHSVs ranging from 0.02 s^{-1} to 0.24 s^{-1}. All products were analyzed with a Hewlett Packard (HP) 6890 Series gas chromatograph (GC) using a flame ionization detector (FID) with an Agilent HP-Al/S column (25 m in length, 0.32 mm inner diameter, and 8 µm film thickness).

5.3   Results

5.3.1   Initial Catalyst Structure

The pre-reaction catalyst was determined by x-ray absorption spectroscopy (XAS) on Ga/SiO$_2$ and Zn/SiO$_2$. The catalysts were dehydrated at 550°C in He and compared to known references at each metal edge (Figure 5.1). The EXAFS fits are given in Table 5.1.
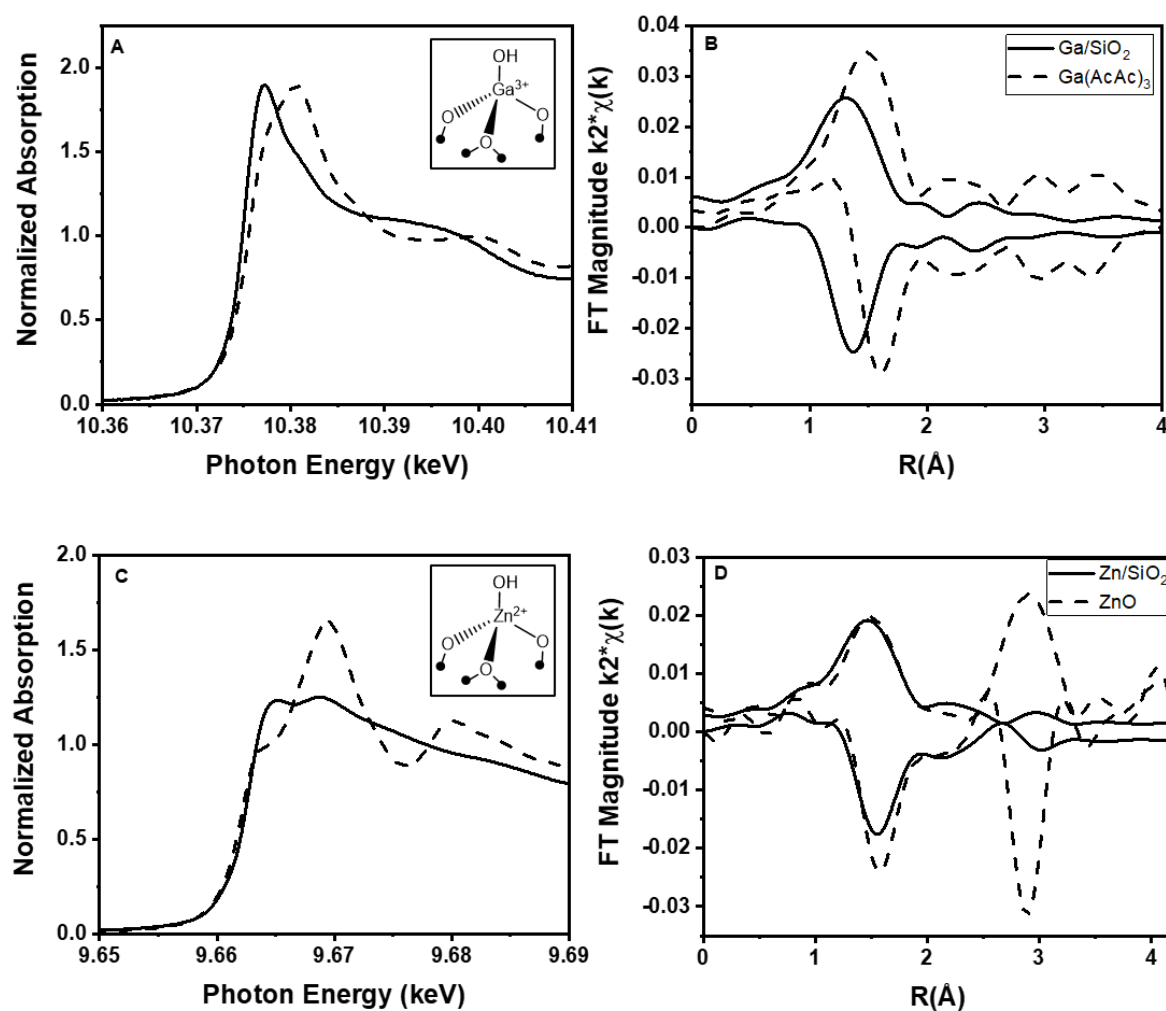
Figure 5.1. XAS of dehydrated catalyst structures for Ga/SiO$_2$ (A-B), and Zn/SiO$_2$ (C-D) compared to the bulk oxides of each metal

Table 5.1. EXAFS fits of the as-prepared structures of Ga/SiO$_2$, and Zn/SiO$_2$ after dehydration at 550°C in He

Sample	XANES Energy (keV)	Scattering Path	CN	R (Å)	$\Delta\sigma^2$ (Å^2)	ΔE_o (eV)	
Ga$_2$O$_3$	10.3751	Ga-O	3.0	2.00	-	-	Ga^{3+} (Td+Oh)
			2.0	1.83	-	-	
Ga(AcAc)$_3$	10.3793	Ga-O	6.0	1.93	-	-	Ga^{3+} (Oh)
Ga/SiO$_2$	10.3751	Ga-O	4.0	1.81	0.006	-2.2	Ga^{3+} (Td)
ZnO	9.6625	Zn-O	4.0	1.98	-	-	Zn^{2+} (Td)
Zn/SiO$_2$	9.6628	Zn-O	4.0	1.95	0.006	-0.6	Zn^{2+} (Td)

*Ga$_2$O$_3$, Ga(AcAc)$_3$, and ZnO are references of known structures

The XANES were used to determine the oxidation state while the EXAFS were used to identify the initial coordination geometry of each catalyst. Ga/SiO$_2$ was compared to Ga$_2$O$_3$, a 50/50 mixture of tetrahedral (Td) and octahedral (Oh) Ga and Oh Ga acetylacetonate (Ga(AcAc)$_3$). Although both references have the same oxidation state, the position of their XANES energies shifts slightly with different geometry. The XANES energy of Td Ga^{3+} (10.3745 keV) is lower than that of Oh Ga^{3+} (10.3793 keV). The XANES energy (10.3751 keV) of Ga/SiO$_2$ is consistent with Td Ga^{3+}. The EXAFS fit reveals that the initial structure of Ga/SiO$_2$ contains 4 Ga-O bonds at 1.81 Å (Table 5.1). The absence of Ga-O-Ga bonds also suggests a single site structure, which is defined as an isolated Ga^{3+} bound to the support.

Similarly, the XANES energy of Zn/SiO$_2$ (9.6628 keV) is like that of ZnO (9.6625 keV), consistent with the Zn^{2+} oxidation state. The EXAFS fit reveals that the structure of Zn/SiO$_2$ contains 4-Zn-O bonds at 1.95 Å (Table 5.1) and lacks Zn-O-Zn bonds. This indicates a single site Zn initial catalyst.

Single site Ga/SiO$_2$ and Zn/SiO$_2$ were obtained with 3+ and 2+ oxidation states respectively. Both catalysts lack second shell metal scattering, indicating that they are isolated ions with 4 metal-oxygen bonds to the support.

5.3.2 Catalyst Reactivity

The same 4-coordinate, tetrahedral, single site catalysts were recently reported to perform ethylene and propylene oligomerization at mild reaction temperatures (250°C) and a range of pressures (1 atm, 30.6 atm). This reactivity was previously attributed to the ability of the single

site catalyst to heterolytically dissociate C-H bond, leading to the formation of a metal alkyl. Higher reaction temperatures lead to increased C-H bond dissociation, which should lead to higher oligomerization rates. Therefore, ethylene oligomerization was performed at 450°C and conversions up to 8% were obtained, which is about twice as high as the conversion achieved at 250°C. The reaction rates of the former were also two orders of magnitude higher than the latter. Oligomerization products containing a maximum of ten carbons were obtained (Table 5.2). In addition, interesting products including methane, ethane, and propylene were also observed due to the increased rate of side reactions occurring at elevated temperature.

Table 5.2. Product selectivity at varying conversions for each catalyst during ethylene oligomerization at 450°C and 1 atm

Catalyst	Conversion (%)*	Selectivity (%)							TOR s^{-1} (x 10^{-2})
		Methane (CH$_4$)	Ethane (C$_2$H$_6$)	Propylene (C$_3$=)	Butenes (C$_4$=)	Hexenes (C$_6$=)	Octenes (C$_8$=)	Decenes (C$_{10}$=)	
Ga/SiO$_2$	3	0.9	22.0	3.7	59.3	10.2	2.5	1.4	3
	5	1.0	26.3	5.2	48.8	11.0	5.8	1.8	2
	8	1.5	32.6	5.9	43.4	10.9	4.0	1.8	2
Zn/SiO$_2$	3	2.5	35.8	1.1	46.5	12.1	1.2	0.8	0.2
	5	3.4	24.2	0.9	46.5	19.7	4.0	1.8	0.2
	7	4.6	21.8	1.2	43.5	23.5	2.7	2.7	0.2

* Conversion was varied using different space velocities over 1g of catalyst in a 3/8 in diameter quartz reactor tube

On Ga/SiO$_2$, at 5% conversion of ethylene, the selectivity towards butenes (C$_4$$^=$) and hexenes (C$_6$$^=$) were 49% and 11% respectively. There was also a 6% and 2% selectivity towards octenes (C$_8$$^=$) and decenes (C$_{10}$$^=$). Unique side products formed under these conditions, indicating secondary reactions occur at higher temperatures. A notable selectivity towards methane (1%), ethane (26%), and propylene (5%) was also observed. Other odd carbon number olefins (pentenes and heptenes) were also formed but could not be distinguished from C$_6$$^=$ and C$_8$$^=$ respectively. However, these reaction products were not observed in previous studies where oligomerization was reacted at 250°C. Similar product distributions were also observed on Zn/SiO$_2$ at 5% conversion. While the selectivity towards typical oligomerization products including C$_4$$^=$ (47%), C$_6$$^=$ (20%), C$_8$$^=$ (4%), and C$_{10}$$^=$ (2%) are very similar, Zn/SiO$_2$ tended to product more methane (4%) and less propylene (1%).

The oligomerization activity on Ga/SiO$_2$ and Zn/SiO$_2$ is unprecedented. Our previous research supports that the onset of oligomerization occurs at temperatures as low as 250°C. Evidence of relevant reaction intermediates suggests that higher temperatures lead to increased C-H bond dissociation leading to higher reaction rates. If only ethylene oligomerization occurred, only even carbon numbered products would be observed. In addition, previous IR studies demonstrate that when exposed to H$_2$, SiO$_2$-supported single sites do not generate Bronsted sites, even at elevated temperatures up to 550°C. Consistent with the lack of acidity on the SiO$_2$ support, no branched hydrocarbons (*e.g.* isobutene) were observed. Therefore, ethylene oligomerization on nonacidic, silica supported catalysts is not expected to result in products containing odd carbon numbers, such as propylene, because cracking (C$_8$$^=$ → iC$_4$$^=$ or C$_3$$^=$ + iC$_5$$^=$) is not anticipated in the absence of H$^+$ sites. The formation of odd carbon number products is likely be due to a secondary reaction. It may be possible that propylene is formed by hydrogenolysis of butene (H$_2$ + C$_4$H$_8$ → CH$_4$ + C$_3$H$_6$), however only a small amount of methane is produced. Methane and propylene are not produced in a 1:1 molar ratio. To understand the production of propylene, the molar dependence of C$_3$$^=$ on C$_4$$^=$ and C$_6$$^=$ were compared (Figure 5.2).
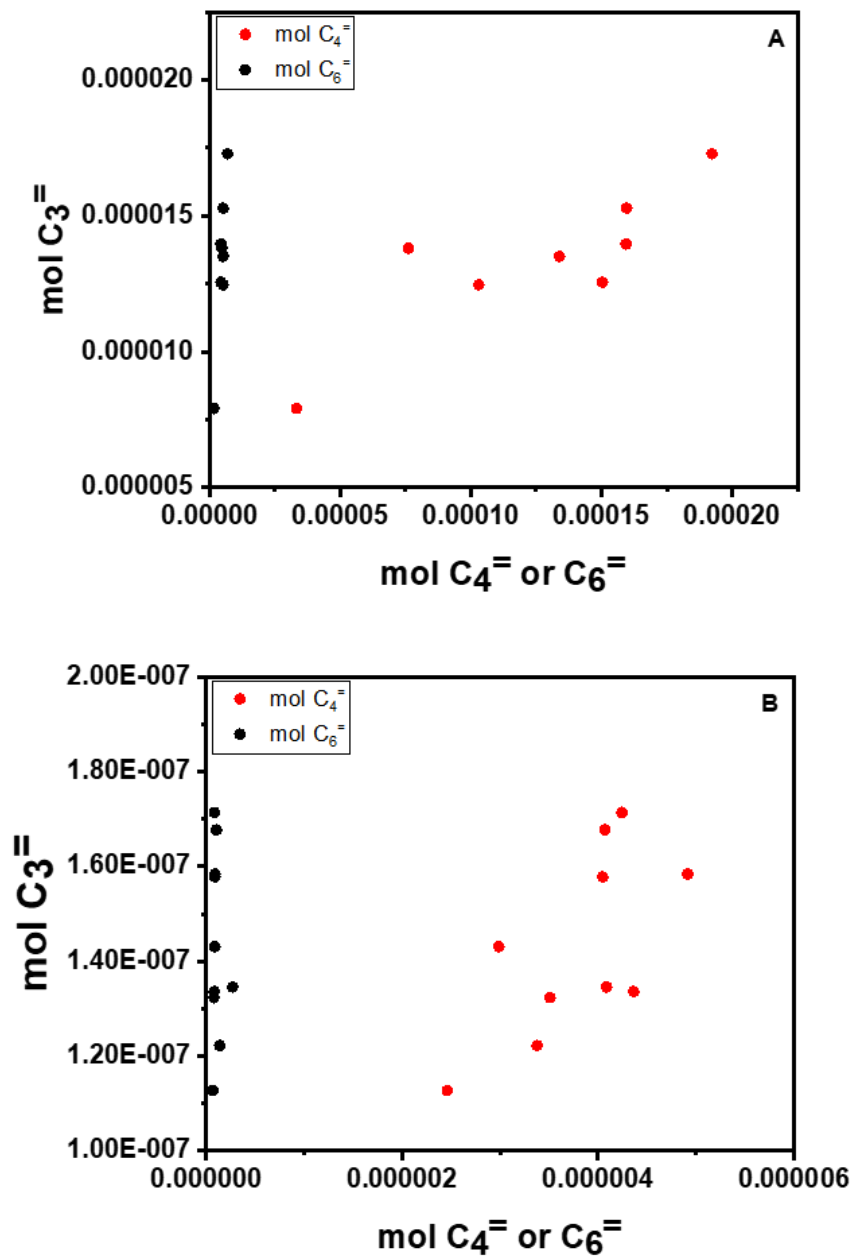
Figure 5.2. Molar dependence of the production of propylene on butenes and hexenes for A) Ga/SiO$_2$ and B) Zn/SiO$_2$

On both Ga/SiO_2 and Zn/SiO_2, a linear dependence on $C_4^=$ was observed while the amount of propylene produced was not related to the production of $C_6^=$. In other words, as the amount of $C_4^=$ increased, so did the amount of $C_3^=$. $C_3^=$ formation is seemingly not due to the presence of $C_6^=$. This suggests that the formation of $C_3^=$ relies on the concentration of $C_4^=$ and could be due to olefin metathesis, as the bond disproportionation between $C_2^=$ and $C_4^=$ can occur resulting in the formation of two $C_3^=$. To investigate this, propylene was used as a reactant at a range of temperatures to observe trends in the product distribution. Activation of propylene occurs at lower temperatures than ethylene. Higher temperature leads to higher conversion and increased contribution from secondary reactions. Propylene conversions up to 8% at 250°C and 12% at 350°C and 450°C were obtained with product distributions shown in Table 5.3.

Table 5.3. Product selectivity at varying conversions for each catalyst during propylene oligomerization at 250°C, 350°C, and 450°C, each at 1 atm

Catalyst	Conversion (%)*	Selectivity (%)							TOR s^{-1}
		Methane (CH$_4$)	Ethylene (C$_2^=$)	Propane (C$_3$H$_8$)	Butenes (C$_4^=$)	Hexenes (C$_6^=$)	Nonenes (C$_9^=$)	Dodecenes (C$_{12}^=$)	
					T=250°C				
Ga/SiO$_2$	1	0.1	5.5	3.9	6.3	8.9	75.1	0.2	9 x 10^{-4}
	3	0.1	5.9	6.3	6.7	7.8	71.9	1.3	12 x 10^{-4}
	5	0.2	7.4	5.3	7.4	16.1	52.3	11.3	9 x 10^{-4}
	8	0.2	10.4	7.7	8.9	23.5	43.4	5.9	14 x 10^{-4}
Zn/SiO$_2$	1	0	3.8	9.2	3.2	50.5	28.1	5.2	8 x 10^{-4}
	3	0	2	6.1	1.3	52.2	29.6	8.8	7 x 10^{-4}
	5	0	5.9	8.9	5.4	36.7	30.8	12.3	4 x 10^{-4}
	8	0	6.2	6.2	6.6	41.4	30	9.6	4 x 10^{-4}
					T=350°C				
Ga/SiO$_2$	2	1.2	12.4	4.4	12.5	6.6	61.8	1.1	4 x 10^{-4}
	5	1.4	13	3.8	15	10.1	54.2	2.5	3 x 10^{-4}
	10	2.6	19.6	3.2	22.7	14.9	35.9	1.1	4 x 10^{-4}
	12	2.9	19.2	5.8	25.4	14.7	31	1	2 x 10^{-4}
Zn/SiO$_2$	2	4.5	25.5	6	21	13	30	0	1 x 10^{-4}
	5	1.2	26	6	26.1	13	20.2	7.5	6 x 10^{-5}
	10	0.8	23.7	4.6	24.6	15.6	23.6	7.1	1 x 10^{-4}
	12	1.2	17	4.9	16.7	29.1	22.2	8.9	8 x 10^{-5}
					T=450°C				
Ga/SiO$_2$	2	6.3	23.4	17.9	19.4	5.2	26.7	1.1	3 x 10^{-3}
	5	5.8	22.6	18.5	21.2	5.5	25.6	0.8	2 x 10^{-3}
	10	8.6	21	25.3	17.7	7.3	15.2	4.9	6 x 10^{-4}
	15	8.7	20.7	30.3	19.3	8.9	11.3	0.8	2 x 10^{-3}
Zn/SiO$_2$	2	7.4	19.7	29.7	19.4	12	11.8	0	3 x 10^{-3}
	5	8.4	21	24.1	18.7	22.6	5.2	0	2 x 10^{-3}
	10	13.5	14.9	27.9	17.1	23.5	3.1	0	1 x 10^{-3}
	15	7.2	16.7	25	16.6	27.1	7.4	0	2 x 10^{-3}

* Conversion was varied using different space velocities over 1g of catalyst in a 3/8 in diameter quartz reactor tube

At 250°C, Ga/SiO$_2$ at 5% conversion of propylene had about 16% selectivity towards C$_6^=$, the primary oligomerization product. Ethylene (7%), propane (5%), and C$_4^=$ (7%), and methane was observed in trace amounts. At 350°C, the selectivity towards C$_6^=$ increased to 15%, and higher molecular weight products were formed on Ga/SiO$_2$. The selectivity towards methane (2%), ethylene (13%), propane (4%), and C$_4^=$ (15%) all increased. The rate increased by an order of magnitude when the reaction temperature increased from 250°C to 350°C. While the rate remained constant with an additional increase in reaction temperature from 350°C to 450°C, the product distributions followed similar trends, with a higher selectivity to unique products. The selectivity towards C$_6^=$ decreased slightly to 6% and the selectivity towards methane (6%), ethylene (22%), propane (19%), and C$_4^=$ (21%) all increased.

Under the same conditions, Zn/SiO$_2$ had very similar product distributions to Ga/SiO$_2$. For instance, at 250°C and 5% propylene conversion, there was 36% selectivity towards C$_6^=$ and 6%, 9%, and 5% selectivity towards ethylene, propane, and C$_4^=$ respectively. These selectivities followed similar trends with increasing reaction temperature similarly to that on Ga/SiO$_2$.

On both catalysts, methane, ethylene, propane, and C$_4^=$ are not expected during propylene oligomerization, but are consistent with the unexpected products observed during ethylene oligomerization. While C$_3^=$ was formed directly from ethylene, C$_2^=$ and C$_4^=$ are formed directly from propylene. This suggests that two competing reactions, ascribed to oligomerization and metathesis, occur as the temperature increases. The results suggest that higher reaction temperatures lead to an increased metathesis rate, due to the increased selectivity to the C$_3^=$ from ethylene and C$_2^=$ and C$_4^=$ from propylene. Therefore, to explore these relative rates, the ratio of product selectivity (S$_{product}$) during propylene reactions were explored as a function of temperature (Figure 5.3). Here, S$_{C2=}$+S$_{C4=}$ corresponds to the rate of metathesis while S$_{C6=}$ corresponds to that of oligomerization.
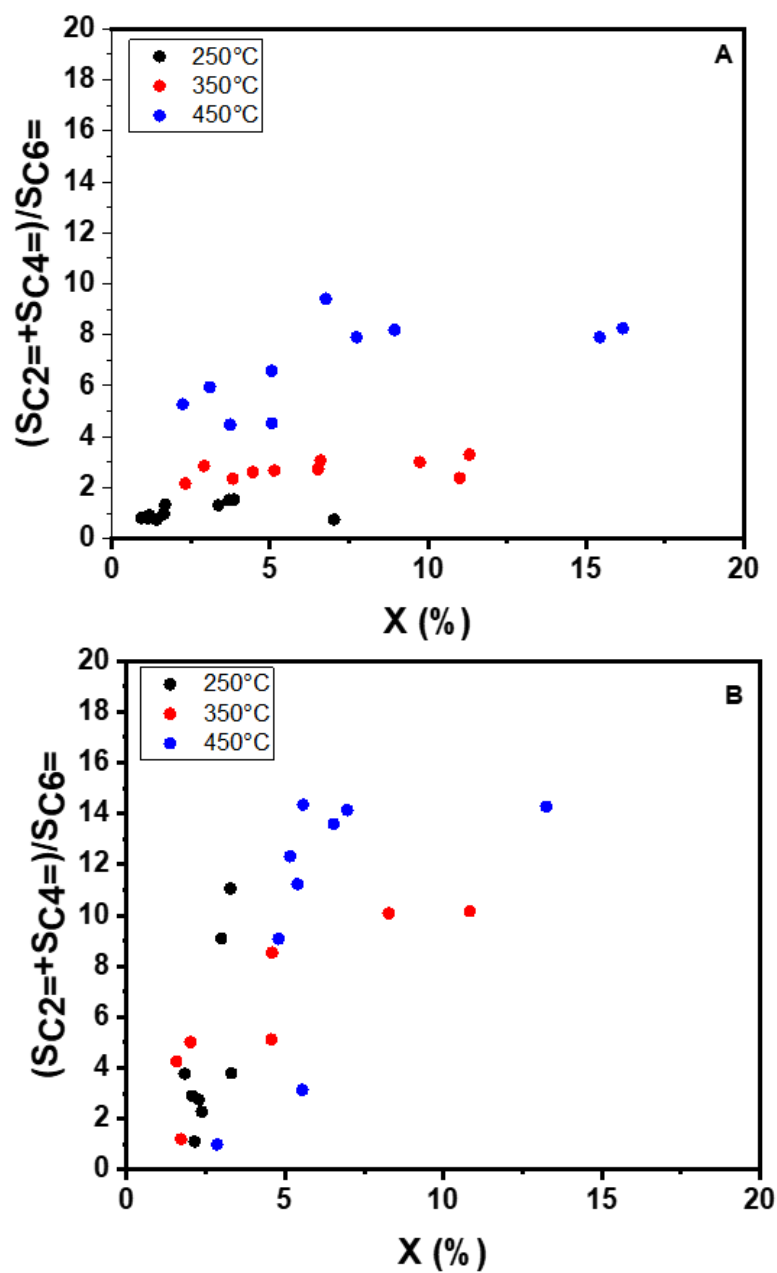
Figure 5.3. Ratio of propylene oligomerization (S $C_6^=$) to propylene metathesis (S $C_2^= $ + S $C_4^=$) as a function of conversion for reaction temperatures at 250°C (black), 350°C (red), and 450°C (blue) for A) Ga/SiO$_2$ and B) Zn/SiO$_2$

On Ga/SiO$_2$, (SC$_2^=$ + SC$_4^=$)/SC$_6^=$ increases with temperature. While there is little difference to the ratio of products observed at 250°C and 350°C, the ratio increases by nearly five times at 450°C. This means that at 450°C, the formation of C$_6^=$ is less favored and forming ethylene and C$_4^=$ is more likely, suggesting that metathesis on these catalysts is favored at high reaction temperature and that metathesis likely has a higher activation energy than oligomerization. On Zn/SiO$_2$, no clear trends with increasing reaction temperature were observed.

5.4   Discussion

This work suggests that multiple reaction pathways are possible on Ga/SiO$_2$ and Zn/SiO$_2$ catalysts, especially at reaction temperatures higher than 350°C. It was previously demonstrated that these same catalysts perform ethylene oligomerization with moderate turnover rates at 250°C. It was proposed that this reactivity was initiated by the activation of C-H bonds leading to the formation of a vinylic intermediate. β-H elimination of the vinyl group resulted in the formation of butadiene and a metal hydride. Once the metal hydride was formed, it was able to facilitate olefin oligomerization. However, higher reaction temperature in ethylene reveals that secondary reactions occur leading to the formation of propylene. This is proposed to be due to olefin metathesis, which is unexpected on metals containing full d electron orbitals, such as Ga^{3+} and Zn^{2+}. Typically, metathesis catalysts have unpaired d electrons, such as W, Mo, and Re, to facilitate the formation of an alkylidene (M=R) intermediate.

For metals like Ga and Zn this would require the chemical reactivity of the empty 4p electron orbitals.[15,16] Here, we propose that this is possible at high reaction temperatures (450°C) and propose a reaction pathway is shown in Figure 5.4, demonstrating the elementary steps proposed to lead to each product (methane, ethane, propylene, and butenes) observed.

149
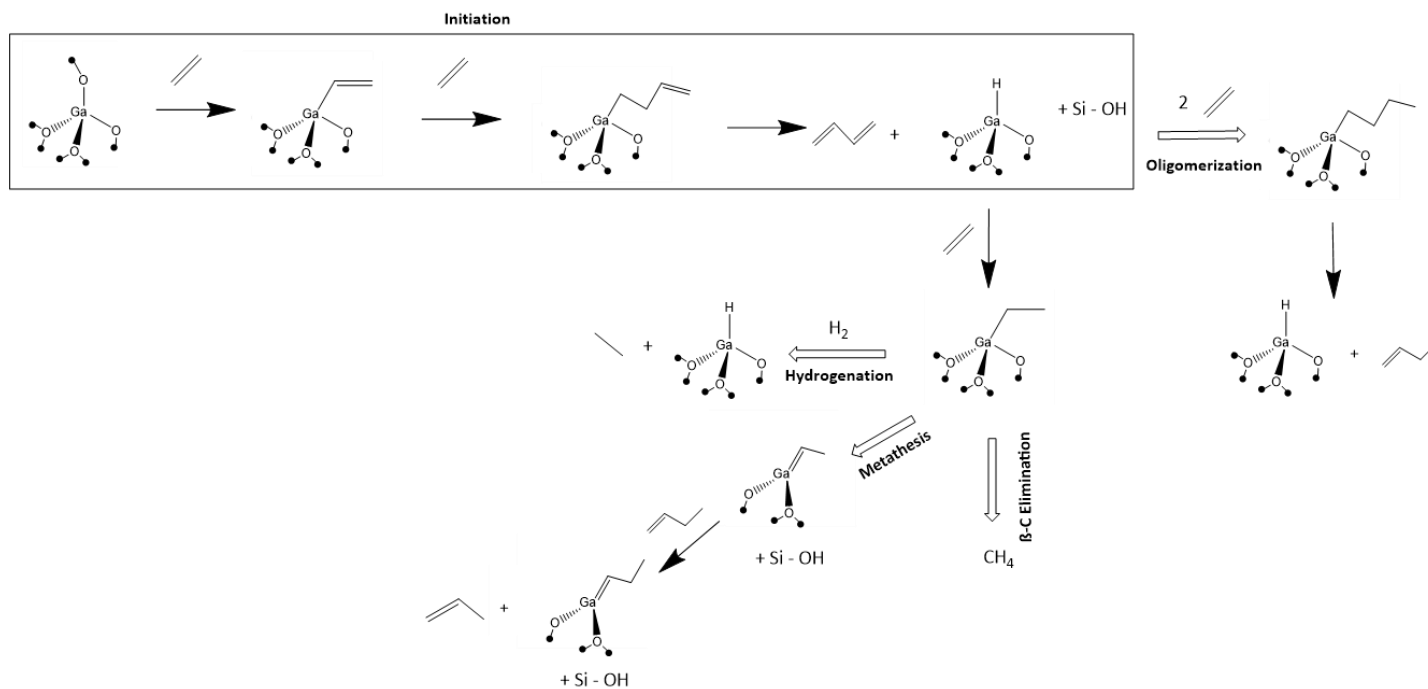
Figure 5.4. Reaction pathway for Ga/SiO$_2$ and Zn/SiO$_2$ at 350°C in the presence of ethylene, although similar reaction scheme can be drawn for propylene feed

The initiation of the initial four coordinate structure occurs by activation of a C-H bond, forming a vinylic intermediate. β-H elimination releases butadiene and forms a metal hydride. Although butadiene was not observed experimentally, it is commonly proposed to be produced during the initiation of oligomerization catalysts.[17] The metal hydride can facilitate oligomerization, which has been shown at temperatures as low as 250°C. When two or more olefins are insert to the metal hydride, longer chain olefins form and are desorbed during termination by β-H elimination. This restores the metal hydride and restarts the catalytic cycle. Alternatively, after initiation, an olefin can activate a C-H bond to form a metal alkyl intermediate, which can undergo three subsequent reaction pathways. First, the activated catalyst can react with H_2, likely arising from the presence of unsaturated products like butadiene, to produce a paraffin by hydrogenation. Hydrogenation has been previously reported on Ga/SiO_2 and Zn/SiO_2 at temperatures as low as 200°C.[12,13] If an olefin reacts instead, an alkylidene intermediate may be formed and can facilitate olefin disproportionation, or metathesis, resulting in the formation of propylene from ethylene and the reverse. Because this intermediate is generated *in situ*, higher reaction temperatures are needed for this pathway to be favorable. Finally, β-C elimination of the vinylic intermediate will lead to the production of small amounts of methane.

While the β-H elimination, olefin insertion, and C-H bond activation elementary steps have been demonstrated on Ga/SiO_2 and Zn/SiO_2, metathesis is unexpected on main group metals.[12,18,19] In fact, metathesis catalysts are usually designed to have a targeted alkylidene ligand to facilitate double bond disproportionation with an olefin.[8,10] Few instances of a alkylidene intermediate being generated *in situ* by α-H elimination have been reported in literature.[20–22] The metal sites in these catalysts are coordinated to various ligands which help facilitate alkylidene formation. In addition, a four-coordinate, zeolite-supported Ni^{2+} catalyst reported propylene formation during ethylene oligomerization, the activity was attributed to the Bronsted acid (H^+) sites of the support.[2] While this is possible in the presence of Bronsted acid sites, the SiO_2 support used in this study is non-acidic and not reactive under these conditions. This implies that all products observed are due to the reactivity of the metal.

As we have previously shown, the shape of the XANES change for both Ga/SiO_2 and Zn/SiO_2 at high temperature in high concentrations of H_2 or ethylene at high treatment temperatures. This was interpreted as the reversible formation of a metal hydride, which can then undergo subsequent alkylation, and concludes that a change in oxidation state is not observed. This means that Ga^{3+}

and Zn^{2+} remain in the +3 and +2 oxidation state respectively, even at temperatures up to 550°C in pure H_2. Many extensive studies on the Ga K edge XANES of various Ga organometallics help eliminate the possibility of a redox cycle occurring between Ga^{3+} and Ga^{1+}.[19,23] Moreover, these changes can better be ascribed to the interaction of the 4s and 4p electrons of Ga with H_2 or ethylene, therefore leading to changes in unfilled 4p states. Propylene production from an ethylene feed was observed on Ga/SiO_2 at temperatures greater than 300°C and is most notable at 450°C. Higher temperatures lead to a slightly increased selectivity towards propylene. Under these conditions, a shoulder is observed in the pre-edge region of the Ga edge XANES, due to the metal-oxygen bond being replaced by a less electronegative element, for example to form a metal-hydrogen or metal-carbon bond, leading to an increased electron density on Ga. This leads to an increase in the 1s orbital energy and decrease in the π^* character of the 4p electrons.

Similar, though less obvious, changes were also observed in the Zn edge XANES and were attributed to the formation of a Zn-hydride. Like Ga, the Zn edge XANES represents a 1s to 4p electron transition. Therefore, the changes observed on Zn/SiO_2 are analogous to those observed on Ga/SiO_2 and are consistent with the formation of the same products, though at a slightly different distribution. A redox reaction is also not possible on Zn^{2+}, as a stable, nonmetallic, lower oxidation state is not available.

To help support our argument that Ga/SiO_2 and Zn/SiO_2 can undergo metathesis, a propylene feed was used to demonstrate that it produces ethylene and $C_4^=$. While both products were observed at reaction temperatures as low as 250°C, reaction temperatures around 450°C led to their formation in about a 1:1 ratio, with an increased rate. If metathesis is truly responsible for this reactivity, an alkylidene intermediate must be formed *in situ*. The increasing ratio of ethylene to $C_4^=$ with reaction temperature suggests that the surface coverage of the active intermediate increases with temperature.

While few instances of molecular compounds containing Ga or Zn methylidene have been reported in literature, these materials are not generally known to exist without being directly synthesized.[24,25] One report on GaAs(100) semiconductors shows that it facilitated the *in situ* formation of Ga methylamine which led to the formation of higher olefins.[26] Later, this was shown to be due to multiple C-H bond activations, which can occur in the presence of solvents and at ambient temperature.[25] Here, a gas phase reaction is performed and high temperatures are required

to observe such metathesis products, which suggests that the alkylidene is formed in large enough concentrations to facilitate metathesis under those conditions.

The alkylidene is typically a stable ligand on high oxidation state metal centers with unpaired d electrons and the resulting M=C bond is polarized such that the alpha carbon bears a partial negative charge. Such complexes are usually electron deficient or contain π donating ligands.[27,28] Conversely, Ga^{3+} and Zn^{2+} have no unpaired d electrons, which suggests that unpaired p electrons allow for the correct orbital overlap and symmetry with the p electrons in the C of ethylene facilitate this chemistry *in situ* (Figure 5.5).[29,30]

There are two types of alkylidenes.[31,32] For the Fischer alkylidene, there are a pair of electrons in the sp2 orbital of the carbon atom, which donates to one empty d orbital of the metal. In the meantime, a pair of d electrons from the metal back donate to the unfilled p orbital of the C atom, forming a M=C double bond. Here, the carbon tends to be positively charged. For the Schrock type alkylidene, on the carbon atom there is one electron in the p orbital, and one electron in the sp3 orbital. The metal also has two electrons, with one in each d orbital. The interaction between these electrons forms a M=C double bond. Two covalent bonds are formed, each polarized towards the carbon, giving it a negative charge. Neither case contains two electrons in a p orbital.

We believe on Ga/SiO_2 or Zn/SiO_2, the O atom in $O-Ga-CH_2-CH_3$ takes one proton from the α-C atom. That leaves the α-carbon atoms two electrons in the p orbital. When the O atom takes the proton, the Ga-O bond also breaks, and the two electrons in the Ga-O bond go with the O atom, leaving Ga with one empty orbital. After those bonds break, both Ga and C change from sp3 hybridization to sp2. The Ga has an empty 4p orbital, and the C atoms has a filled 2p orbital. Those two orbitals will overlap and form a π bond. With the previous Ga-C sigma bond, this now forms a Ga=C double bond.
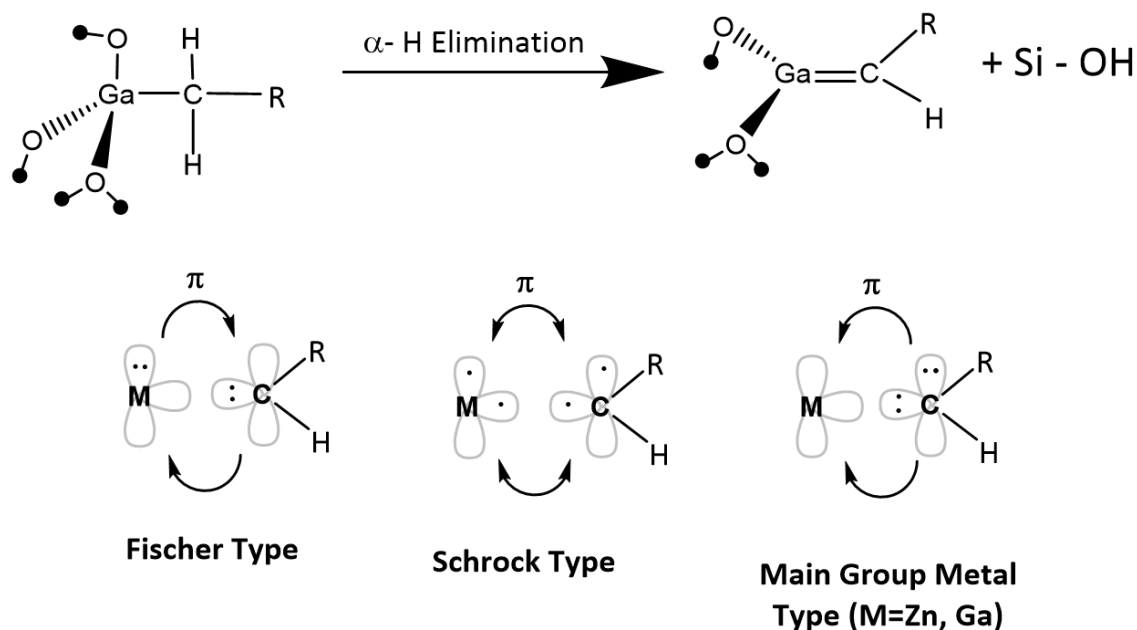
Figure 5.5. Activation of Ga-alkyl to form methylidene with corresponding orbital symmetry compared to traditional metathesis catalysts

It is proposed that the Ga or Zn alkylidene if formed by α-hydrogen abstraction, which was previously reported on d_0 early transition metal compounds to occur under a specific set of conditions.[20–22] This was related to the homolytic cleavage of a M-C bond. The α–hydrogen atom is activated when the metal attracts electron density from an alkyl C-H bond. While the unfilled 5d orbital of transition metals participates in M=C bond formation, it is thought that the presence of H_2 or olefins reduces the energy of the lowest unoccupied molecular orbital in Ga^{3+} and Zn^{2+}. This would make the orbital energy and symmetry align with that of the empty 4p orbitals of a carbenium species and allow for the formation of a M=C bond.

This would be one of the first reports of high temperature, *in situ* formation of an alkylidene complex to facilitate metathesis. However, neither direct spectroscopic observation of the *in situ* formation of an alkylidene complex nor classical, room temperature metathesis reaction data are available. As demonstrated through our work on ethylene oligomerization using the same catalysts, the reaction intermediates are not observed at room temperature. Instead, there is a thermal equilibrium which is favored at high temperatures. Therefore, although the catalysts are activated at high temperature, high concentrations of the active intermediate are not maintained after cooling to room temperature, even in a high concentration of H_2 or hydrocarbon.

5.5   Conclusion

High temperature olefin reactions on Ga/SiO_2 and Zn/SiO_2 have multiple reaction pathways. Among these, oligomerization occurs. This is significant because neither metal reduces to a metallic state, allowing for activity to maintained at temperatures higher than what is commercially performed. Interesting product selectivity which arises under high reaction temperatures suggests that metathesis occurs leading to the formation of propylene from ethylene and ethylene and $C_4^=$ from propylene. In an ethylene feed, propylene is observed at temperatures above 300°C. In propylene, ethylene and $C_4^=$ are formed at temperatures as low as 250°C and increase selectivity with reaction temperatures up to 450°C until a 1:1 ratio is achieved.

Ga^{3+} and Zn^{2+} have no unpaired d electrons, which makes this chemistry unprecedented. Metathesis requires the formation of an alkylidene intermediate, which was not observed directly under reaction conditions. However, the formation of this reaction intermediate is reasonable using the 4p electron orbitals of Ga^{3+} and Zn^{2+}, which are lower in energy and more available for bonding in the presence of H_2 and olefins. Consequently, the formation of this intermediate occurs under a specific set of reaction conditions and is seemingly favored at reaction temperatures greater than 300°C, where a higher selectivity towards metathesis products is observed.

5.6   Acknowledgements

5.7   References

1. Perea, L.A.; Wolff, T.; Hilfert, L.; Edelmann, F.T.; Hamel, C.; Seidel-Morgenstern, A. Alumino-mesostructured Ni catalysts for the direct conversion of ethene to propene. *Journal of Catalysis*. **2013**, 305, 154–168.

2. Iwamoto, M. One Step Formation of Propene from Ethene or Ethanol through Metathesis on Nickel Ion-loaded Silica. *Molecules*. **2011**, 16, 7844–7863.

3. Iwamoto, M. Conversion of Ethene to Propene on Nickel Ion-loaded Mesoporous Silica Prepared by the Template Ion Exchange Method. *Catal Surv Asia*. **2008**, 12, 28–37.

4. Rouhi, A.M. Olefin Metathesis: Big-Deal Reaction. *Chem. Eng.* **2002**, 80, 29–38.

5. Grubbs, R. H.; Tumas, W. Polymer synthesis and organotransition metal chemistry. *Science*. **1989**, 243, 907–915.

6. Banks, R.L.; Bailey, G.C. Olefin Disproportionation. A New Catalytic Process. *I&EC Product Research and Development*. **1964**, 3, 170–173.

7. Mol, J.C. Industrial applications of olefin metathesis. *Journal of Molecular Catalysis A: Chemical*. **2004**, 213, 39–45.

8. Astruc, D. The metathesis reactions: from a historical perspective to recent developments. *New Journal of Chemistry*. **2005**, 29, 42–56.

9. Lwin, S.; Wachs, I. E. Reaction Mechanism and Kinetics of Olefin Metathesis by Supported ReOx/Al2O3 Catalysts. *ACS Catal.* **2016**, 6, 272–278.

10. Fuerstner, A. *Alkene Metathesis in Organic Synthesis*. (Springer, 2003).

11. Adams, C.T.; Brandenberger, S.G. Mechanism of olefin disproportionation. *Journal of Catalysis*. **1969**, 13, 360–363.

12. Schweitzer, N. M.; Hu, B.; Das, U.; Kim, H.; Greeley, J.; Curtiss, L.A.; Stair, P.C.; Miller, J.T.; Hock, A.S. Propylene Hydrogenation and Propane Dehydrogenation by a Single-Site Zn2+ on Silica Catalyst. *ACS Catal.* **2014**, 4, 1091–1098.

13. Cybulskis, V. J.; Pradhan, S.U.; Lovon-Quintana, J.J.; Hock, A.S.; Hu, B.; Zhang, G.; Delgass, W.N.; Ribeiro, F.H.; Miller, J.T. The Nature of the Isolated Gallium Active Center for Propane Dehydrogenation on Ga/SiO2. *Catal Lett.***2017**, 147, 1252–1262.

14. Ressler, T. WinXAS: a Program for X-ray Absorption Spectroscopy Data Analysis under MS-Windows. *J. Synchrotron Rad.* **1998**, 5, 118–122.

15. Koch, D.; Chen, Y.; Golub, P.; Manzhos, S. Revisiting π backbonding: the influence of d orbitals on metal–CO bonds and ligand red shifts. *Phys. Chem. Chem. Phys.* **2019**, 21, 20814–20821.

16. Landis, C.R.; Weinhold, F. Valence and extra-valence orbitals in main group and transition metal bonding. *Journal of Computational Chemistry*. **2007**, 28, 198–203.

17. Brogaard, R. Y.; Olsbye, U. Ethene Oligomerization in Ni-Containing Zeolites: Theoretical Discrimination of Reaction Mechanisms. *ACS Catal.* **2016**, 6, 1205–1214.

18. Getsoian, A.B.; Das, U.; Camacho-Bunquin, J.; Zhang, G.; Gallagher, J.R.; Hu, B.; Cheah, S.; Schaidle, J.A.; Ruddy, D.A.; Hensley, J.E.; Krause, T.R.; Curtiss, L.A.; Miller, J.T.; Hock, A.S. Organometallic model complexes elucidate the active gallium species in alkane dehydrogenation catalysts based on ligand effects in Ga K-edge XANES. *Catalysis Science & Technology*. **2016**, 6, 6339–6353.

19. Fryzuk, M.D.; Mao, S.S.H.; Zaworotko, M.J.; MacGillivray, L.R. The first stable zirconium alkylidene complex formed via .alpha.-hydrogen abstraction: synthesis and x-ray crystal structure of [.eta.5-C5H3-1,3-(SiMe2CH2PPri2)2]Zr:CHPh(Cl). *J. Am. Chem. Soc.* **1993**, 115, 5336–5337.

20. Brammell, C.M.; Pelton, E.J.; Chen, C-H.; Yakovenko, A.A.; Weng, W.; Foxman, B.M; Ozerov, O.V. Hafnium alkyl complexes of the anionic PNP pincer ligand and possible alkylidene formation. *Journal of Organometallic Chemistry*. **2011**, 696, 4132–4137.

21. Wengrovius, J.H.; Schrock, R.R. Attempts to prepare alkylidene zirconium complexes by α-hydrogen atom abstraction. *Journal of Organometallic Chemistry*. **1981**, 205, 319–327.

22. Fleischman, S.D.; Scott, S.L. Evidence for the Pairwise Disposition of Grafting Sites on Highly Dehydroxylated Silicas via Their Reactions with Ga(CH3)3. *J. Am. Chem. Soc.* **2011**, 133, 4847–4855.

23. Bauer, H.; Orzechowski, L.; Escalona, A.; Jansen, G.; Harder, S. Synthesis and Structure of a Dimeric Iminophosphorane Stabilized Zinc Carbene: (ZnCR2)2. *Organometallics*. **2017**, 36, 4883–4890.

24. Machle-Mossmer, C.; Sirsch, P.; Anwander, R. Gallium Methylene. *Angewandte Chemie International Edition*. **2019**, 58.

25. Kemp, N.T.; Singh, N.K. Evidence of carbon–carbon bond formation on GaAs(100) via Fischer–Tropsch methylene insertion reaction mechanism. *Chem. Commun.* **2005**, 4348–4350.

26. Goodman, H.; Mei, L.; Gianetti, T.L. Molecular Orbital Insights of Transition Metal-Stabilized Carbocations. *Front. Chem.* **2019**, 7.

27. Thorn-Csányi, E.; Zilles, J.U. Structure/property relationship of Schrock-type alkylidene complexes based on tungsten and molybdenum. *Journal of Molecular Catalysis A: Chemical*. **2002**, 190, 85–100.

28. Hoffmann, R.; Woodward. Conservation of orbital symmetry. *Accounts of Chemical Research*. **1968**, 1, 17–22.

29. Mango, F.D. Molecular Orbital Symmetry Conservation in Transition Metal Catalysis. in *Advances in Catalysis* (eds. Eley, D. D., Pines, H. & Weisz, P. B.) vol. 20 291–325 (Academic Press, 1969).

30. Grela, K. *Olefin Metathesis: Theory and Practice*. (John Wiley & Sons, 2014).

31. Crabtree, R. H. *The Organometallic Chemistry of the Transition Metals*. (John Wiley & Sons, 2019).

6. HIGH TEMPERATURE OLEFIN OLIGOMERIZATION ON SINGLE SITE COBALT (II) CATALYSTS

6.1   Introduction

Oligomerization is used industrially to upgrade the light olefins produced from processes like steam cracking, dehydrogenation, and fluid catalyzed cracking to produce heavier, energy-dense olefins. While the catalytic oligomerization of ethylene to produce linear alpha olefins (LAO) is one of the most commercially successful processes, producing over 1 million tons annually, many oligomerization catalysts produce a wide distribution of products containing even carbon numbers up to C_{14}-C_{20}.[1–3] An increasing demand for LAO (1-butene and 1-hexene) has necessitated the development of catalysts to selectively oligomerize olefins to obtain controlled product distributions.

Commercial processes utilize Ni-based homogeneous catalysts, though they require chemical activators, which often inhibit regenerability and lead to thermal instability.[4–8] Consequently, in order to obtain a high selectivity for LAO, mild reaction temperatures ranging from 30°C-170°C and high pressures (up to 27 atm) are generally utilized.[9–11] Although these homogenous Ni^{2+} catalysts offer high oligomerization rates, the selectivity is often tailored to favor low molecular weight products.[7,12,13] Consequently, new oligomerization catalysts are being developed to replace the commercial Ni-based homogeneous catalysts, which have dominated industry for decades.

The design of heterogenous oligomerization catalysts has been centered around developing molecular complexes involving Group 4 to Group 10 transition metals including Ti, Fe, Co, Zr, and Hf, where the metal identity is thought to play a critical role in the reaction selectivity and catalyst lifetime. These catalysts are often synthesized with targeted alkyl and sterically bulky ligands to facilitate specific elementary steps leading to oligomerization. The specific catalyst structures are usually maintained by limiting the reaction conditions to those similar to commercial processes.[14–17]

However, our previous research suggests that heterogeneous, silica-supported single site catalysts containing an isolated ion on a support are ideal alternatives to facilitate oligomerization with tunable product selectivity and offer flexibility in reaction conditions. These catalysts initiate oligomerization by activating C-H and H-H bonds. This means that higher temperatures lead to increased oligomerization rates, which is not true for the molecular catalysts.

Here, we report that silica supported Co^{2+} single site catalysts (Co/SiO_2) are active for olefin oligomerization at temperatures higher than 350°C. Unlike Ni^{2+}, Co/SiO_2 is resistant to reduction, allowing it to maintain oligomerization activity at high reaction temperatures. Through this, we introduce the possibility of tandem catalysis to directly convert alkanes to longer chain olefins, which could improve the current oligomer production technology by providing better heat management and reducing process costs.

6.2   Materials and Methods

6.2.1   Catalyst Preparation

Single site Co/SiO_2 was prepared following standard catalyst synthesis procedures previously reported in literature, resulting in a 3.1 wt% catalyst.[18]

Strong electrostatic adsorption (SEA) technique was used to synthesize Co/SiO_2. First, 2.50 g of hexamine cobalt chloride ($Co(NH_3)_6Cl_3$ – Sigma-Aldrich) were dissolved in 25.0 mL of Millipore water in a 50.0 mL beaker while 10.0 g of SiO_2 (Davisil 636 silica gel, Sigma-Aldrich, 35-60 mesh, surface area = 480 m^2/g, pore volume = 0.75 cm^3/g) were suspended in 50.0 mL of Millipore water in a 100 mL beaker. A 30% ammonium hydroxide (NH_4OH) solution was then added to the SiO_2 solution until the pH reached 11. This high pH deprotonates the surface SiOH groups and, additionally, adsorbs sites on the charged particle. After the increase in pH, both the hexamine cobalt chloride solution and the SiO_2 solution were mixed and stirred for 5 minutes to ensure proper dispersion. The SiO_2 was then decanted from the mixture and the remaining solids were triple rinsed with Millipore water before being vacuum filtrated. This solid catalyst was then allowed to dry in the oven at 125°C for 12 hours before being calcined at 300°C for 3 hours.

6.2.2   *In Situ* X-ray Absorption Spectroscopy (XAS)

In-situ XAS was performed at the 10-BM sector at the Advanced Photon Source at Argonne National Laboratory. All measurements were performed at the Co K (7.709 keV) edge in transmission mode in fast scan from 250 eV below the edge to 800 eV above the edge. The catalyst was pressed into a stainless-steel sample holder and was then placed into a leak-tight cell with valves allowing for gas flow. Co/SiO_2 was dehydrated at 550°C in He, cooled to room temperature, sealed, and scanned to measure the initial catalyst structure. Subsequent studies were performed

160

by increasing the temperature rapidly in pure H_2 from room temperature to 550°C. The catalyst was cooled to 300°C in pure H_2 and exposed to pure C_2H_4 once the temperature stabilized.

The data was processed using the WinXAS v.3.2 software[19] to find the coordination number and bond distance using standard procedures. Feff6 calculations were performed using CoO (CN=6, R=2.13 Å) for reference. A least squared fit for the first shell of r-space and isolated q-space were performed on the k^2 weighted Fourier transform data over the range of 2.7 to 10 $Å^{-1}$ in each spectrum to fit the magnitude and imaginary components.

6.2.3 H_2/D_2 Isotope Exchange

H_2/D_2 isotopic exchange was performed using a Micromeritics Autochem II 2920 chemisorption analyzer, equipped with a residual gas analyzer (RGA-Model 200, Stanford Research Systems). Approximately 0.050 to 0.100 g of the Co/SiO_2 catalysts were loaded into a quartz U-tube reactor and initially treated in flowing air (8.3-16.7 cm^3s^{-1} g_{cat}^{-1}, 99.999% UHP, Matheson Tri-Gas) at 500°C for dehydration of the surface. The target temperatures for isotope exchange were then increased from 200°C to 550°C, each with a new load of catalyst. When the desired temperature was reached (in flowing He), mixture of 5% H_2 in balance Ar was flowed over the catalyst for 1 hour. The isotope exchange was switched to 5% D_2 in balance Ar for an additional 1 to 2 hours, until HD detector response reached a baseline. By switching the gases from H_2 to D_2, the chemisorbed H_2 on the Co sites reacted with D_2 to form HD. This gas switching procedure was carried out twice to assure accuracy and stability of the quantified moles over time. Background corrections were performed by carrying out the experiments on both the empty quartz tube and pure SiO_2 loads at the same weight loading. The combination of H_2, D_2, and HD was detected using the RGA. The H_2 and D_2 consumption corresponded to the HD formation stoichiometrically. Thus, the moles of HD formed for each experiment were averaged and normalized by the moles of Co in the Co/SiO_2 samples.

6.2.4 Catalyst Evaluation – Propane Dehydrogenation and Propylene Hydrogenation

Propane dehydrogenation and propylene hydrogenation tests were both carried out in a continuous flow fixed-bed reactor in a vertical, 3/8-inch outer diameter glass reactor tube. The reactor tube was loaded with Co/SiO_2 and SiO_2 for a total mass of 1.0 g.

Propane dehydrogenation was performed using 3% C_3H_8 and 1% H_2 (with the balance in N_2) at 1 atm with a loading mixture of 0.100 g Co/SiO_2 and 0.900 g SiO_2. First, the catalyst was increased to 100°C in 100 cm^3/min of N_2 and held for 15 minutes to dehydrate the catalyst. Then, the temperature was ramped up to 550°C in either 100 cm^3/min H_2 or N_2 and held for 30 minutes until the temperature stabilized. The reaction was performed at 550°C under atmospheric pressure with various flowrates of C_3H_8, H_2, and N_2.

Propylene hydrogenation was performed using 1% C_3H_6 and 3% H_2 and had a catalyst bed mixture of 0.250 g Co/SiO_2 and 0.750 g SiO_2. The catalyst was dehydrated in 100 cm^3/min of N_2 at 100°C for 15 minutes before pretreatment. There were three different pretreatments for the propylene hydrogenation tests: (1) increased temperature to 200°C in 100 cm^3/min of N_2 and held for an hour, (2) increased temperature to 200°C in 100 cm^3/min of H_2 and held for an hour, and (3) increased temperature to 550°C in 100 cm^3/min of H_2 and held for an hour before being cooled to 200°C. All hydrogenation reactions were performed at 200°C with 70 cm^3/min of H_2, 22 cm^3/min of C_3H_8, and 12 cm^3/min of N_2 at 1 atm.

The products were analyzed with a Hewlett Packard (HP) 6890 Series GC with a Restek Rt-Alumina Bond/Na_2SO_4 GC column (30 m in length, 0.32 mm inner diameter, and 0.5 μm film thickness). Then, conversion (X) and selectivity (S) rates were calculated for the desired products. Conversion was calculated by the molar difference between the hydrocarbon reactant (propane for dehydrogenation or propylene for hydrogenation) in the inlet and outlet (Equation 6.1). The selectivity of propane and propylene was determined from the gas product distribution (Equation 6.2). Turnover rates (TOR) were calculated on differential conversions (Equation 6.3).

$$X = \frac{\text{moles of reactant in inlet} - \text{moles of propane in outlet}}{\text{moles of propane in inlet}} * 100\% \qquad 6.1$$

$$S = \frac{\text{moles of } C_3H_6}{\text{moles of } C_3H_6 + \frac{2*\text{moles of } C_2}{3} + \frac{\text{moles of } CH_4}{3}} * 100\% \qquad 6.2$$

$$TOR = \frac{\text{moles of ethylene converted}}{\text{moles of Co in } CO/SiO_2} * 100\% \qquad 6.3$$

6.2.5   Catalyst Evaluation – Olefin Oligomerization

Oligomerization tests were performed at atmospheric pressure in pure ethylene or pure propylene using a fixed bed reactor of 3/8-inch outer diameter. The weight of catalyst loaded into the reactor ranged from 0.5 g to 1 g and was diluted with silica to reach a total of 1 g. The catalyst was treated in 50 ccm of N_2 while it ramped to 250°C for the reaction. The reaction was performed in 100% C_2H_4 using GHSVs ranging from 0.08 s^{-1} to 0.38 s^{-1}. Products from the atmospheric pressure reactor were analyzed with a Hewlett Packard (HP) 6890 Series gas chromatograph (GC) using a flame ionization detector (FID) with an Agilent HP-Al/S column (25 m in length, 0.32 mm inner diameter, and 8 µm film thickness).

Oligomerization was also performed in a high-pressure-capable, fixed bed reactor of 1/2-inch outer diameter. Up to 2 g of catalyst was loaded into the reactor. The reactor was pressurized to 500 psig (34 atm) and the catalyst was treated in 100 ccm of N_2 while it ramped to the desired temperature (300°C – 500°C) for the reaction. The reaction was performed in a mixture of 10 ccm 5% CH_4/N_2 for an internal standard and varying flowrates of 100% C_2H_4 (10-50 ccm) at a total pressure of 500 psig. Products were analyzed with a Hewlett Packard (HP) 7890 Series gas chromatograph (GC) using a flame ionization detector (FID) with an Agilent HP-1 column (60 m in length, 0.32 mm inner diameter, and 25 µm film thickness). Conversion and selectivity using Equations 6.4 and 6.5. TOF (turnover frequency) was also calculated as shown below by Equation 6.6.

$$\text{ethylene conversion (\%)} = \frac{\text{moles of carbon in the overall detected products}}{\text{overall moles of carbon detected at the outlet}} * 100\% \qquad 6.4$$

$$C_n\text{selectivity} = \frac{\text{moles of carbon in } C_n \text{ group}}{\text{moles of carbon in the overall detected products}} * 100\% \qquad 6.5$$

$$\text{TOF} = \frac{\text{moles of ethylene converted}}{\text{moles of Co in Co/}SiO_2} * 100\% \qquad 6.6$$

6.3   Results

6.3.1   Initial Catalyst Structure

XAS was performed at the Co K edge (7.709 keV) for Co/SiO$_2$ dehydration at 550°C in He to measure the initial catalyst structure. The XANES provides information about the oxidation

state and coordination geometry, while the EXAFS provides information about the coordination and bond distance.

The XANES of Co/SiO_2 was compared to that of CoO (Co^{2+}, Oh). CoO has a XANES energy of 7.721 keV. In addition, Co^{2+} in CoO has a small pre-edge feature at 7.7097 keV. Co/SiO_2 has a XANES energy of 7.721 keV and a pre-edge feature at 7.708 keV (Figure 6.1a), which is consistent with tetrahedral (Td) Co^{2+}. The pre-edge energy varies slightly with coordination geometry, which is determined by EXAFS. According to the crystal field theory, for Co^{2+} (d7), the partially filled eg orbitals in the octahedral (Oh) geometry have a higher energy than the t orbitals in the Td geometry. The pre-edge is the 1s-eg transition in Oh and the 1s-t transition in Td. Therefore, the pre-edge energy of Td complexes is lower than those of Oh geometry, as has been also observed on Ni/SiO_2 compared to NiO.[20] In addition, the intensity of the pre-edge feature is higher for Td compounds than Oh compounds because the centrosymmetry of the Oh does not allow for d-p mixing. Td is not centrosymmetric, allowing for d-p mixing and higher p orbital contributions.[21,22]

CoO has 6 Co-O bonds at 2.13 Å (Oh). The k^2 weighted EXAFS of Co/SiO_2 (Figure 6.1b) was fit to determine that there are 4 Co-O bonds at 1.97 Å (Table 6.1). In addition, the EXAFS for Co/SiO_2 lacks Co-O-Co second shell scattering, which is present in CoO. The structure of Co/SiO_2 is consistent with Co^{2+} having on 4 Co-O bonds to the support and is defined as a single site catalyst (*i.e.* isolated Co^{2+} ion bound to the SiO_2 support).
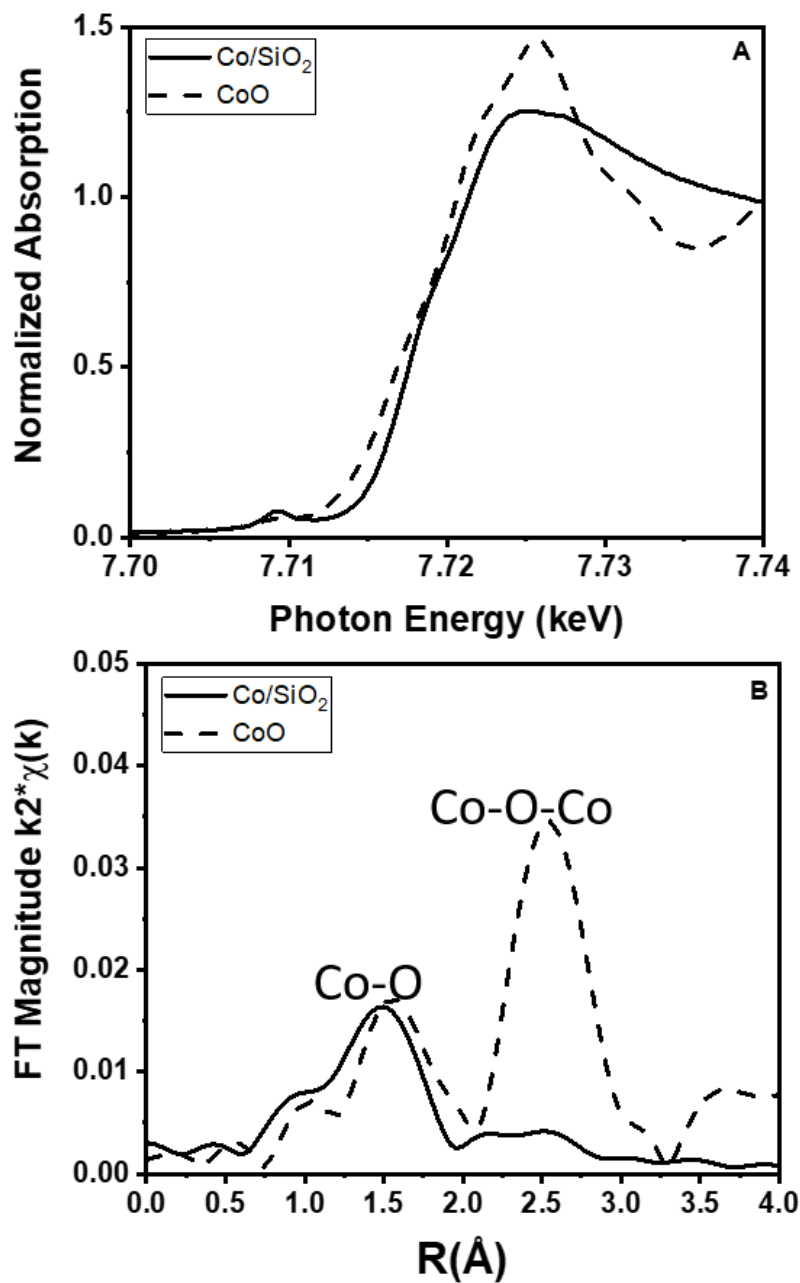
Figure 6.1. XAS containing A) XANES and B) EXAFS of the dehydrated catalyst (550°C, He) compared to a CoO (Co^{2+}) reference

Table 6.1. EXAFS fits of the as-prepared structure of Co/SiO$_2$ after dehydration at 550°C in He

Sample	Pre-edge Energy (keV)	XANES Energy (keV)	Scattering Path	CN	R (Å)	$\Delta\sigma^2$ (Å^2)	ΔE_o (eV)	
CoO	7.7097	7.7210	Co-O	6.0	2.13	-	-	Co^{2+} (Oh)
				12.0	3.03	-	-	
Co/SiO$_2$	7.7093	7.7171	Co-O	4.0	1.97	0.006	-4.2	Co^{2+} (Td)

*CoO are references of known structures

The 4-coordinate, tetrahedral structure, with no evidence of Co-O-Co higher shell bonds of Co/SiO$_2$ is consistent with previous single site structures reported for Co^{2+} dehydrogenation catalysts.[18,23] This is also consistent with the structures of other silica supported single site catalysts recently studied within this group (Ga^{3+}, Zn^{2+}, Ni^{2+}).

6.3.2 Propane Dehydrogenation and Propylene Hydrogenation

Propane dehydrogenation was performed with and without H$_2$ cofeed to evaluate the selectivity toward propylene. Dehydrogenation in the presence of H$_2$ is a more rigorous way to test for selective performance towards the production of propylene, since the presence of H$_2$ promotes the side reaction, hydrogenolysis. High propylene selectivity (98%) was maintained in propane dehydrogenation at 550°C, even in a reactant stream containing 3% C$_3$H$_8$ and 2% H$_2$ in N$_2$. In addition, the activity of Co/SiO$_2$ gradually increased with time, although Co/SiO$_2$ was not tested for longer than 4 hours, as has been done previously.[18] The turnover rates (TOR) for Co/SiO$_2$ was calculated by normalizing the amount of propylene production by the moles of metal on the surface of the catalyst (3.1%). At 5% conversion, the propylene selectivity was 98% and the TOR was 0.8 h^{-1}.

Co/SiO$_2$ also performs the microscopic reverse reaction of propane dehydrogenation (propylene hydrogenation) at lower reaction temperatures. Propane was the only product indicating few side reactions occurred at 200°C. The influence of H$_2$ pretreatment on propylene hydrogenation activity at 200°C was explored to demonstrate how the catalysts behave in the presence of H$_2$ (Table 6.2).

Table 6.2. Initial TORs for Co/SiO$_2$ at 15% conversion during propylene hydrogenation performed at 200°C in 1% C$_3$H$_6$ and 3% H$_2$ after treatment various pretreatments

Pretreatment	Co/SiO$_2$: Initial TOR (1/h)
200°C N$_2$	1.0
200°C H$_2$	1.2
550°C H$_2$	1.3

The initial TOR of the catalysts treated in H$_2$ at 200°C and 550°C was compared to that of the dehydrated catalyst (200°C N$_2$). Pretreatment in H$_2$ leads to higher initial TOR than what was achieved on the dehydrated catalyst. However, after approximately 30 minutes, the TOR for all pretreatment conditions stabilized to approximately the same value.

6.3.3 Olefin Oligomerization

Like the structural characterizations, the catalytic rates and selectivities for propane dehydrogenation and propylene hydrogenation of Co/SiO$_2$ is very similar to reported performance[18], reaction intermediates and elementary reaction steps suggesting that these may also be catalytic for olefin oligomerization.

At 1 atm and increasing temperatures between 250°C and 450°C, the space velocity of pure C$_2$H$_4$ was varied to control the conversion. Up to 1% conversion was obtained with stable performance for at least 40 hours on Co/SiO$_2$. At 250°C, the conversion was negligible (0.1%). When the temperature was increased to 350°C, the conversion increased to 0.5%. At 450°C, the conversion increased to 1.0% which suggests that high temperature is needed to activate C-H bonds and initiate oligomerization (Table 6.3). Turnover rate (TOR) was calculated by normalizing the rate of butene formation by the total moles Co.

Table 6.3. Product selectivity at varying conversions for each catalyst during ethylene oligomerization at 250°C-450°C and 1 atm (WHSV = 1.8 h^{-1})

Temperature (°C)	Conversion (%)*	Selectivity (%)						TOR (s^{-1})
		Methane (CH$_4$)	Ethane (C$_2$H$_6$)	Propylene (C$_3^=$)	Butenes (C$_4^=$)	Hexenes (C$_6^=$)	Octenes (C$_8^=$)	
250	0.1	1.0	32.2	0.2	62.2	0.4	0.0	3.0x10^{-6}
350	0.5	1.5	25.3	0.3	66.9	4.7	1.4	2.1x10^{-4}
450	0.5	4.0	36.4	0.3	53.2	4.8	1.4	1.0x10^{-3}

Co/SiO$_2$ is most selective towards dimers, *e.g.* butenes (50-60%). Hexenes (C$_6^=$) (5-10%) and octenes (C$_8^=$) (1-2%) are also observed. Interestingly, there is also a high selectivity (15-35%) towards ethane. At low conversion oligomerization leads to formation of C$_4^=$ with an equilibrium distribution of 1-butene, cis-2-butene, and trans-2-butene. No isobutene (iC$_4^=$) was observed on Co/SiO$_2$, indicating that there is no skeletal isomerization and only olefin isomerization occurs.

Higher reaction pressures support a higher partial pressure of ethylene. Therefore, while spanning the same range of temperatures, oligomerization was performed at 500 psig (34 atm). The conversion was most notable at temperatures above 350°C. For example, while the conversion was limited to 0.7% at 300°C, it increased to 18% at 375°C and 33% at 400°C. Finally, at 500°C, the conversion reached nearly 100% (Table 6.4). Under these temperatures, Co/SiO$_2$ is known to be thermally stable, as it can perform alkane dehydrogenation at temperatures up to 600°C. The product distribution of the gas phase products was measured (Table 6.4) while the liquid products obtained at high ethylene conversion were analyzed offline for a qualitative understanding of the higher hydrocarbons formed.

Table 6.4. Product selectivity and conversion for ethylene oligomerization at varying temperatures ranging from 300°C-500°C and 34 atm

T (°C)	WHSV (h^{-1})	Conv. (%)	TOR (s^{-1})	Selectivity (%)						
				CH$_4$	C$_2$H$_6$	C$_3^=$	C$_4^=$	C$_5^=$	C$_6^=$	C$_7^=$+
300[a]	0.4	0.7	4.5 x10^{-5}	0.0	0.0	1.9	38.1	7.5	25.3	25.7
350[a]	1.9	3.0	1.0 x10^{-3}	0.0	1.0	2.5	33.9	11.3	25.6	25.0
350[a]	1.1	4.6	9.7 x10^{-4}	0.0	1.1	2.4	34.5	11.2	25.6	24.8
350[a]	0.2	7.3	2.6 x10^{-4}	0.0	1.8	2.9	40.2	12.2	25.3	17.2
375[a]	0.4	18.3	1.3 x10^{-3}	0.1	1.1	5.3	19.0	18.0	29.6	26.8
375[a]	0.9	13.5	2.4 x10^{-3}	0.1	1.0	5.1	17.0	14.0	11.7	51.1
400[a]	1.9	16.2	5.7 x10^{-3}	0.2	2.4	10.6	34.2	22.8	19.6	10.2
400[a]	0.9	19.1	3.4 x10^{-3}	0.7	3.5	20.9	30.2	11.6	4.2	28.9
400[a]	0.4	32.7	2.3 x10^{-3}	0.4	1.6	9.0	16.2	11.4	21.6	39.7
425[b]	9.4	86.9	1.5 x10^{-1}	0.5	0.9	2.9	3.5	6.9	5.2	80.0
450[b]	5.6	98.5	1.0 x10^{-1}	6.5	9.2	9.7	17.6	2.5	13.0	40.8
500[a]	2.8	99.3	1.0 x10^{-1}	7.8	11.2	10.6	4.9	2.0	8.4	54.5

[a] Catalyst loading: 2.00 g of Co/SiO$_2$. [b] Catalyst loading: 1.00g of Co/SiO$_2$.

At 300°C, Co/SiO$_2$ has a 0.7% conversion under 500 psi of C$_2$H$_4$ and most of the products are the expected oligomers, with C$_4^=$, C$_6^=$ and C$_8^=$ production. Small fractions of C$_3$ and C$_3^=$ (propane and propylene), C$_5^=$ and C$_7^=$ are detected. As the temperature increases to 350°C, the conversion ranges between 3.0% and 7.3%, depending on the space velocities. At this temperature, the C$_4^=$ and C$_6^=$ isomers are still the highest yield product and maintain the same proportion observed for the lower temperature, around 30 to 40% and 25%, respectively. An increase in C$_5^=$ and the formation of ethane are also observed. The amount of C$_5^=$ isomers increases to about 12%, while a small yield, 1.5% of ethane forms. The yield of products higher than C$_7^=$ are about 17 to 25%.

At 400°C, the conversion increases significantly. An increase of 5 times, from 10 ccm to 50 ccm, in the flowrate decreases conversion by about a half, from 33% to 16%. The trend observed in C$_4$ and C$_6$ products at higher temperatures are like those at lower temperature, and at 16.2% conversion the selectivity is about 34% and 20%, respectively. However, the selectivity of C$_3$ and C$_5$ products increased significantly, to 11% and 23% respectively, and the selectivity of C$_{7+}$ products decreased to 10%. As the conversion reached 32%, the amount of C$_4$ olefin isomers and C$_5$ decreased to 17% and 11%, while C$_6$ slightly increased and C$_{7+}$ increased significantly. The C$_3$ and C$_2$H$_6$ production remained roughly the same, while a trace amount of CH$_4$ was produced.

At 500°C at a WHSV of 34.1h^{-1}, at nearly complete conversion (99.4%) of C$_2$H$_4$, 5% of the products are C$_4$ olefin isomers with only 2.0% C$_5$ and more than 70% are a mixture of C$_6^+$ olefins. A significant increase in the amount of low molecular weight products was also observed, with CH$_4$ and C$_2$H$_6$ yields of 8% and 11%, respectively, indicating an increase in thermal cracking. GC-MS analysis was performed on liquid products and revealed the presence of a mixture of C$_5$ and C$_6$ alkanes and alkenes, as well as the presence of some benzene and toluene products. Thus, as the conversion increases at high temperatures, an increase in light alkanes and higher molecular weights are observed due to additional increased side reactions, *e.g.*, thermal cracking, isomerization and aromatization.

Likewise, propylene oligomerization was performed at 250°C-450°C and atmospheric pressure with product selectivities, consistent with oligomerization (Table 6.5).

Table 6.5. Product selectivity at varying conversions for each catalyst during propylene oligomerization at 250°C - 450°C and 1 atm (WHSV = 1.9 h^{-1})

Temperature (°C)	Conversion (%)*	Selectivity (%)							TOR (s^{-1})
		CH_4	$C_2^=$	C_3H_8	$C_4^=$	$C_6^=$	$C_9^=$	$C_{12}^=$	
250	0.5	3.5	0.6	29.5	4.3	35.9	24.1	2.0	2.3x10^{-6}
350	1.0	1.2	7.8	26.4	13.6	15.3	35.0	1.0	4.3x10^{-4}
450	2.7	8.1	9.8	41.8	7.7	14.4	18.2	0.1	1.3x10^{-3}

Higher conversion of propylene was observed than ethylene at atmospheric pressure on Co/SiO$_2$. In addition, small amounts of products from side reactions were also observed. At 250°C, Co/SiO$_2$ was most selective toward $C_6^=$ (36%), but the reaction rate was low. Typical oligomerization products including $C_9^=$ (24%) and $C_{12}^=$ (2%) were also formed. Other products including CH$_4$ (4%), $C_2^=$ (0.6%), $C_4^=$ (4%) and C$_3$H$_8$ (30%) were also observed.

An increase in temperature also led to an increase in reaction rate. For instance, at 350°C and a WHSV of 1.9 h^{-1}, the conversion doubled from 0.5% at 250°C to 1%. In addition, the $C_6^=$ selectivity decreased from 36% to 15% while the $C_9^=$ selectivity increased to from 24% to 35%. At 450°C, the conversion further increased to about 3%. Here, the $C_6^=$ and $C_8^=$ selectivities were approximately 15% and 18% respectively.

For oligomerization using pure olefins (ethylene or propylene) and varying reaction conditions, the product distributions on each catalyst can be predicted by determining a Schulz Flory coefficient, which inherently compares the rate of olefin insertion, or propagation (α), and β-hydride elimination, or termination $(1 - \alpha)$. Higher α means that there is a higher tendency to form higher molecular weight products. It is noted that α is higher for propylene oligomerization than ethylene oligomerization at atmospheric pressure and 1% conversion (Figure 6.2).
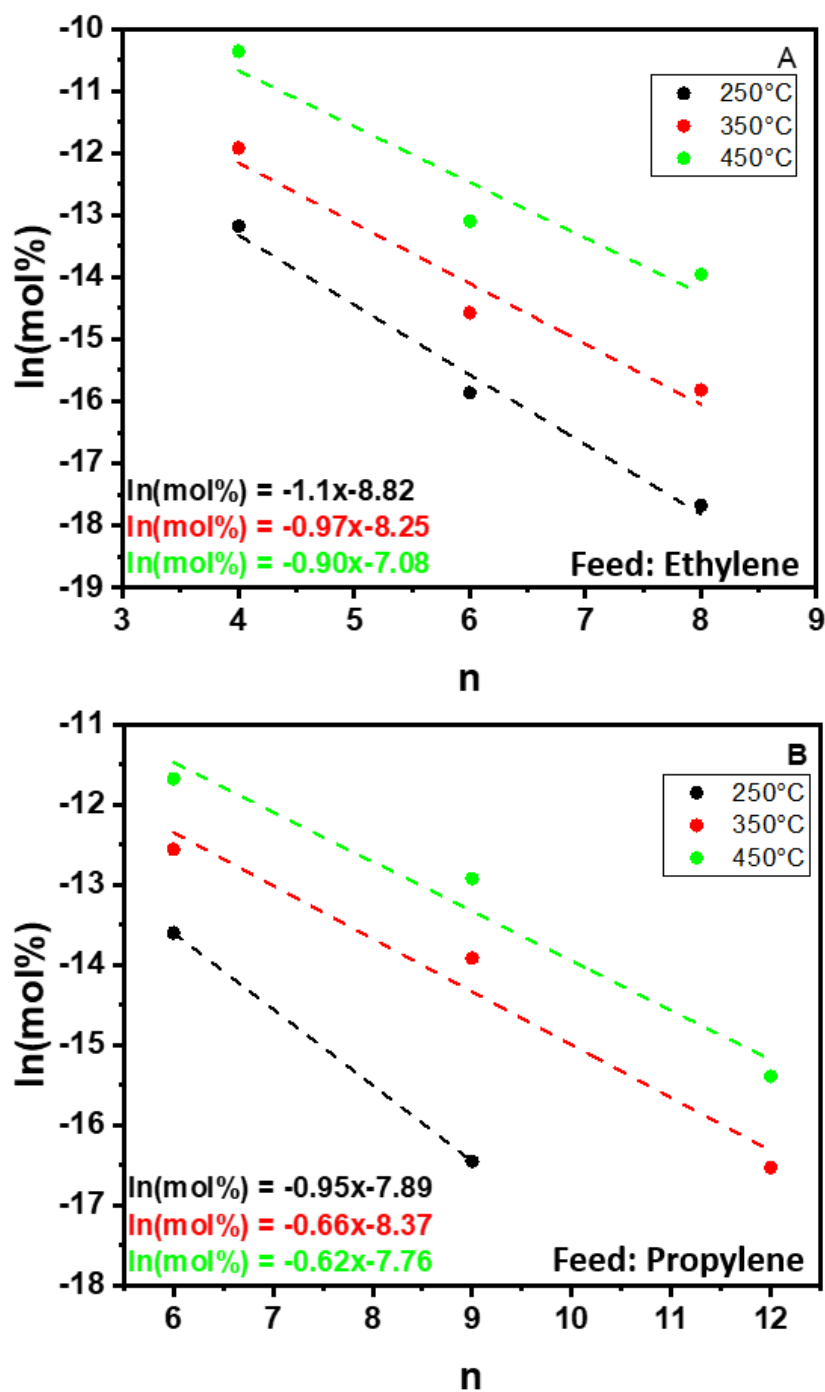
Figure 6.2. Schultz Flory distribution of linear hydrocarbons during A) ethylene and B) propylene oligomerization at increasing temperatures (250°C -450°C) and atmospheric pressure for 0.1-1% conversion

For ethylene oligomerization at atmospheric pressure, the coefficient of propagation (α) increases from 0.33 at 250°C to 0.38 at 350°C. At 450°C α further increases to 0.41. This indicates that at higher temperatures, there is an increased formation of higher molecular weight hydrocarbons. Similar trends are observed for atmospheric pressure propylene oligomerization though α is consistently higher at a given reaction temperature. At 250°C α is 0.39 and it increases to 0.52 and 0.54 at 350°C and 450°C respectively.

Increased pressure for ethylene oligomerization from 1 atm to 34 atm led to a decrease in α with increasing reaction temperature due to increased side reactions observed with increasing ethylene conversion (Figure 6.3).
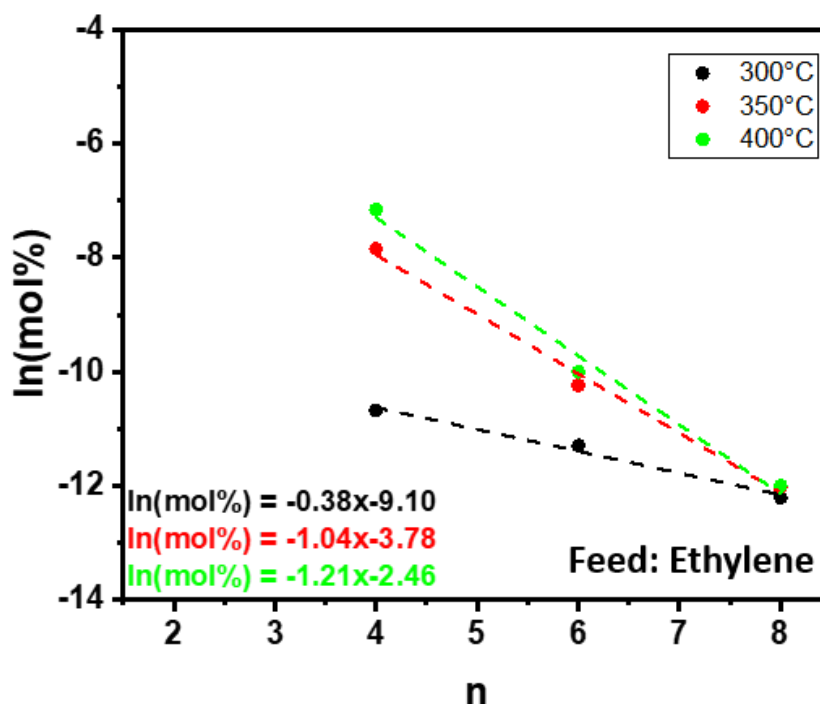
Figure 6.3. Schultz Flory distribution of linear hydrocarbons during ethylene oligomerization at increasing temperature and 34 atm forc0.7% conversion at 300°C (black), 7.3% conversion at 350°C (red), and 16.2% conversion at 400°C (green)

This means that at 34 atm as the temperature increases from 300°C to 350°C and 400°C, α decreases from 0.47 to 0.35 and 0.30 respectively. However, these α were calculated using only gas phase productions. Higher conversions led to the increase of higher molecular weight hydrocarbons, which were collected as liquids and not included in this analysis.

6.3.4 Co/SiO₂ Structure Under Reaction Conditions

Operando XAS was used to identify the structure of Co/SiO₂ during the catalytic process. In H_2 with increasing temperatures from 300°C to 550°C, no changes to the XANES or EXAFS were observed. This shows that the catalyst structure does not change at high temperatures, even in the presence of H_2. In addition, when C_2H_4 was exposed to the catalyst at 300°C, the structure did not change (Figure 6.4). In addition, the absence of second shell metal-oxygen-metal scattering in the EXAFS indicates that the single site Co^{2+} structure is maintained at high temperature in H_2.
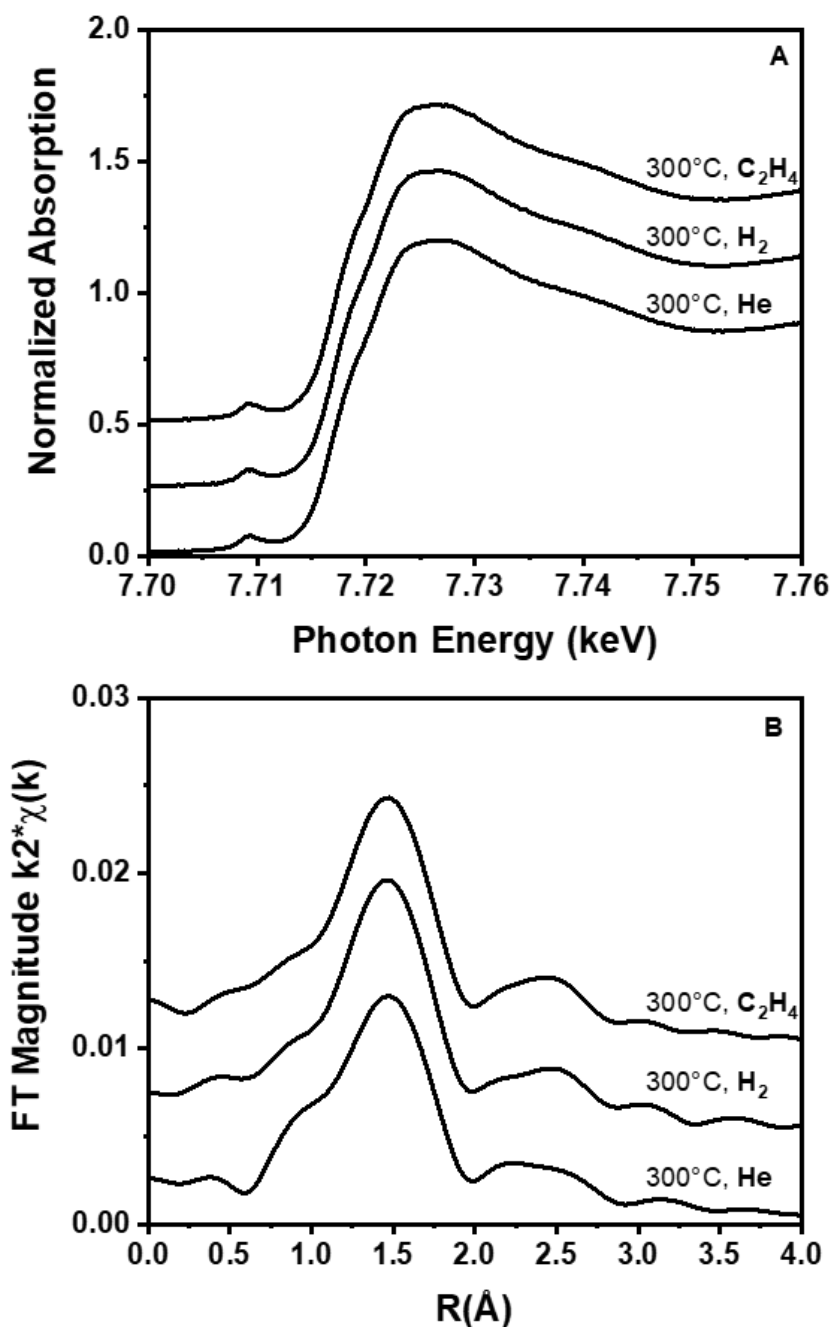
Figure 6.4. Operando XAS for Co/SiO$_2$ at 300°C dehydrated in He and treated sequentially in H$_2$ and C$_2$H$_4$ in both A) normalized Co K edge XANES and B) k2 weighted EXAFS

Metal-hydrogen bonds are not detected by EXAFS, and the loss of M-O bonds has been suggested to be due for formation of M-H bonds.[18,24,25] While changes have been observed in pure

H_2 on Ga^{3+} and Zn^{2+} single site catalysts, Co^{2+} does not notably change. This could be due to the electron configuration of each single site metal. Ga^{3+} and Zn^{2+} are d10 and have no unpaired d electrons, while Co^{2+} is d7. The former tends to prefer 4-coordinate geometries while the latter can participate in various bonding configurations. Therefore, these results do not exclude the formation of Co-H bonds, but instead suggests that if Co-H bonds are formed, the surface coverage is low and on average, Co-O bonds are not lost. In addition, it is possible that ethylene assisted hydride formation occurs on Co^{2+}, as has been proposed for Ni^{2+}.[35] Due to the similarly between C and O, M-O and M-C bonds cannot be distinguished by XAS. Therefore, if M-O bonds are lost as M-C bonds are gained, the total coordination number would look similar. This would imply that a transition state involving C_2H_3-Co-H is possible. Such transition state could increase the energy barrier for Co-H formation, consistent with the low reaction rates.

Further, identification of how each catalyst reacts with H_2 was studied using H_2/D_2 isotope exchange experiments, in which the amount of HD formed corresponds to the number of metal hydride sites present on the surface. It was previously demonstrated that as a single site catalyst heterolytically dissociates H_2, it forms a M-H bond and a proton that coordinates to the M-O-Si bond in the support. Protonation of the latter leads to breaking of the M-O bond and formation of a new Si-OH group. On Co/SiO_2, after H_2 treatment at 250°C, about 0.26 mol HD/mol Co was formed. This value nearly doubled to 0.56 mol HD/mol Co at 450°C. Thus, the stoichiometric ratio suggests that the uptake of H_2 absorbed by the catalysts increases with increasing temperature.

6.4   Discussion

Consistent with literature for single site Co/SiO_2 propane dehydrogenation catalysts, XAS indicates the initial, dehydrated structure is a Co^{2+} ion with 4 Co-O bonds at 1.97 Å to the SiO_2 support. In addition, the Co^{2+} also does not reduce to metallic Co after treatment in H_2 or hydrocarbons (*e.g.* propane or ethylene) at temperatures up to 550°C.[26] Unlike Ni^{2+}, which begins to reduce near 250°C, single site Co^{2+} ions are resistant to reduction to metallic nanoparticles up to about 750°C, likely due to the distance between Co-Co neighbors.[20,27]

On similar single site catalysts, it was previously proposed that H_2 is heterolytically dissociated across the M-O-Si bond in single site catalysts forming a M-H and Si-O-H.[26,28–31] Small changes in XAS were interpreted as indirect evidence of M-H, which is an important oligomerization reaction intermediate. However, due to its low atomic number, there is no

scattering from H atoms in the M-H bond, for example.[28,30,31] These changes were not observed on the Co/SiO$_2$ catalyst. Instead, when treated in high temperatures and pure H$_2$ or C$_2$H$_4$, the average structure observed by XAS remained unchanged. It is possible that low concentrations of Co-H have formed, though not spectroscopically detected, as evidenced by Co/SiO$_2$ reaction with H$_2$ in H$_2$/D$_2$ isotope exchange experiments. The molar fraction of Co-H is estimated to be about 0.26 mol/mol of Co at 250°C. At 450°C, this increases to 0.56 mol/mol of Co, or about twice as much as formed at 250°C. While Co/SiO$_2$ can heterolytically dissociate H$_2$, low rates are obtained at low temperatures of about 200°C and become more significant at temperatures above 350°C. Through this, we can make a stable, non-reducible, high-temperature oligomerization catalyst.

Co^{2+} has been previously explored as an oligomerization catalyst, but frequently requires a co-catalyst or contained targeted alkyl ligand to facilitate ethylene oligomerization at lower temperatures.[32] Here, the catalytic reactivity on Co/SiO$_2$ in both dehydrogenation and oligomerization requires high temperatures, and suggests that C-H bonds in paraffins and olefins can be activated at temperatures above 300°C. In both reaction schemes, Co hydrides and alkyls are formed *in situ*. In the oligomerization reactions reported in this study, the absence of H$_2$ suggests that it is necessary to first activate a vinyl C-H bond of ethylene, forming a Co-C$_2$H$_3$ and Si-O-H. C-H activation of ethylene can occur as low as 300°C, as demonstrated by the ethylene oligomerization reactivity. At this low temperature, however, the rates and surface coverage are low and almost negligible conversion is obtained. Nevertheless, ethylene activation is possible, as evidence by olefin hydrogenation activity. As the catalytic performance in olefin oligomerization indicates, higher temperatures and pressure favor higher rates and conversions.

For both heterogeneous and homogeneous catalysts, Co^{2+} has a much lower intrinsic TOR than Ni^{2+}.[33] In a recent study by Xu *et al* [34], CoO clusters supported on N-doped carbon supports were reported with maximum conversion of 32% for ethylene oligomerization at 80°C and 31 atm, with about 50% C$_2$H$_4$ and balance He. In our study, the single site Co/SiO$_2$ catalysts were evaluated at 250°C and 34 atm in 100% C$_2$H$_4$ and displayed negligible ethylene oligomerization conversion. Significant conversions were only observed at much higher temperatures, starting at 300°C. Previous reports have shown that CoO clusters reduce around 320°C[35,36]. High conversion for ethylene oligomerization for the latter catalyst is only possible since the single site Co^{2+} is resistant to reduction up to high reaction temperature, 750°C.[27]

The Cossee-Arlman mechanism is generally accepted for transition metal-based catalysts, such as Ni^{2+} ions on mesoporous supports, like zeolites.[37–39] Initiation is thought to occur by heterolytic dissociation of a vinyl C-H bond of ethylene forming a Ni^{2+}-C_2H_3 and an Al-O(H)-Si Bronsted acid site. An additional ethylene insertion and β-H elimination give a stoichiometric yield of butylene and Ni^{2+}-hydride intermediate. Olefin propagation occurs by additional ethylene insertion forming longer Ni^{2+}-alkyl intermediates. β-H elimination of these longer alkyl gives the oligomerization products, *i.e.* C_6 and C_8, and recovers the Ni^{2+}-hydride. In zeolites, even in those which prior to reaction do not have Bronsted sites, the formed acid sites lead to secondary reactions of the primary oligomer products, *e.g*, isomerization and cracking, leading to branched olefins and olefins with odd carbon numbers, for example, propylene and i-pentene.[37]

The results for Co/SiO_2 oligomerization are consistent with the Cossee-Arlman mechanism, and oligomerization products follow a Schulz Flory distribution. Propylene hydrogenation suggest that Co/SiO_2 activate C-H bonds in alkanes and olefins at temperatures as low as 200°C. Although the intrinsic rate of Co^{2+} is low, significant catalytic rates are possible at higher reaction temperatures since the active site is difficult to reduce to a metallic species. On zeolite catalysts, initiation leads to Bronsted acid sites; while on SiO_2 supports, initiation leads to non-acidic silanol groups. This is expected to lead to a different product distribution. On the former, isomerization and cracking occur giving high selectivity to branched and odd numbered olefin products. On silica, at low temperature a typical Schulz-Flory product distribution is obtained; while (much) higher temperatures favors low selectivity to olefin hydrogenation, hydrogenolysis, isomerization and even aromatization products. Finally, Co/SiO_2 oligomerization leads to higher molecular weight products.

The reaction intermediates and reaction steps generally accepted for the Cossee-Arlman oligomerization mechanism[40–42] are similar to those thought responsible for olefin hydrogenation and alkane dehydrogenation of heterogeneous single site catalysts[26,28–31]. For all three reactions (olefin oligomerization and hydrogenation and alkane dehydrogenation), metal hydride and alkyl intermediates are key intermediates, though the reaction conditions differ. In addition, β-hydrogen elimination is necessary to yield olefin products by oligomerization and alkane dehydrogenation. The proposed relationship between the three pathways is shown in Figure 6.5, where Co-H is common amongst the two catalytic cycles.
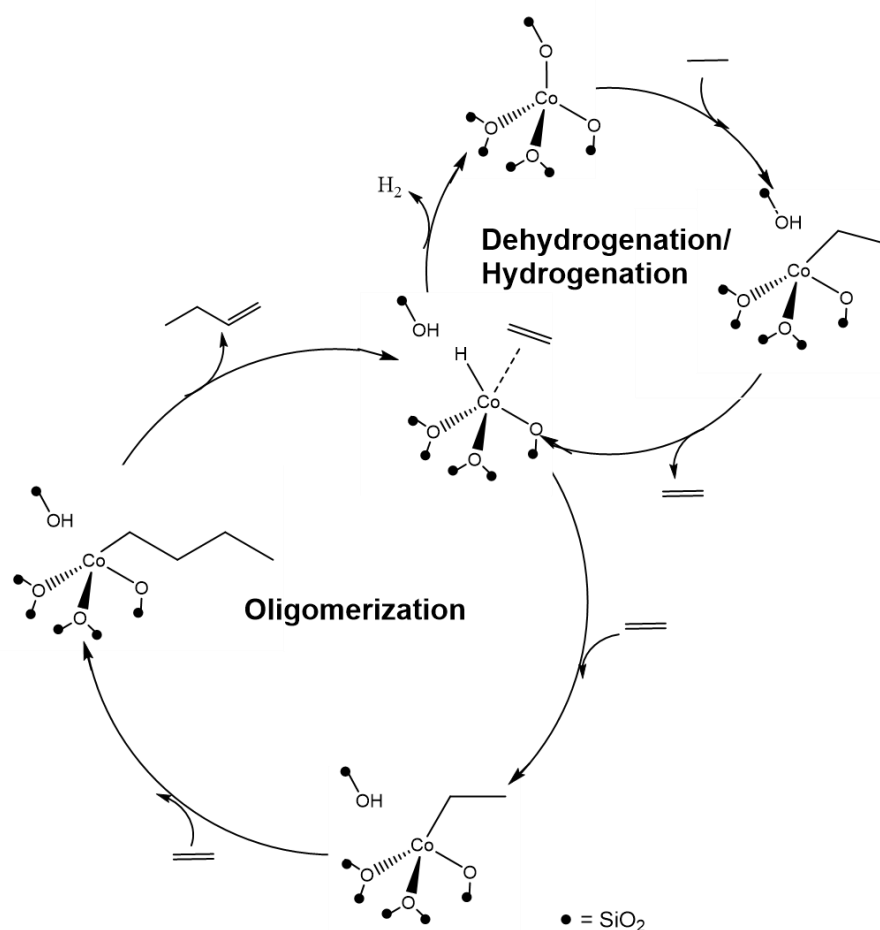
Figure 6.5. Proposed pathways for alkane dehydrogenation, alkene hydrogenation and ethylene oligomerization share common Co hydride and Co alkyl reaction intermediates

Although alkane dehydrogenation and olefin oligomerization occur at about the same temperature, the former is favored at low pressure, while the latter is favored at high pressure. Thus, higher molecular weight products were not observed during dehydrogenation.

Olefin hydrogenation was previously studied at low temperature and hydrogen partial pressure and the rate would be expected to increase with increasing temperature and pressure, for example at 500°C. During higher temperature oligomerization low selectivity to aromatics suggests that small amounts of H_2 may also have been produced. These would be expected to saturate olefins giving small amounts of alkanes. While H_2 was not directly detected, it is likely to be formed during the initiation of oligomerization, where butadiene formation is proposed.[38]

Interestingly, Co^{2+} requires a higher reaction temperature and have a lower reaction rate than the Ni^{2+}, Ga^{3+} and Zn^{2+} single site catalysts recently reported by our group. Theory-based studies

suggest that this is attributed to the stability of the d electron orbitals under reaction conditions, which could contribute to the instability of Co-H under these conditions.[33]

The high temperature stability of Co^{2+} conceives the possibility of tandem catalysis combining dehydrogenation and oligomerization for the direct conversion of alkanes to oligomers. The separation of unreacted alkanes and liquid oligomers can be achieved in the absence of a membrane. Although high olefin pressures are required for non-trivial oligomerization activity, it is not necessarily a detriment to dehydrogenation. Due to thermodynamic limitations, dehydrogenation is typically performed at 1 atm. In a system where tandem catalysis is implemented, high pressure can shift the equilibrium to favor the production of oligomers while improving the dehydrogenation rate. Likewise, with dehydrogenation being highly endothermic and oligomerization being highly exothermic, this could provide better heat management in the overall reaction pathway.

6.5   Conclusion

In this work, we synthesized Co/SiO_2 using standard catalyst preparation techniques, which had an initial catalyst structure containing 4 Co-O bonds to the SiO_2 support and the hydrogenation/ dehydrogenation activity was benchmarked against literature to confirm the desired initial catalyst structure was single site. Co^{2+} ions on this catalyst were resistant to reduction at high reaction temperatures up to 500°C and pure H_2 and C_2H_4, *i.e.* no metallic Co was observed. Here, we report that oligomerization is mechanistically related to alkane dehydrogenation and olefin hydrogenation through the formation of metal alkyls and metal hydrides, which are typically accepted for both catalytic cycles.

Traditionally, homogenous olefin oligomerization catalysts are generally tailored to give highly selective product distributions, primarily for production of chemical intermediates, for example, 1-butene. Due to the high reaction temperature and multiple catalytic pathways which occur on these heterogeneous Co/SiO_2 catalysts, high selectivity to a single product seems unlikely. However, limited deactivation, facile regenerability and structural stability make this ideal for production of transportation fuels, especially, diesel and distillate fuels. With vast amounts of ethane available in shale gas production, especially in remote areas, excess olefin production could be converted to premium motor fuels by olefin oligomerization on Co/SiO_2 catalysts. The products are primarily linear olefins, with small amounts of aromatics. The products are also sulfur free and

have no polyaromatic compounds. Mild hydrogenation of the products yields a premium diesel fuel for local markets.

6.6   Acknowledgement

6.7   References

1. Metzger, E. D.; Comito, R. J.; Hendon, C. H.; Dincă, M. Mechanism of Single-Site Molecule-Like Catalytic Ethylene Dimerization in Ni-MFU-4l. *J. Am. Chem. Soc.* **2017**, 139, 757–762.

2. Breuil, P.A.R.; Magna, L.; Olivier-Bourbigou, H. Role of homogeneous catalysis in oligomerization of Olefins: focus on selected examples based on Group 4 to Group 10 transition metal complexes. *Catalysis Letters*. **2015**, 145, 173–192.

3. Nicholas, C. P. Applications of light olefin oligomerization to the production of fuels and chemicals. *Applied Catalysis A: General*, **2017**, 543, 82–97.

4. Sydora, O.L. Selective Ethylene Oligomerization. *Organometallics*. **2019**, 38, 997–1010.

5. Lavrenov, A.V.; Karpova, T.R.; Buluchevskii, E.A.; Bogdanets, E.N. Heterogeneous oligomerization of light alkenes: 80 years in oil refining. *Catal. Ind.* **2016**, 8, 316–327.

6. Keim, W. Nickel: An Element with Wide Application in Industrial Homogeneous Catalysis. **1990**, 29, 235-244.

7. Forestière, A.; Olivier-Bourbigou, H.; Saussine, L. Oligomerization of Monoolefins by Homogeneous Catalysts. *Oil & Gas Science and Technology - Rev. IFP* **2009**, 64, 649–667.

8. Keim, W. Oligomerization of Ethylene to α-Olefins: Discovery and Development of the Shell Higher Olefin Process (SHOP). *Angewandte Chemie.* **2013**, 52,12492–6.

9. Mathys, G. M. K.; Martens, L. R. M.; Baes, M. A., Verduijn, J. P.; Huybrechts, D. R. C. 1997. Alkene oligomerization. US Patent 20040006250, filed April 14, 2003, and issued January 8, 2004.

10. Brown, S. H.; Godsmark, J. S.; Mathys, G. M. K. 2010. Olefin oligomerization process. US Patent 20070173676A1, filed June 1, 2004, and issued August 31, 2010.

11. Verrelst, W. H.; Martens, L. R. M. 1995. Oligomerization and catalysts therefor. French Patent WO1995022516A1, filed February 22, 1994, and issued August 24, 1995.

12. Killian, C. M.; Johnson, L. K.; Brookhart, M. Preparation of Linear α-Olefins Using Cationic Nickel(II) α-Diimine Catalysts. *Organometallics*. **1997**, 16, 2005–2007.

13. Finiels, A.; Fajula, F.; Hulea, V. Nickel-based solid catalysts for ethylene oligomerization – a review. *Catal. Sci. Technol.* **2014**, 4, 2412–2426.

14. Champouret, Y.D.M.; Fawcett, J.; Nodes, W.J.; Singh, K.; Solan, G.A. Spacially Confined M2 Centers (M = Fe, Co, Ni, Zn) on a Sterically Bulky Binucleating Support: Synthesis, Structures and Ethylene Oligomerization Studies. *Inorg. Chem.* **2006**, 45, 9890–9900.

15. Tobisch, S.; Ziegler, T. Catalytic Oligomerization of Ethylene to Higher Linear α-Olefins Promoted by the Cationic Group 4 [(η5-Cp-(CMe2-bridge)-Ph)MII(ethylene)2]+ (M = Ti, Zr, Hf) Active Catalysts: A Density Functional Investigation of the Influence of the Metal on the Catalytic Activity and Selectivity. *J. Am. Chem. Soc.* **2004**, 126, 9059–9071.

16. Mise, T.; Kageyama, A.; Miya, S.; Yamazaki, H. On the Mechanism of Oligomerization of Propylene by (C5Me5)2MCl2/Methylalumoxane Catalysts (M = Zr, Hf). *Chem. Lett.* **1991**, 20, 1525–1528.

17. McGuinness, D.S.; Gibson, V.C.; Wass, D.F.; Steed, J.W. Bis(carbene)pyridine Complexes of Cr(III): Exceptionally Active Catalysts for the Oligomerization of Ethylene. *J. Am. Chem. Soc.* **2003**, 125, 12716–12717.

18. Hu, B.; Getsoian, A.B.; Schweitzer, N.M.; Das, U.; Kim, H.; Niklas, J.; Poluektov, O.; Curtiss, L.A.; Stair, P.; Miller, J.T.; Hock, A.S. Selective propane dehydrogenation with single-site CoII on SiO2 by a non-redox mechanism. *Journal of Catalysis*. **2015**, 322, 24–37.

19. Ressler, T. WinXAS: a Program for X-ray Absorption Spectroscopy Data Analysis under MS-Windows. *J. Synchrotron Rad.* **1998**, 5, 118–122.

20. Zhang, G.; Yang, C.; Miller, J. T. Tetrahedral Nickel(II) Phosphosilicate Single-Site Selective Propane Dehydrogenation Catalyst. *ChemCatChem*. **2017**, 10, 961–964.

21. Manceau, A.; Gorshkov, A.I.; Drits, V.A. Structural chemistry of Mn, Fe, Co, and Ni in manganese hydrous oxides: Part I. Information from XANES spectroscopy. *American Mineralogist*. **1992**, 77, 1133–1143.

22. Holzapfel, M.; Proux, O.; Strobel, P.; Darie, C.; Borowski, M.; Morcrette, M. Effect of iron on delithiation in Li x Co 1−y Fe y O 2 . Part 2: in-situ XANES and EXAFS upon electrochemical cycling. *Journal of Materials Chemistry*. **2004**, 14, 102–110.

23. Estes, D.P.; Siddiqi, G.; Allouche, F.; Kovtunov, K.V.; Safonova, O.V.; Trigub, A.L.; Koptyug, I.V.; Coperet, C. C–H Activation on Co,O Sites: Isolated Surface Sites versus Molecular Analogs. *J. Am. Chem. Soc.* **2016**, 138, 14987–14997.

24. Schweitzer, N. M.; Hu, B.; Das, U.; Kim, H.; Greeley, J.; Curtiss, L.A.; Stair, P.C.; Miller, J.T.; Hock, A.S. Propylene Hydrogenation and Propane Dehydrogenation by a Single-Site Zn2+ on Silica Catalyst. *ACS Catal.* **2014**, 4, 1091–1098.

25. Getsoian, A.B.; Das, U.; Camacho-Bunquin, J.; Zhang, G.; Gallagher, J.R.; Hu, B.; Cheah, S.; Schaidle, J.A.; Ruddy, D.A.; Hensley, J.E.; Krause, T.R.; Curtiss, L.A.; Miller, J.T.; Hock, A.S. Organometallic model complexes elucidate the active gallium species in alkane dehydrogenation catalysts based on ligand effects in Ga K-edge XANES. *Catalysis Science & Technology*. **2016**, 6, 6339–6353.

26. Cesar, L.G.; Yang, C.; Lu, Z.; Ren, Y.; Zhang, G.; Miller, J.T. Identification of a Pt 3 Co Surface Intermetallic Alloy in Pt–Co Propane Dehydrogenation Catalysts. *ACS Catalysis*. **2019**, 9, 6, 5231–5244.

27. Hu, B.; Getsoian, A.B.; Schweitzer, N.M.; Das, U.; Zhang, G.; Kraft, S.J.; Childers, D.J.; Lanci, M.P.; Miller, J.T.; Hock, A.S.. Isolated FeII on Silica As a Selective Propane Dehydrogenation Catalyst. *ACS Catalysis.* **2015**, 5, 3494–3503.

28. Cybulskis, V. J.; Pradhan, S.U.; Lovon-Quintana, J.J.; Hock, A.S.; Hu, B.; Zhang, G.; Delgass, W.N.; Ribeiro, F.H.; Miller, J.T. The Nature of the Isolated Gallium Active Center for Propane Dehydrogenation on Ga/SiO2. *Catal Lett.***2017**, 147, 1252–1262.

29. Tellmann, K.P.; Gibson, V.C.; White, A.J.P.; Williams, D.J. Selective Dimerization/Oligomerization of α-Olefins by Cobalt Bis(imino)pyridine Catalysts Stabilized by Trifluoromethyl Substituents: Group 9 Metal Catalysts with Productivities Matching Those of Iron Systems. *Organometallics*. **2005**, 24, 280–286.

30. Pellizzeri, S.; Barona, M.; Berales, V.; Miro, P.; Liao, P.; Gagilardi, L.; Snurr, R.Q.; Getman, R.B. Catalytic descriptors and electronic properties of single-site catalysts for ethene dimerization to 1-butene. *Catalysis Today*. **2018**, 312, 149–157.

31. Xu, Z.; Chada, J.P.; Xu, L.; Zhao, D.; Rosenfeld, D.C.; Rogers, J.L.; Hermans, I.; Mavikakis, M.; Huber, G.W. Ethylene Dimerization and Oligomerization to 1-Butene and Higher Olefins with Chromium-Promoted Cobalt on Carbon Catalyst. *ACS Catalysis*. **2018**, 8, 2488–2497.

32. Souza, L.D.; Jiao, L.; Regalbuto, J R.; Miller, J.T.; Kropf, A.J. Preparation of silica- and carbon-supported cobalt by electrostatic adsorption of Co (III) hexaammines. *J.Catal.* **2007**, 248, 165–174.

33. Garces, L.J.; Hincapie, B.; Zerger, R.; Suib, S.L. The Effect of Temperature and Support on the Reduction of Cobalt Oxide: An in Situ X-ray Diffraction Study. *The Journal of Physical Chemistry C*. **2015**, 119, 5484–5490.

34. Joshi, R., Zhang, G., Miller, J. T. & Gounder, R. Evidence for the Coordination–Insertion Mechanism of Ethene Dimerization at Nickel Cations Exchanged onto Beta Molecular Sieves. *ACS Catal.* **2018**, 8, 11407–11422.

35. Brogaard, R. Y.; Olsbye, U. Ethene Oligomerization in Ni-Containing Zeolites: Theoretical Discrimination of Reaction Mechanisms. *ACS Catal.* **2016**, 6, 1205–1214.

36. Henry, R.; Komurcu, M.; Ganjkhanlou, Y.; Brogaard, R.Y.; Lu, L.; Jens, K.J.; Berlier, G.; Olsbye, U. Ethene oligomerization on nickel microporous and mesoporous-supported catalysts: Investigation of the active sites. *Catalysis Today,* **2018**, 9, 154–163.

37. Forget, S.; Olivier-Bourbigou, H.; Delcroix, D. Homogeneous and Heterogeneous Nickel-Catalyzed Olefin Oligomerization: Experimental Investigation for a Common Mechanistic Proposition and Catalyst Optimization. *ChemCatChem*, **2017**, 9, 2408–2417.

38. Britovsek, G. J. P.; Malinowski, R.; McGuinness, D.S.; Nobbs, J.D.; Tomov, A.K.; Wadsley, A.W.; Young, C.T. Ethylene Oligomerization beyond Schulz−Flory Distributions. *ACS Catal.* **2015**, 4, 6922-6925.

39. Agapie, T. Selective ethylene oligomerization : Recent advances in chromium catalysis and mechanistic investigations. *Coordination Chemistry Reviews*. **2011**, 255, 861–880.

7. SUMMARY

This work highlights new catalyst compositions to convert the light alkanes in shale gas to fuel-range higher molecular weight hydrocarbons. This is traditionally envisioned as a two-step process consisting of dehydrogenation and oligomerization, performed in separate reactors under different reaction conditions. The first part of this thesis explores the formation of Pt-Cr bimetallic nanoparticles. Through this, it was found that catalysts containing different nominal loadings of Cr had different catalyst performance, despite having nearly identical bulk structures by both XAS and XRD. While XAS and XRD confirm the presence of bimetallic nanoparticles with a two-phase composition (Pt and Pt_3Cr), these are insufficient to determine the structure of the catalytic surface. To determine the precise structure of the active catalytic surface, a new method of surface analysis was developed using bulk characterization techniques.

Catalyst performance tests of Pt_3Cr/SiO_2 catalysts in propane dehydrogenation resulted in additional minor product formation that were believed to be higher molecular weight hydrocarbons attributed to oligomerization. This is reasonable because the Pt_3Cr/SiO_2 has residual Cr_2O_3 and Cr^{3+} single sites on the SiO_2, which were previously reported to be active in oligomerization. Similar results have been seen on the Pt_3Co/SiO_2 and Pt_3Fe/SiO_2 alloys explored in our group, where residual Co^{2+} and Fe^{2+} single sites were on the SiO_2 respectively. This has led to interest in single site catalysts for oligomerization to convert the olefins produced by dehydrogenation to fuel ranged products, including long-chain, linear paraffins and olefins (diesel), in addition to branched products and aromatics (gasoline).

Therefore, the second part of this thesis aims to convert the olefins obtained by dehydrogenation to higher molecular weight hydrocarbons using silica supported single site catalysts. Single site catalysts were previously shown to perform dehydrogenation but have much lower rates than Pt-based catalysts. Here, single site Ga^{3+}, Zn^{2+}, and Co^{2+} were explored and compared to Ni^{2+}. It is unprecedented for main group metals like Ga^{3+} and Zn^{2+} to perform oligomerization. In addition, the product distributions vary significantly across these catalysts. A mechanistic understanding of oligomerization on these catalysts was developed by using advanced *in situ* characterizations to identify relevant reaction intermediates and the conditions in which they form (*i.e.* metal hydrides and metal alkyls).

Key conclusions of this work are discussed in further detail below.

7.1 The formation of bimetallic nanoparticles and implications on synthesis

Understanding the formation of bimetallic catalysts, especially on the nanoscale, begins with detailed characterizations of the catalyst structure. Advanced characterizations using synchrotron radiation (XAS and XRD) are powerful tools for identifying the structures of small nanoparticles. Specifically, it is important to determine if the nanoparticles contain an ordered phase (alloy) or a disordered phase (solid solution). For the former, the appropriate morphology and phase must also be assigned. Sometimes, more than one phase can be present, so it is important to determine if the phase containing the promoter is on the surface. In this thesis, 3-5 nm Pt-Cr nanoparticles are explored. Although the alloys explored in literature frequently use post transition metal promoters (*e.g.* In, Zn, Sn), Cr is a transition metal and is challenging to reduce. In the former, high reducibility of the promoter oxide leads to the formation of multiple phases (*e.g.* PtM, Pt_3M) and morphologies (*i.e.* core shell, full alloy, covered alloy). In the latter, it was difficult to facilitate the reduction of CrO_x thus forming Pt-Cr bonds. This led to the formation of partial core shells (Pt core with Pt_3Cr surface) at reduction temperatures less than 550°C, core shells at reduction at 550°C, and full Pt_3Cr alloy at reduction at 800°C. A promoter rich phase was not achieved, as has been seen in the past for Pt-In and Pt-Zn. This is critical because it means that the targeted metal ratio during synthesis, in addition to how the materials are treated after synthesis, can all change the catalyst structure.

The structural evolution of a catalyst containing 2 wt% Pt and 3 wt% Cr was studied as a function of reduction temperature. This was only possible due to the *in situ* capabilities available for XAS and XRD measurements. Through catalyst characterizations of the reduced, oxidized, and surface structures, it was noted that Pt nanoparticles form first at low reduction temperatures. Although the metal oxides of Pt and Cr are deposited on the SiO_2 surface, the reduction of PtO_x is more kinetically favorable than Cr_2O_3, thus, Pt is initially reduced. Pt activates H_2, reducing Cr_2O_3 at lower temperatures than in the absence of Pt, thus facilitating a solid-state reaction. Small amounts of metallic Cr are incorporated in the initially formed Pt nanoparticles as low as 250°C. At this temperature, the nanoparticles are Pt-rich. The surface analysis, however, indicates that the surface has more metallic Cr than the reduced nanoparticle, but that a full monolayer has not yet formed. In addition, the EXAFS of the particle interior shows little Cr. These analyses are consistent with a mechanism of alloy formation where catalytic reduction of nearby Cr_2O_3 leads to a surface alloy.

The incorporation of the promoter begins at the surface and moves toward the core. Low temperatures are needed for the reaction for the initial particle to form. Though, because Cr_2O_3 is challenging to reduce, higher temperatures are needed to facilitate full alloy formation.

7.2 Identifying the precise structure of nanoparticle is critical for understanding their reactivity

Pt and Pt_3Cr have similar lattice parameters and are difficult to distinguish in bulk. By XRD, the near proximity of monometallic Pt and Pt_3Cr reflection positions make it difficult to distinguish between the two phases in small nanoparticles. This is addressed by using synchrotron radiation to determine the phases present in the nanoparticles at various stages of nanoparticle formation. The high flux of the synchrotron XRD gives better signal to noise and the high energy x-rays allow for increased sensitivity for heavy scatters, for example, Pt nanoparticles compared to SiO_2. Likewise, synchrotron XAS is used to determine the local arrangement of Pt atoms. Slight shifts in the XANES energy with increasing reduction temperature suggest a greater effect of Cr on the Pt nanoparticle, consistent with increased Cr incorporation. However, when two nanoparticles have similar structures, these bulk averaged techniques sometimes do not reflect the actual nanoparticle structure.

For instance, in Chapter 2, two Pt-Cr bimetallic catalysts with varying nominal Cr content were introduced. Although their catalytic performance was different (*i.e.* different trends in selective behavior), their bulk characterizations were nearly identical. To address this, a method of surface analysis was used to identify the precise structure of nanoparticles. This method works by reducing nanoparticles at a given temperature and subsequently exposing to air, resulting in surface oxidation. The difference between the two raw spectra result in a new spectrum corresponding to the active catalytic surface. Through this, it was found that low reduction temperatures lead to the formation of core shells, while higher reduction temperatures lead to the formation of full alloys. This chapter highlights that a precise understanding of the catalytic surface of nanoparticles is critical for relating their structure to activity. Both the composition and reduction temperature affect the resulting structure and morphology.

Chapter 3 presents multiple examples using the surface analysis method for understanding the specific structures of nanoparticles. A series of Pt-Co catalysts were prepared with varying nominal Co concentrations. Here, it was found that higher concentrations of Co led to more Co

rich alloy phases. Unlike the Pt-Cr catalysts, the core of the Pt-Co nanoparticles tended to be more Co rich, while the surface structure maintained a Pt_3Co phase. Here, multiple ordered phases were achieved (*i.e.* Pt_3Co, PtCo). Because CoO is easier to reduce that Cr_2O_3, the incorporation of the former occurred at lower reduction temperatures. Finally, a series of Pt-V catalysts were prepared with varying nominal V concentrations. Like Pt-Cr, it was challenging to promote the formation of a full Pt_3V alloy. This example highlights that to perform experiments studying the electronic properties of a catalyst, the precise surface structure must be identified to ensure a single phase throughout the nanoparticle otherwise the resulting measurement will be a weighted average of the phases present.

7.3   Geometric effects contribute to high propane dehydrogenation selectivity

In intermetallic alloy literature, there is a debate over whether geometric or electronic effects control the high selectivity of bimetallic catalysts. Though the electronic effects were not studied in this thesis, it is proposed that the geometric effects, or breaking up the number of Pt atoms next to each other, leads to higher olefin selectivity during propane dehydrogenation. When an alloy is formed, the promoter reduced the size of the Pt ensemble. Like the commercially available Pt_3Sn catalyst, Pt-Cr forms Pt_3Cr-both of which are FCC. Although Cr is less electronegative than both Pt and Sn, it has fewer electrons (3d), while Sn has more electrons (4p). Therefore, if electrons were transferred between Pt and its promoter, it would be expected that Pt-Cr and Pt-Sn would behave differently. If electronic properties controlled the catalytic selectivity and the electron transfer theory is correct, Cr, which has vacant d-orbitals, will withdraw electron density from Pt. This change would increase the density of states, increase the adsorption energy, and increase coking rates, which is not favorable for dehydrogenation. The changes expected due to electronic effects would not be consistent with those caused by geometric modifications in isolated Pt atoms that lead to higher olefin selectivity. A thorough study of Pt-Cr catalysts revealed that those containing a full monolayer coverage of Pt_3Cr have higher olefin selectivity ($> 97\%$) compared to partially covered Pt surfaces (88%).

7.4 Dehydrogenation and oligomerization share common reaction intermediates

Chapters 4 and 6 propose a mechanistic relationship between dehydrogenation and oligomerization, both of which have well understood reaction pathways, though a direct connection between the two has not been reported. Based on observations seen on the alloy catalysts, like Pt-Cr, it is believed that olefin oligomerization could be conducted at reaction temperatures typical of alkane dehydrogenation. However, due to different reaction conditions of dehydrogenation (500°C -750°C and atmospheric pressure) and oligomerization (150°C -200°C and 10-15 atm), there are no known commercial technologies at high temperatures, that alone perform both reactions, especially in a single reactor. Single site catalysts were previously shown to perform dehydrogenation but have much lower rates than Pt-based catalysts. These are stable at high temperatures and the reactions are thought to occur through the same intermediates (metal hydrides (M-H) and metal alkyls (M-R)) as oligomerization. The scope the second half of this thesis was focused on implementing non-traditional, non-acidic single site catalysts for high temperature oligomerization and showing that the M-H is the active species for oligomerization.

In dehydrogenation (550°C, 1 atm), it has been proposed that an alkane is inserted to the 4-coordinate single site catalyst metal center, forming a metal alkyl. β-hydride elimination to the metal alkyl leads to the formation of an olefin and a metal hydride intermediate. The initial 4-coordinate catalyst structure is reformed by C-H bond activation. In hydrogenation (200°C, 1 atm), the microscopic reverse of dehydrogenation that occurs at lower reaction temperatures, the single site catalyst can activate H_2 to form a metal hydride. Metal hydrides can facilitate olefin insertion to form a metal alkyl and produce a paraffin when it is desorbed from the metal surface. The initial catalyst structure is reformed.

Similarly, oligomerization proceeds through the metal hydride intermediate. Ethylene can insert to form a metal alkyl intermediate. Sequential insertion (propagation) leads to the formation of longer chain olefins, until β-H elimination (termination) facilitates the desorption of the reaction product. When the metal hydride intermediate is reformed, the catalyst can go through the catalytic cycle again.

Hydrogenation/dehydrogenation and oligomerization are related through the formation of the same reaction intermediates and the ability to perform the same elementary reaction steps, though different reaction conditions are required. Evidence of Ga-H and Zn-H was determined by XAS, IR, and isotope exchange. When the hydride is formed, it can perform subsequent alkylation.

However, there is no experimental evidence of Co-H. Experimental and theoretical studies on Ga^{3+} demonstrate that the pre-formation of Ga-H is not necessary to facilitate oligomerization. Instead, catalyst initiation can occur by the activation of C-H bonds to form a vinylic metal alkyl. The desorption of butadiene leads to the formation of a metal hydride, which can facilitate oligomerization.

7.5   Single site catalysts perform olefin transformation reactions

The reaction conditions to facilitate oligomerization on Ga^{3+}, Zn^{2+}, and Co^{2+} were also explored in Chapters 4, 5, and 6. On each of these single sites, high reaction temperatures lead to higher rates and the formation of unexpected reaction products.

At 250°C, the reaction rates are low, however, the product distribution is limited to only oligomerization catalysts. For instance, while Zn^{2+}, like Ni^{2+}, favors primarily dimerization (ethylene to butylene), Ga^{3+} and Co^{2+} favor the formation of some higher molecular weight hydrocarbons (up to $C_8^=$ at 250°C and 1 atm). Under these conditions, trace methane and alkanes are also observed, indicating that H_2 is formed *in situ*. Likewise, reaction rates are ordered such that Zn^{2+}~$Co^{2+} < Ga^{3+} < Ni^{2+}$.

When the reaction temperature is increased to 450°C, Ni^{2+} cannot perform oligomerization because it reduces to Ni^0. However, Ga^{3+}, Zn^{2+}, and Co^{2+} resist reduction. At 450°C and 1 atm, reaction rates nearly doubled for all catalysts. Although oligomerization is observed, unprecedented products, like propylene, are also formed. This was interpreted as olefin metathesis. This was confirmed by performing reactions using propylene, thus leading to the formation of ethylene and butylene.

This chemistry is unprecedented on $Ga^{3+}$and Zn^{2+}. The heterolytic C-H and H_2 bond activation is critical for this performance and, therefore, higher reaction rates can be achieved at higher reaction temperatures. Through this, it was concluded that a suitable oligomerization catalyst is one that has high thermal stability and forms metal-hydrogen and metal-carbon bonds (as has been shown for dehydrogenation). Although both $Ga^{3+}$and Zn^{2+} are atypical oligomerization catalysts, they can form the necessary intermediates required to facilitate the reaction (*i.e.* metal hydride and metal alkyl). By changing the identity of the active metal, we can increase control of the resulting product distribution and can lead to variability in the process conditions because unlike Ni^{2+}, neither Ga^{3+} nor Zn^{2+} will reduce to a lower oxidation state, even at high temperatures in H_2.

Co^{2+} is a transition metal like Ni^{2+}, however, does not perform oligomerization under the same conditions. While Ni^{2+} performs oligomerization at low temperature, Co^{2+} only reacts with reasonable rates at higher temperatures.

7.6   Ending Remarks

This thesis highlights the synthesis, characterization, and catalytic performance of both bimetallic alloy and single site catalysts to be used in dehydrogenation and oligomerization, respectively. However, a common thread remains that the precise structure of the active catalyst and reaction intermediates is needed to understand the catalytic performance. Through this, the determination of structure-function relationships can be made, thus shedding light on catalyst design principles needed to control reaction conditions, product distributions, and activity.

APPENDIX A. METHOD FOR SURFACE ANALYSIS USING BULK TECHNIQUES

A.1   Description of the Analysis

While the combination of bulk techniques like XAS and XRD can indicate that two phases are present in bimetallic nanoparticles (*e.g.* Pt and Pt_3M), for catalytic applications it is essential to determine the composition and structure of the surface. Both XAS and XRD are bulk-averaged techniques, so the data reflects an average measurement across the entire particle. However, the surface of nanoparticles is sensitive to chemical reactions. For example, if the surface of a Pt-based nanoparticle is exposed to air at room temperature, it will surface-oxidize, resulting in the loss of Pt-Pt and Pt-M bonds to the formation of Pt-O bonds.[1] This works similarly to H_2-O_2 titration, which is commonly used to measure the dispersion of Pt-based nanoparticles.[2–4] While this technique is a reliable way of measuring the metal surface area during room temperature reactions, there are sometimes problems when low concentrations of metals are present, like in commercial catalysts (*e.g.* Pt/Al_2O_3). While other methods like CO chemisorption could also be used to measure the Pt dispersion, the ability to determine the surface area of bimetallic surfaces is particularly challenging when the promoter (*e.g.* Cr, Co, Fe) also absorbs the probe molecule. The method of identifying the surface compositions developed within our group is element specific and relies on room temperature surface reactions. A visual representation is provided in Figures 2.8 and 3.3 above.[5] While this approach was introduced in Chapter 2 and elaborated upon with further case studies in Chapter 3, Appendix A will provide the steps for completing the analysis, in addition to the challenges and limitations of this method.

A.2   Example using 2Pt3Cr/SiO₂

XAS provides information about the local geometry of Pt, while XRD indicates the specific phases present. In Chapter 2, two Pt-Cr bimetallic catalysts were introduced ($2Pt1Cr/SiO_2$ and $2Pt3Cr/SiO_2$). While the former had a low Cr content and never formed a full alloy, the latter had increasing Cr incorporation until a core shell ($Pt@Pt3Cr$) formed after reduction at 550°C and a full alloy formed after reduction at 800°C.

The catalyst structure was measured by XAS and XRD after reduction at increasing temperatures and subsequent room temperature exposure to air after each H_2 treatment. First, the

reduced spectrum provides information about the bulk structure. Typically, experimenters believe that this information is enough to understand the complete catalyst structure. However, this does not provide information about the catalytic surface, which can vary with synthesis methods, pre-treatment, and reaction conditions. However, post reduction exposure to air also provides essential information. The spectra of an oxidized nanoparticle could be fit directly to learn information about the averaged atomic structure of subsurface layers plus the oxidized surface. Taking this a step further, the method of difference analysis can be used to identify the surface structure. By subtracting the oxidized from reduced spectra, the constant, non-oxidized core is removed so that only the remaining surface layer can be analyzed. This is performed by subtracting the oxidized from reduced k^0-weighted spectrum, which results in a pattern corresponding to the surface of the nanoparticle. After the k^2-weighted chi spectrum of the difference EXAFS is Fourier transformed, the data can be fit to obtain coordination numbers and bond distances corresponding to the surface structure. An example of the Fourier transform magnitude of each of these three spectra is provided in Figure A.1.
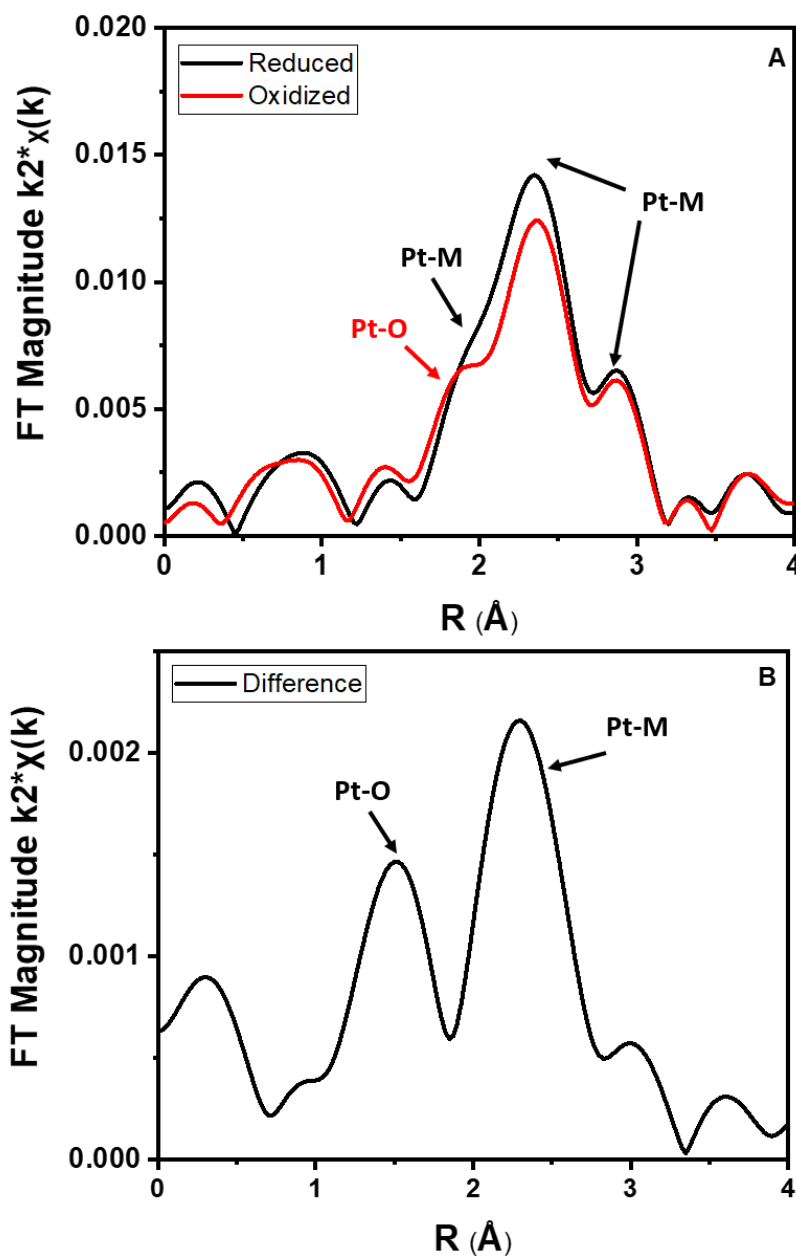
Figure A.1. A) Reduced (black) and oxidized (red) Fourier transform magnitude of $2Pt3Cr/SiO_2$ and B) difference spectra

From Figure A.1, it is evident that the changes upon oxidation are small. Surface oxidation leads to the loss of Pt-M bonds and the formation of Pt-O bonds, which can be used to measure the number of surface Pt atoms, or dispersion, since when the nanoparticles are fully oxidized, $CN_{Pt-O} = 4$. The subsequent surface oxidation results in a small shoulder at approximately 1.8 Å

and a loss of intensity of metal-metal scattering at approximately 2.4 Å and 2.9 Å. If the fit Pt-O coordination number was 0.7, then the fraction of oxidized Pt would be $0.7/4 = 0.175$, or about 18% dispersion. This method of surface oxidation for probing the surface structure works well for small particles (2-6 nm), where at least 15% of the atoms are on the surface. For particles < 2 nm, where the dispersion is nearly 100%, the complete loss of Pt-M to the formation of Pt-O is observed. The coordination number can be used to calculate the dispersion, so it is limited by the accuracy of the EXAFS fitting. When the nanoparticles are too large, the dispersion is small and there is a larger error in this measurement.

In order to obtain the difference spectra, the reduced and oxidized spectra must normalized in XANES and shifted to the same XANES energy (E_o), which is the inflection point in the normalized absorption curve, or where the second derivative reaches 0. Failure to shift the oxidized spectra to the same XANES energy as the reduced spectra will result in artificial peaks in the Fourier transform magnitude. Once E_o is set for both spectra, a k^0-weighted chi can be extracted. Then, a difference operation can be performed while interpolating the data array. In WinXAS software, the appropriate menu for this is shown in Figure A.2.
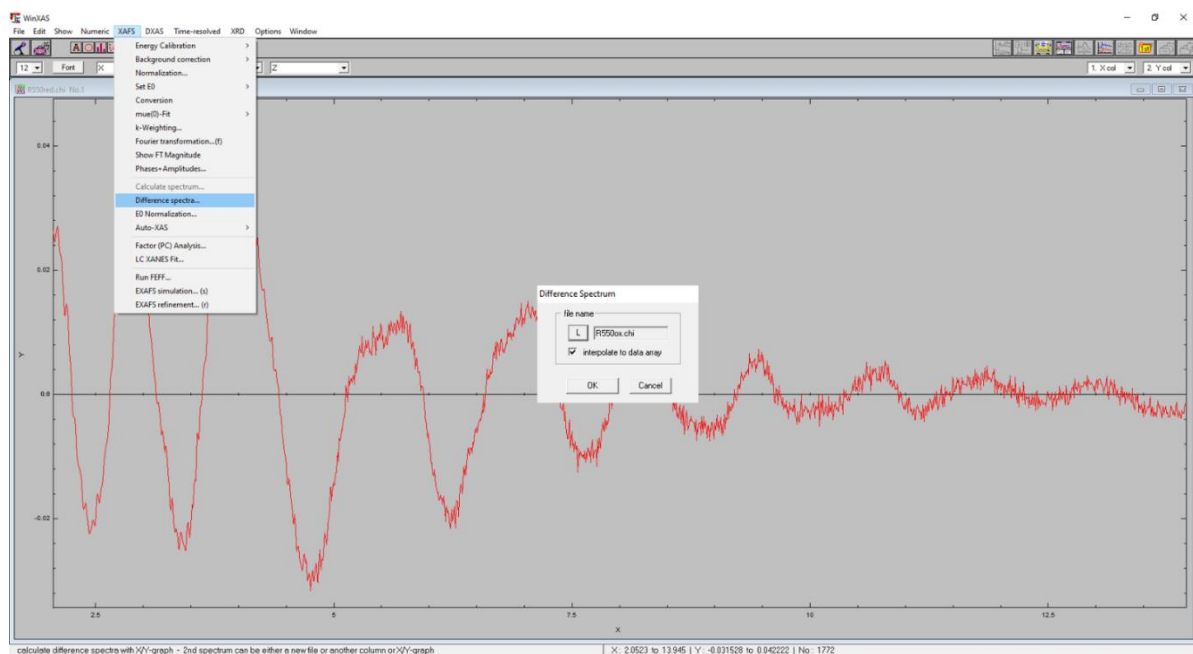
Figure A.2. WinXAS window of difference spectrum command

Once the difference analysis is performed, a k^0-weighted spectrum will be recovered with lower overall intensity than in either of the original spectrum (Figure A.3). This is because,

presumably, the unchanged core, which contains metal-metal bonds, is subtracted out. This can be k^2-weighted and then a Fourier transform can be performed to obtain a spectrum like that in Figure A.4.

Figure A.3. WinXAS window of k^0-weighted chi of the difference spectrum (reduced-oxidized)

Figure A.4. WinXAS window of resulting Fourier transform magnitude of the k^2-weighted difference spectrum

In order to fit the Fourier transform magnitude of the difference spectra, Pt-M and Pt-O scattering pairs are needed. The Pt-M and Pt-O scattering pairs can be obtained using experimental references. While Pt-O can be obtained from a PtO reference, 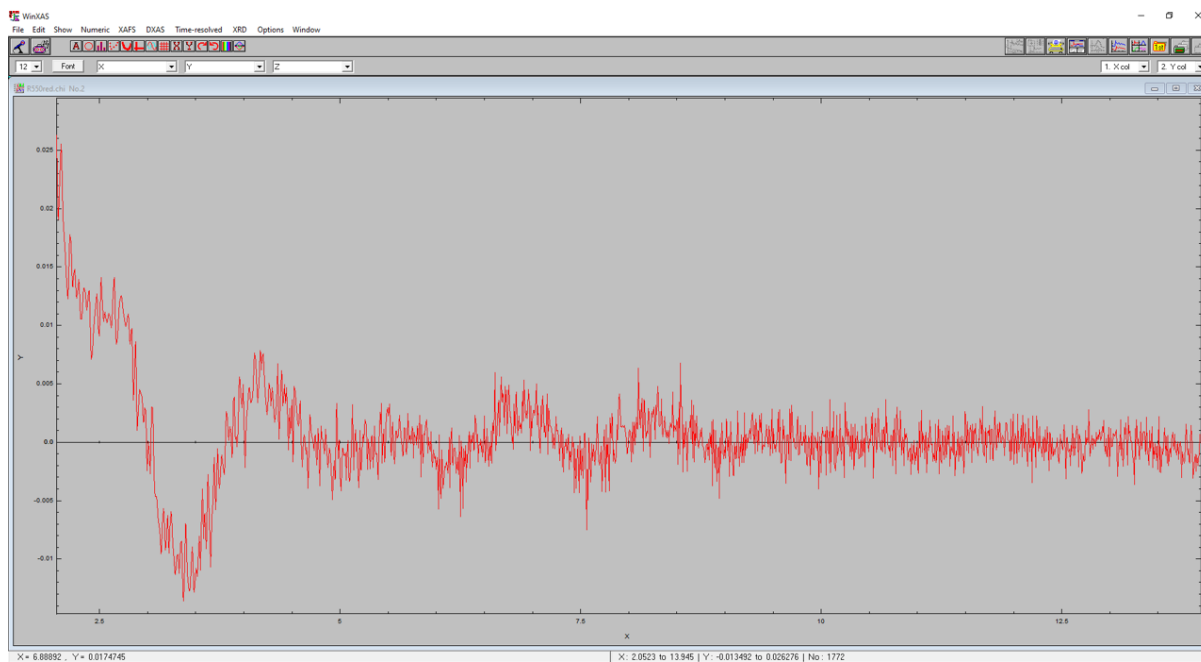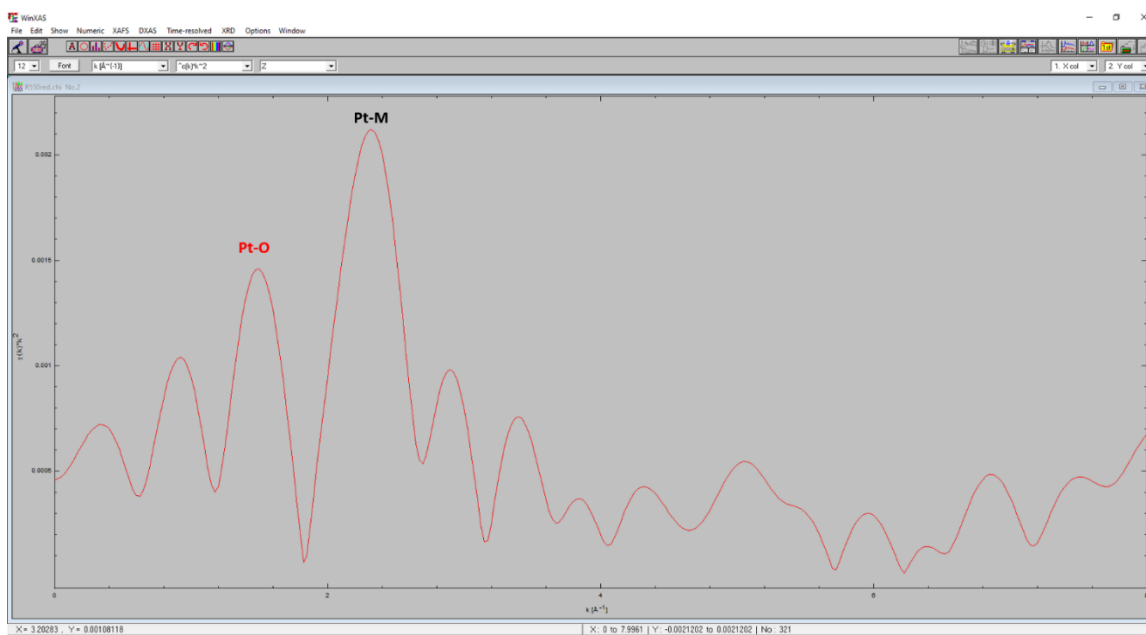an appropriate experimental reference for a new Pt-M phase is sometimes difficult to determine. Instead, FEFF6, in combination with an approximated bond distance obtained from a cif file of a known structure, can be used to extract phase (.pha) and amplitude (.amp) files for each scattering pair. Once the Pt-O .pha file is created, it must be shifted by π radians to put it in phase with the metal-metal bonding from the Pt-M scattering pair. Using WinXAS, the .pha file can be opened and modified using the commands shown in Figure A.5.
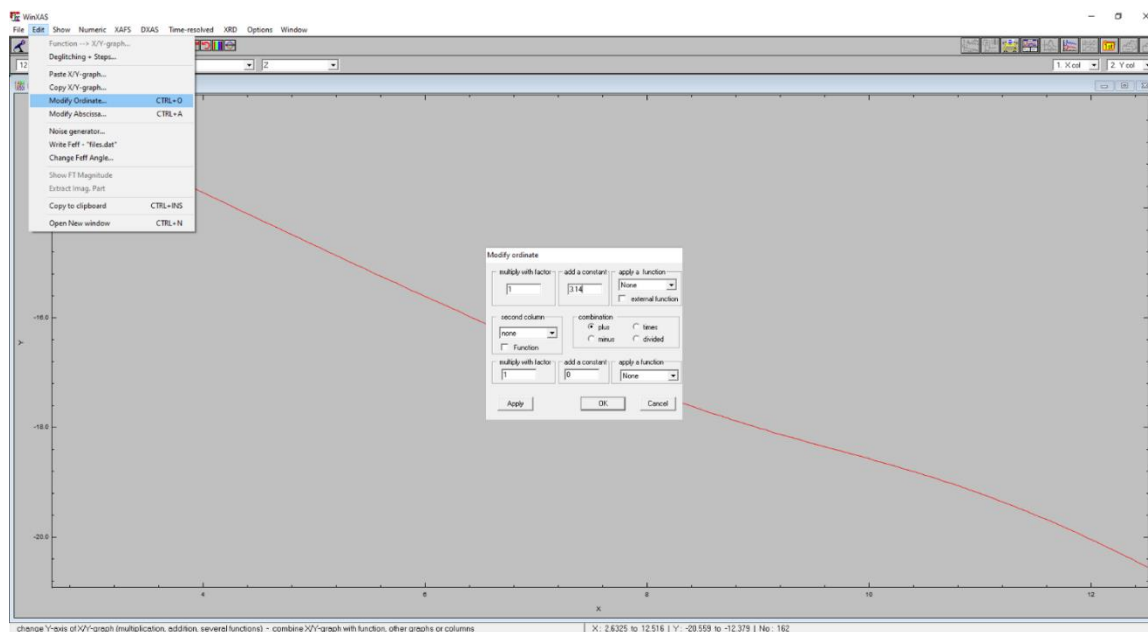
Figure A.5. WinXAS window of shifting Pt-O pha file

The difference Fourier transform magnitude can then be fit in real and imaginary space using standard fitting procedures. As has been discussed in Chapter 2, increasing the reduction temperature of 2Pt3Cr/SiO$_2$ leads to slightly larger particles with increased Cr incorporation, as evidenced through a Pt-Cr/Pt-Pt coordination number ratio at the surface approaching 0.5, which is characteristic of a bulk Pt$_3$Cr phase. Similar difference analysis was performed using XRD,

which is much more sensitive to particle size. Figure A.6 shows that when the sample was subsequently oxidized by XRD, the FWHM decreased, *i.e.* decreased peak broadening. This holds true when the peaks are broad. However, when peaks are sharpened with larger particle size, no changes are observed.
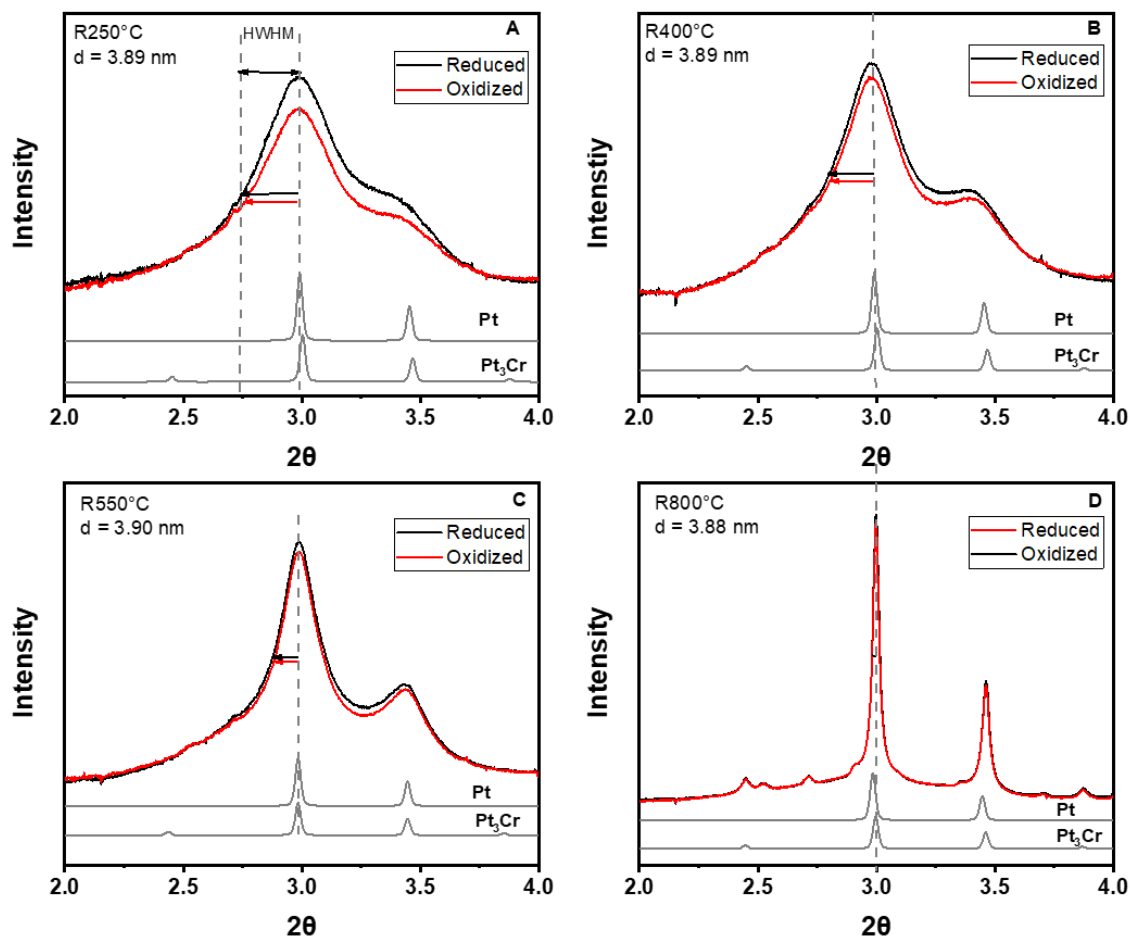
Figure A.6. Reduced and oxidized XRD as a function of reduction temperature

The decrease in intensity and narrowing of the x-ray reflections is consistent with the loss of an ordered metallic phase to the formation of amorphous oxides. The degree of which this change decreases with increasing reduction temperature, as the particle size increases. Likewise, it is evident that the peak becomes more symmetric n the higher angle side. This suggests that while both Pt and Pt_3Cr are present in the average nanoparticle structure, a surface reaction is occurring

between air and Pt_3Cr. Through this method, surface Pt_3Cr was identified and a core shell structure was confirmed after reduction at temperatures higher than 550°C. The resulting difference XRD pattern is obtained from the direct subtraction of the raw data.

A.3   Challenges and Limitations

Identifying the surface structure of nanoparticles is challenging. While this approach should work for any catalytic system where only the surface layer changes with a given reaction, it is extremely sensitive to particle size. Particle size is indirectly proportional to the dispersion. For example, a 2 nm nanoparticle has a dispersion of about 50%. In order to perform this analysis, the particles must be smaller than approximately 6-7 nm and have at least 15% of atoms on the surface. In larger particles, only a small fraction of atoms is exposed and the changes resulting from the surface reaction are convoluted by the bulk.

This approach has been used to measure the surface structure (and degree of alloying) on varying Pt-M systems (M = Cr, V, Co, Fe) and some Ni-M systems (M = Mo).[5–9] While it has only been performed using reduction and subsequent room temperature oxidation, it can also be performed under reaction conditions (*e.g.* high temperature and in the presence of hydrocarbons). The specific target reaction should be considered to prevent restructuring in the bulk.

A.4   References

1. Gallagher, J.R.; Li, T.; Zhao, H.; Liu, J.; Lei, Y.; Zhang, X.; Ren, Y.; Elam, J.W.; Meyer, R.J.; Winans, R.E.; Miller, J.T. In situ diffraction of highly dispersed supported platinum nanoparticles. *Catal. Sci. Technol.* **2014**, 4, 3053–3063.

2. Benson, J.E.; Boudart, M. Hydrogen-oxygen titration method for the measurement of supported platinum surface areas. *Journal of Catalysis*. **1965**, 4, 704–710.

3. Suh, D.J.; Park, T.J.; Ihm, S.K. Hydrogen/Oxygen Titration Method for Measurement of Pd Dispersion on Supported Catalysts. *Journal of Catalysis*. **1994**, 149, 486–488.

4. Akhtar, M.; Tompkins, F.C. The hydrogen/oxygen titration on platinum films. Determination of the catalytically-active area. *Trans. Faraday Soc.* **1971**, 67, 2454–2460.

5. LiBretto, N.J., Yang, C., Ren, Y., Zhang, G.; Miller, J.T. Identification of Surface Structures in Pt3Cr Intermetallic Nanocatalysts. *Chemistry of Materials*. **2019**, 31, 5, 1597–1609.

6. Purdy, S.C.; Ghanekar, P.; Mitchell, G.; Kropf, A.J.; Zemlyanov, D.Y.; Ren, Y.; Ribeiro, F.; Delgas, W.N.; Greeley, J.; Miller, J.T. Origin of Electronic Modification of Platinum in a Pt3V

Alloy and Its Consequences for Propane Dehydrogenation Catalysis. *ACS Appl. Energy Mater.* **2020**, 3, 2, 1410-1422.

7. Cesar, L.G.; Yang, C.; Lu, Z.; Ren, Y.; Zhang, G.; Miller, J.T. Identification of a Pt 3 Co Surface Intermetallic Alloy in Pt–Co Propane Dehydrogenation Catalysts. *ACS Catalysis*. **2019**, 9, 6, 5231–5244.

8. Yang, F.; LiBretto, N.J.; Komarneni, M.R.; Zhou, W.; Miller, J.T.; Zhu, X.; Resasco, D.E. Enhancement of m-Cresol Hydrodeoxygenation Selectivity on Ni Catalysts by Surface Decoration of MoOx Species. *ACS Catal.* **2019**, 9, 7791–7800.

9. Wegener, E.C.; Bukowski, B.C.; Yang, D.; Wu, Z.; Kropf, A.J.; Delgas, W.N.; Greeley, J.; Zhang, G.; Miller, J.T. Intermetallic Compounds as an Alternative to Single-atom Alloy Catalysts: Geometric and Electronic Structures from Advanced X-ray Spectroscopies and Computational Studies. *ChemCatChem*. **2019**, 12, 5.

APPENDIX B. CALCULATING THE SHELL THICKNESS IN CORE SHELL NANOPARTICLES

B.1   Background and Importance

Quantifying the thickness of the shell in core-shell nanoparticles is important for determining the electronic properties of a material.[1,2] In many cases, there is an influence of the subsurface layer on the properties of the catalytic surface. While Appendix A described the method for identifying the composition of the surface structure, it does not provide a method to obtain a qualitative understanding. This appendix will go through the calculations to determine the shell thickness, as has been introduced in Chapter 2.

B.2   Example Calculations and Description

Chapter 2 describes 2Pt3Cr/SiO_2 at increasing reduction temperatures. While below reduction at 550°C, a partial core-shell was obtained, reduction at 550°C yielded a core-shell with a Pt_3Cr shell and Pt core, and reduction at 800°C led to a full Pt_3Cr alloy. As the reduction temperature increased, the Cr incorporation increased leading to sequentially increasing shell thickness. In order to calculate the shell thickness of the core shell, the total particle size is needed (TEM), in addition to the number of Pt-Pt and Pt-Cr bonds in both the bulk and surface. For guidance, the key variables, which can be obtained by a combination of characterization techniques (TEM, XAS, XRD), are illustrated in Figure B.1.
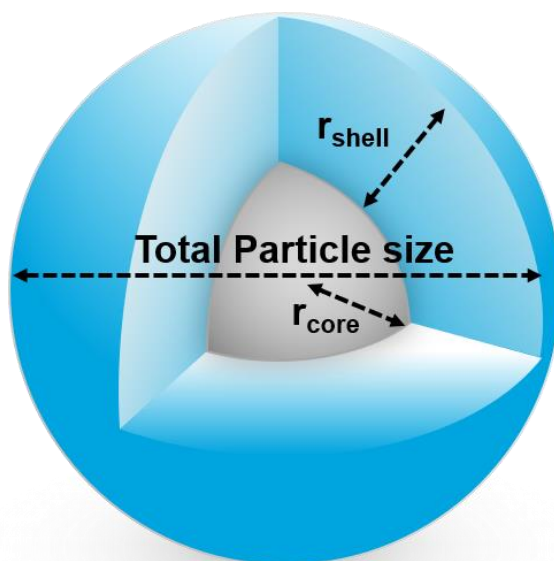
Figure B.1. Key variables on core shell nanoparticles

Using 2Pt3Cr/SiO$_2$ after reduction at 550°C as an example, the following variables are key:

1. Total particle size = 2.5 nm = 25Å

2. Bulk geometry = 2.4 Pt-Cr bonds and 8.1 Pt-Pt bonds

3. Surface geometry = 2.4 Pt-Cr bonds and 4.2 Pt-Pt bonds

4. Pt-Cr bond distance in bulk Pt$_3$Cr = 2.73 Å

The steps for calculating the shell thickness is described below:

1. Using the total particle size, calculate the volume of the nanoparticle (assuming the nanoparticle is a sphere)

$$V_{nanoparticle} = \frac{4}{3}\pi(\frac{total\ particle\ size}{2})^3$$

$$V_{nanoparticle} = \frac{4}{3}\pi(\frac{25\ \text{Å}}{2})^3 = 8181\ \text{Å}^3$$

2. Using the Pt-Cr bond distance in bulk Pt$_3$Cr (R$_{ideal,Pt-Cr}$), calculate the volume of the unit cell (also assuming spherical geometry)

$$V_{unit\ cell} = \frac{4}{3}\pi(\frac{R_{ideal,Pt-Cr}}{2})^3$$

$$V_{unit\ cell} = \frac{4}{3}\pi(\frac{2.73\ \text{Å}}{2})^3 = 11\ \text{Å}^3$$

3. Determine the number of atoms in the total nanoparticle

$$\#Atoms_{nanoparticle} = \frac{V_{nanoparticle}}{V_{unit\ cell}}$$

$$\#Atoms_{nanoparticle} = \frac{8181\ \text{Å}^3}{11\ \text{Å}^3} = 744\ atoms$$

4. Use the bulk XAS ratio to determine the amount of Pt in the core vs. shell

Assume all 2.4 Pt-Cr bonds is due to alloy formation. In a bulk Pt₃Cr structure, $\frac{CN_{Pt-Cr}}{CN_{Pt-Pt}} =$ 0.5. Therefore, $\frac{2.4}{x} = 0.5$, where x is the number of Pt-Pt bonds due to alloy formation. In this case, x = 4.8. If there are 4.8 Pt-Pt bonds due to alloy formation, this means that $\frac{4.8}{8.1} =$ 60% of Pt bonding is in the Pt₃Cr shell while 40% is in the Pt core.

5. Determine the number of Pt atoms in the core

$$\#Atoms_{core} = \%Pt_{core} * \#Atoms_{nanoparticle}$$

$$\#Atoms_{core} = 0.4 * 744\ atoms = 398\ atoms$$

6. Calculate the volume of the core

$$V_{core} = \#Atoms_{core} * V_{unit\ cell}$$

$$V_{core} = 398\ atoms * 11\ \text{Å}^3 = 3272\ \text{Å}^3$$

7. Calculate the radius of the core

$$r_{core} = (\frac{3}{4\pi}V_{core})^{1/3}$$

$$r_{core} = (\frac{3}{4\pi}3272\ \text{Å}^3)^{1/3} = 10\ \text{Å}$$

8. Calculate the radius of the shell

$$r_{shell} = \frac{total\ particle\ size - 2r_{core}}{2}$$

$$r_{shell} = \frac{25 \text{ Å} - 2 * 10 \text{ Å}}{2} = 2.5 \text{ Å} = 0.25 \, nm$$

In order to make these approximations, the location of the promoter (*i.e.* surface or interior) must be determined using a combination of XAS and XRD, in addition to the method of surface analysis described in Appendix A. The thickness of the shell can be correlated to the promoter incorporation and may control the electronic properties of the nanoparticle (*i.e.* thicker shells lead to larger shifts in XANES energy, until a full alloy is formed).

B.3   References

1. Wu, Z.; Bukowski, B.C.; Li, Z.; Milligan, C.; Zhou, L.; Ma, T.; Wu, Y.; Ren, Y.; Ribeiro, F.H.; Delgass, W.D.; Greeley, J.; Zhang, G.; Miller, J.T. Changes in Catalytic and Adsorptive Properties of 2 nm Pt3Mn Nanoparticles by Subsurface Atoms. *J. Am. Chem. Soc.* **2018**, 140, 40, 14870-14877.

2. Purdy, S.C.; Ghanekar, P.; Mitchell, G.; Kropf, A.J.; Zemlyanov, D.Y.; Ren, Y.; Ribeiro, F.; Delgas, W.N.; Greeley, J.; Miller, J.T. Origin of Electronic Modification of Platinum in a Pt3V Alloy and Its Consequences for Propane Dehydrogenation Catalysis. *ACS Appl. Energy Mater.* **2020**, 3, 2, 1410-1422.

APPENDIX C. GA-H FORMATION AND SUBSEQUENT OLIGOMERIZATION (SUPPORTING CHAPTER 4)

Ga-H is considered a key intermediate in facilitating olefin oligomerization. The energy landscape of Ga-H formation and the subsequent ethylene oligomerization on the Ga sites containing different geometries are outlined in Figures C.1-C.5 and Tables C.1-C.5. The heterolytic cleavage of the C(sp2)-H bond in ethylene results in a loss of a Ga-O bond and the formation of a vinylic alkyl containing a C atom bearing a negative charge and neighboring hydroxyl group (Ga-C_2H_3). The initial activation of ethylene is endothermic with a free energy change of +0.84 eV and the activation barrier of the step is 1.70 eV. The resulting hydroxyl group becomes distant from the Ga site such that the resulting Ga-O bond distance increases from 1.88 Å to 2.92 Å.

A subsequent ethylene can insert in the Ga-vinyl intermediate. A migratory insertion reaction leads to the [Ga-butenyl]$^+$ species. The surface reaction between two ethylene molecules leads to the formation of butadiene. β-H elimination causes butadiene to desorb from the metal center, thus forming a Ga-H intermediate. Here, the migratory insertion of ethylene is the rate limiting step, with an intrinsic activation barrier of 2.80 eV. This is consistent with the energy barriers previously reported for Zn/SiO_2 following an elementary steps with a similar geometry of transition states for propane dehydroegnation.[3] For Zn/SiO_2, there is a 2.0 eV activation barrier for β-H elimination on a [Zn-propyl]$^+$ intermediate. On the Ga/SiO_2 site used in our model, there is a slightly higher barrier for β-H elimination (2.41 eV), which may be due to the longer attached carbon chain. The effective barrier of the formation of Ga-H is approximately 3.46 eV (Figure C.1). Once the Ga-H site is formed, it can facilitate subsequent oligomerization.

The formation of Ga-H has a high energy barrier, likely due to the endothermic nature of the first ethylene activation, which results in the high energies of all intermediates in the following steps. The formation of Ga-H and butadiene is made favorable on the 4CN Ga site (consistent with experimental evidence) by implementing an initial dehydration step between two adjacent Si-OH groups (Figure S12). With a low chemical potential of water in the environment, there is high thermodynamic favorability in a dehydration reaction initiated by the two adjacent Si-OH groups. The intrinsic enthalpy of dehydration is +1.62 eV, and the result is consistent with the dehydration calculations based on a similar silica model. Also, the partial pressure of water is estimated to be

less than 10^{-6} atm based on a typical composition of the UHP grade pure ethylene gas cylinder. Dehydration was performed using a water partial pressure of 10^{-9} atm, resulting in a lower free energy by approximately 0.2 eV. The effective barrier of the hydride formation decreased from 3.46 eV to 3.1 eV. Further, due to the amorphous nature of SiO_2 and the limitation of the DFT unit cell, there may exist less contained sites that demonstrate an even higher thermodynamic favorability of the dehydration process, which further lowers the energy barrier of the formation of Ga-H (Figure C.5, Table C.5).

Figure C.1. Top and side views of key intermediates and transition states of Ga-H formation of 4CN Ga site (Si = blue, O = red, H= white, Ga = green)

Table C.1. Bond distances of key intermediates during Ga-H formation of a 4CN Ga site

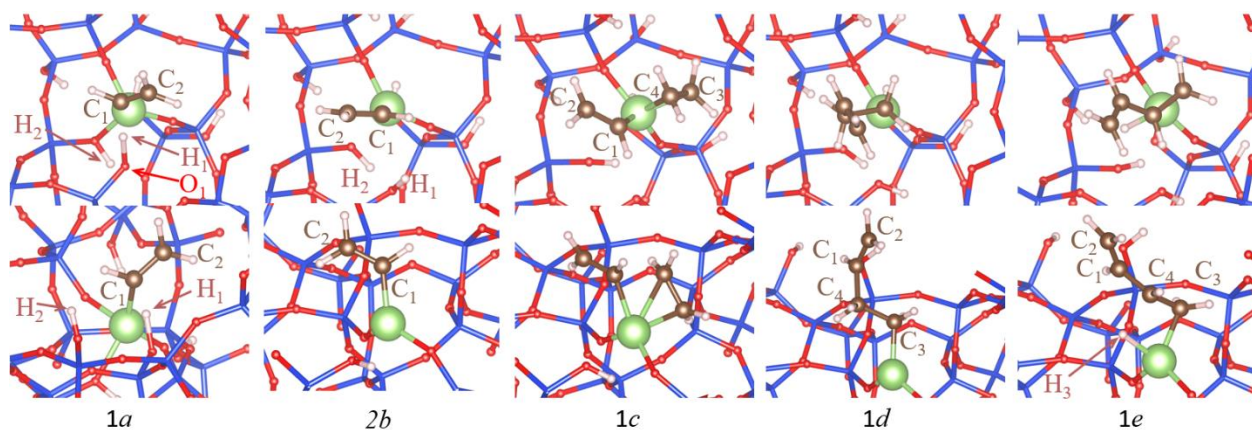| Intermediate*	Bond	Length (Å)	Free Energy (eV)	Energy (eV)
1a	$Ga - C_1$	2.22	1.70	0.97
	$O_1 - H_1$	1.33		
1b	$Ga - C_1$	1.98	0.66	-0.07
	$O_1 - H_1$	0.96		
1c	$Ga - C_1$	2.16	3.46	1.73
	$Ga - C_3$	2.03		
	$Ga - C_4$	2.36		
1d	$Ga - C_3$	2.00	0.59	-1.14
1e	$Ga - C_3$	2.05	3.00	1.27
	$Ga - H$	1.68		

* Intermediates shown in Figure C.1
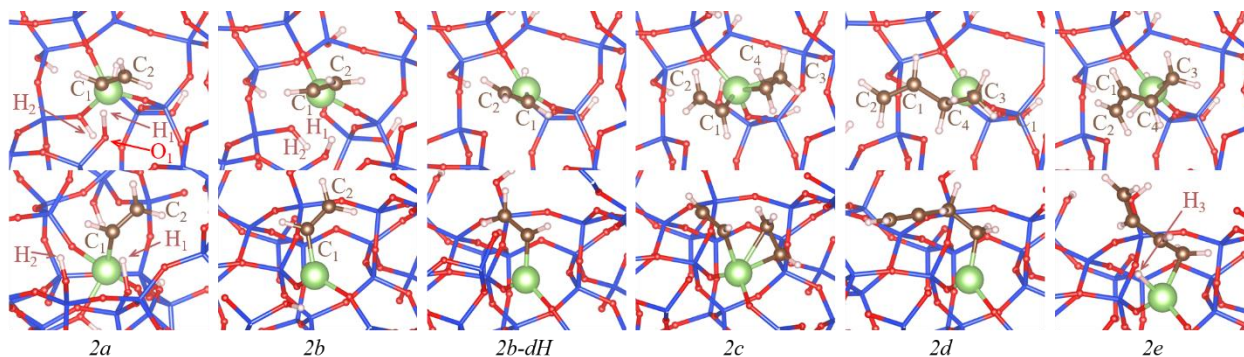
Figure C.2. Top and side views of key intermediates and transition states of Ga-H formation on post-dehydrated 4CN Ga site (Si = blue, O = red, H= white, Ga = green)

Table C.2. Bond distances of key intermediates during Ga-H formation on post-dehydrated 4CN Ga site

Intermediate*	Bond	Length (Å)	Free Energy (eV)	Energy (eV)
2a	$Ga - C_1$	2.22	1.70	0.97
	$O_1 - H_1$	1.33		
2b	$Ga - C_1$	1.98	0.66	-0.07
	$O_1 - H_1$	0.96		
2b − dH	$Ga - C_1$	1.96	0.47	1.55
2c	$Ga - C_1$	2.10	3.10	3.13
	$Ga - C_3$	2.04		
	$Ga - C_4$	2.34		
2d	$Ga - C_3$	2.00	0.40	0.43
2e	$Ga - C_3$	2.06	2.84	2.87
	$Ga - H_3$	1.71		

* Intermediates shown in Figure C.2

Figure C.3. Top and side views of key intermediates and transition states of ethylene oligomerization on Ga-H generated from post-dehydrated 4CN Ga (Si = blue, O = red, H= white, Ga = green)

Table C.3. Bond distances of key intermediates during ethylene oligomerization on Ga-H generated from post-dehydrated 4CN Ga

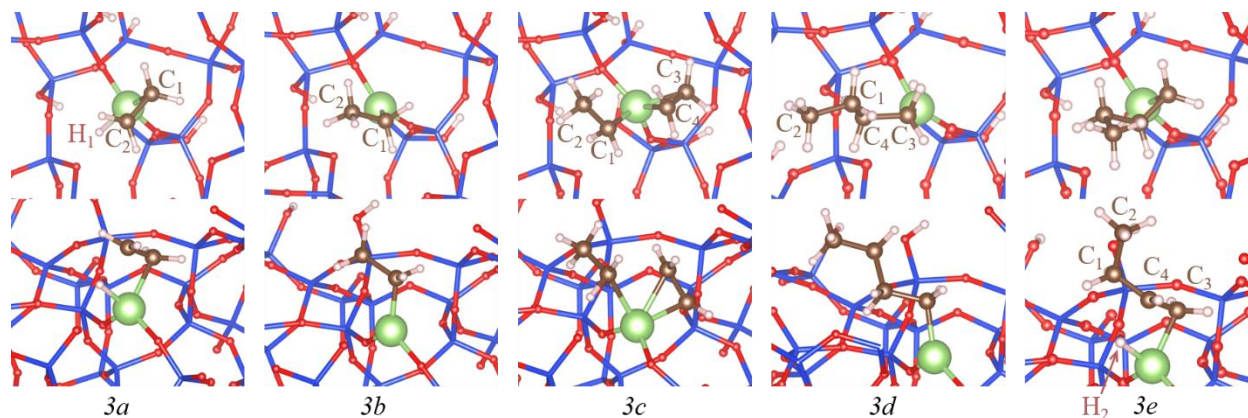| Intermediate*	Bond	Length (Å)	Free Energy (eV)	Energy (eV)
3a	Ga – C$_1$	2.11	1.99	1.07
	Ga – H$_1$	1.68		
3b	Ga – C$_1$	1.99	-0.68	-1.61
3c	Ga – C$_1$	2.20	2.25	0.43
	Ga – C$_3$	2.03		
	Ga – C$_4$	2.22		
3d	Ga – C$_3$	1.99	-0.90	-2.71
3e	Ga – C$_3$	2.09	1.67	-0.14
	Ga – H$_2$	1.67		

* Intermediates shown in Figure C.3

Figure C.4. Top and side views of key intermediates and transition states of ethylene oligomerization on Ga-H generated from 4CN Ga (Si = blue, O = red, H= white, Ga = green)

Table C.4. Bond distances of key intermediates during ethylene oligomerization on Ga-H generated from 4CN Ga

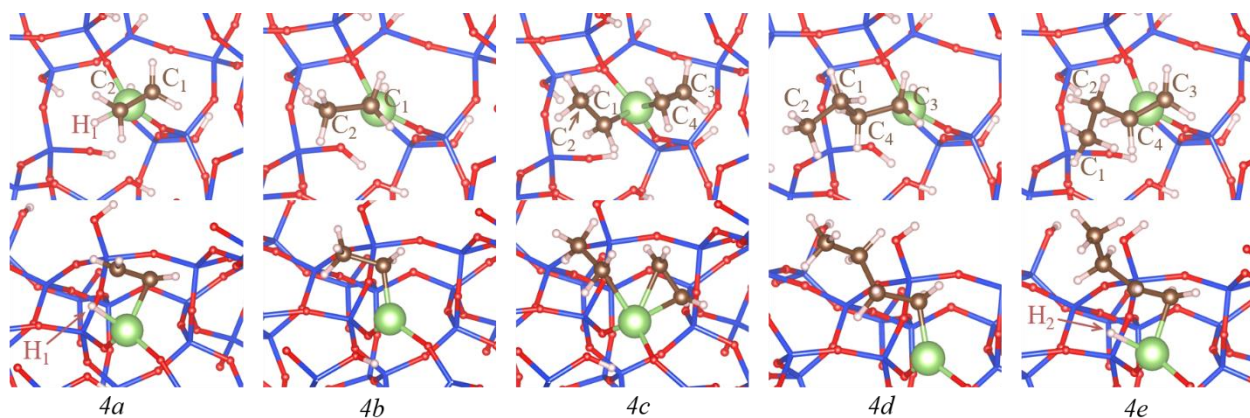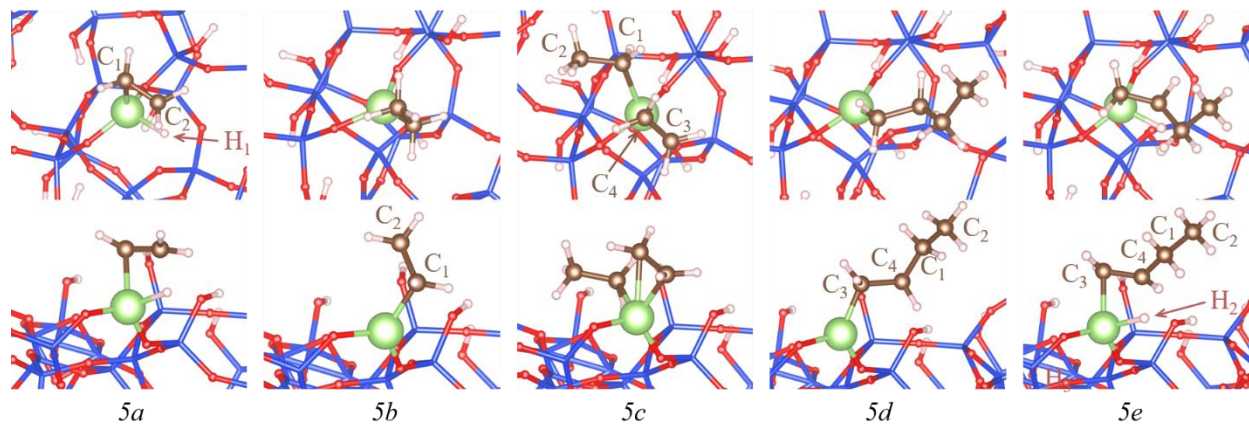| Intermediate*	Bond	Length (Å)	Free Energy (eV)	Energy (eV)
4a	Ga – C_1	2.10	1.94	1.02
	Ga – H_1	1.69		
4b	Ga – C_1	2.00	-0.50	-1.42
4c	Ga – C_1	2.28	2.48	0.69
	Ga – C_3	2.00		
	Ga – C_4	2.24		
4d	Ga – C_3	2.00	-0.64	-2.43
4e	Ga – C_3	2.09	1.69	0.11
	Ga – H_2	1.69		

* Intermediates shown in Figure C.4

Figure C.5. Top and side views of key intermediates and transition states of ethylene oligomerization on a Ga-H located in a less constrained, 3CN environment (Si = blue, O = red, H= white, Ga = green)

Table C.5. Bond distances of key intermediates during ethylene oligomerization on Ga-H generated from less constrained, 3CN Ga

Intermediate*	Bond	Length (Å)	Free Energy (eV)	Energy (eV)
5a	Ga – C_1	2.10	1.30	0.87
	Ga – H_1	1.71		
5b	Ga – C_1	1.98	-0.77	-1.20
5c	Ga – C_1	2.28	1.14	0.08
	Ga – C_3	2.04		
	Ga – C_4	2.26		
5d	Ga – C_3	1.98	-1.25	-2.31
5e	Ga – C_3	2.09	1.10	0.04
	Ga – H_2	1.70		

* Intermediates shown in Figure C.5

Figure C.6 shows the free energy diagram of ethylene oligomerization on Ga-H generated from 4CN sites with and without dehydration and from a 3CN site (less constrained) using the energies from Tables C.3, C.4, and C.5. While there is no difference in the general shape of the three free energy diagrams, the magnitude of the activation energies varies by up to 1.9 eV. The difference may be due to the steric hindrance originated from the local constrained environment. For example, on the less constrained Ga-H site, as the metal site binds to an ethyl group (intermediate 5b in Figure C.5), the α-carbon of the alkyl chain, the Ga atom, and two adjacent oxygen atoms form a co-planar geometry. However, the 4CN Ga site contains one additional Ga-O bond. The ethyl group cannot form a co-planar geometry with two Ga-O bonds. On the 4CN site with dehydration, the ethylene activation, ethylene insertion, and b-H elimination steps exhibit relatively high intrinsic barriers (1.99, 2.93 and 2.57 eV, respectively). For the less constrained, 3CN Ga-H site, accompanied with the exothermic nature of the formation of [Ga-n-butyl]$^+$ intermediate, the barriers are lowered (1.30, 1.39, and 2.35 eV, respectively).. The DFT analysis highlights the possibility of a wide range of kinetic barriers of ethylene oligomerization on Ga-H sites with different strain conditions.
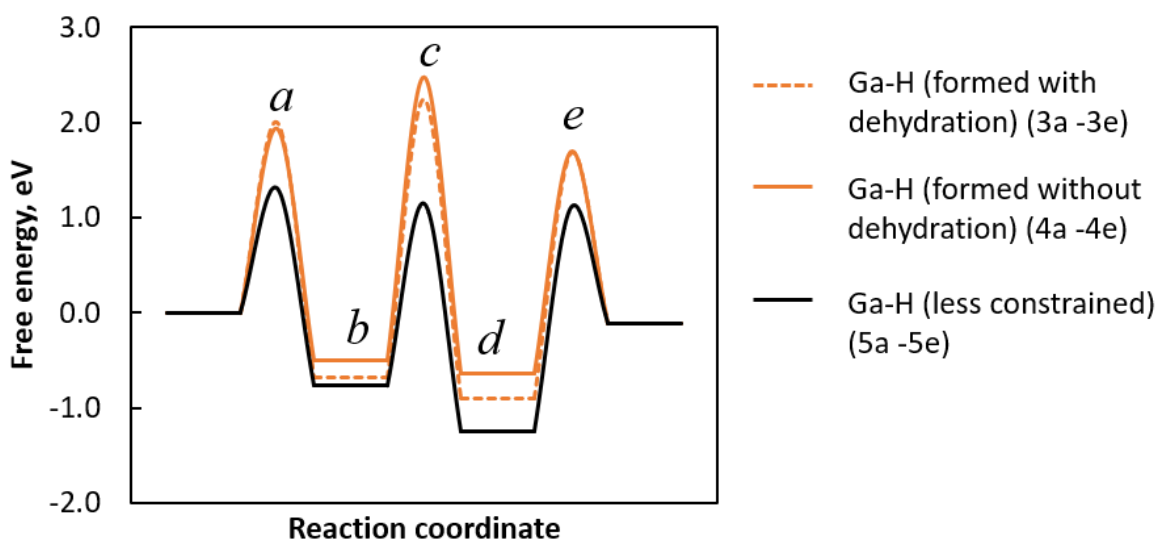

Figure C.6. Free energy landscapes of ethylene oligomerization on three types of Ga-H site: Ga-H formed without (orange, solid) and with (orange, dashed) dehydration, and a Ga-H located in a less constrained environment (black, solid)

VITA

Nicole LiBretto

Education

Purdue University, West Lafayette, IN   Graduation: July 2020
Doctor of Philosophy, Chemical Engineering

Stony Brook University (SUNY), Stony Brook NY   Graduation: May 2016
Bachelor's in Engineering, Chemical and Molecular Engineering with Energy Technology Specialization

Academic Employment
Research Assistant- (PhD, chemical engineering), Advised by Dr. Jeffrey T. Miller)
- Design and synthesize new catalysts for shale gas conversion (dehydrogenation, oligomerization)
- *In situ* characterization of catalysts using synchrotron radiation
- Understand the driving forces of high olefin selectivity in alloy catalysts for dehydrogenation
- Study reaction intermediates on non-traditional oligomerization catalysts
- Build atmospheric and high-pressure reactors for catalyst testing

National Renewable Energy Lab, Golden CO
Catalyst Design and Development Intern   June 2019-September 2019
- Synthesis and characterization of ternary phosphide catalysts
- Design of *in situ* electrochemistry cell to study structure of catalyst by x-ray absorption spectroscopy
- Data mining to form database of adsorption energy values and gain insight for predictive catalysis

Presentations at Professional Meetings
- LiBretto, Nicole; Zhang, Guanghui; Miller, Jeffrey T. (2019, June) Identification of Surface Structures in Pt_3Cr Intermetallic Nanocatalysts Oral Presentation presented at North American Catalysis Society Meeting, Chicago, IL
- LiBretto, Nicole; Zhang, Guanghui; Miller, Jeffrey T. (2019, April) Identification of Surface Structures in Pt_3Cr Intermetallic Nanocatalysts Poster presented at Chicago Catalysis Club, Naperville, IL
- LiBretto, Nicole; Zhang, Guanghui; Miller, Jeffrey T. (2018, October) Pt_3Cr catalysts for Propane Dehydrogenation Poster presented at CISTAR biannual meeting, Albuquerque, NM

Academic Awards
Outstanding Mentor Award   May 2019
CISTAR NSF Research Center Graduate Fellow   (2017- 2020)
Purdue University Ross Fellowship   (2016)

Professional Memberships
American Chemical Society (ACS)

PUBLICATIONS

1. LiBretto, Nicole J.; Cesar, Laryssa G.; Saxena, Arunima; Quigley, Aubrey; Nargund, Rhea; Edwards, Ethan; Rajamani; Zhang, Guanghui; Miller, Jeffrey T. High Temperature Olefin Oligomerization on Single Site Cobalt (II) Catalyst. ACS Catalysis (2020, *in preparation*).

2. LiBretto, Nicole J.; Xu, Yinan; Quigley, Aubrey; Nargund, Rhea; Jeffrey; Zhang, Guanghui; Miller, Jeffrey T. Olefin Metathesis on Silica-Supported Ga^{3+} and Zn^{2+} Single Site Catalysts. Journal of American Chemical Society (2020, *in preparation*).

3. LiBretto, Nicole J.; Xu, Yinan; Quigley, Aubrey; Edwards, Ethan; Nargund, Rhea; Vega-Vila; Juan Carlos; Saxena, Arunima; Gounder, Rajamani; Greeley, Jeffrey; Zhang, Guanghui; Miller, Jeffrey T. Olefin Oligomerization on Main Group Ga^{3+} and Zn^{2+} Single Site Catalysts. Nature Catalysis (2020, *in preparation*).

4. Downes, Courtney A.; LiBretto, Nicole J.; Harman-Ware, Anne E.; Happs, Renee M.; Ferrell III, Jack R.; Habas, Susan E.; Schaidle, Joshua A. Electrocatalytic CO_2 Reduction over Cu_3P Nanoparticles Generated via a Single-Source Precursor Route. (2020, *in preparation*).

5. LiBretto, Nicole J.; Bui, Tuong; Zubair, Muhammad; Unocic, Kinga; Baddour, Frederick G.; Griffin, Michael B.; Wegener, Evan C.; Miller, Jeffrey T.; Schaidle, Joshua A.; Bedford, Nicholas M.; Habas, Susan E. Structural Tunability in Ternary Metal Phosphides for Enhanced Catalytic Performance in Hydrodeoxygenation of Biomass-Derived Model Compounds. (2020, *in preparation*).

6. Pauletto, Gianluca; Mendil, Mathilde; LiBretto, Nicole; Mocellin, Paolo; Miller, Jeffrey T.; Patience, Gregory S. Short contact time CH4 partial oxidation over Ni based catalyst at 1.5 MPa. Chemical Engineering Journal (2020, submitted).

7. Pauletto, Gianluca; LiBretto, Nicole; Boffito, Daria C.; Miller, Jeffrey T.; Jentys, Andreas; Patience, Gregory S.; Lercher, Johannes. Design of Ni/CeO2 Supported FeCr Alloy Gauze for Methane Partial Oxidation. Applied Catalysis B (2020, *in preparation*).

8. Dou, Jin-Hu; Arguilla, Maxx Q.; Luo, Yi; Li, Jian; Zhang, Weizhe; Sun, Lei; Mancuso, Jenna L.; Yang, Luming; Chen, Tianyang; Parent, Lucas R.; Skorupskii, Grigorii; Libretto, Nicole J.; Sun, Chenyue; Miller, Jeffrey T.; Kong, Jing; Hendon, Christopher H.; Sun, Junliang; Dincă, Mircea. Atomically Precise Single Crystal Structures of Conductive 2D π-Conjugated MOFs. Nature Catalysis (2020, submitted).

9. Zhang, G.; LiBretto, N.J.; Purdy, S.C.; Cesar, L.G.; Miller, J.T. Surface Structure Determination of Catalytic Alloy Nano-Particles by X-ray Absorption Spectroscopy. Springer Handbook of Advanced Catalyst Characterization (2020, submitted).

10. Escorcia, Nicole J.; <u>LiBretto, Nicole J</u>.; Miller, Jeffrey T.; Li, Christina W. Colloidal Synthesis of Well-Defined Bimetallic Nanoparticles for Alkane Dehydrogenation. ACS Catalysis (2020, submitted).

11. Ko, Jeonghyun; Muhlenkamp, Jessica; Bonita, Yolanda; <u>LiBretto, Nicole</u>; Miller, Jeffrey; Hicks, Jason; Schneider, William. Experimental and computational investigation of the role of P in moderating ethane dehydrogenation performance over Ni-based catalysts. Industrial & Engineering Chemistry Research (2020, submitted).

12. Banda, Harish; Dou, Jin-Hu; Chen, Tianyang; <u>LiBretto, Nicole J</u>.; Miller, Jeffrey T.; Dinca, Mircea. Non-porous coordination polymer as a high-capacitance supercapacitor electrode through Li+ intercalation. Nature Materials (2019, submitted).

13. Marshall-Roth, Travis; <u>LiBretto, Nicole J</u>.; Wrobel, Alexandra; Anderton, Kevin; Ricke, Nathan D.; Van Voorhis, Troy; Betley, Theodore; Miller, Jeffrey T.; Surendranat, Yogesh. A Pyridinic Fe-N$_4$ Macrocycle Effectively Models the Active Sites in Fe/N-Doped Carbon Electrocatalysts. Nature Catalysis (2019, submitted).

14. Deshmukh, Swapnil; Easterling, Leah; Manheim, Jeremy; <u>LiBretto, Nicole</u>; Weideman, Kyle; Miller, Jeffrey; Kenttämaa, Hilkka; Agrawal, Rakesh. Analyzing and Tuning the Chalcogen-Amine-Thiol Complexes for Tailoring of Chalcogenide Syntheses. Inorganic Chemistry (2020, accepted).

15. Wang, Yuxan; Cao, Liang; <u>LiBretto, Nicole</u>; Li, Xing; Li, Chenyang; Wang, Yidong; He, Connie; Lee, Jinsung; Gregg, John; Zong, Han; Su, Dong; Miller, Jeffrey T.; Mueller, Tim; Wang, Chao. Ensemble Effect in Bimetallic Electrocatalysts for CO$_2$ reduction. Journal of the American Chemical Society, 141, 42, 16635-16642 (2019).

16. Yang, Feifei; <u>LiBretto, Nicole J</u>.; Miller, Jeffrey T.; Zhu, Xinlu; Resasco, Daniel E. MoO$_x$-modified Ni catalysts with Unique Properties for Hydrodeoxygenation of m-cresol. ACS Catalysis, 9, 7791-7800 (2019).

17. <u>LiBretto, Nicole J</u>.; Yang, Ce; Ren, Yang; Zhang, Guanghui; Miller, Jeffrey T. Identification of Surface Structures in Pt$_3$Cr Intermetallic Nanocatalysts. Chemistry of Materials, 31, 1597-1609 (2019).

18. Li, Zhe; Yu, Liang; Milligan, Cory; Ma, Tao; Zhou, Lin; Cui, Yanran; Qi, Zhiyuan; <u>LiBretto, Nicole</u>; Xu, Biao; Luo, Junwei; Shi, Enzheng; Wu, Zhenwei; Xin, Hongliang; Delgass, Nicholas W.; Miller, Jeffrey T.; Wu, Yue. Two-dimensional transition metal carbides as supports for tuning the chemistry of catalytic nanoparticles, Nature Communications, 9 (2018).

PATENTS

1. <u>LiBretto, Nicole</u>; Zhang, Guanghui; Miller, Jeffrey T. Zinc (II) and Gallium (III) Catalysts for Olefin Reactions. U.S. Provisional Patent Docket No. 68538-01 (2019)

2. <u>LiBretto, Nicole</u>; Purdy, Stephen; Wegener, Evan; Wu, Zhenwei; Miller, Jeffrey T. Novel Catalyst Compositions Used for Converting Shale Gas to Transportation Fuels. U.S. Provisional Patent Application No. 62/545,972 (2018)